The background of the cover is a deep space image filled with numerous galaxies of various colors (red, orange, blue, green) and sizes, set against a dark black background. A prominent white signal line, resembling a spectral or light curve, runs horizontally across the middle of the image. It starts with a very sharp, tall peak on the left side, then continues with a series of smaller, irregular peaks and troughs, ending with another sharp peak on the right side. The text is overlaid on this background.

EARLY PHASES OF GALAXY FORMATION:  
A DETAILED STUDY OF STAR-FORMING GALAXIES  
AT COSMIC NOON

MARIO LLERENA





UNIVERSIDAD  
DE LA SERENA  
CHILE



DEPARTAMENTO  
ASTRONOMÍA

# **Early phases of galaxy formation: a detailed study of star-forming galaxies at Cosmic Noon**

Mario Llerena





# UNIVERSIDAD DE LA SERENA

CHILE

## **Doctoral Thesis**

To fulfill the requirements for the degree of  
Doctor of Philosophy in Astronomy  
at Universidad de La Serena under the supervision of  
Prof. Dr. Ricardo Amorín (Astronomy, Universidad de La Serena)

**Mario Llerena**

July 11, 2023

**Dissertation Committee:**

Dr. Valentino González (Universidad de Chile)

Dr. Lucia Guaita (Universidad Andrés Bello)

Dr. Paulina Troncoso (Universidad Central)

Dr. Rodrigo Carrasco (Gemini Observatory/NSF's NOIRLab)

**Doctoral Advisory Committee:**

Dr. Antonela Monachesi (ULS)

Dr. Facundo Gómez (ULS)

Dr. Rodrigo Carrasco (Gemini Observatory/NSF's NOIRLab)

**Cover Image:** Color mosaic of the Epoch 1 JWST/NIRCam observations for the *Cosmic Evolution Early Release Science Survey* (CEERS, [Bagley et al., 2023](#)). These data consist of NIRCam imaging in six broadband filters (F115W, F150W, F200W, F277W, F356W, and F444W) and one medium band filter (F410M) over four pointings of the Extended Groth Strip (EGS) Hubble Space Telescope (HST) legacy field (Right Ascension: 14h 16m 59.99s, Declination: 52° 30' 0.0"). Full image available in this [link](#). The white line is an example of the rest-UV spectrum of a metal-poor star-forming galaxy as described in Chapter 3.

**Credit:** NASA/STScI/CEERS/TACC/S. Finkelstein/M. Bagley/R. Larson/Z. Levay (2022)

# Contents

	<b>Page</b>
<b>Abstract</b>	<b>7</b>
<b>Resumen</b>	<b>9</b>
<b>1 Introduction</b>	<b>12</b>
1.1 Galaxy formation . . . . .	12
1.1.1 Assembly of galaxies . . . . .	13
1.1.2 How do galaxies sustain star formation? . . . . .	15
1.2 Cosmic history of the Universe . . . . .	17
1.2.1 Galaxies in the Epoch of Reionization . . . . .	18
1.2.2 The Cosmic Noon . . . . .	22
1.3 Metal content in star-forming galaxies . . . . .	24
1.3.1 Mass-Metallicity relation . . . . .	25
1.3.2 Relative chemical abundances . . . . .	27
1.4 Gas kinematics and stellar feedback . . . . .	29
1.5 Scope of this Thesis . . . . .	32
<b>2 Methodology</b>	<b>34</b>
2.1 Spectroscopy at Cosmic Noon . . . . .	34

2.1.1	The VUDS survey . . . . .	37
2.1.2	The VANDELS survey . . . . .	37
2.2	Spectral Energy Distribution fitting . . . . .	38
2.3	Photoionization models . . . . .	40
<b>3</b>	<b>Rest-UV properties of CIII] emitters at <math>z \sim 3</math></b>	<b>43</b>
3.1	Context . . . . .	43
3.2	Methodology . . . . .	45
3.2.1	Sample selection . . . . .	45
3.2.2	Systemic redshift and basic properties of the sample . . . . .	47
3.2.3	Stacking procedure . . . . .	50
3.2.4	Line measurements . . . . .	59
3.3	Results . . . . .	60
3.3.1	Identification of UV absorption and emission lines . . . . .	60
3.3.2	Relation of EW(CIII]) with luminosity and stellar mass . . . . .	65
3.3.3	Diagnostic diagrams based on UV emission lines . . . . .	66
3.3.4	An apparent EW(Ly $\alpha$ )-EW(CIII]) correlation . . . . .	69
3.3.5	A relation between stellar metallicity and the CIII] and Ly $\alpha$ equivalent widths	71
3.3.6	C/O ratio and its relation with EW and physical parameters . . . . .	74
3.3.7	On the relation of SFR with EW(CIII]) and C/O . . . . .	77
3.4	Discussions . . . . .	78
3.4.1	On the stellar mass-metallicity relation of CIII] emitters at $z \sim 3$ . . . . .	78
3.4.2	On the stellar metallicity - C/O relation at $z \sim 3$ . . . . .	82
3.4.3	Caveats related with stacking methods . . . . .	85
3.4.4	Analysis of non-detected CIII] emitters in the parent sample . . . . .	86
3.5	Conclusions . . . . .	89

---

<b>4</b>	<b>Ionized kinematics of low-mass SFGs at <math>z \sim 3</math></b>	<b>91</b>
4.1	Context . . . . .	91
4.2	Data and sample selection . . . . .	93
4.2.1	Sample selection from rest-frame UV spectroscopy . . . . .	93
4.2.2	Rest-frame optical spectroscopy . . . . .	94
4.3	Physical parameters of the final sample . . . . .	98
4.3.1	Spectral Energy Distribution modeling . . . . .	98
4.3.2	Emission-line fluxes and EWs . . . . .	103
4.3.3	SFR surface density . . . . .	110
4.4	Results . . . . .	111
4.4.1	Ionizing sources: Diagnostic diagrams . . . . .	111
4.4.2	Ionization parameter . . . . .	113
4.4.3	EW relations . . . . .	114
4.4.4	Electron densities and temperatures . . . . .	115
4.4.5	Oxygen and Carbon abundance . . . . .	116
4.4.6	Ionized gas kinematics . . . . .	120
4.5	Discussions . . . . .	124
4.5.1	Mass-Metallicity and Fundamental Metallicity relations . . . . .	124
4.5.2	The C/O-O/H relation . . . . .	126
4.5.3	Outflow properties and their relation with star formation rate density . . . . .	128
4.5.4	Effects of stellar feedback on chemical abundances . . . . .	131
4.6	Conclusions . . . . .	133
<b>5</b>	<b>Characterization of EELGs at <math>z \gtrsim 4</math> with JWST data</b>	<b>136</b>
5.1	Context . . . . .	137
5.2	Data . . . . .	138
5.2.1	Photometry catalogs . . . . .	138

---

5.2.2	Templates of EELGs . . . . .	138
5.3	Synthetic NIRCам observations . . . . .	139
5.4	Results . . . . .	140
5.4.1	Color-color diagrams . . . . .	140
5.4.2	Physical parameters . . . . .	146
5.4.3	NIRSpec spectroscopy . . . . .	149
5.4.4	Ionization source and scaling relations . . . . .	151
5.5	Summary . . . . .	153
<b>6</b>	<b>Conclusions and perspectives for future</b>	<b>156</b>
6.1	Concluding remarks . . . . .	156
6.2	My perspectives for future work . . . . .	159
	<b>Bibliography</b>	<b>162</b>
	<b>Publications</b>	<b>176</b>
	<b>Acknowledgements</b>	<b>178</b>

## Abstract

Strong nebular emission is ubiquitous in galaxies that contribute to cosmic reionization at  $z \gtrsim 6$ . High-ionization UV metal lines, such as CIII] $\lambda$ 1908Å, show high equivalent widths (EW) in these early galaxies, suggesting harder radiation fields at low metallicity than low- $z$  galaxies of similar stellar mass. Understanding the physical properties driving the observed UV nebular line emission at high- $z$  requires large and very deep spectroscopic surveys. Feedback from massive stars plays a crucial role in regulating the growth of young star-forming galaxies (SFGs) and in shaping their interstellar medium (ISM). This feedback contributes to the removal and mixing of metals via galactic outflows and to the clearance of neutral gas, which facilitates the escape of ionizing photons. Analogs of such systems at lower- $z$  are crucial to understanding the early phases of galaxy formation.

In this Thesis, we aim to investigate the properties of extreme emission-line galaxies and their role in the evolution of galaxies throughout the history of the Universe. Specifically, we first study in detail the physical properties of a significant and representative sample of star-forming galaxies rapidly assembling at  $z \sim 2 - 4$  covering a wide range of parameters with stacked and single spectra from deep surveys. Later, we present new near-IR follow-up spectroscopy that is used to study the impact of stellar feedback on the chemical abundances of the ISM in a sample of SFGs with strong emission lines at  $z \sim 3$ . These are the two papers that constitute the main body of this Thesis.

In our first paper, we study the mean properties of a large representative sample of 217 galaxies showing CIII] emission at  $2 < z < 4$ , selected in the VANDELS survey. These CIII] emitters have a broad range of UV luminosities, allowing for a detailed stacking analysis to characterize their stellar mass, star formation rate (SFR), and metallicity as a function of the UV emission line ratios, EWs, and the carbon-to-oxygen (C/O) abundance ratio. Stacking provides unprecedented high signal-to-noise (S/N) spectra for CIII] emitters over more than three decades in luminosity, stellar mass, and SFR. This enables a full spectral fitting to derive stellar metallicities for each stack. Moreover, we use diagnostics based on photoionization models and UV line ratios to constrain the ionization sources of the galaxies and derive the C/O abundance. Reliable CIII] detections ( $S/N \geq 3$ ) represent  $\sim 30\%$  of the parent sample. However, stacked spectra of non-detections ( $S/N < 3$ ) show weak ( $EW \lesssim 2\text{\AA}$ ) CIII] emission, suggesting that this line is common in normal star-forming galaxies at  $z \sim 3$ . On the other hand, extreme CIII] emitters ( $EW(\text{CIII])} \gtrsim 8\text{\AA}$ ) are exceedingly rare ( $\sim 3\%$ ) in VANDELS. The UV line ratios of the sample suggest no ionization source other than massive stars. Stacks with larger  $EW(\text{CIII])}$  show larger  $EW(\text{Ly}\alpha)$  and lower metallicity, but not all CIII] emitters are  $\text{Ly}\alpha$  emitters. The stellar metallicities of CIII] emitters are not significantly different from that of the parent sample, increasing from  $\sim 10\%$  to  $\sim 40\%$  solar for stellar masses  $\log(M_*/M_\odot) \sim 9-10.5$ . The stellar mass-metallicity relation of the CIII] emitters is consistent with previous works, exhibiting a strong evolution from  $z = 0$  to  $z \sim 3$ . The C/O abundances of the sample range between 35%-150% solar, with a noticeable increase with FUV luminosity and a smooth decrease with the CIII] EW. Finally, we discuss for the first time the CIII] emitters in the C/O-Fe/H and the C/O-O/H planes simultaneously. We find that they follow stellar and nebular abundance trends consistent with those of Milky Way halo and thick-disk stars and local HII galaxies, respectively. A qualitative agreement is also found with chemical evolution models, which suggests that CIII] emitters at  $z \sim 3$  are experiencing an active phase of chemical enrichment.

In our second paper, we selected 35 low-mass SFGs ( $7.9 < \log(M_*/M_\odot) < 10.3$ ) at  $z \sim 3$  from deep optical spectroscopic surveys based on their CIII] emission. We present new follow-up near-

infrared (NIR) observations providing access to their rest-optical emission lines. We characterized the galaxies' gas-phase metallicity and C/O abundance using a  $T_e$ -based method via photoionization models and the  $[\text{OIII}]\lambda 1666 / [\text{OIII}]\lambda 5007$  ratio. We find line ratios and rest-frame EWs characteristic of high-ionization conditions powered by massive stars. Our sample displays mean rest-frame  $\text{EW}([\text{OIII}]\lambda 5007)$  of  $\sim 560\text{\AA}$ , while about 15% of them show  $\text{EW}([\text{OIII}]\lambda\lambda 4959, 5007) > 1000\text{\AA}$  and  $\text{EW}(\text{CIII}) > 5\text{\AA}$ , closely resembling those now seen in Epoch of Reionization (EoR) galaxies with JWST. We find high  $T_e$  values, which imply low gas-phase metallicities  $12+\log(\text{O}/\text{H}) \sim 7.5 - 8.5$  (mean of 17% solar) and C/O abundances from 23% to 128% solar, with an apparent increasing trend with metallicity. These results confirm the low gas-phase metallicities estimated for the global population discussed in our first paper. Our sample follows the mass-metallicity relation at  $z \sim 3$ , with some galaxies showing lower gas-phase metallicities thus resulting in significant deviations from the mass-metallicity-SFR relation. Moreover, we discuss the differences found in metallicity based on methods that depend on the electron temperature and calibrations using emission lines. Next, we use the spectra to identify ionized outflow signatures through broad emission line wings detected after Gaussian modeling of their emission lines profiles. From our  $[\text{OIII}]\lambda\lambda 4959, 5007$  line profile modeling, we find that 65% of our sample shows an outflow component, which is found both blue- or red-shifted relative to the ionized gas systemic velocity, and have mean maximum velocities of  $v_{\text{max}} \sim 280 \text{ km s}^{-1}$ . We find a weak correlation between  $v_{\text{max}}$  and the star-formation rate surface density ( $\Sigma_{\text{SFR}}$ ) such as  $v_{\text{max}} = (2.41 \pm 0.03) \times \Sigma_{\text{SFR}}^{(0.06 \pm 0.03)}$ . Moreover, we find that the mass-loading factor  $\mu$  of our galaxy sample is typically lower than in more massive galaxies from literature but is higher than in typical local dwarf galaxies. In the stellar mass range covered by our sample, we find that  $\mu$  increases with  $\Sigma_{\text{SFR}}$  thus suggesting that for a given stellar mass, denser starbursts in low-mass galaxies produce stronger outflows. Our results complement the picture drawn by similar studies at lower redshift, suggesting that the removal of ionized gas in low-mass SFGs driven by stellar feedback is regulated by their stellar mass *and* by the strength and concentration of their star formation, i.e.  $\Sigma_{\text{SFR}}$ .

Finally, we present an ongoing project where we exploit the new medium and broadband NIRCам photometry in the Extended Groth Strip (EGS) Field obtained from the JWST Cosmic Evolution Early Release Science Survey (CEERS) to identify extreme emission-line galaxies (EELG) candidates at  $z \gtrsim 4$  selected from their extreme  $[\text{OIII}]\lambda 5007$  and  $\text{H}\alpha$  EWs. We perform synthetic NIRCам observations based on empirical templates of local metal-poor starbursts to establish new color-based selection criteria. This is then used to select 521 candidates with  $\text{EW}([\text{OIII}]) \gtrsim 450\text{\AA}$  at  $3.8 < z < 8.5$ . Based on multiband SED fitting, we find that they have low-stellar masses ( $\log(M_*/M_\odot) \sim 8.05$ ), high specific SFR ( $> 10^{-8} \text{ yr}^{-1}$ ), high ionization parameters ( $\log U \sim -2.16$ ), low dust attenuation ( $A_V \sim 0.34 \text{ mag}$ ) and young ages (12.5 Myr after the onset of the star-forming episode). We validate our method with a subsample of candidates that are spectroscopically confirmed with JWST/NIRSpec Prism and medium-resolution observations. This work represents the first step of a more detailed analysis allowing the full characterization of young EELGs from  $z \sim 4$  to well within the EoR.

## Resumen

La emisión nebular intensa es una característica común observada en las galaxias que contribuyen a la reionización cósmica a corrimientos al rojo  $z \gtrsim 6$ . Los altos anchos equivalentes (EW, en inglés) de las líneas metálicas ultravioleta (UV) de alta ionización, como CIII] $\lambda$ 1908Å, sugieren la presencia de campos de radiación más intensos y una menor metalicidad comparado con galaxias a bajo  $z$  de similar masa estelar. Comprender las propiedades físicas que permiten la emisión intensa de dichas líneas nebulares requiere estudios espectroscópicos amplios y muy profundos. La retroalimentación de las estrellas masivas juega un papel crucial en la regulación del crecimiento de las jóvenes galaxias con formación estelar (SFG, en inglés) y en regular las propiedades de su medio interestelar (ISM, en inglés). Esta retroalimentación contribuye a la remoción y mezcla de metales a través de vientos galácticos y también a la remoción de gas neutro, lo que facilita el escape de fotones ionizantes. Los análogos de tales sistemas a  $z$  menores son cruciales para comprender las primeras fases de la formación de galaxias.

En esta Tesis, nuestro objetivo es investigar las propiedades de galaxias con líneas de emisión extremas (EELG, en inglés) y entender su papel en la evolución de las galaxias a lo largo de la historia del Universo. Específicamente, primero estudiamos en detalle las propiedades físicas de una muestra significativa y representativa de galaxias en formación de estrellas que se ensamblan rápidamente a  $z \sim 2 - 4$ . La muestra cubren una amplia gama de parámetros. Usamos espectros apilados y espectros individuales con líneas de emisión UV obtenidos con relevamientos profundos. Más adelante, presentamos espectroscopía del IR cercano que usamos para estudiar el impacto de la retroalimentación estelar y los vientos galácticos en las abundancias químicas del ISM en una muestra de SFG a  $z \sim 3$ . Estos son los dos trabajos que constituyen el cuerpo principal de esta Tesis.

En nuestro primer artículo, estudiamos las propiedades globales de una gran muestra representativa de 217 galaxias con emisión de CIII] a  $2 < z < 4$ , seleccionadas en el relevamiento VANDELS. Estos emisores de CIII] tienen una amplia gama de luminosidades UV, lo que permite un análisis de detallado para caracterizar su masa estelar, tasa de formación de estrellas (SFR, en inglés) y metalicidad estelar en función de razones de flujos de líneas de emisión UV, sus EWs y la abundancia relativa de carbono a oxígeno (C/O). Usamos espectros apilados los cuales proporcionan espectros medios de alta señal a ruido (S/N), sin precedentes, para emisores de CIII] en un rango de tres órdenes de magnitud en luminosidad, masa estelar y SFR. Esto permite un ajuste del espectro FUV completo para derivar metalicidades estelares para cada espectro apilado. Además, utilizamos diagnósticos basados en modelos de fotoionización y razones de flujo de líneas UV para restringir las fuentes de ionización de las galaxias y derivar las abundancias de C/O. Las detecciones confiables de CIII] ( $S/N \geq 3$ ) representan  $\sim 30\%$  de la muestra principal. Sin embargo, los espectros sin detección de CIII] ( $S/N < 3$ ) muestran una emisión débil ( $EW \lesssim 2\text{Å}$ ) CIII], lo que sugiere que esta línea es común en las galaxias con formación estelar normal a  $z \sim 3$ . Por otro lado, los emisores CIII] extremos ( $EW(\text{CIII])} \gtrsim 8\text{Å}$ ) son extremadamente raros ( $\sim 3\%$ ) en VANDELS. Las razones de flujo de las líneas UV sugieren que no hay otra fuente dominante diferente a las estrellas masivas. Los espectros con mayor EW(CIII]) muestran mayor EW(Ly $\alpha$ ) y menor metalicidad, pero no todos los emisores CIII] son emisores Ly $\alpha$ . Las metalicidades estelares de los emisores CIII] no son significativamente diferentes de las de la muestra principal, aumentando de  $\sim 10\%$  a  $\sim 40\%$  solar para masas estelares  $\log(M_*/M_\odot) \sim 9-10.5$ . La relación masa-metalicidad estelar de los emisores CIII] es consistente con trabajos previos, exhibiendo una fuerte evolución de  $z = 0$  a  $z \sim 3$ . Las abundancias de C/O de la muestra oscilan entre el 35%-150% solar, con un aumento notable con la luminosidad FUV y una suave disminución con el

EW(CIII]). Finalmente, discutimos por primera vez la posición de los emisores de CIII] en los planos C/O-Fe/H y C/O-O/H, simultáneamente. Encontramos que tanto la abundancia nebular como la estelar siguen tendencias consistentes con las de las estrellas de disco grueso y halo de la Vía Láctea y las galaxias HII locales, respectivamente. También se encuentra una concordancia cualitativa con los modelos de evolución química, lo que sugiere que los emisores CIII] en  $z \sim 3$  están experimentando una fase activa de enriquecimiento químico.

En nuestro segundo artículo, seleccionamos 35 SFG de baja masa ( $7.9 < \log(M_*/M_\odot) < 10.3$ ) a  $z \sim 3$  de estudios espectroscópicos ópticos profundos basados en su emisión de CIII]. Presentamos nuevas observaciones de seguimiento espectroscópico en el infrarrojo cercano (NIR, en inglés) que brindan acceso a sus líneas de emisión óptica en reposo. Con ellos, caracterizamos la metalicidad nebular de las galaxias y la abundancia relativa C/O utilizando un método basado en  $T_e$  a través del coeficiente  $\text{OIII]}\lambda 1666/[\text{OIII]}\lambda 5007$  y modelos de fotoionización. Encontramos razones de línea y EW característicos de condiciones de alta ionización impulsadas por estrellas masivas. Nuestra muestra  $\text{EW}([\text{OIII]}\lambda 5007)$  de  $\sim 560\text{\AA}$  en promedio, mientras que aproximadamente el 15% de ellos muestra  $\text{EW}([\text{OIII]}\lambda\lambda 4959, 5007) > 1000\text{\AA}$  y  $\text{EW}(\text{CIII])} > 5\text{\AA}$ , muy parecidos a los observados en las galaxias de época de reionización (EoR) con JWST. Encontramos valores altos de  $T_e([\text{OIII}])$ , lo que implica bajas metalicidades nebulares  $12+\log(\text{O}/\text{H}) \sim 7.5 - 8.5$  (media de 17% solar) y abundancias de C/O entre 23% al 128% solar, con un aparente incremento con la metalicidad. Estos resultados confirman las bajas metalicidades nebulares estimadas para la población general de SFGs discutidas en nuestro primer artículo. Nuestra muestra sigue la relación masa-metalicidad en  $z \sim 3$ , con algunas galaxias que muestran metalicidades en fase gaseosa más bajas, lo que resulta en desviaciones significativas de la relación masa-metalicidad-SFR. Además, discutimos las diferencias encontradas en la metalicidad con base en métodos que dependen de la temperatura de los electrones y calibraciones usando líneas de emisión. A continuación, usamos los espectros para identificar evidencias de gas ionizado acelerado a altas velocidades a través de las componentes anchas detectadas en las líneas al modelar sus perfiles con modelos Gaussianos. A partir de nuestro modelo de dos Gaussianas del doblete  $[\text{OIII]}\lambda\lambda 4959, 5007$ , encontramos que el 65% de nuestra muestra presenta una componente ancha, que se encuentra desplazado hacia el azul o hacia el rojo en relación con la velocidad sistémica del gas ionizado, y tienen velocidades máximas medias de  $v_{\text{max}} \sim 280 \text{ km s}^{-1}$ . Encontramos una correlación poco significativa entre  $v_{\text{max}}$  y la densidad superficial de la tasa de formación de estrellas ( $\Sigma_{\text{SFR}}$ ) como  $v_{\text{max}} = (2.41 \pm 0.03) \times \Sigma_{\text{SFR}}^{(0.06 \pm 0.03)}$ . Además, encontramos que en nuestra muestra, el viento tiene un factor de carga en masa  $\mu$  que es, en promedio, menor que en las galaxias más masivas de la literatura, pero es más alto que en las típicas galaxias enanas locales. En el rango de masa estelar cubierto por nuestra muestra, encontramos que  $\mu$  aumenta con  $\Sigma_{\text{SFR}}$ , lo que sugiere que para una masa estelar dada, los estallidos de formación estelar más densos en galaxias de baja masa producen vientos más intensos. Nuestros resultados complementan el escenario planteado por estudios similares con menor corrimiento al rojo, que sugiere que los vientos galácticos impulsados por formación estelar reciente en galaxias de baja masa están regulados por su masa estelar y por la fuerza y concentración de su formación estelar, es decir,  $\Sigma_{\text{SFR}}$ .

Finalmente, presentamos un proyecto en curso en el que explotamos la nueva fotometría NIRCam de banda ancha y media en el campo Extended Groth Strip (EGS) obtenido del JWST Cosmic Evolution Early Release Science Survey (CEERS) para identificar candidatas a EELG a  $z \gtrsim 4$  seleccionados por sus altos EW en  $[\text{OIII]}\lambda 5007$  y  $\text{H}\alpha$ . Realizamos observaciones sintéticas con NIRCam basadas en plantillas empíricas de galaxias locales pobres en metales y con estallidos intensos formación estelar para establecer nuevos criterios de selección basados en el color. Esto luego se usa para seleccionar

---

521 candidatos con  $EW([\text{OIII}]) \gtrsim 450\text{\AA}$  a  $3.8 < z < 8.5$ . Con base en el ajuste SED multibanda, encontramos que tienen masas estelares bajas ( $\log(M_*/M_\odot) \sim 8.05$ ), SFR específico alto ( $>10^{-8}$  año $^{-1}$ ), altos parámetros de ionización ( $\log U \sim -2.16$ ), baja atenuación de polvo ( $A_V \sim 0.34$  mag) y joven (12.5Myr después del inicio del episodio de formación estelar). Validamos nuestro método con una submuestra de candidatos que se confirman espectroscópicamente con JWST/NIRSpec Prism y observaciones de resolución media. Este trabajo representa el primer paso de un análisis más detallado que permite la caracterización completa de EELG jóvenes desde  $z \sim 4$  hasta dentro de la EoR.

# Introduction

This Thesis aims at shedding new light on the early phases of galaxy evolution by exploring the physical properties of young galaxies that are actively forming a significant fraction of their stellar mass. To understand how galaxies evolve, it is important first to understand how they are formed and the physical mechanisms involved in their growth. Once a galaxy is formed, there are a range of different physical processes that work across many scales that will impact the final state of a galaxy. In this Chapter, a brief description of the context in which this Thesis resides is discussed. This Chapter 1 is divided into four sections. In Sec. 1.1, I start by briefly outlining our current galaxy formation and evolution model and the complex scenario in which galaxies form stars and grow in mass. This is followed in Sec. 1.2 by a description of the cosmic history of the Universe, with particular emphasis on the sources that ionize the Universe at the earliest epochs and the epoch when galaxies were more actively forming stars. In Sec. 1.3, I summarise the information we obtain by studying the metal content in galaxies and the physical processes that shape it. In Sec. 1.4, an overview of the stellar feedback is presented. Finally, in Sec. 1.5, the questions that are addressed in this Thesis are highlighted.

## 1.1 Galaxy formation

Galaxies are gravitationally bound systems consisting of baryonic material (mainly stars, gas, and dust) embedded in the potential well of extensive dark matter halos. They are the fundamental building blocks of the large-scale Universe, and studying their formation and evolution is an active area of research in astrophysics and cosmology.

In a cosmological framework, the  $\Lambda$ CDM – where  $\Lambda$  stands for the cosmological constant related to the so-called dark energy and CDM stands for cold dark matter – model (Peebles, 1984; Blumenthal et al., 1984; Carroll, 2001) has become the leading theoretical paradigm that can predict the formation of structure in the Universe while reproducing the properties of the Cosmic Microwave Background (CMB) with a few number of parameters (e.g., Planck Collaboration et al., 2020). Therefore, the  $\Lambda$ CDM is currently the golden standard for setting the most advanced cosmological simulations which are able to reproduce the observed properties of galaxies (e.g., Schneider, 2006).

Based on results from the Planck satellite (Planck Collaboration et al., 2020), our Universe is spatially flat and dominated by dark matter and dark energy accounting for about  $\sim 95\%$  of the energy density. Normal matter (the one that we can actually *see*) makes up for the remaining  $\sim 5\%$  and is referred collectively to as baryons. In this context, dark energy is a constant that behaves just like the energy density of the vacuum and drives the Universe’s accelerated expansion. On the other hand, dark matter is assumed to be a collisionless form of cold matter that does not interact with baryonic matter besides gravitational interactions and accounts for  $\sim 84\%$  of the matter density.

As dark matter is the dominant contributor to the matter density of the Universe, it builds the key ingredient for the formation of galaxies, which are expected to form at the centers of dark matter overdensities, usually known as halos, by gravitational collapse of baryonic matter (see Vogelsberger et al., 2020, for a review). Dark matter collapse is halted when a halo is virialized, occurring once the self-gravity is balanced by kinetic energy due to thermal motions. This happens once the matter density reaches a mean density 200 times the critical density of the Universe, which is confirmed by numerical simulations (e.g., Cole & Lacey, 1996). CDM N-body simulations (e.g., Millennium simulations Springel et al., 2005) predict that the large-scale distribution of dark matter is not completely homogeneous but instead exhibits a web-like structure consisting of voids, filaments, and halos. One key feature of galaxy formation is that structures form hierarchically, i.e., small halos form earliest and merge into more massive halos later (see a more detailed description in Sec. 1.1.1). The  $\Lambda$ CDM model, therefore, provides a distribution of halos where galaxies can form, and the details of their formation rely on baryonic physics.

Simulating baryons is, therefore, crucial to making predictions for the visible Universe. Hydrodynamical simulations – e.g., IllustrisTNG (Springel et al., 2018) for large-volume simulations or Auriga (Grand et al., 2017) for zoom-in simulations – have successfully been directly confronted with observational data providing important tests for galaxy formation models, and they reproduce galaxy populations that agree remarkably well with observations. However, many detailed predictions of these simulations are still sensitive to the underlying implementation of a wide range of astrophysical processes such as gas cooling, star formation, stellar feedback, supermassive black hole formation, and radiation fields, which is a complex interplay to describe the formation of galaxies.

Among the plethora of observables that are reproduced with simulations is the galaxy stellar mass function which is shaped by stellar and active galactic nuclei (AGN) feedback in low and high mass galaxies, respectively (Genel et al., 2014). Also, the distribution and properties of gas around galaxies including the circumgalactic medium (CGM), the intracluster medium (ICM), and the intergalactic medium (IGM) (Peeples et al., 2019) or color of galaxies as a function of galaxy stellar mass can now be reasonably well reproduced by cosmological simulations (Trayford et al., 2015; Nelson et al., 2018). Large-volume hydrodynamical simulations broadly reproduce many galaxy scaling relations including the Mass-Size relation (Shen et al., 2003) and the Mass-Metallicity relation (Torrey et al., 2019), which are crucial to track their evolution.

### 1.1.1 Assembly of galaxies

In the standard  $\Lambda$ CDM paradigm, an important feature is that galaxies are formed *bottom-up*. This means that the first structures to form in the Universe are low-mass dark haloes that progressively merge to produce larger and more massive structures (Peebles, 1980; Blumenthal et al., 1984). Small

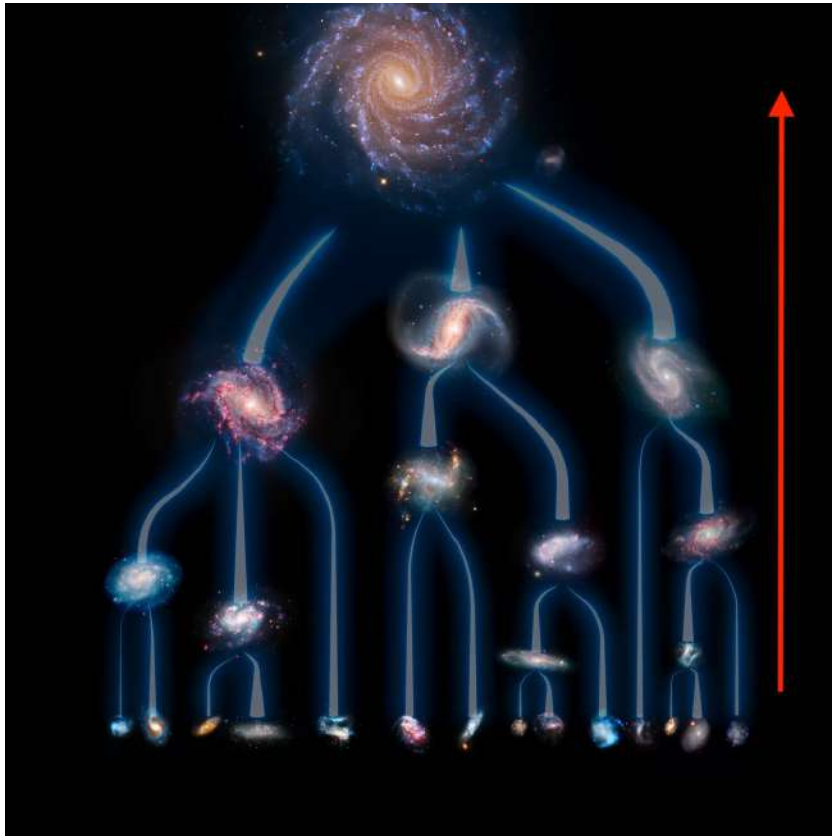


Figure 1.1.1: Schematic diagram of the hierarchical assembly where small halos, acting as galactic building blocks, formed first, only to merge into larger galaxies over the lifetime of the Universe. The red arrow is the direction of the time passing. Credit: ESO/L. Calçada. Figure taken from this [link](#).

dark matter halos form first because small overdensities are able to overcome the cosmological expansion and collapse first, and halo growth continues through a combination of essentially smooth accretion and mergers of dark matter halos, which serve as places of galaxy formation. This process continues until today, making galaxy formation an ongoing process. An illustrative scheme of the assembly is displayed in Fig. 1.1.1.

Baryons then infall into the dark potential wells of such small overdensities; they cool and form stars and rotationally supported galaxies (Fall & Efstathiou, 1980). Therefore, merging is considered one of the main mechanisms for assembling mass in galaxies (Kauffmann et al., 1993; Bell, 2004). Since low-mass galaxies are the building blocks in this hierarchical scenario, they are essential for a better understanding of the early phases of galaxy evolution.

But galaxies also can grow in mass through rapid episodes of star formation. In this case, for instance, mergers and fainter interactions with gas-rich companions can also drive short-lived starburst episodes and trigger the formation of new stars (Starkenburg et al., 2016) with a subsequent increase in their stellar mass content. But not only real interactions with companions are needed since galaxies can also grow in mass by smooth gas accretion from the cosmic web in their surrounding IGM, which triggers star-forming episodes in H $\alpha$ -bright, off-center clumps (Ceverino et al., 2016). For this reason, understanding the mechanisms by which gas is converted into stars is essential to describe the assembly of galaxies.

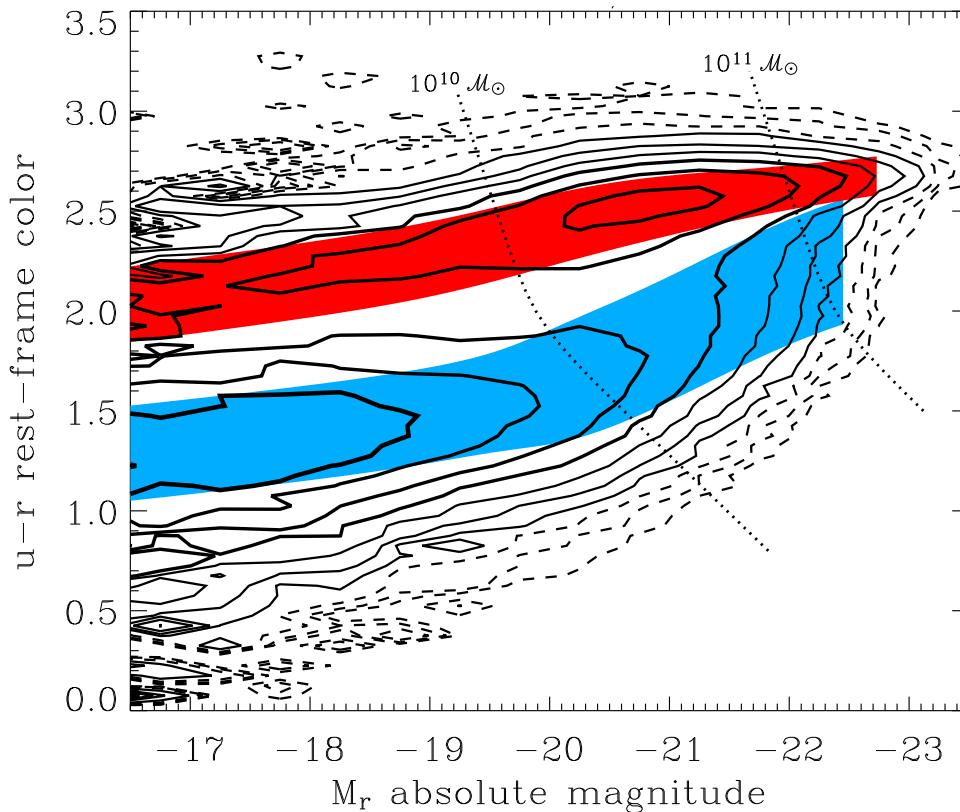


Figure 1.1.2: Illustration of galaxy bimodality. The contours are the density of Sloan Digital Sky Survey (SDSS) galaxies in color-luminosity space after correction for selection effects. The red and blue shaded regions show the mean and dispersion of the red and blue sequences based on the fitting described by [Baldry et al. \(2004\)](#). Figure taken from [Silk & Mamon \(2012\)](#).

### 1.1.2 How do galaxies sustain star formation?

A notable observation of large samples of galaxies is that there is a clear bimodality in several properties that describe the galaxy population in the present-day Universe ([Baldry et al., 2004](#)), but it is observed to already exist at half of the age of the Universe ([Bell et al., 2004](#)). This bi-modality is predominantly expressed in terms of galaxies' colors, in which two clear peaks are identified corresponding to a red and a blue sequences, which are generally ascribed to early-type and late-type galaxies, respectively. An example of such bimodality in local galaxies is displayed in Fig. 1.1.2.

The origin of galaxy bimodality lies in the relation between galaxy mass, the dominant mode of stellar mass growth (in situ star formation versus growth through merging), and the rate at which this happens ([Trayford et al., 2015](#)). Besides understanding the details of this bimodality, a number of big questions dominate present-day extragalactic astronomy. These include the exact interplay between feedback from star formation and supermassive black hole growth and gas in the ISM and CGM or the connection between galaxies observed at different cosmic times.

Blue galaxies tend to have a spiral structure (e.g., [Strateva et al., 2001](#)), while red galaxies tend to be elliptical galaxies residing in over-dense regions (e.g., [Peng et al., 2010b](#)). In particular, galaxies in the blue cloud are actively forming new stars, and they are called Star-Forming Galaxies (SFG). In

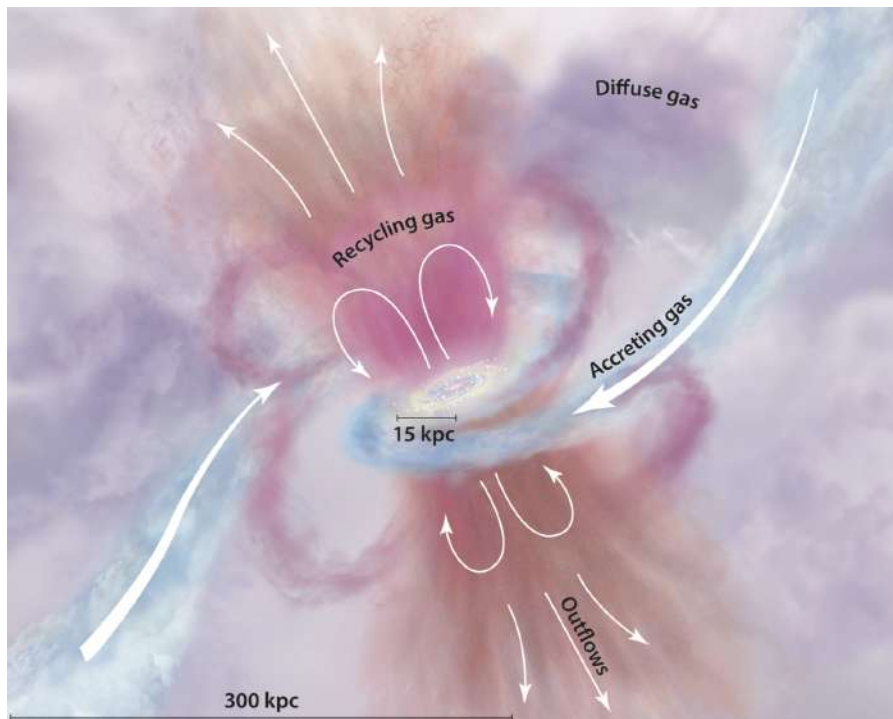


Figure 1.1.3: A cartoon view of the CGM. The galaxy's red central bulge and blue gaseous disk are fed by filamentary accretion from the IGM (blue). Outflows emerge from the disk in pink and orange, while gas that was previously ejected is recycled. The diffuse gas halo in varying tones of purple includes gas likely contributed by all these sources and mixed together over time. Figure taken from [Tumlinson et al. \(2017\)](#).

this Thesis, our focus is on this kind of galaxies.

Gas is the raw material that makes a galaxy form stars or not. An illustration of the complexity of gas accretion to sustain the formation of new stars is shown in Fig. 1.1.3. The space between the stars in a galaxy is usually called the interstellar medium (ISM), and many different physical processes occur in this region, occupied by mainly gas and dust. The gas surrounding galaxies outside their ISM and inside their virial radii is known as the CGM. The gas outside the CGM is usually known as IGM. The CGM is a reservoir of gas that can be accreted into the ISM to condense and form stars. Inflows from the IGM feed the gas in this reservoir. The gas reservoir in the ISM is used to form molecular clouds and stars. But this gas is not confined to the interior of the galaxy. The ISM can lose mass via outflows due to galactic winds produced by stellar or AGN feedback. Such winds can be driven by supernova explosions and/or energetic radiation and jet flows originating from supermassive black holes. Also, the gas in the ISM evolves chemically, i.e., their metal content can change with time. Stellar winds and supernova explosions at the end stages of the lives of stars chemically enrich the ISM. On the other hand, the ISM gas can also gain mass due to inflows of accreted material along the CGM and also with recycled material that was previously expelled from the ISM but is re-accreted afterward. All these different states of matter (hot gas, cold gas, stars, accretion disks around black holes) emit photons that can be observed with different sensitivities.

Star formation in galaxies is a complex process, but as a driver ingredient, details of the different phases of the gas are important to interpret the observations of galaxies.

## 1.2 Cosmic history of the Universe

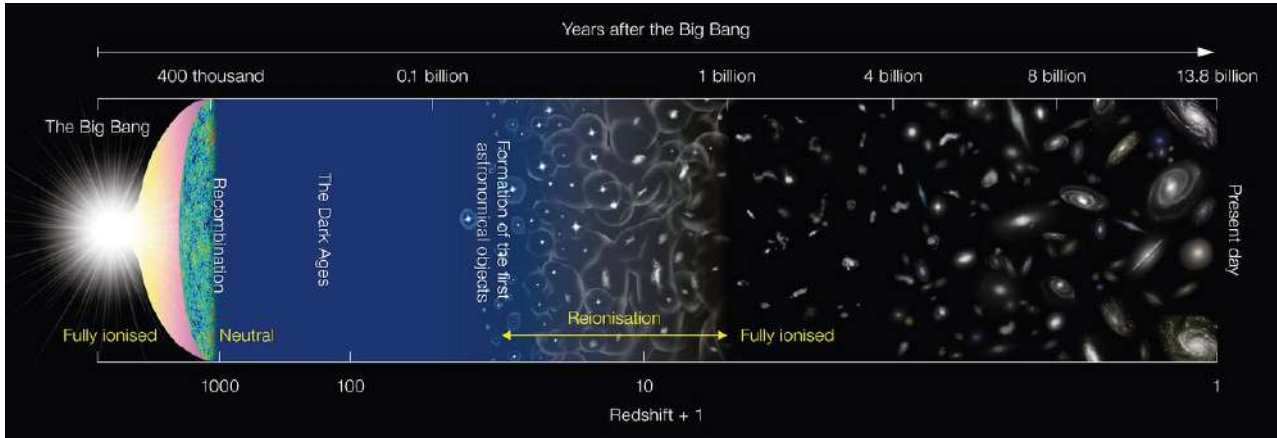


Figure 1.2.1: Illustration of the evolution of the Universe since the Big Bang, about 13.8 Gyr ago. The major early epochs are highlighted in the illustration and the time (not to scale) after the Big Bang. The Universe was in a neutral state 0.4 Myr after the Big Bang and remained that way until the light from the first generation of stars started to ionize the hydrogen. After  $\sim 1$  Gyr, the gas in the Universe was completely ionized. Credit: NAOJ. The figure is taken from this [link](#).

Understanding galaxies' detailed process of evolution implies studying their changes along the cosmic history of  $\sim 13.8$  Gyr from the Big Bang to the present day (Planck Collaboration et al., 2020). A diagram picturing the evolution of the Universe is shown in Fig. 1.2.1. In the first 0.4 Myr of this long evolutionary history, the Universe was filled with a hot, dense fog of ionized gas. As the Universe cooled and expanded, electrons and protons were able to combine to form the first neutral atoms. When this happened, thermal energy could travel freely throughout the Universe. This radiation has cooled and been red-shifted by a factor of  $\sim 1100$  due to the expansion of the Universe. Today we observe the remnants of this radiation as the CMB, which has revealed that the very early Universe contained tiny density fluctuations (on the order of  $10^{-5}$  K in temperature) and is crucial for the  $\Lambda$ CDM model as we mentioned in Sec. 1.1.

After the CMB became imprinted on the Universe, the entire Universe became opaque due to the absorbing effects of atomic hydrogen (or HI). This began a long period known as the *Dark Ages*, dominated by the absence of stars and the extremely dense intervening HI gas (e.g., Miralda-Escudé, 2003). Over time, areas of higher gas density started to collapse under gravity, and the neutral matter began to clump together. According to simulations (e.g., Yoshida et al., 2003), the slow cooling in halos of  $10^6 M_{\odot}$  led to the formation of a central core with a mass of  $10^2$  to  $10^3 M_{\odot}$  of gas cooled to  $\sim 200$  K. This core may cool and collapse, igniting nuclear fusion in their cores and leading to the emergence of the first massive stars, known as Population III (Pop III). Such massive stars emit a large fraction of their light as photons with energies greater than 13.6 eV that can ionize hydrogen, which heats the surrounding IGM, once again ionizing the hydrogen and creating regions of ionized hydrogen (or HII regions), heating the gas to  $T \sim 10^4$  K, and affecting the formation of subsequent stars.

The first generations of galaxies started to form in halos with masses  $\sim 10^7 - 10^9 M_{\odot}$ . They formed stars efficiently, but their gas was susceptible to being blown out due to the effects of the first supermassive stars exploding as supernovae and the weak gravitational potential wells in such

relatively low-mass systems. In more massive halos, galaxies more resistant to major gas losses were formed with strong star formation and are reminiscent of a subset of present-day galaxies (e.g., [Gnedin, 2000](#); [Wise, 2019](#)). All these star-forming haloes contribute to reionizing the neutral IGM. They create small bubbles of ionized gas surrounding bright energy sources. As these bubbles grow and punch ever-larger holes into the neutral Universe, they eventually begin to overlap, enabling ionizing radiation to propagate farther through the IGM (e.g., [Wise, 2019](#)).

On the other hand, the first stars also significantly alter the chemical composition of the gas in the Universe (e.g., [Heger & Woosley, 2002](#)). Through nucleosynthesis in the cores of these short-lived stars and as a result of powerful supernovae, a fraction of the Universe’s initial constituents of hydrogen and helium were converted into carbon (C), oxygen (O), nitrogen (N), iron (Fe), and other heavier elements, which are collectively known as metals.

Once most of the Universe was reionized, approximately 1Gyr after the Big Bang at redshift ( $z$ )  $\sim 6$ , light across the entire electromagnetic spectrum could travel unimpeded through the cosmos, eventually revealing the Universe as we see it today. This marked the end of the so-called Epoch of Reionization (EoR), which constitutes a big transition in the Universe. We note that we are referring to the reionization of hydrogen. Other elements, such as helium are fully reionized at later times ( $z \sim 3$ ) until the quasar population is built up in sufficient numbers (e.g., [Furlanetto & Oh, 2008](#)).

## 1.2.1 Galaxies in the Epoch of Reionization

The EoR has profound implications for the interpretation of observations and marks a comprehensive change in the physical state of the gaseous Universe. However, understanding the cause and the development of this phenomenon is a challenging task. While the timescales over which reionization ended are well established around redshift  $z \sim 6$  (e.g., [Mason et al., 2019](#); [Yang et al., 2020](#); [Paoletti et al., 2020](#)), when the reionization started, which is established at  $z \sim 11$  ([Planck Collaboration et al., 2016](#)) and the nature of the sources of the ionizing photons are still unclear.

Since almost all baryonic matter after the Big Bang is hydrogen and helium, the very first generation of Pop III stars must have formed out of probably pure H/He gas since heavy elements can be produced only in the interior of stars (e.g., [Bromm et al., 1999](#)). These stars are potentially very massive, up to several  $100 M_{\odot}$ , as a consequence of inefficient gas cooling and hence poor fragmentation of pre-stellar cores at these early epochs (e.g., [Bromm et al., 1999](#); [Abel et al., 2002](#)).

The first Pop III stars are thought to be too few to produce enough ionizing photons to sustain reionization and they have short lifetimes that rapidly pollute their environment with metals ([Meiksin, 2005](#)). Other candidates as sources of the reionization are bright quasars that are efficient producers of HI ionizing photons but tend to appear too late for the ionization of hydrogen – although they are important for the reionization of helium – (e.g., [Fan et al., 2006](#); [Worseck et al., 2016](#)). They can ionize large bubbles of HI even at distances up to several Mpc out at  $z \sim 6$ . However, their space density is too low at high- $z$  to provide the cosmic photoionization rate required to keep the IGM ionized at  $z > 3$ . Some authors have also suggested that a population of fainter AGNs may be responsible for the bulk of ionizing photons (e.g., [Giallongo et al., 2015](#); [Grazian et al., 2018](#)).

On the other hand, alternative candidates are SFGs. Based on the ultraviolet (UV) luminosity

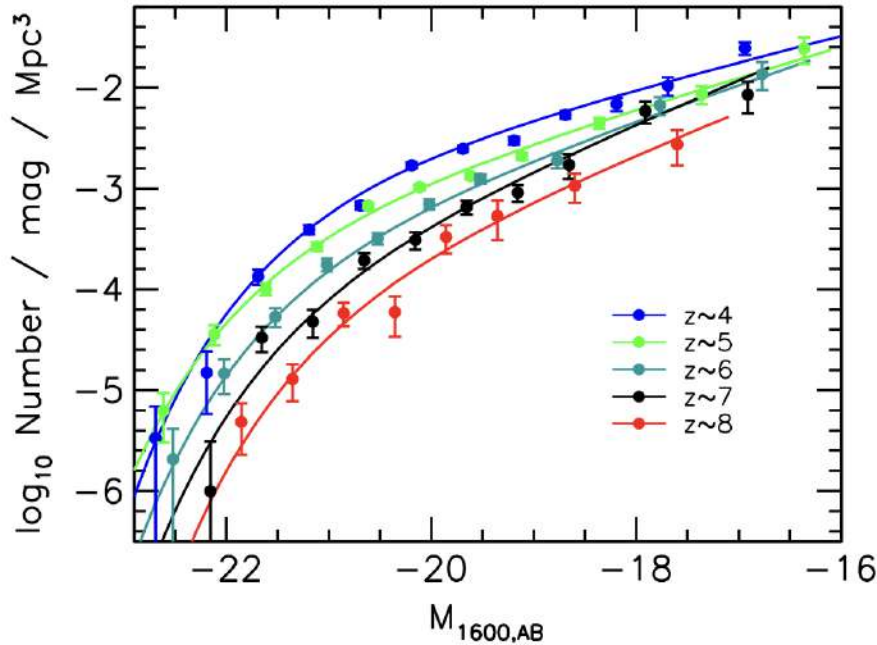


Figure 1.2.2: UV luminosity functions at  $z \sim 4$  (blue solid circles),  $z \sim 5$  (green solid circles),  $z \sim 6$  (light blue solid circles),  $z \sim 7$  (black circles), and  $z \sim 8$  (red solid circles) with their corresponding Schechter fits in solid line. Figure taken from [Bouwens et al. \(2015\)](#).

function, i.e., the number of galaxies per unit volume at a given UV luminosity, the steeper faint-end observed in the EoR suggests that low luminosity galaxies provide a substantial contribution to the overall luminosity density in the UV and therefore to the overall ionizing background ([Bouwens, 2016](#)). In Fig. 1.2.2 are displayed the observational results of the UV luminosity function for  $4 \leq z \leq 8$ . The  $z > 6$  luminosity function shows a clear turnover at the bright end, relative to lower redshifts, and suggests that there has been little or not evolution in the characteristic luminosity towards brighter galaxies in time. Much effort is being put into determining how easily ionizing photons can escape their host galaxies in order to be able to ionize the IGM (e.g., [Gnedin et al., 2008](#)).

Recent works by [Naidu et al. \(2022\)](#); [Matthee et al. \(2022\)](#), based on the fraction of Ly $\alpha$  emitters (LAEs) over time, support a late-completed and rapid reionization purely dominated by more massive and bright UV galaxy systems. On the other hand, semi-empirical models like those in [Finkelstein et al. \(2019\)](#), based on observational constraints on the UV luminosity function during the EoR, suggest an early-completed reionization conducted primarily by numerous low-mass galaxies. Alternatively, other works suggest a slower and more extended reionization process based on the evolution of the fraction of LAEs in the EoR (e.g., [Pentericci et al., 2018b](#)). This is an ongoing debate, and studying galaxies' properties is an important step toward seeing the whole picture.

Based on photometric data of EoR galaxies, SFGs are bluer than their counterparts at lower- $z$ , and their  $\beta$ -slopes are consistent with a young ( $< 50$  Myr), dust-poor population with stellar metallicity  $0.2 Z_{\odot}$  ([Finkelstein et al., 2012](#)). Insight into the massive stellar populations of  $z > 6$  galaxies has emerged from the spectroscopic detections of UV metal emission lines, in particular, because the strong Ly $\alpha$  is strongly attenuated by the neutral IGM and the subsequent low transmission at those redshifts (see [Dijkstra, 2014](#), for a review). Observationally, the fraction of LAEs drops at  $z \gtrsim 6$  (e.g., [De Barros et al., 2017](#)), as is displayed in Fig. 1.2.3. This is an effect due to the resonant nature

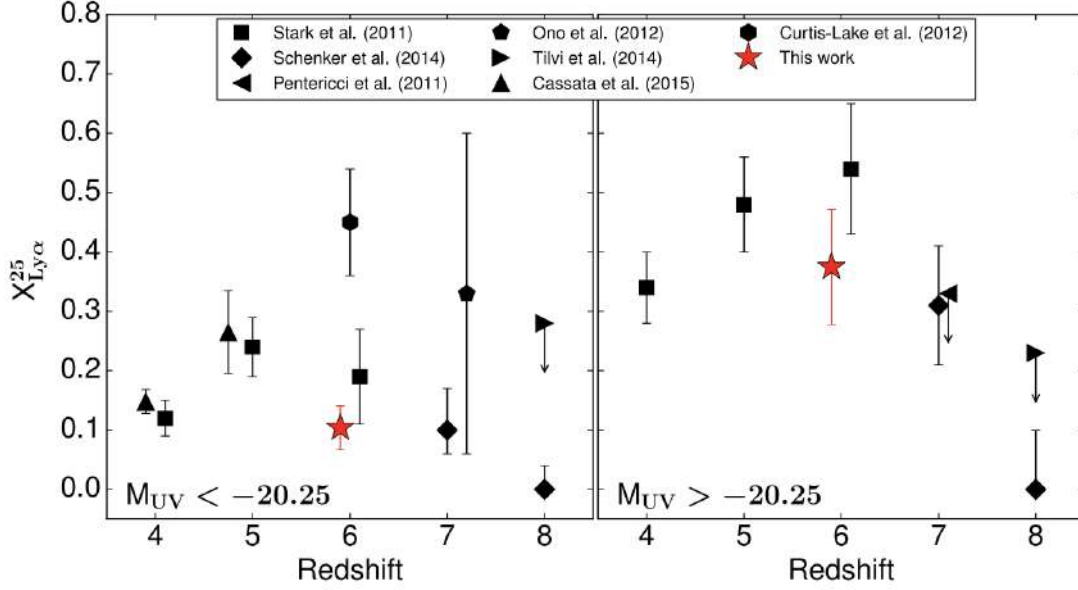


Figure 1.2.3: Fraction of LAEs (with Ly $\alpha$  equivalent width  $> 25 \text{ \AA}$ ,  $X_{Ly\alpha}^{25}$ ) at  $4 \leq z \leq 8$  for the brightest ( $M_{UV} < -20.25$ , left panel) and faintest ( $M_{UV} > -20.25$ , right panel) galaxies. The points are observational results from literature described in De Barros et al. (2017). Figure taken from De Barros et al. (2017).

of Ly $\alpha$ , i.e., its energy corresponds exactly to the energy difference between the ground state of the first excited state. As long as Ly $\alpha$  photons propagate through the medium, they are not just absorbed by a neutral hydrogen atom, but they are re-emitted almost immediately but in another direction, i.e., they are resonantly scattered (e.g., Laursen, 2010). However, it is possible to observe LAEs in the EoR (e.g., Roberts-Borsani et al., 2016; Witten et al., 2023) if they reside in over-dense regions where copious amounts of ionizing photons are produced by an unusually abundant galaxy population (e.g., Dayal & Ferrara, 2018). These over-dense regions require a population of fainter ionizing sources in the vicinity of bright galaxies in order to generate HII regions large enough to explain the visibility of their Ly $\alpha$  lines (e.g., Castellano et al., 2016; Endsley & Stark, 2022). As we already mentioned, it is likely that SFGs gradually ionize their immediate surroundings such that they are encompassed in large bubbles of ionized gas, thus resulting in a highly inhomogeneous ionization structure of the IGM. Eventually, these bubbles percolate and overlap until, ultimately, almost all of the IGM is ionized (e.g., Gnedin, 2000).

Over the last few years, deep near-infrared (NIR) observations of galaxies during the reionization era have reported the presence of UV emission lines with unusually high EWs, such as CIV $\lambda$ 1550 $\text{\AA}$ , HeII $\lambda$ 1640 $\text{\AA}$ , OIII] $\lambda$ 1663 $\text{\AA}$ , or CIII] $\lambda$ 1908 $\text{\AA}$  (see Stark, 2016, for a review). The nebular CIII] $\lambda$ 1908 emission line has now been confidently detected in UV-selected galaxies at  $z > 6$  (Stark et al., 2015; Stark, 2016; Hutchison et al., 2019) and reflects enhanced electron temperatures and harder radiation fields from metal-poor gas and stars, young stellar populations, and large ionization parameters (e.g., Jaskot & Ravindranath, 2016). The presence of such intense UV metal lines is consistent with the extreme equivalent widths (EW) optical line emission suggested by the Spitzer/IRAC colors (Smit et al., 2014; Stark et al., 2015). There thus appears to be a subset of  $z > 6$  galaxies with extreme radiation fields and moderately metal-poor gas such that collisionally excited metal lines are enhanced by the high electron temperature of the ionized gas. Such systems, with high EWs in nebular lines,

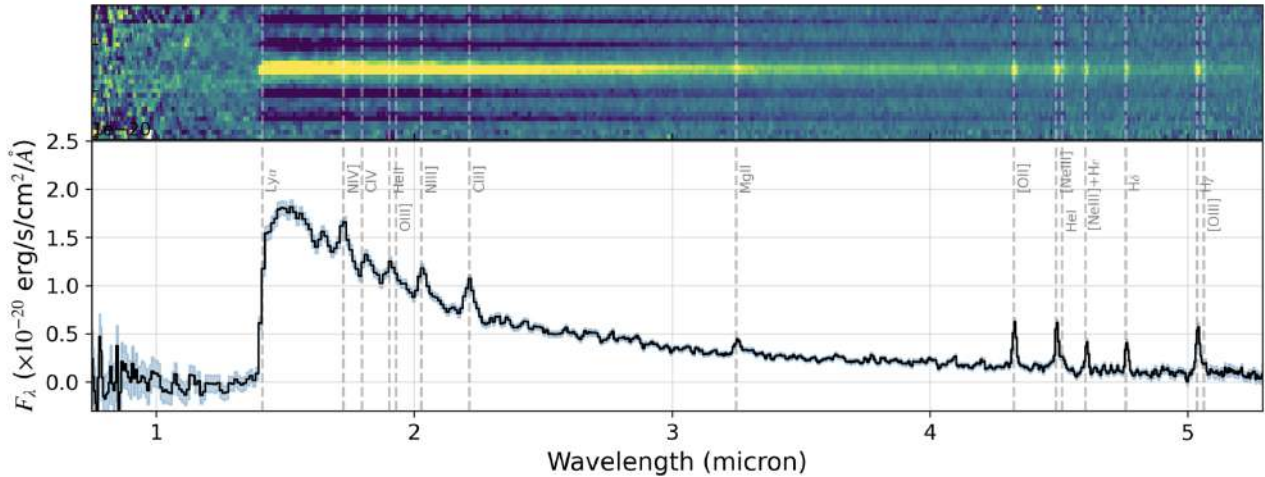


Figure 1.2.4: 2D (top) and 1D (bottom) spectra of GN-z11 using PRISM/CLEAR configuration of NIRSpec. Prominent emission lines present in the spectra are marked. The S/N of the continuum is high, and the emission lines are clearly seen in both the 1D and 2D spectra at  $z = 10.603$ . Figure taken from [Bunker et al. \(2023b\)](#).

are commonly known as Extreme Emission-line galaxies (EELGs). EELGs are galaxies that emit strong spectral lines caused by the ionization of gas within the galaxy. These lines provide important information about the physical and chemical properties of the gas and the stars within the galaxy. A detailed characterization of the rest-frame UV spectra of SFGs at  $z \gtrsim 6$  is thus essential to understand their ionization properties and thus shed new light into the reionization process.

As the JWST era dawns, more details of these sources are obtained while writing this Thesis, and surely more discoveries will be unveiled in the coming future. An example of the spectrum of a galaxy deep into the EoR is shown in Fig. 1.2.4, where clear emission lines are observed with exquisite signal-to-noise (S/N). In the pre-JWST era, analogs of such extreme systems at lower redshifts have been crucial to understanding the physical properties of such sources.

For example, because the UV metal lines trace the systemic redshift, they constrain the typical velocity offset of Ly $\alpha$  in galaxies which depends on the covering fraction and kinematics of neutral hydrogen within the galaxy and plays a major role in regulating the transfer of Ly $\alpha$  through a partially neutral IGM. The larger the velocity offset, the less the IGM will attenuate Ly $\alpha$  because the line photons will be redshifted further into the damping wing by the time they encounter neutral hydrogen. This leads to differences in Ly $\alpha$  profiles between leaker and non-leaker galaxies but also in their nebular properties, as probed by LAEs at  $z \sim 2$  (e.g., [Naidu et al., 2022](#)). Similar results are found with galaxies at even lower redshifts (e.g., [Izotov et al., 2018](#)).

In this Thesis, our approach is to study analogs to the galaxies in the EoR at the cosmic epoch known as the *Cosmic Noon* by exploiting the information from their spectroscopic properties using ground-based facilities.

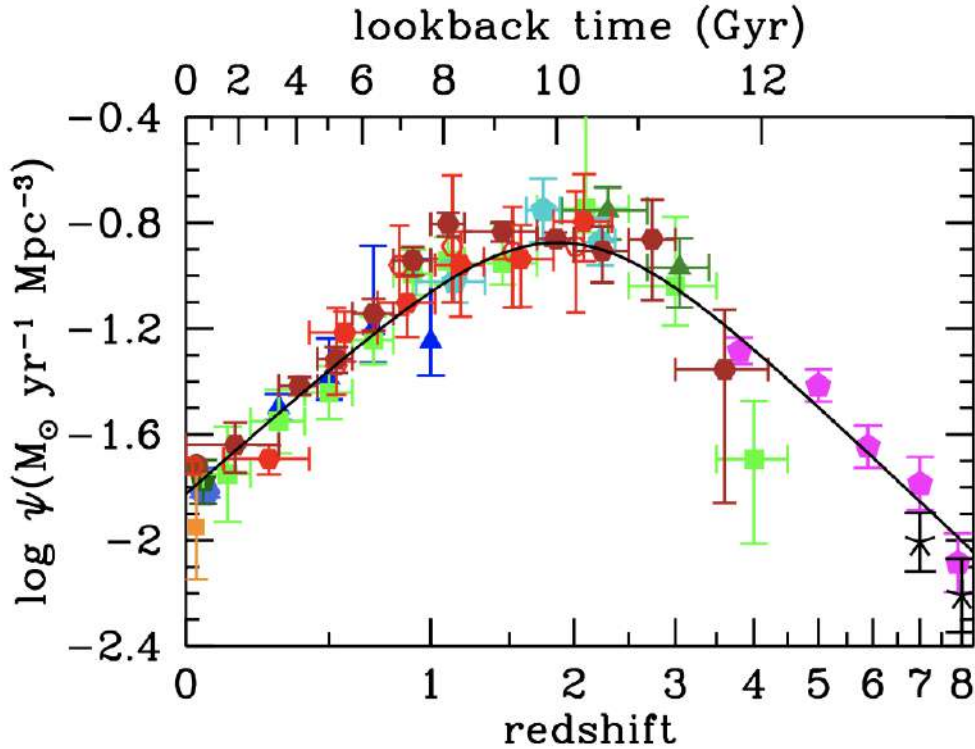


Figure 1.2.5: The history of the CSFR density estimated using various ways to measure the SFR (different colors and symbols). Below redshift  $z < 2$ , surveys agree that the CSFR increases up to  $z \sim 2$ . Above  $z > 3$ , UV surveys indicate a decline in the CSFR. The rise in the CSFR in the first  $\sim 3$  Gyr follows the assembly of halos, while the decline in the last 10 Gyr results from declining cooling rates in hot halos, the overall exhaustion of neutral hydrogen gas, and AGN feedback. Figure taken from [Madau & Dickinson \(2014\)](#).

## 1.2.2 The Cosmic Noon

After the EoR ended, galaxies continued to grow at increasing rates, until about 3 Gyr after the Big Bang in an epoch called as Cosmic Noon. The cosmic star formation history describes how the stellar mass formed per year in an average volume of the Universe has changed along the cosmic time (see Fig. 1.2.5). A variety of observations agrees that the cosmic star formation rate (CSFR) was higher in the past and that it has been declining since the last 10 Gyrs or equivalently at  $z < 2$  (e.g., [Sobral et al., 2013](#); [Madau & Dickinson, 2014](#)). At the same time, a galaxy with the same stellar mass was forming stars roughly ten times faster, on average, at redshift  $z = 2$  than galaxies with a similar stellar mass do today (e.g., [Whitaker et al., 2012](#)). Beyond  $z \sim 2$ , observations indicate that the CSFR density declines to the highest redshifts. Theoretically, the evolution of the CSFR density is understood by the accretion rate of gas on halos and the interplay between star formation, and the strength and mechanism of feedback (e.g., [Madau & Dickinson, 2014](#)). This period, when the star formation rate (SFR) density peaks, is called the Cosmic Noon and happened roughly  $\sim 2 - 3$  Gyr after the Big Bang.

Roughly half of the stellar mass observed today was formed by the end of this period before  $z \sim 1$  (see the left panel in Fig. 1.2.6). At the same time, before the peak activity (before  $z \sim 3$ ), less than  $\sim 10\%$  of the stellar mass was formed. These observations favor a *downsizing* scenario for galaxy formation (e.g., [Pérez-González et al., 2008](#)) where most of the stellar mass of today's massive

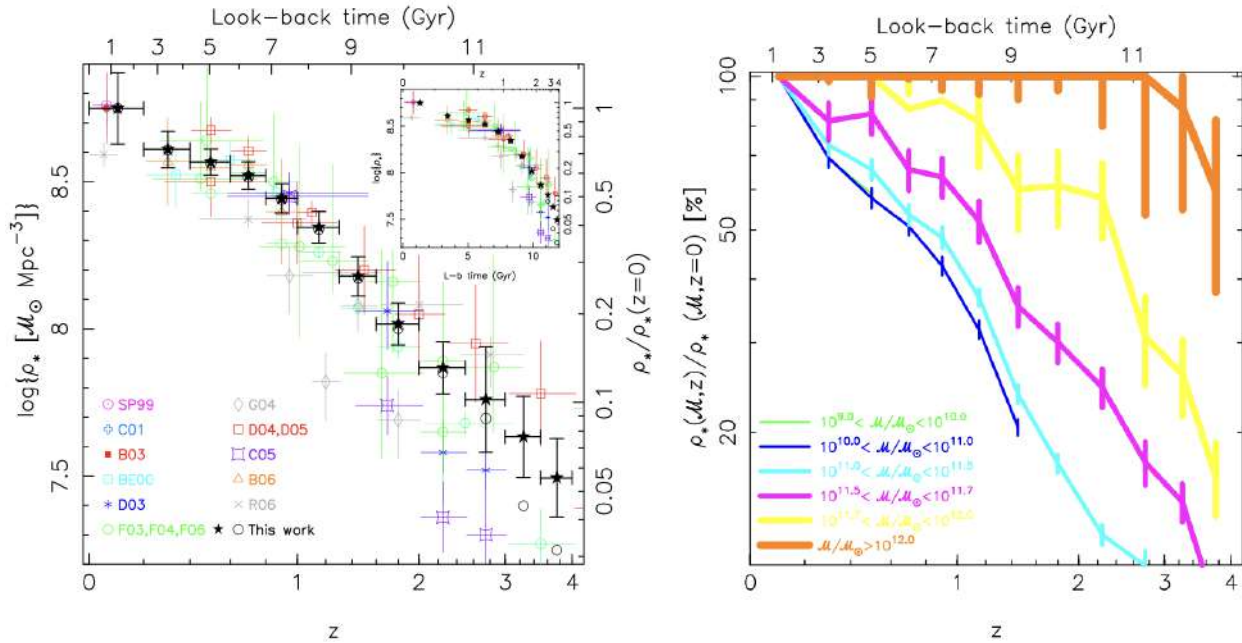


Figure 1.2.6: *Left panel:* Evolution of the stellar mass density of the Universe as a function of redshift. The corresponding look-back times are displayed in the top horizontal axis. *Right panel:* Fraction of the local stellar mass density already assembled at a given redshift for several mass intervals. Figures taken from Pérez-González et al. (2008).

galaxies (with stellar masses  $> 10^{12} M_\odot$ ) is formed in this period and earlier than less massive today's galaxies (with  $< 10^{11} M_\odot$ ) which assembled most of their mass content at later times and more slowly (see the right panel in Fig. 1.2.6). This indicates that over time, star-formation activity shifts to smaller systems.

On the other hand, by dividing the average values of the CSFR density by the stellar mass density estimates, the specific SFR shows a continuous increase as redshift increases (e.g., Tasca et al., 2015; Khusanova et al., 2020). After the Cosmic Noon, the specific SFR drops, and given that their inverse is a proxy of the characteristic stellar mass doubling time, the assembly of mass content is slowed-down. Similarly, as mentioned before, there is a difference in the evolution of galaxies depending on their present-day stellar mass. For example, the most massive galaxies ( $> 10^{11.7} M_\odot$ ) presented very large specific SFRs at high redshift, and they could double their stellar mass in a short period of 0.1 Gyr at  $z = 3-4$  (e.g., Pérez-González et al., 2008).

The study of SFGs at Cosmic Noon has been an active research area in recent years, driven by the availability of large observational datasets from ground- and space- telescopes and spectrographs. These datasets have enabled researchers to study the properties of emission-line galaxies at this redshift range, where the Universe was much younger, and the galaxies were much smaller and more active than they are today (see Shapley, 2011, for a review). Given the phase of intense star formation in this epoch, this is ideal for studying the assembly of many emission-line galaxies. A more detailed description of the spectroscopy studies at Cosmic Noon is presented in Chapter 2.

Detailed multiwavelength observations of young, rapidly forming low-mass galaxies at Cosmic Noon provides a unique opportunity to understand the physical and chemical processes that were driving the evolution of galaxies during this crucial period and their connection with their role during

the cosmic reionization. Analogs to primeval galaxies have been found in this period (e.g., [Amorín et al., 2017](#)), and they are ideal test beds to study the details of their physical properties and their early assembly.

### 1.3 Metal content in star-forming galaxies

One of the galaxies' fundamental properties is their ISM's chemical abundances, which can inform us, among other properties, of the metal content of the proto-stellar clouds in which stars form or the historical enrichment by generations of stellar populations. Even though the evolution of the ISM of individual galaxies is very complex, the metal content plays a crucial role in the production and strength of nebular lines, which act as cooling channels for the ISM. While the ISM is chemically enriched by supernovae and stellar winds in the late stages of stellar evolution, such as the Asymptotic Giant branch (AGB) phase, the metallicity may also be lowered due to dilution from inflowing pristine (metal-poor) gas and/or outflows of metal-enriched gas. The metal content is sensitive to the star-formation history (SFH) of each galaxy (see [Maiolino & Mannucci, 2019](#), for a review).

Fortunately, the information on the metal content in galaxies is imprinted in their spectra; particularly, the metallicity of the ISM ionized gas (so-called gas phase metallicity) is imprinted in their emission lines. Gas-phase metallicity, generally referred to as oxygen abundance because it dominates the total metal budget in mass, can be estimated by temperature-sensitive collisionally excited lines. These lines are sensitive to the abundance of metals because they depend on the amount of atoms in the gas, the electron temperature, and the electron density of the gas. As mentioned before, the electron temperature is sensitive to the total gas-phase metal abundance because metals act as coolants in the ISM in a star-forming region. As the ISM cools, there are fewer collisional excitations, and the strength of collisionally excited lines decreases (see [Kewley et al., 2019](#), for a review).

The gas-phase metallicity can be determined from a wide variety of emission lines from the UV through to the IR. The traditional method for deriving metallicity, which is known as the *Direct Method*, is based on the electron temperature from sensitive auroral lines in the optical spectrum (see [Pérez-Montero, 2017](#), for a detailed tutorial). Such auroral lines are weak and are often not detected in the metal-rich galaxies, and then the method is limited to a subset of galaxies. To overcome this problem, Strong-line calibrations are an alternative method that provides relations between auroral line metallicities and strong line flux ratios (e.g., the calibrators presented in [Bian et al., 2018](#); [Pérez-Montero et al., 2021](#)). This method is particularly useful at high- $z$  where weak auroral lines are challenging to detect.

Both methods have their limitations. For example, the unseen ionization stages need to be considered to estimate the total metallicity and not only the observed ion abundance. Also, the temperature structure observed in star-forming regions may alter the total amount of metals calculated with a particular mean zone temperature. About the calibrations, they rely on the fact that HII regions with auroral lines represent all HII regions and galaxies. We aim to address this open problem in this Thesis, particularly in Chapter 4.

### 1.3.1 Mass-Metallicity relation

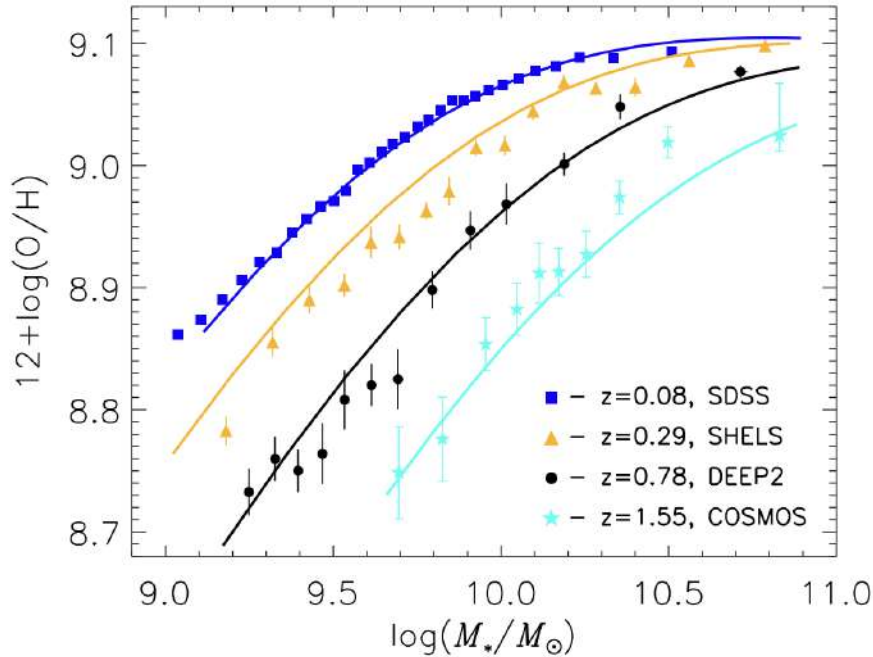


Figure 1.3.1: MZR for  $z < 1.6$ . The symbols are observational data at different redshifts, while the solid curves are the MZR determined from the numerical models. Figures taken from [Zahid et al. \(2014\)](#).

The gas-phase metallicity of galaxies encodes information on how physical processes drive the evolution of galaxies. The emergence of scaling relations, such as the mass-metallicity relation (MZR, [Lequeux et al., 1979](#); [Tremonti et al., 2004](#)), provides key insights into the physical mechanisms involved in the growth and evolution of galaxies. Using SDSS spectra in the local Universe, a tight correlation is found between stellar mass and metallicity, spanning over three orders of magnitude in stellar mass and a factor of 10 in metallicity. It indicates that the galaxies with the lower stellar masses are found to be also more metal-poor. The relation is relatively steep from  $10^{8.5}$  to  $10^{10.5} M_{\odot}$ , but flattens for higher stellar masses ([Tremonti et al., 2004](#)). As a reference of the shape of the relation, see the blue line in Fig. 1.3.1.

A tight correlation between the stellar mass and their metal content is found at different redshifts (see Fig. 1.3.1). The slope and normalization of the MZR may evolve with redshift (e.g., [Sanders et al., 2021](#)), which is explained in simulations by the higher gas content at higher redshifts ([Torrey et al., 2019](#)). At  $z \sim 2 - 4$ , the MZR has been studied using both the gas-phase metallicity (e.g., [Erb et al., 2006](#); [Troncoso et al., 2014](#); [Sanders et al., 2021](#)) and the stellar metallicity (e.g., [Sommariva et al., 2012](#); [Cullen et al., 2019](#); [Calabrò et al., 2021](#)), finding a strong redshift evolution towards lower metallicities at a given stellar mass. In Fig. 1.3.2, the MZR at  $z \sim 3.4$ , in both stellar and gas-phase, are shown.

Importantly, the scatter of galaxies around the median MZR correlates with other observables such as the SFR, which is known as the fundamental metallicity relation (FMR, [Mannucci et al., 2010](#); [Curti et al., 2020](#)) and introduces an anticorrelation between metallicity and SFR. According to the FMR, galaxies of the same stellar mass show higher SFR if they have lower metallicities. The

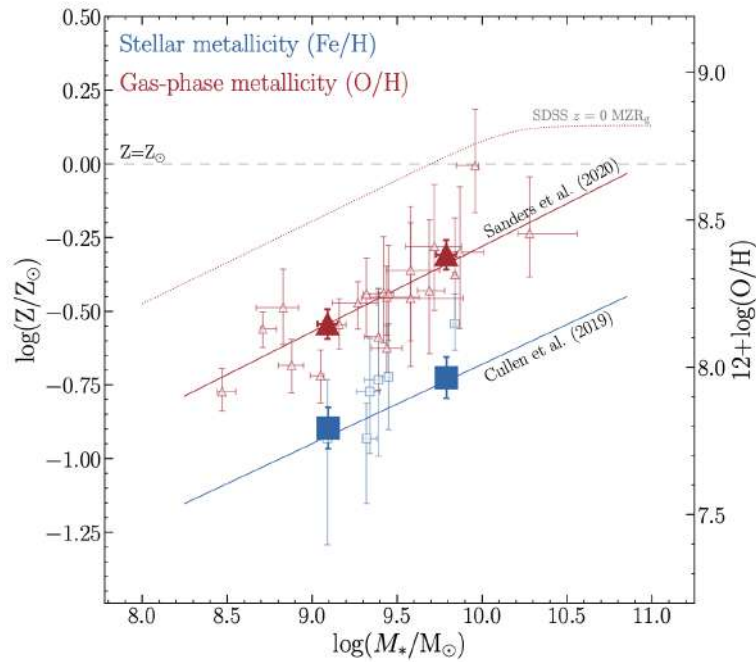


Figure 1.3.2: The MZR for stars ( $Z_*$ , blue squares) and nebular gas ( $Z_g$ , red triangles) at  $z \sim 3.4$ . The small open data points show  $Z_*$  and  $Z_g$  for individual galaxies, and the large filled data points show the low- $Z_*$  and high- $Z_*$  stacks. The blue and red solid lines show, respectively, previous determinations of  $MZR_*$  and  $MZR_g$  at  $z \sim 3.4$  from Cullen et al. (2019) and Sanders et al. (2020). The red dotted line shows the diffuse ionized gas (DIG)-corrected  $MZR_g$  at  $z \sim 0$  from (Sanders et al., 2020), and the horizontal dashed grey line indicates the value of solar metallicity. On the right-hand side of the y-axis, the value of  $\log(\text{O}/\text{H})+12$  for the  $Z_g$  data is displayed. Figure taken from Cullen et al. (2021).

existence of such anticorrelation has been reported in numerous observational studies (e.g., Curti et al., 2020; Sanders et al., 2021) and established up to redshift  $z \sim 3.5$ . However, Torrey et al. (2018) points out that the strength of the correlation – especially for low-mass galaxies at high redshift – may be reduced if models with particularly strong and/or bursty feedback are used. Additionally, the age of the stellar populations plays a role in shaping the FMR because galaxies with younger stellar populations ( $< 150$  Myr) and more bursty star-formation tend to show lower gas-phase metallicities at a given stellar mass compared with galaxies with older stellar populations (Duarte Puertas et al., 2022).

The MZR itself is explained by different scenarios, which indicates how complex and how informative is the metal content in galaxies. Such scenarios include outflows, mainly due to supernovae, which are very common in starburst galaxies, both in the local Universe and at high redshifts (e.g., Steidel et al., 2010; Heckman et al., 2015; Matthee et al., 2021). These outflows are observed to have metallicities higher than the ISM of the host galaxies (Chisholm et al., 2018). Therefore they could be a channel to remove metals efficiently to the CGM from the ISM of low-mass galaxies due to their shallower potential wells (Tremonti et al., 2004). Alternatively, the MZR can be interpreted as a sequence of evolutionary stages in a downsizing context where high-mass galaxies evolve more rapidly and at higher redshifts than low-mass ones (e.g., Somerville & Davé, 2015). Because of it, low-mass galaxies have converted a smaller amount of gas into stars, and then they have lower metal content. Similarly, the more significant gas fraction observed in low-mass galaxies (e.g., Erb et al., 2006) could be linked to the ongoing infall of metal-poor gas, which, once mixed with the existing

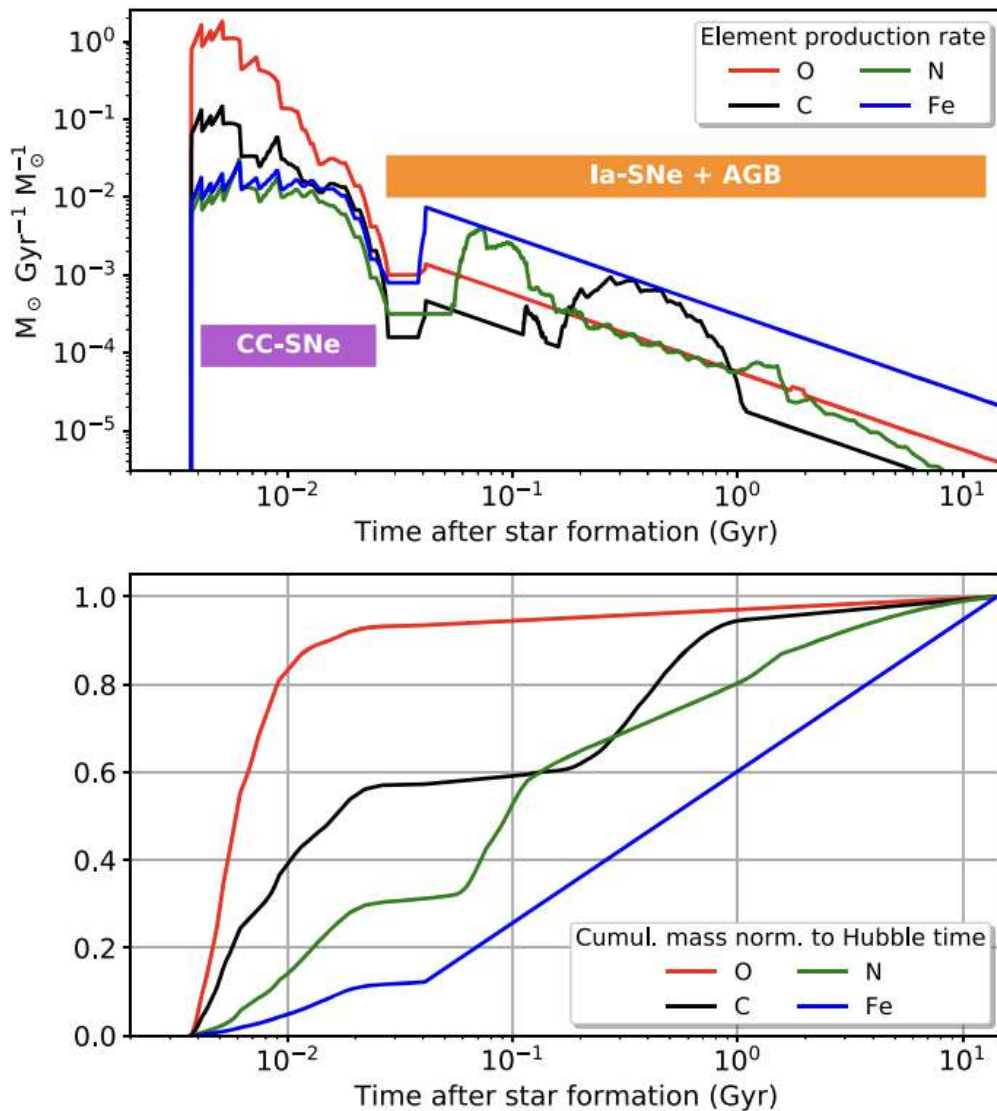


Figure 1.3.3: Timescales of production of various elements (O, C, N, and Fe) for a single population of stars of solar metallicity created together along a given initial mass function, based on chemical evolution models. On the top panel, the production rate normalized to  $1M_{\odot}$  of formed stars is displayed. On the bottom panel, the cumulative mass-produced, normalized to the amount after 1 Hubble time, is shown. Figure taken from [Maiolino & Mannucci \(2019\)](#).

ISM, contributes to reducing metallicity. Other possible explanations include changes in the initial mass function (IMF) (e.g., [Mollá et al., 2015](#)) or accretion from enriched recycled gas into the ISM of high-mass galaxies (e.g., [Ma et al., 2016](#)) as we mentioned in Sec. 1.1.2.

### 1.3.2 Relative chemical abundances

Not only the total metal content gives us information about the ISM of galaxies. The relative abundances between different nucleosynthetic elements produced in stars of different masses and lifetimes are other indicators of the chemical content of galaxies and help us to understand the evolution of

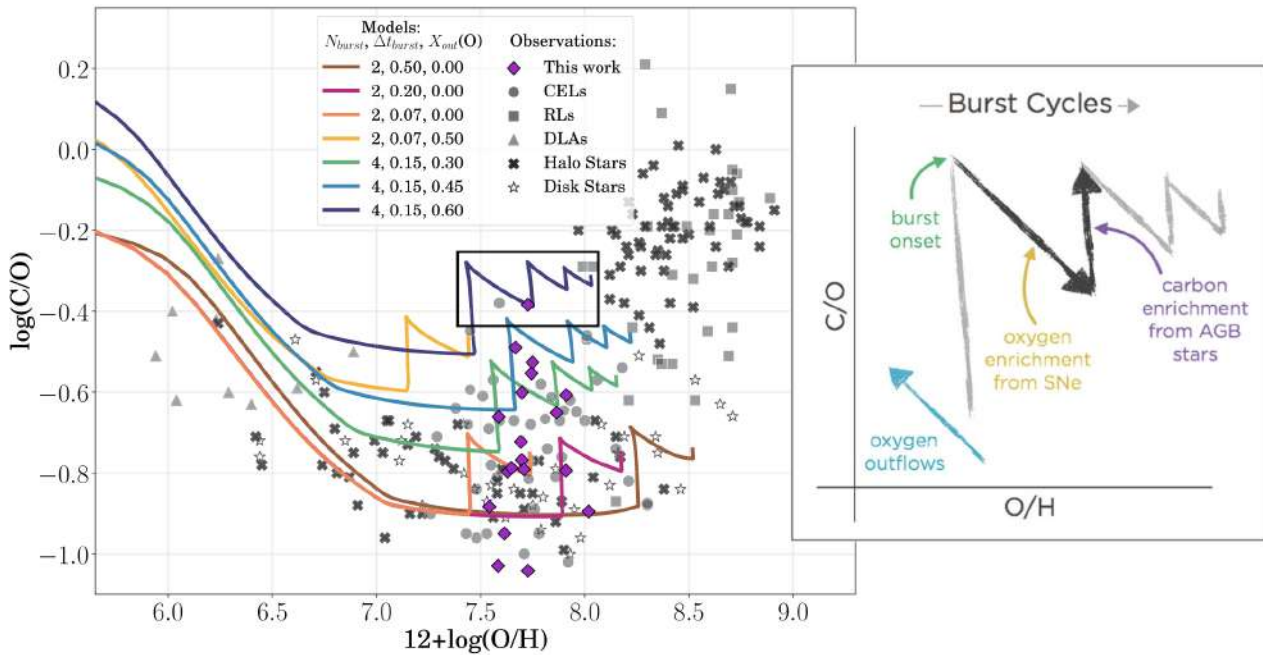


Figure 1.3.4: *Left panel:* Relation between  $\log(C/O)$  and  $\log(O/H)$  with observations (symbols) and chemical evolution models (solid lines). Observations are a compilation of metal-poor dwarf galaxies, Milky Way stars, and damped Ly $\alpha$  emitters, according to the legend. The properties of the models (Berg et al., 2019) are provided in the legend, where the numbers refer, in order, to the number of bursts ( $N_{burst}$ ), the burst duration ( $\Delta t_{burst}$ ), and the fraction of new oxygen exiting the galaxy via outflows ( $X_{out}(O)$ ). *Right panel:* Illustration of the sawtooth pattern for the model in the black square in the left panel with the possible physical sources modifying the C and O abundances. Figure taken from Berg et al. (2019).

galaxies. C, N, and O are thought to originate primarily from stars of different mass ranges; for instance, O is synthesized mostly in massive stars (MSs;  $M_{\star} > 8 M_{\odot}$ ) and by the associated core-collapse supernovae (CC-SNe), as shown by the red line in Fig. 1.3.3 where the timescale of their production, based on chemical evolution models, is displayed. Most of the O is produced before the first  $\sim 30$  Myr. On the other hand, C and N (black and green lines respectively in Fig. 1.3.3) are partly produced in massive stars but they are mostly produced in intermediate-mass stars (IMs;  $2 < M_{\star} < 8 M_{\odot}$ ) and by the associated AGB phase or by the associated Type Ia supernovae at longer timescales  $\gtrsim 40$  Myr (Henry et al., 2000; Maiolino & Mannucci, 2019).

This leads to clear advantages of using relative abundances since they can be used as chemical clocks of the SFH of a galaxy. For example, the N/O abundance ratio is a suitable indicator of the time that has elapsed since the bulk of star formation occurred in single starbursts (Edmunds & Pagel, 1978). On the other hand, since N is a secondary element (i.e., its yield depends on the previous amount of C and O in the stars) for a wide metallicity range, its relation with a primary element, such as O, is relatively independent of the chemodynamical effects, such as outflows or inflows (e.g., Edmunds, 1990). This ratio has been extensively studied in local galaxies (e.g., Pérez-Montero & Contini, 2009) and has been found to an increase in N/O with stellar mass since most of the sampled SDSS galaxies lie in the metallicity range for the production of secondary N. This relation was used by Amorín et al. (2010) to study the chemical evolution of compact galaxies with very high specific SFRs, generally known as Green Pea (GP) galaxies.

Alternatively, the C/O abundance ratio may also provide us with general trends in the evolutionary state of a galaxy and its ISM. Unfortunately, no intense C emission lines are in the optical, which is usually accessible in the local Universe, and the most prominent spectral features of C require observations from space (e.g., [Esteban et al., 2014](#)). For this reason, Cosmic Noon is an ideal range to observe the rest-UV where one of the most intense lines is CIII] $\lambda$ 1908 (e.g., [Shapley et al., 2003](#)).

The C/O ratio has been studied in local dwarf galaxies and HII regions of disk galaxies (e.g., [Garnett et al., 1995](#); [Chiappini et al., 2003](#); [Esteban et al., 2014](#); [Peña-Guerrero et al., 2017](#); [Berg et al., 2019](#)). In evolved, metal-enriched galaxies, an increase of C/O with increasing metallicity above one-fifth solar metallicity has been observed. Still, the relation flattens at lower metallicities ( $12+\log(\text{O}/\text{H}) < 8$ ), showing a significant scatter of C/O values for a given metallicity ([Garnett et al., 1995](#); [Berg et al., 2016, 2019](#), e.g., see Fig. 1.3.4). Chemical evolution models with different prescriptions have been developed to understand the evolution of C/O with metallicity (e.g., [Carigi, 1994](#); [Henry et al., 2000](#); [Chiappini et al., 2003](#); [Mattsson, 2010](#); [Carigi & Peimbert, 2011](#); [Mollá et al., 2015](#); [Vincenzo & Kobayashi, 2018](#)) but several variables remain unconstrained, especially at high redshifts.

The observed trend can be explained because C is primarily produced by the triple- $\alpha$  process in both massive and low- to intermediate-mass stars. Still, in massive stars, carbon arises almost exclusively from the production due to metallicity-dependent stellar winds, mass loss, and ISM enrichment which are greater at higher metallicities ([Henry et al., 2000](#)). An alternative explanation is that the delayed release of C relative to O in younger and less metal-rich systems is the driver of this trend ([Garnett et al., 1995](#)). In the right panel in Fig. 1.3.4, the processes that may affect the position of galaxies in the C/O-O/H planes based on models are illustrated. For example, in the first Myr, after the onset of the burst, O is produced in CC-SNe, causing the C/O to decrease as O/H increases. After that, when the carbon production in AGB stars becomes more important, the C/O increases but the O/H remains. This may be the reason why the  $\log(\text{C}/\text{O})$  values for  $z \sim 0 - 2$  galaxies show a large dispersion of  $\sim 0.17$  dex over an extensive range in gas-phase metallicities. This scatter is well reproduced by chemical evolution models, as can be seen in Fig. 1.3.4, which suggests that the C/O abundance is very sensitive to the detailed SFH, where longer burst durations and lower star formation efficiencies correspond to low C/O ratios ([Berg et al., 2019](#)).

Therefore, measurements of C/O for galaxies at different metallicities remain crucial. In this Thesis, we aim to study C/O abundance in SFGs at Cosmic Noon given that they can lead to variations in their observed CIII] $\lambda$ 1908 emission (e.g., [Jaskot & Ravindranath, 2016](#); [Nakajima et al., 2018b](#)).

## 1.4 Gas kinematics and stellar feedback

Ionized gas kinematics provides valuable insights into the structure, dynamics, and evolution of galaxies. It is crucial to infer important properties of galaxies, such as their mass distribution, rotation, and turbulent motions. From an observational perspective, emission lines are used to obtain information about the velocity of the gas and velocity dispersions which are used to map the dynamical structure of the ISM. In particular, NIR spectroscopy, mainly H $\alpha$  or [OIII] $\lambda$ 5007, has probed that a large proportion ( $\gtrsim 80\%$ ) of the more massive galaxies have rotational disks at Cosmic Noon with higher velocity dispersions, i.e., more turbulent, than present-day spirals (e.g., [Wisnioski et al., 2019](#)). As

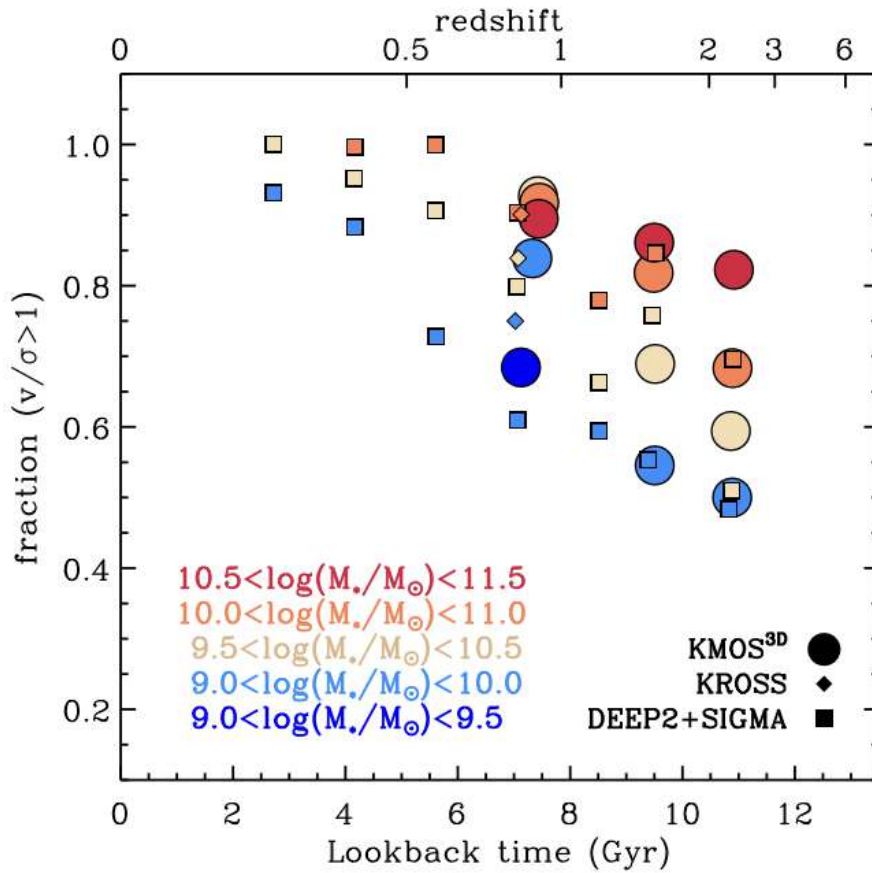


Figure 1.4.1: Evolution of the fraction of rotation-dominated SFGs (with the ratio of intrinsic rotation velocity to velocity dispersion  $> 1$ ) based on ionized gas  $H\alpha$  kinematics for resolved main-sequence SFGs as a function of stellar mass. Figure taken from [Wisnioski et al. \(2019\)](#).

can be seen in Fig. 1.4.1, this fraction is reduced for less massive galaxies ( $\lesssim 10^{10}M_{\odot}$ ), and then a large fraction is dominated by the turbulent gas. In this way, massive SFGs settled earlier into more rotationally-dominated mature disks, gradually followed by lower-mass galaxies at later times (e.g., [Kassin et al., 2012](#)). Constraining the physical drivers of the gas turbulence at high- $z$  thus still proves difficult and gas accretion from the cosmic web, disk instabilities, and stellar feedback have been proposed as energy sources of such turbulence (e.g., [Übler et al., 2019](#); [Förster Schreiber & Wuyts, 2020](#)).

Stellar feedback refers to the injection of energy, momentum, and mass into the ISM by massive stars. This feedback owes to a combination of ionizing radiation, radiation pressure, stellar winds, and supernovae. As we already mentioned in Sec. 1.3.1, it is likely responsible for the mass build-up of galaxies and their size growth, the inefficiency of star formation, their chemical enrichment, and the observed turbulence of the ISM.

In particular, stellar feedback in low-mass galaxies can expel gas from the shallow potential wells, reducing the reservoirs fueling star formation and keeping a low metal content (e.g., [Davé et al., 2017](#)). Galactic winds, generally called outflows, should be particularly effective at the peak epoch of star formation. Then, galaxies at Cosmic Noon are ideal laboratories to probe stellar feedback (see [Förster Schreiber & Wuyts, 2020](#), for a review). The properties of the outflows are probed to depend

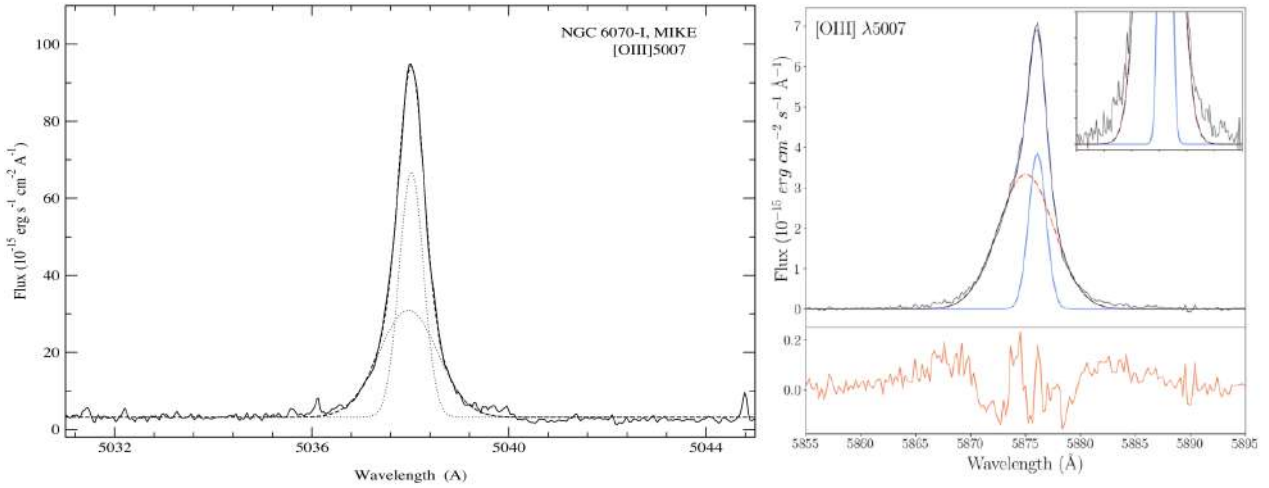


Figure 1.4.2: Multicomponent fitting of the  $[\text{O III}]\lambda 5007\text{\AA}$  profile of a Giant HII region (left panel) and a Green Pea galaxy (right panel). The profile shows that two Gaussian components are required to reproduce emission-line profiles in both cases. Figure taken from [Firpo et al. \(2010\)](#) (left panel) and [Hogarth et al. \(2020\)](#) (right panel).

on the properties of the host galaxy. For example, it is observed that the velocity of outflows increases as a function of SFR and galaxy stellar mass ( $M_*$ ) (e.g., [Weiner et al., 2009](#)), which is also seen in simulations (e.g., [Muratov et al., 2015](#)).

Winds are identified through their kinematic imprint. Observationally, two alternatives to probe outflows are both rest-UV interstellar absorption features and optical nebular emission lines, which probe neutral and warm ionized gas phases. These probes include centroid velocity offsets and broad wings of blueshifted interstellar absorption relative to the systemic redshift (e.g., from stellar features) and redshifted Ly $\alpha$  profile. In this Thesis, we will focus on probing outflows by broad line emission typically underneath a narrower Gaussian component arising from star-forming regions. Outflowing gas of SFGs at  $z \sim 2$  has been reported both from optical emission lines such as  $[\text{O III}]\lambda 5007$  or H $\alpha$  (e.g., [Förster Schreiber et al., 2019](#); [Übler et al., 2022](#)) as well as UV absorption lines (e.g., [Steidel et al., 2010](#); [Jones et al., 2018](#); [Calabrò et al., 2022](#)). Optical rest-frame emission lines can trace denser outflowing gas, providing an instantaneous snapshot of the ongoing ejective feedback; therefore, in principle, they are less contaminated by tenuous gas around galaxies ([Concas et al., 2022](#)). Such broad line emission is observed in GP ([Amorín et al., 2012b](#); [Hogarth et al., 2020](#)), HII regions ([Firpo et al., 2010](#)), LAEs ([Matthee et al., 2021](#)), i.e., galaxies with intense star-formation activity. In Fig. 1.4.2 examples of the  $[\text{O III}]\lambda 5007\text{\AA}$  profiles of an HII region (left panel) and a GP galaxy (right panel) showing broad components are displayed.

Notably, one of the main suspects in aiding the escape of ionizing photons is galaxy scale outflows (e.g., [Chisholm et al., 2017](#); [Kim et al., 2020](#); [Hogarth et al., 2020](#), and references therein). These outflows are expected to remove surrounding neutral gas, thus clearing a pathway for ionizing photons to escape efficiently. However, it is often challenging to reconcile the timescales of such strong galactic outflows with the timescale of production and the escape of ionizing photons in a galaxy.

Understanding how the presence of highly ionized gas outflows affects the properties of host galaxies gives insights into how the stellar feedback from young stars plays an essential role in the escape of ionizing photons and regulating the metal content and star formation in galaxies. In particular,

in the low-mass regime, it is still in debate how important stellar feedback is in injecting energy and momentum into the ISM because tension is found between observations (e.g., [Concas et al., 2022](#); [Marasco et al., 2023](#)) and simulations (e.g., [Nelson et al., 2019a](#); [Pandya et al., 2021](#)).

## 1.5 Scope of this Thesis

The motivation and aims of this research can be understood in the context described in the previous sections. The following Chapters in this Thesis can roughly be divided into three topics: i) the global properties of rest-UV emission-line galaxies at  $z \sim 3$  (Chapter 3), ii) the ionized gas kinematics as a tracer of stellar feedback in extreme emission-line galaxies at  $z \sim 3$  (Chapter 4), and iii) the characterization of photometrically-selected extreme emission-line galaxies at  $z > 4$  with new JWST observations (Chapter 5).

Strong nebular emission is ubiquitous in galaxies that contribute to cosmic reionization at redshift  $z \gtrsim 6$ . High-ionization UV metal lines, such as CIII] $\lambda$ 1908Å, show high EWs in these early galaxies, suggesting harder radiation fields at low metallicity than low- $z$  galaxies of similar stellar mass. Understanding the physical properties driving the observed UV nebular line emission at high- $z$  requires large and very deep spectroscopic surveys, now only accessible from ground-based facilities to  $z \sim 4$ . In Chapter 3, we study the mean properties of a large representative sample of 217 galaxies showing CIII] $\lambda$ 1908Å emission at  $2 < z < 4$ , selected from a parent sample of  $\sim 750$  main-sequence star-forming galaxies in the VANDELS survey. Stacking provides unprecedented high S/N spectra for CIII] $\lambda$ 1908Å emitters over more than three decades in luminosity, stellar mass, and SFR. The first set of questions that are addressed is related to:

- i) What is the nature of CIII] $\lambda$ 1908Å emitters?
- ii) What are the physical conditions that favor CIII] $\lambda$ 1908Å emission?
- iii) Is CIII] $\lambda$ 1908Å useful for redshift determinations at  $z > 6$ ?
- iv) Are these galaxies chemically young?

Feedback from massive stars plays a crucial role in regulating the growth of young SFGs and in shaping their ISM. This feedback contributes to removing and mixing metals via galactic outflows and the clearance of neutral gas, facilitating the escape of ionizing photons. Our goal in Chapter 4 is to study the impact of stellar feedback on the chemical abundances of the ISM in a sample of SFGs with strong emission lines at  $z \sim 3$ . We selected 35 low-mass SFGs ( $7.9 < \log(M_*/M_\odot) < 10.3$ ) from deep spectroscopic surveys based on their CIII] $\lambda$ 1908 emission. We used new follow-up NIR observations to examine their rest-optical emission lines and identify ionized outflow signatures through broad emission line wings detected after Gaussian modeling of [OIII] $\lambda\lambda$ 4959,5007 profiles. The second set of questions that are addressed include:

- i) What are the ISM properties of CIII] emitters?
- ii) Are outflows shaping the properties of EELGs?

iii) How important is stellar feedback in low-mass galaxies at Cosmic Noon?

EELGs are ideal laboratories for studying extreme ISM conditions and are expected to resemble the properties of the first galaxies in the EoR. As mentioned, our knowledge of such systems relies on rare analogs at lower redshifts, as we explore in Chapters 3 and 4. In the JWST era, individual galaxies can be studied directly deep into the EoR. In Chapter 5, we propose a new method to select EELGs at  $z \gtrsim 4$  based on their JWST photometry. We also characterize their global properties. The last set of questions that are addressed include:

- i) Is the new broad-band photometry from JWST/NIRCam useful to select EELGs?
- ii) What are the observed physical properties of EELGs in the EoR?

Throughout this Thesis, we assume a flat  $\Lambda$ CDM cosmology with the following parameters:  $\Omega_M = 0.3$ ,  $\Omega_\Lambda = 0.7$ ,  $H_0 = 70 \text{ km s}^{-1} \text{ Mpc}^{-1}$ . We adopt a [Chabrier \(2003\)](#) IMF. We consider the solar metallicity  $Z_\odot = 0.0142$ ,  $\log(\text{O}/\text{H})_\odot = 8.69$ , and  $\log(\text{C}/\text{O})_\odot = -0.26$  ([Asplund et al., 2009](#)). We assume by convention a positive EW for emission lines and rest-frame EW is reported. We use the following notation for metallicity for consistency with local conventions:  $[X/Y] = \log(X/Y) - \log(X/Y)_\odot$ .

## Methodology

The methodological approach of this Thesis is to study the properties of SFGs at Cosmic Noon by exploiting a wide range of observations, with a particular emphasis on their rest-UV and optical spectra. In this Chapter, a brief description of the large surveys used to build our parent samples and the key techniques to extract physical information about the galactic systems are summarized. This Chapter 2 is divided into three sections. In Sec. 2.1, the two large optical surveys used to select the galaxies studied in this Thesis are presented. This is followed in Sec. 2.2 by the description of the modeling of the spectral energy distribution (SED) of galaxies based on photometry to obtain information from galaxies, such as their stellar mass content. Finally, in Sec. 2.3, a description of photoionization models that are used to estimate the chemical abundances in galaxies is presented.

### 2.1 Spectroscopy at Cosmic Noon

Our knowledge of galaxies at Cosmic Noon starts from their identification with large photometric samples and then their confirmation via spectroscopy. This dataset has allowed statistical descriptions of the population and also increasingly detailed studies of subsets from spectrally and spatially resolved data (see a Review on [Förster Schreiber & Wuyts, 2020](#)). Multi-wavelength campaigns have been concentrated in selected regions of the sky, so-called deep fields, which include (not limited to) targeted fields such as the Great Observatories Origins Deep Survey (GOODS), the Cosmic Evolution Survey (COSMOS), the All-wavelength Extended Groth strip International Survey (AEGIS), and the UKIDSS Ultra-Deep Survey (UDS). Such deep fields have yielded rich data sets of photometry which are ready to build samples for detailed follow-up studies for their confirmation and to extract further information about such systems.

Observations at optical to near-IR wavelengths, from ground- and space-based facilities, form a major part of probing the rest-frame UV to optical emission from  $2 < z < 4$  galaxies. Fig. 2.1.1 identifies salient spectral features on a model spectrum created for an example SFG at  $z = 2.3$  and shows how they shift across the various atmospheric bandpasses from  $1 < z < 3$ . These features include:

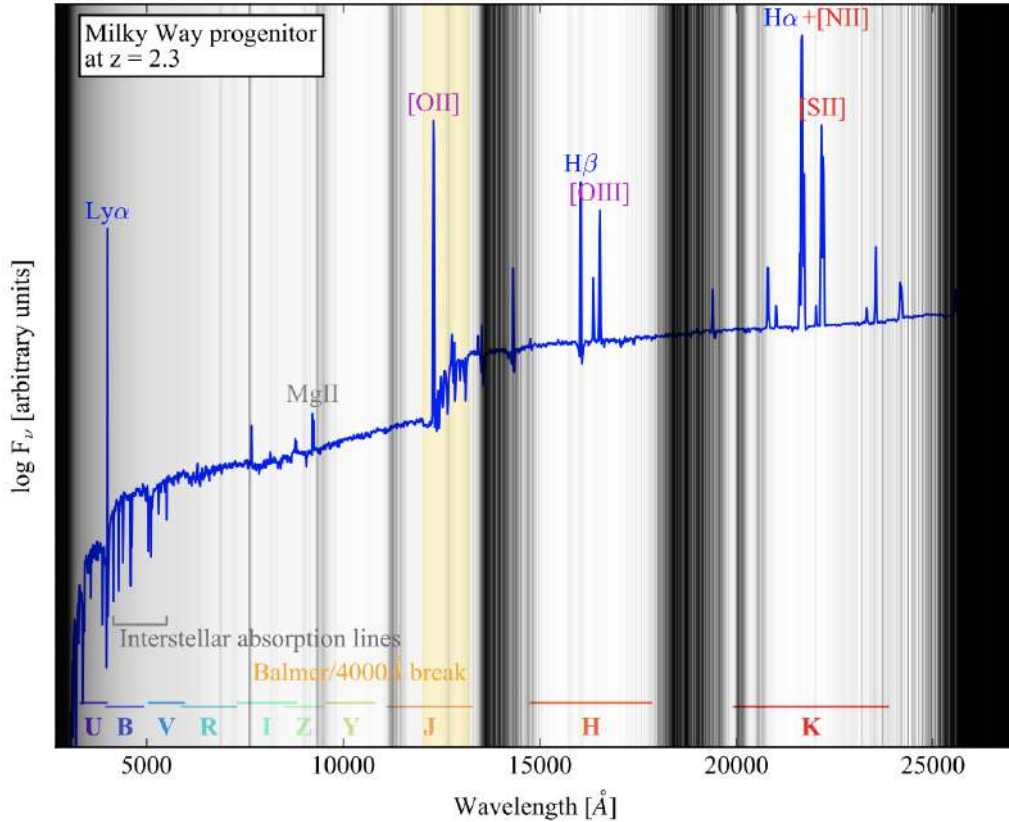


Figure 2.1.1: Synthetic spectrum of an illustrative SFG at  $z = 2.3$  plotted in observed wavelength vs. logarithmic flux density units. The spectrum was produced using the code BAGPIPES (Carnall et al., 2018) for the properties of a Milky Way-mass progenitor galaxy. The dark-to-light grey shading scales with increasing atmospheric transparency and the main photometric bandpasses are indicated at the bottom. Figure taken from Förster Schreiber & Wuyts (2020).

- i) Hydrogen recombination and atomic forbidden emission lines from warm ionized gas excited by star formation, AGN, and shock activity (e.g., Baldwin et al., 1981). These emission lines include Ly $\alpha$  1216, H $\beta$  4861, H $\alpha$  6563, [OII] $\lambda$ 3726,3729, and [OIII] $\lambda$ 4959,5007. Such emission lines provide diagnostics of nebular conditions, dust attenuation, galaxy dynamics, and gas outflows.
- ii) A rich suite of far-UV (in the range  $\sim 1200 - 2000\text{\AA}$ ) interstellar low- and high-ionization atomic absorption lines. These lines include SiII $\lambda$ 1260, the blend OI+SiII $\lambda$ 1303, CII $\lambda$ 1334, SiIV $\lambda$ 1393,1402, CIV $\lambda$ 1548,1550, FeII $\lambda$ 1608, and AlII $\lambda$ 1670. Examples of these lines are marked with red and blue lines in Fig. 2.1.2. Such lines are useful to trace gas outflows/inflows. This far-UV range also includes various other absorption and emission features from stellar photospheres and winds which allows studies of stellar metallicities (e.g., Cullen et al., 2019).
- iii) Prominent stellar wind features such as NV $\lambda$ 1238, 1242, SiIV $\lambda$ 1393, 1402, CIV  $\lambda$ 1548,1550, and HeII $\lambda$ 1640 from massive hot stars are also observed in the rest-UV spectra. These wind features appear as broad blueshifted absorption for weaker winds or as a P Cygni-type profile in dense winds (Leitherer et al., 1995). Examples of such lines are marked with magenta lines in Fig. 2.1.2.
- iv) Finally, collisionally excited, semi-forbidden transitions that are attributed to nebular regions

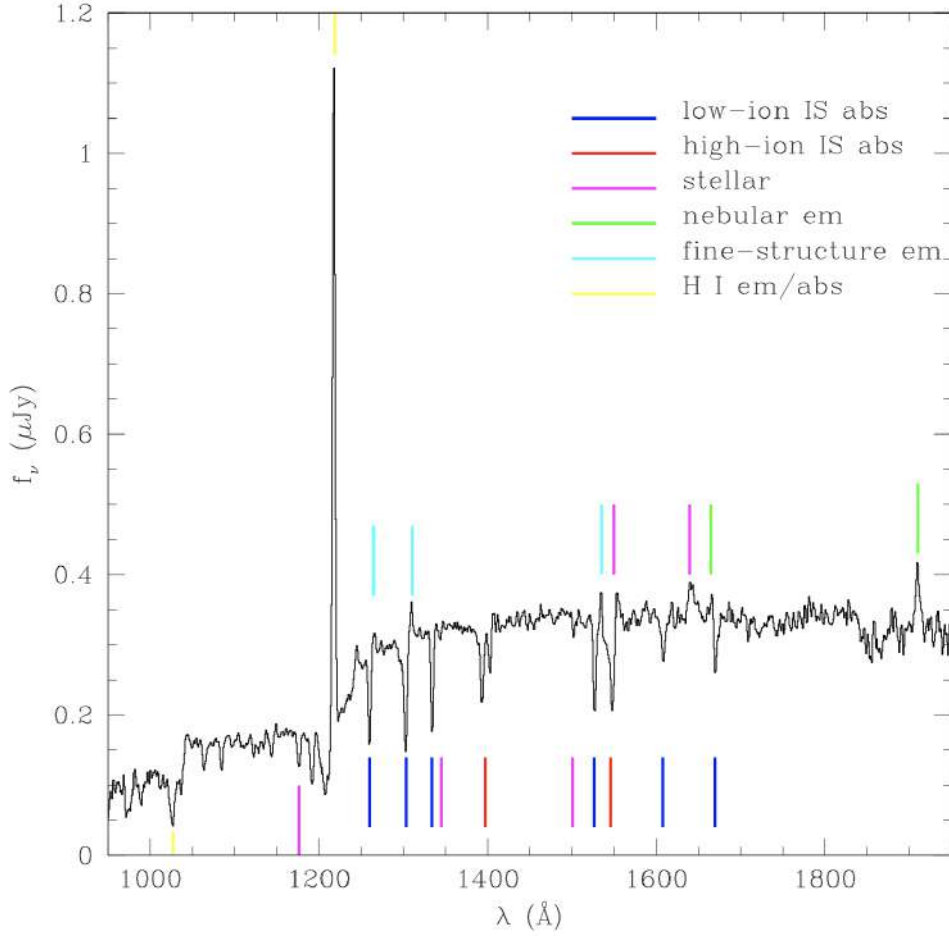


Figure 2.1.2: A composite rest-frame UV spectrum constructed from  $\sim 800$  individual LBG spectra. The spectrum is dominated by the emission from massive O- and B-type stars, and the shape of the UV continuum is modified shortward of Ly $\alpha$  by a decrement due to IGM HI absorption. Several different sets of UV features are marked as described in the text. The cyan lines mark the Si II\* fine-structure emission whose origin is ambiguous, the yellow lines mark emission and absorption due to interstellar HI. Figure taken from [Shapley et al. \(2003\)](#).

photoionized by radiation from massive stars such as OIII] $\lambda\lambda$ 1661,1666 and CIII] $\lambda\lambda$ 1906,1909, are also included in the rest-UV spectra (see emission lines marked with green lines in Fig. 2.1.2). The doublet is a combination of [CIII] $\lambda$ 1906.68Å, a forbidden magnetic quadrupole transition, and CIII] $\lambda$ 1908.73Å, a semi-forbidden electro-dipole transition (here, we are referring to vacuum wavelength), with an ionizing potential of 24.4 eV. This doublet is typically the brightest UV metal line in SFGs at intermediate redshift ( $z \sim 3$ , e.g., [Shapley et al., 2003](#)) and has been proposed as an alternative to search for galaxies in the reionization era ([Stark et al., 2014](#)), instead of the strongly attenuated Ly $\alpha$ . Some searches have been successful, reporting high EW(CIII]) in the observed spectra of galaxies at  $z > 6$  ([Stark et al., 2015, 2017](#); [Mainali et al., 2017](#); [Laporte et al., 2017](#); [Hutchison et al., 2019](#)), but other studies failed in detecting the line in strongly star-forming systems ([Sobral et al., 2015](#); [Schmidt et al., 2016](#)). In particular, the CIII] $\lambda\lambda$ 1906,1909 doublet is of great interest for this Thesis given that this is the main emission line we use to select galaxies and build our samples.

Large and deep surveys such as the Lyman Break Galaxy (LBG) survey of  $z \sim 3$  (Steidel et al., 2003), VIMOS Ultra Deep Survey (VUDS, Le Fèvre et al., 2015; Tasca et al., 2017), MUSE Hubble Ultra Deep Survey (Bacon et al., 2017), and VANDELS (McLure et al., 2018; Pentericci et al., 2018a; Garilli et al., 2021), have targeted SFGs at mainly  $z \sim 2 - 4$  to study the physical properties of SFGs with intense rest-UV emission lines. Significant improvements have been made also in the local universe with relatively large samples of metal-poor SFGs in The COS Legacy Spectroscopic Survey (CLASSY, Berg et al., 2022). In this Thesis, our samples at Cosmic Noon are built mainly using data from the VUDS and VANDELS surveys, which are described in the following subsections.

### 2.1.1 The VUDS survey

The VIMOS Ultra Deep Survey\* (VUDS, Le Fèvre et al., 2015) is a spectroscopic redshift survey of  $\sim 10000$  very faint galaxies to study the major phase of galaxy assembly  $2 < z < 6$ . The survey covers  $1 \text{ deg}^2$  in 3 separate fields: COSMOS (10h00m04.0s,  $+02^\circ 12' 40''$ ), Extended-Chandra Deep Fields (ECDFS, 03h32m28.0s,  $-27^\circ 48' 30''$ ) and VVDS-02h (02h26m00.0s  $-04^\circ 30' 00''$ ). The target selection was based on an inclusive combination of photometric redshifts ( $z_{\text{phot}} + 1\sigma \geq 2.4$  and  $i_{AB} \leq 25$ ) and LBG color-color selection criteria (e.g., Daddi et al., 2004). Each of the targeted fields has extensive very deep multi-band photometry ranging from u-band to Spitzer-IRAC  $4.5 \mu\text{m}$  band.

A total of 16 pointings were observed with the Visible MultiObject Spectrograph (VIMOS, Le Fèvre et al., 2003) on the ESO-VLT. Fifteen pointings were observed with both the Low Resolution (LR) blue grism covering  $3650 \leq \lambda \leq 6800 \text{ \AA}$  and the LR red grism covering  $5500 \leq \lambda \leq 9350 \text{ \AA}$ , leading to a full wavelength coverage of  $3650 \leq \lambda \leq 9350 \text{ \AA}$ . With slits  $1''$ -wide, these grisms provide a spectral resolution  $R = 230$ . On average, 600 individual slits were observed simultaneously. The remaining pointing was taken with the Medium Resolution (MR) grating ( $R=580$ ) for targets at  $z > 4.5$  which are not included in this Thesis.

To reach a total integration of 14h per slit, each of the LR blue or LR red grism observations consisted on average of 13 observing blocks (OBs) executed at the telescope. Each OB includes three spectroscopic exposures of 1250 to 1350s obtained by dithering  $0.75''$  along the slit. The observations were carried out in clear conditions during dark time with a seeing  $< 1''$  and air-mass lower than 1.5.

The survey has a completeness in redshift measurement of 74% for the most reliable measurements, down to  $i_{AB}=25$ , and measurements are performed all the way down to  $i_{AB}=27$ . The redshift distribution of the main sample peaks at  $z = 3 - 4$  and extends over a large redshift range mainly in  $2 < z < 6$ . At  $3 < z < 5$ , the galaxies cover a large range of luminosities  $-23 < M_U < -20.5$ , stellar mass  $10^9 < M_*/M_\odot < 10^{11}$ , and star formation rates  $1 < \text{SFR}/[M_\odot \text{ yr}^{-1}] < 10^3$ .

### 2.1.2 The VANDELS survey

The VANDELS<sup>†</sup> (McLure et al., 2018; Pentericci et al., 2018a) survey is an extragalactic ESO Public Spectroscopic Survey carried out using also the VIMOS spectrograph (Le Fèvre et al., 2003) on the

\*<https://cesam.lam.fr/vuds/>

<sup>†</sup><http://vandel.s.inaf.it>

VLT. It was designed to obtain ultra-deep medium-resolution spectra with sufficiently high S/N to allow measurement of spectral lines from the individual brighter sources, or from the stacked spectra of the fainter sources. The surveys targeted two deep fields: Chandra Deep Field South (CDFS, 03h32m30s,  $-27^{\circ}48'28''$ ) and UDS (02h17m38s,  $-05^{\circ}11'55''$ ). Both fields offer deep optical–near-IR HST imaging provided by the CANDELS survey (Koekemoer et al., 2011) and are covered by high-quality, publicly available, optical–near-IR imaging data from a wide variety of different ground-based telescopes.

VANDELS targets are selected on the basis of photometric redshifts and their physical properties, basically their specific SFR (sSFR), from SED fitting. Three main types of galaxies are included in the survey: (i) Bright SFGs in the redshift range  $2.4 \leq z_{\text{phot}} \leq 5.5$  with  $i_{\text{AB}} \leq 25$  and  $\text{sSFR} > 0.6 \text{ Gyr}^{-1}$  (ii) Faint SFGs in the redshift range  $3 \leq z_{\text{phot}} \leq 7$  (median  $z_{\text{phot}} = 3.5$ ) with  $25 \leq H_{\text{AB}} \leq 27$ ,  $i_{\text{AB}} \leq 27.5$  and  $\text{sSFR} > 0.3 \text{ Gyr}^{-1}$  (iii) massive passive galaxies at  $1.0 \leq z_{\text{phot}} \leq$  with  $H_{\text{AB}} \leq 22.5$  and  $\text{sSFR} < 0.1 \text{ Gyr}^{-1}$ . The survey also includes AGN candidates and Herschel-detected sources.

The observations were carried out using the MR grism with  $1''$ -wide slits which provides a spectral resolution of  $R=650$  and a mean dispersion of  $2.5 \text{ \AA}/\text{pixel}$  in the wavelength range  $4800\text{--}9800\text{\AA}$ . A nested slit strategy was adopted according to which within a given pointing, the brightest objects appear on a single mask and are observed for 20 hours, fainter objects appear on two masks and are observed for 40 hours of exposure time, while the faintest objects appear on four masks and are observed 80 hours exposure time. Single exposures of 20 min long were grouped in threes, resulting in an OB of 1 hr. Most observations were carried out in dark time and 92% of observations have an average airmass less than 1.4 with seeing below  $1''$  in almost 90% of the observations.

A total of 2087 spectra of galaxies were published in the final VANDELS Data Release (Garilli et al., 2021). These galaxies are included in the redshift range  $1 < z < 6.5$ , with stellar masses in the range  $10^{8.3} < M_{\star}/M_{\odot} < 10^{11.7}$ .

## 2.2 Spectral Energy Distribution fitting

The analysis of the SED of galaxies estimates a large amount of physical information about their properties which include their SFH, stellar metallicity, abundance patterns, stellar IMF, the total mass in stars, the physical state of gas and dust reddening (see Conroy, 2013, for a review). The SED describes the emission of radiation by galaxies due to different physical processes across the electromagnetic spectrum and is crucial to, for instance, determining the colors of galaxies when observed in various photometric filters. All the different physical processes occurring in galaxies leave their imprint on the global and the detailed shape of their SEDs. For example, the UV-NIR emission of SFGs (excluding strong AGN activity) arises from stellar light, either directly or reprocessed by the gas and dust of the surrounding ISM, and then their SEDs contain information about the stars of a galaxy, such as the stellar mass-to-light ratio, and also the surrounding ISM, such as the total dust mass.

However, models are necessary to connect the physical properties of a galaxy with its observed SED and to extract information from it. In the simplest scenario, a galaxy is a group of stars that includes numerous, low-luminosity, low-mass stars, but also bright, short-lived, massive O- and B-type stars. The scenario is more complex if we consider that such stars have different metallicities and

ages since not all of them were born simultaneously. In this sense, a simplification for the modeling of galactic SEDs is that the emitted light can be represented through a sum of spectra of *simple stellar populations* (SSPs), where an SSP is an idealized single-age, single-abundance ensemble of stars whose distribution in mass depends on both the assumed IMF and the assumed age of the ensemble. SSPs are basic ingredients in the modeling of galactic SEDs (see [Walcher et al., 2011](#), for a more detailed description).

Therefore, to construct SSPs one needs spectra from single stars with a variety of properties such as metallicities, masses, or temperatures, which can be obtained from theoretical (e.g., [Martins et al., 2005](#)) or empirical libraries (e.g., [Sánchez-Blázquez et al., 2006](#)). Regarding the age of the ensemble, isochrones, calculated in discrete steps in time, are usually used which consider the position of stars of the same age in the Hertzsprung-Russel diagram and then integrate the spectra of all stars along the isochrone to compute the total flux at a given age (e.g., [Charlot & Bruzual A, 1991](#)). In recent years, binary stellar populations have also been included in the construction of SSPs in order to incorporate binary mass transfer and its effect on stellar evolution pathways – e.g., Binary Population and Spectral Synthesis (BPASS, [Eldridge et al., 2017](#)).

Then the amount of stars for a given mass is computed from an IMF and stellar evolution models. The IMF, which describes the distribution in mass of a putative Zero-Age Main Sequence stellar population, is usually limited between a minimum ( $\sim 0.05 - 1.0M_{\odot}$ ) and maximum ( $\sim 100 - 150M_{\odot}$ ) stellar mass, and is typically modeled as a simple power-law model ([Salpeter, 1955](#)), a broken power-law ([Kroupa, 2001](#)), or a lognormal form ([Chabrier, 2003](#)), which are most commonly used. Examples of SSPs at different ages are shown in Fig. 2.2.1.

But we know that galaxies are not SSPs and are indeed a mix of stellar populations depending on their episodes of star formation. With the SSPs in hand, a SFH should be assumed to track the evolutions of stellar populations and estimate their physical properties. The SFHs describe how the SFR evolves with time and is usually assumed to be constant, exponentially declining/increasing (so-called  $\tau$  models), delayed exponentially declining, or even nonparametric SFHs.

We should also notice that the radiation from stars is also absorbed and processed by the gas and dust in the ISM. This absorption must be accounted for when comparing SSP models with UV/optical observations and a treatment of the radiative transfer of the stellar light through the ISM and subsequent ISM emission is necessary to understand the full UV–IR SED. Both, dust and gas in the ISM are actually included in SED fitting codes. For instance, dust absorbs and scatters much of the UV starlight and re-radiates it into the IR. Also, the ISM gas can be modeled, assuming that it is ionized by the radiation field of the stars which can be included with photoionization models (see next Sec. 2.3). Such nebular emission includes intense emission lines (see Sec. 2.1) which can represent an increase of flux in a given filter that should be modeled including this component in the model in order to constrain correctly their physical properties. The effect of nebular emission therefore cannot be ignored at high- $z$ , where high-SFR, low-metallicity galaxies are common (e.g., [Schaerer & de Barros, 2010](#)).

Several codes that perform SED fitting are available in the market. A list of codes is summarized in this [link](#) and includes the code BAGPIPES ([Carnall et al., 2018](#)) which is extensively used in this Thesis and is a Bayesian spectral fitting code written purely in Python where models can be built up to the desired level of complexity by specifying the number of model components, for example, dust and nebular-emission prescriptions and SFH components.

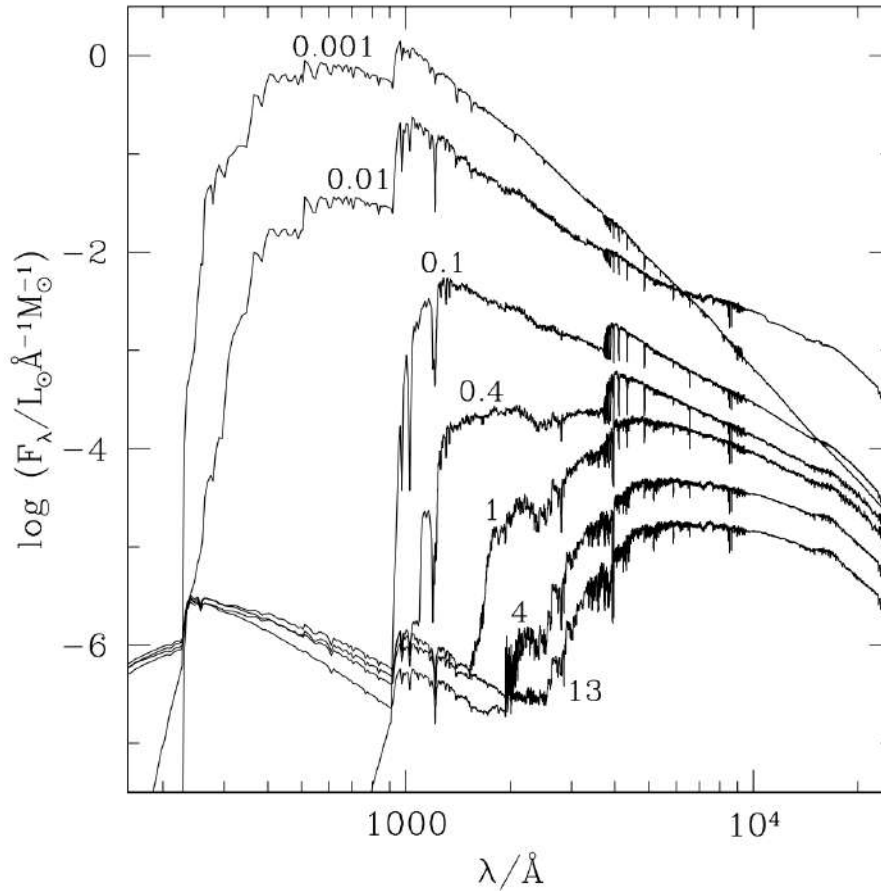


Figure 2.2.1: Spectral evolution of SSPs at constant solar metallicity. In these models, empirical stellar spectral libraries are considered and extended blueward of 3200Å and redward of 9500Å. Ages are indicated next to the spectra (in Gyr). Figure taken from [Bruzual & Charlot \(2003\)](#).

## 2.3 Photoionization models

The inclusion of the nebular emission to interpret the SED of a galaxy is particularly important in galaxies at low metallicity and at young ages. As we mentioned in Sec. 2.2, one approach is to include such components based on predictions from photoionization models.

Photoionization models are computational tools used to study the properties of ionized gas. These models simulate the interaction between ionizing radiation (typically from hot, massive stars or an active galactic nucleus) and the ISM gas, which leads to the ionization of atoms depending on their energy. Photoionization models have been key in understanding the ionization state and physical conditions of various astrophysical objects such as the ionization structure of HII regions (e.g., [Morisset et al., 2016](#)).

The models calculate the ionization fraction of the gas as a function of depth, which can be used to predict the emission and absorption properties of the gas after taking into account the SED of the ionizing radiation, the geometry of the gas (e.g., spherical, cylindrical, or plane-parallel), the density and temperature of the gas, and the chemical composition of the gas.

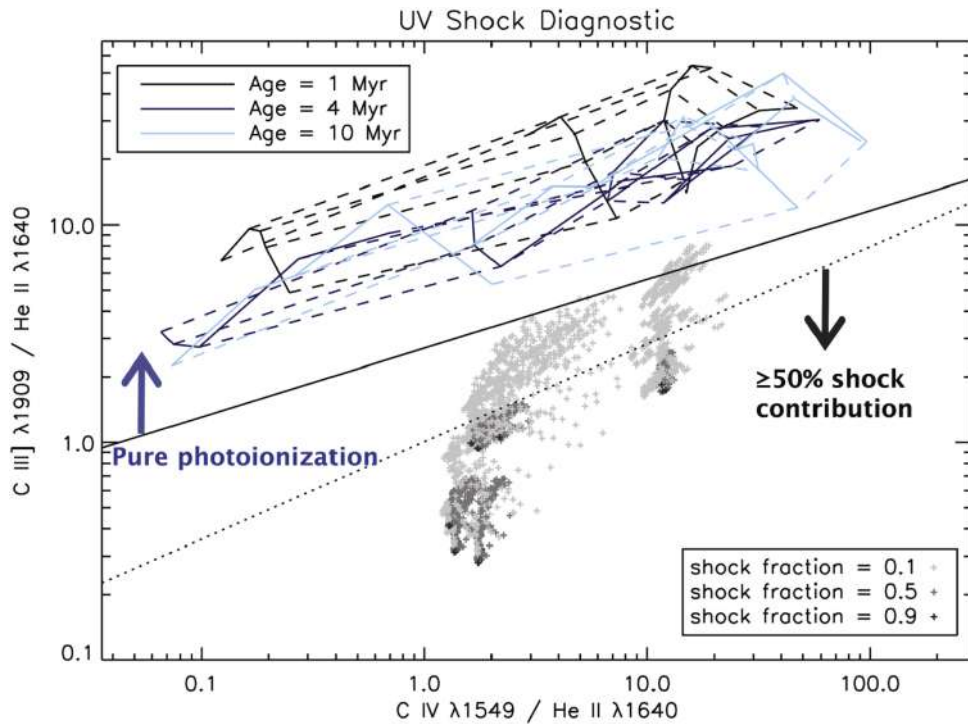


Figure 2.3.1: Predictions of  $\text{C III]}\lambda 1909/\text{He II}\lambda 1640$  vs.  $\text{C IV}\lambda 1549/\text{He II}\lambda 1640$  based on photoionization models. Solid and dashed lines show pure photoionization model grids where solid lines correspond to constant  $U$  and dashed lines correspond to constant metallicity ( $Z = 0.001\text{--}0.006$ ). Each grid is color-coded by burst age. On the other hand, gray crosses show the predicted line ratios from the photoionization+shock models. Darker colors indicate a higher shock contribution. The shocked gas is at  $Z=0.003$  in all models. The solid black line separates pure photoionized from shock models. Figure taken from [Jaskot & Ravindranath \(2016\)](#).

Based on those calculations, predictions and interpretations of the relative strength of some of the main nebular lines can be done and is an alternative method to constrain, for instance, the gas-phase metallicity (see [Maiolino & Mannucci, 2019](#), for a more detailed discussion) or the source of ionization (e.g., [Gutkin et al., 2016](#); [Feltre et al., 2016](#); [Jaskot & Ravindranath, 2016](#)). An example of the use of photoionization models to separate galaxies based on the dominant source of ionization (pure massive stars or massive stars + shocks) is displayed in Fig. 2.3.1. One of the advantages of this method is the wide range of properties that can be explored (e.g., extremely metal-poor gas) or the intense ionizing spectrum (e.g., [Schaerer, 2003](#); [Kewley et al., 2013](#); [Jaskot & Ravindranath, 2016](#)). However, they may be simplistic with simplified geometrical assumptions that do not reflect the complexity of galaxies.

Detailed photoionization codes, such as Cloudy ([Ferland et al., 2013](#)) or Mappings ([Sutherland & Dopita, 1993](#)), are generally used to generate a grid of models out of which a number of line ratios are extracted and proposed as diagnostic of the gas metallicity or chemical abundances (e.g., [Pérez-Montero & Amorín, 2017](#); [Byler et al., 2020](#)). However, most of them assume that chemical abundances scale proportionally to solar, except generally for N whose abundance is assumed to scale with the global metallicity (e.g., [Nicholls et al., 2017](#)).

The effect of dust is generally included, both in terms of dust extinction and in terms of dust depletion of chemical elements, and the assumptions on dust distribution affect the resulting structure

of the HII region (e.g., [Stasińska & Szczerba, 2001](#)).

The primary quantities that are varied in the grid of parameters are metallicity and ionization parameters, defined as the dimensionless ratio of the incoming photon flux density and gas density at the cloud surface, normalized by the speed of light. Metallicity and ionization parameters are, for a given shape of the ionizing flux, the two parameters most important in affecting the flux ratios of the main nebular lines, and are often subject to degeneracies, in the sense that most emission line ratios depend on both parameters.

UV nebular lines encode precious information on the physical conditions of the ionized gas in galaxies. Different photoionization models, used to understand the role of age, ionization parameter, metallicity, and dust on the emergent UV nebular lines, struggle to explain their origin and strength (e.g., [Jaskot & Ravindranath, 2016](#); [Gutkin et al., 2016](#); [Feltre et al., 2016](#); [Nakajima et al., 2018b](#); [Byler et al., 2018](#); [Hirschmann et al., 2019](#)). However, so far, all models require the presence of hard radiation fields to be able to reproduce the observed UV emission lines with high ionization potentials, which also leads to more extreme ionization conditions in the ISM (e.g., high EWs and line ratios). Constraining available models with large and representative samples of emission line galaxies is therefore needed to improve our understanding of the physical mechanisms producing UV emission lines, thus paving the way for future extensive studies of galaxies at  $z > 6$ .

After a brief introduction to the techniques we will use in the Thesis, in the following Chapter 3 we start presenting the analysis and results obtained in this Thesis and the lessons we learned.

## Rest-UV properties of CIII] emitters at $z \sim 3^*$

In this Chapter, we study the mean properties of a large representative sample of 217 galaxies showing CIII] $\lambda$ 1908 (hereafter CIII]) emission at  $2 < z < 4$ , selected from a parent sample of  $\sim 750$  main-sequence SFGs in the VANDELS survey. These CIII] emitters have a broad range of UV luminosities, allowing for a detailed stacking analysis to characterize their stellar mass, SFR, and metallicity as a function of the UV emission line ratios, EWs, and the C/O abundance ratio. Our analysis is based on stacked spectra which provide unprecedented high S/N spectra for CIII] emitters over more than three decades in luminosity, stellar mass, and SFR. This enables a full spectral fitting to derive stellar metallicities for each stack. Moreover, we use diagnostics based on photoionization models and UV line ratios to constrain the ionization sources of the galaxies and derive the C/O abundance.

The Chapter is organized as follows. In Section 3.2, we present the sample selection, the basic properties of the sample, and our stacking method. In Section 3.3, we present a qualitative and quantitative description of the emission and absorption line detections via different emission-line diagnostics, the estimation of metallicities, C/O abundances, and different correlations found for our sample. In Section 3.4, we discuss our results, focusing on the stellar mass-metallicity relation and the C/O-metallicity relation. Finally, Section 3.5 presents our conclusions.

### 3.1 Context

The reionization of the Universe is an outstanding problem that still remains unsolved. While the time scales over which reionization ended are well established around redshift  $z \sim 6$  (e.g. [Mason et al., 2019](#); [Yang et al., 2020](#); [Paoletti et al., 2020](#)), the dominant sources of photons responsible for the transformation of the dominant neutral hydrogen into a mostly ionized medium have yet to be determined. Faint low-mass star-forming galaxies are considered candidates to lead reionization in this era due to their large number density and weak gravitational potential, favoring the strong and effective feedback needed to open low HI density paths for photons to escape (e.g., [Wise et al., 2014](#); [Robertson et al., 2015](#); [Bouwens et al., 2016](#); [Finkelstein et al., 2019](#)). However, the contribution

---

\*Based on [Llerena et al. \(2022\)](#) “The VANDELS survey: Global properties of CIII] $\lambda$ 1908Å emitting star-forming galaxies at  $z \sim 3$ ”, *Astronomy & Astrophysics*, Volume 659, id.A16, 31 pp.

of additional sources with higher ionizing photon efficiency, such as luminous, massive starburst galaxies (e.g. [Naidu et al., 2020](#); [Endsley et al., 2021](#)) and AGNs (e.g. [Grazian et al., 2018](#)) might have a significant contribution (e.g. [Dayal et al., 2020](#), and references therein).

A detailed characterization of the rest-frame UV spectra of SFGs at  $z \gtrsim 6$  is thus essential to understand their ionization properties and thus shed new light into the reionization process. In the last few years, deep NIR observations of galaxies during the reionization era have reported the presence of UV emission lines with unusually high EWs, such as CIV $\lambda$ 1550Å, HeII $\lambda$ 1640Å, OIII] $\lambda$ 1663Å, or CIII] $\lambda$ 1908Å (see [Stark, 2016](#), for a review). As we mentioned in Sec. 2.1, constraining available models with large and representative samples of emission line galaxies is therefore needed to improve our understanding of the physical mechanisms producing UV emission lines, thus paving the way for future extensive studies of galaxies at  $z > 6$ . Emission lines are relevant not only to understanding the physical conditions governing these early galaxies but also to providing a tool for their spectroscopic redshift identification. This is especially relevant at  $z > 6$ , where absorption features are weak and a significant drop in the number of galaxies with Ly $\alpha$  emission, often the strongest emission line in the UV, is observed due to the sharp increase of absorption by a predominantly neutral IGM (e.g., [Fan et al., 2006](#); [Pentericci et al., 2014](#); [Cassata et al., 2015](#); [Fuller et al., 2020](#)).

At low- $z$ , studying UV emission lines requires space-based spectroscopy. Studies using *Hubble Space Telescope* (HST) observations of relatively small samples showed that strong CIII] emission is generally present in the spectra of local low-metallicity galaxies (e.g., [Garnett et al., 1995](#); [Leitherer et al., 2011](#); [Berg et al., 2016, 2018](#); [Senchyna et al., 2017](#); [Ravindranath et al., 2020](#)). However, the characterization of larger samples spanning a wider range of properties (e.g. stellar masses, SFRs, metallicities) requires a stronger observational effort that has precluded studies with statistical significance. This is different at  $2 < z < 4$ , where both Ly $\alpha$  and CIII] are redshifted into the optical and can be probed over larger samples with ground-based 8-10m-class telescopes. Also, galaxies at  $z > 2$  are likely to be more similar to those at  $z > 6$  (see [Shapley, 2011](#), for a review). Several studies now routinely report CIII] emission (along with other strong emission and absorption lines) in galaxies at cosmic noon, either from small samples of relatively bright galaxies ([Steidel et al., 1996](#); [Erb et al., 2010](#); [Steidel et al., 2014](#); [Amorín et al., 2017](#); [Du et al., 2020](#)), fainter gravitationally lensed galaxies ([Pettini et al., 2000](#); [Christensen et al., 2012](#); [Stark et al., 2014](#); [Rigby et al., 2015](#); [Berg et al., 2018](#); [Vanzella et al., 2021](#)), or in high S/N stacks from larger galaxy samples ([Steidel et al., 2001](#); [Shapley et al., 2003](#); [Le Fèvre et al., 2019](#); [Nakajima et al., 2018a](#); [Feltre et al., 2020](#)).

Deep surveys such as the VUDS ([Le Fèvre et al., 2015](#)) or the MUSE Hubble Ultra Deep Field Survey (HDFS, [Bacon et al., 2017](#)) have recently studied large samples of CIII] emitters. [Le Fèvre et al. \(2019\)](#) showed that only 24% of the VUDS galaxies at  $2.4 < z < 3.5$  shows CIII] emission, but only in  $\sim 1\%$  this emission is as intense as the values found at  $z > 6$ , i.e.  $\text{EW}(\text{CIII])} \gtrsim 10\text{-}20\text{\AA}$ . [Amorín et al. \(2017\)](#) showed that extreme CIII] emitters at  $2 < z < 4$  in VUDS are very strong LAEs characterized by very blue UV spectra with weak absorption features and bright nebular emission lines. These galaxies present high excitation, low metallicities, and low C/O abundances ratios, similar to the values expected to be common in most of the galaxies during the first 500 Myr of cosmic time.

Using stacking of a large sample of LAEs from the MUSE HDFS, [Feltre et al. \(2020\)](#) found that the mean spectra of LAEs with larger Ly $\alpha$  EW, fainter UV magnitudes, bluer UV spectral slopes, and lower stellar masses show the strongest nebular emission. [Maseda et al. \(2017\)](#) arrived at similar conclusions for a sample of 17 CIII] emitters at  $z \sim 2$  in the MUSE HDFS. For these galaxies, they found a correlation between  $\text{EW}(\text{CIII])}$  and  $\text{EW}([\text{OIII}]\lambda 5007)$ , linking the properties of the stronger

CIII] emitters to those of the EELGs (Maseda et al., 2014; Amorín et al., 2015). These are low-metallicity starbursts defined by their unusually high  $\text{EW}([\text{OIII}]\lambda 5007) \gtrsim 200 \text{ \AA}$  (see also, Tang et al., 2021; Matthee et al., 2021). At lower- $z$ , the GP galaxies (Cardamone et al., 2009; Amorín et al., 2010, 2012a), are EELGs and they include objects for which Lyman continuum leakage has been directly measured (Izotov et al., 2016; Guseva et al., 2020; Wang et al., 2021). These galaxies show prominent UV nebular lines, including high EW CIII] (Schaerer et al., 2018; Ravindranath et al., 2020).

While EELGs are likely analogs of the bright-end of reionization-era galaxies, the more common population of normal, main-sequence SFGs showing moderate or low EW(CIII]) still needs to be fully characterized at  $z > 2$ . This requires large very deep samples achieving sufficiently high S/N spectra to detect and study the fainter CIII]-emitters. In this Chapter, we aim at exploiting the unprecedented ultra-deep spectra provided by the VANDELS survey (McLure et al., 2018; Pentericci et al., 2018a) to assemble a large unbiased sample of main-sequence SFG CIII] emitters at  $2 < z < 4$  and characterize their main physical properties as a function of their UV line emission and chemical abundances.

Moreover, as different chemical elements are produced by stellar populations at different timescales, the relative abundance of elements enables us to obtain constraints on the SFH of galaxies (Maiolino & Mannucci, 2019). As we mentioned in Sec. 1.3.2, the C/O abundance ratio is a powerful indicator because most of the oxygen is synthesized in massive stars ( $> 8M_{\odot}$ ), while carbon is produced in massive and intermediate-mass stars. Thus, a time delay in the production of carbon and its ejection to the ISM makes C/O a measurable *chemical clock* for the relative ages of the stellar populations in galaxies (Garnett et al., 1995) and an important indicator to constraint chemical evolution models (Vincenzo & Kobayashi, 2018).

In this Chapter, we focus on the average properties of CIII] emitters using the spectral stacking technique. One key goal is to study, for the first time at this redshift, the relation between the mean stellar metallicity and C/O abundances of galaxies, which is discussed in terms of other physical properties of the sample. This will be useful to interpret future observations with JWST at higher redshifts where only the rest-frame UV spectral lines would be accessible. In the next Chapter 4, we will present a second study based on individual galaxies.

## 3.2 Methodology

### 3.2.1 Sample selection

In this work, we use spectra from VANDELS (McLure et al., 2018; Pentericci et al., 2018a), an ESO public spectroscopic survey conducted with VIMOS at the *Very Large Telescope*. VANDELS obtained unprecedented high S/N optical spectra of  $\sim 2100$  galaxies at redshift  $1.0 \leq z \leq 7.0$  in the UKIDSS Ultra Deep Survey (UDS: 02:17:38, -05:11:55) and the Chandra Deep Field South (CDFs: 03:32:30, -27:48:28) fields (see more information in Sec. 2.1.2). In short, VANDELS targets can be classified according to their selection criteria as bright SFGs in the range  $2.4 \leq z \leq 5.5$  and Lyman-break galaxies (LBGs) in the range  $3.0 \leq z \leq 7.0$ , and a smaller sample of passive galaxies ( $1.0 \leq z \leq 2.5$ ) and AGN candidates. In this work, we only select galaxies from the SFGs and LBGs targets.

Our sample is drawn from VANDELS DR3, which consists of 1774 galaxies –a subset of the

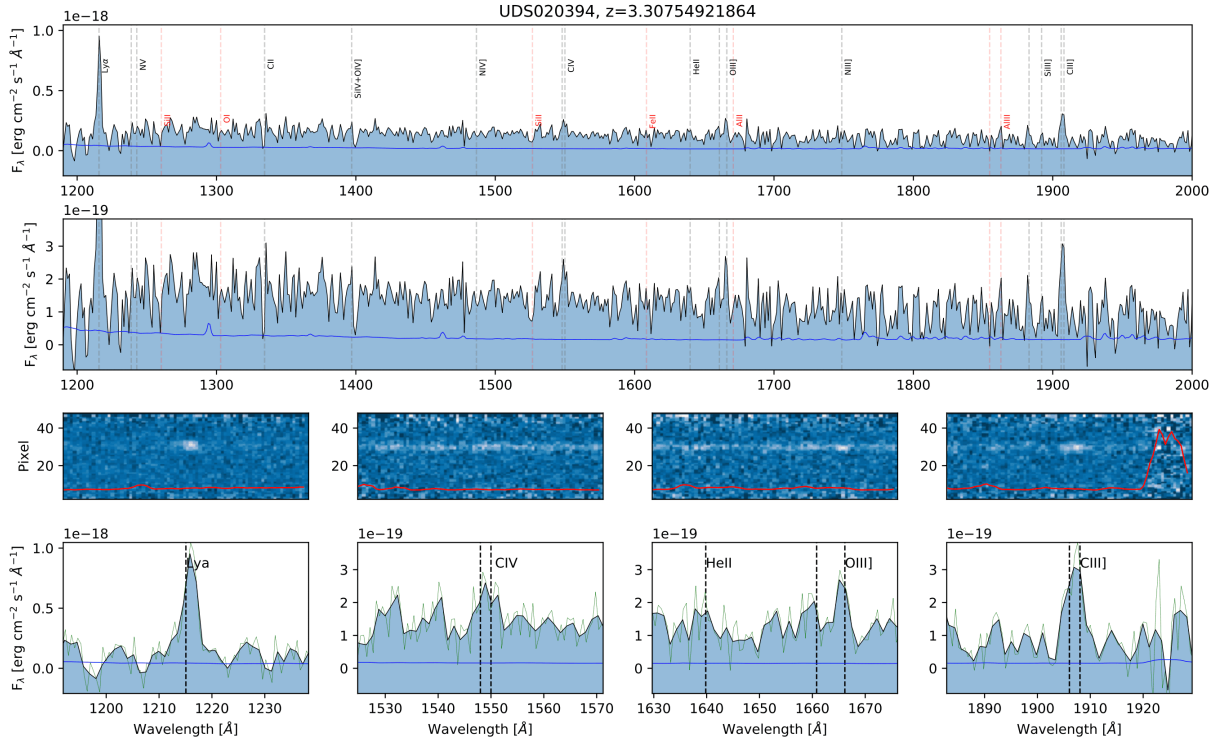


Figure 3.2.1: Spectrum of UDS20394, one of the more intense CIII] emitters in the C3 sample, whose estimated parameters are  $\log(M_*/M_\odot)=9.32$ ,  $\text{SFR}=4.01 M_\odot \text{ yr}^{-1}$ ,  $M_{FUV} = -20$ ,  $M_{K_s} = -20.46$ ,  $\text{EW}(\text{Ly}\alpha)=19.2\text{\AA}$ , and  $\text{EW}(\text{CIII])}=12.3\text{\AA}$ . The green faint line is the de-redshifted VANDELS spectrum and the black line is the same but resampled by a factor of 2. The blue line in the upper panels is the error spectrum. The red line in the intermediate panels is the scaled sky spectrum.

2087 galaxies included in the VANDELS final data release (Garilli et al., 2021). We select galaxies with spectroscopic redshift quality flag 3 or 4, which means 95% and 100% of confidence in their spectroscopic redshift (McLure et al., 2018). We select galaxies at  $2 < z < 4$  to ensure that the CIII] emission lines are included in the spectral range provided by the VANDELS spectra. Detection of CIII], typically the strongest nebular emission line in the sample, at  $\text{S/N} > 3$  is required to ensure proper measurement of the systemic redshift. With this constraint, from a parent sample of 746 galaxies with the above redshift range and quality flags, a first sample of 225 galaxies is selected by their CIII] emission (130 in the CDFS field and 95 in the UDS field).

We cross-match the sample of CIII] emitters with the 7Ms CDF-S catalog (Luo et al., 2017) and the  $\sim 200\text{-}600\text{Ks}$  X-UDS catalog (Kocevski et al., 2018) in order to discard galaxies with X-ray emission within 3 arcsec of separation. We also discard galaxies with spectral features consistent with AGNs or with strong sky residuals. A total of 8 galaxies were excluded from the sample. A more detailed analysis of the AGN sample in VANDELS will be presented in Bongiorno et al., (in prep.) Our final sample of CIII] emitting galaxies is made of 217 galaxies (hereinafter C3 sample), which represents  $\sim 30\%$  of the parent sample. Figure 3.2.1 shows the rest-frame spectrum of one of the galaxies in the C3 sample. Some of the expected UV absorption and emission lines are marked by vertical lines. Detected emission lines that are relevant to our study are shown in both 1D and 2D spectra and marked in different zoom-in panels.

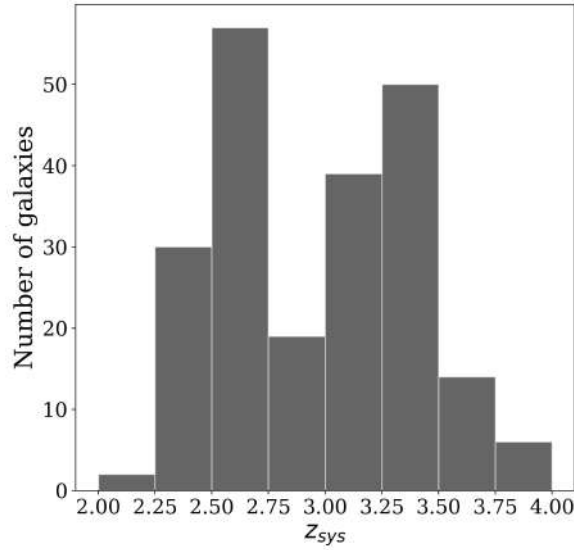


Figure 3.2.2: Systemic redshift distribution of the CIII] emitting galaxies in the C3 sample.

### 3.2.2 Systemic redshift and basic properties of the sample

In order to prepare the C3 sample for the stacking procedure, we follow the methodology described in [Marchi et al. \(2019\)](#) to derive accurate systemic redshifts ( $z_{sys}$ ) using the nebular CIII] line. In [Figure 3.2.2](#) we present the resulting  $z_{sys}$  distribution for the C3 sample, which spans the range of  $2.17 - 3.82$  ( $\langle z_{sys} \rangle = 2.98$ ,  $\sigma = 0.43$ ). Compared with the spectroscopic redshifts ( $z_{spec}$ ) of the sample reported in [McLure et al. \(2018\)](#), the systemic redshifts are slightly larger with a mean difference  $\Delta(z_{sys} - z_{spec}) = 0.002$ , that corresponds to  $\sim 4\text{\AA}$  at the rest-wavelength of CIII].

The physical properties of the C3 sample and the remaining galaxies in the VANDELS DR3 parent sample at  $2 < z < 4$  are obtained from the SED fitting using the Bayesian Analysis of Galaxies for Physical Inference and Parameter EStimation (BAGPIPES<sup>†</sup>) code. BAGPIPES is a state-of-the-art Python code for modeling galaxy spectra and fitting spectroscopic and photometric observations ([Carnall et al., 2018](#)), which has been now applied to the VANDELS final data release ([Garilli et al., 2021](#)). For this Chapter, the BAGPIPES code is run fixing the redshift and using the 2016 updated version of the [Bruzual & Charlot \(2003\)](#) models using the MILES stellar spectral library ([Falc3n-Barroso et al., 2011](#)) and updated stellar evolutionary tracks of [Bressan et al. \(2012\)](#) and [Marigo et al. \(2013\)](#). The stellar metallicity is fixed to 0.2 Solar and the nebular component is included in the model assuming an ionization parameter  $\log(U) = -3$ . We choose to fix these parameters to typical mean values found in SFGs at similar redshift (e.g. [Cullen et al., 2019](#); [Runco et al., 2021](#)) to minimize the effects of possible degeneracies affecting the models (see, e.g. [Castellano et al., 2014](#)). We note, however, that the results presented in subsequent sections remain unchanged if we allow these parameters to vary within typically observed ranges. Dust attenuation is modeled using the [Salim et al. \(2018\)](#) model. The SFH is parameterized using an exponentially increasing  $\tau$ -model. We obtain a mean value for the timescale  $\tau = 5.49$  Gyr for the C3 sample ( $\tau = 5.36$  Gyr for the parent sample), which essentially implies constant star-formation. On the other hand, we obtain a

<sup>†</sup><https://bagpipes.readthedocs.io/en/latest/>

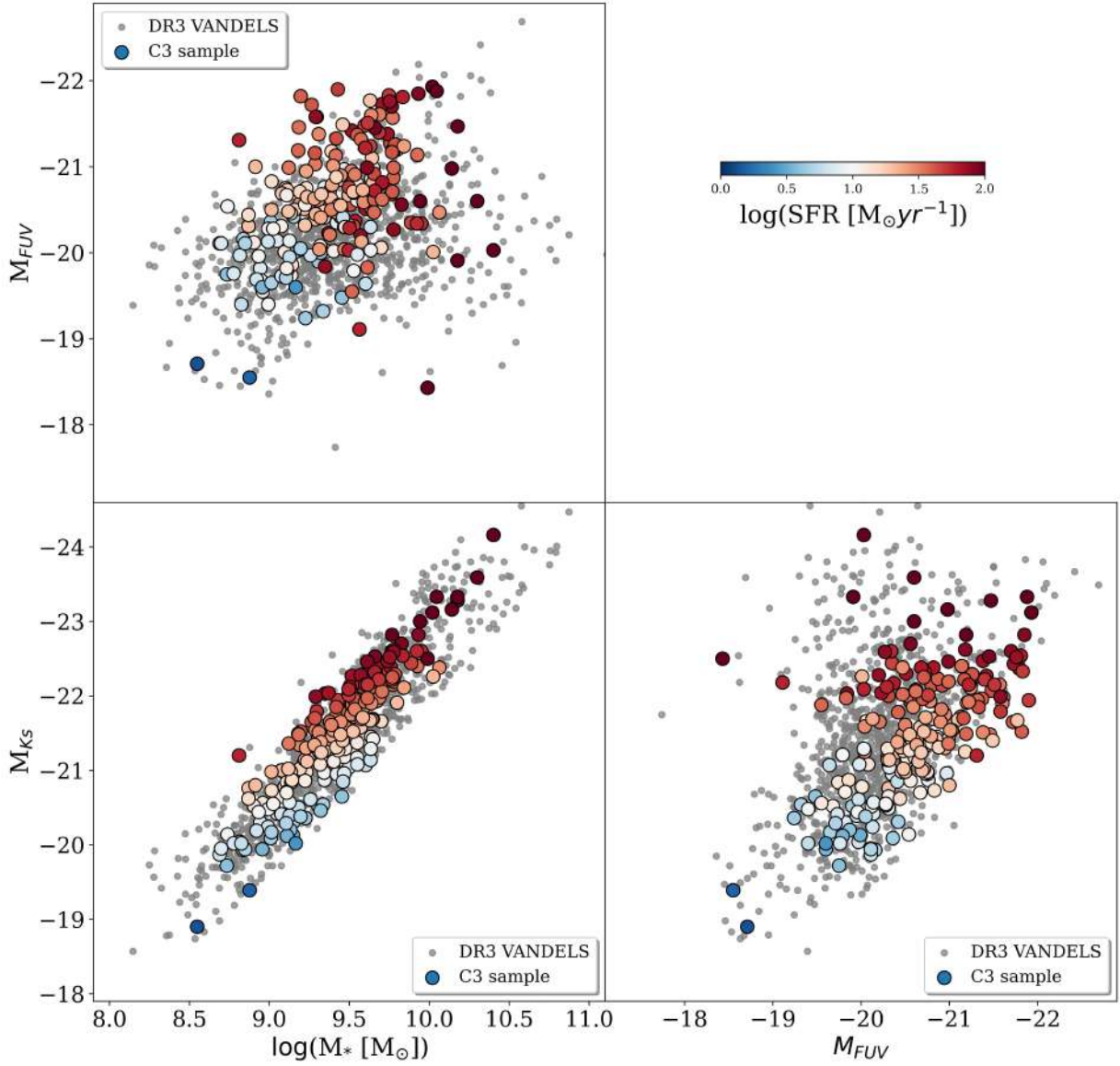


Figure 3.2.3: Relations between the resulting BAGPIPES parameters in the VANDELS main-sequence galaxies. The galaxies of the C3 sample are color-coded by star formation rate. Gray points are VANDELS galaxies of the parent sample that were not included in the C3 sample.

mean age, i.e. the time since SFH begins, of 228 Myr for the C3 sample (270 Myr for the parent sample). The ages obtained from the SED fitting are thus longer than the timescales ( $< 20\text{Myr}$ ) in which the EW(CIII)] changes with age, according to photoionization models assuming continuous star formation (Jaskot & Ravindranath, 2016).

In Figure 3.2.3, we present some relations between the parameters extracted from the SED fitting, such as stellar mass, and rest-frame luminosity in different filters. The C3 sample is color-coded by SFR, which range from  $\log \text{SFR} [M_\odot \text{yr}^{-1}] = 0.13\text{--}2.89$  ( $\langle \log \text{SFR} [M_\odot \text{yr}^{-1}] \rangle = 1.33$ ,  $\sigma = 0.42$ ). The stellar masses of the C3 sample span from  $\log(M_*/M_\odot) = 8.54$  to 10.40 with a mean value of  $\langle \log(M_*/M_\odot) \rangle = 9.41$  ( $\sigma = 0.33$ ). The FUV(1500) luminosity, tracing the young stellar component of galaxies, spans from  $M_{FUV} = -21.93$  to  $-18.43$  mag, with a mean value of  $\langle M_{FUV} \rangle = -20.55$  mag ( $\sigma = 0.65$ ). The K<sub>s</sub> band, which better traces the evolved stellar component, ranges be-

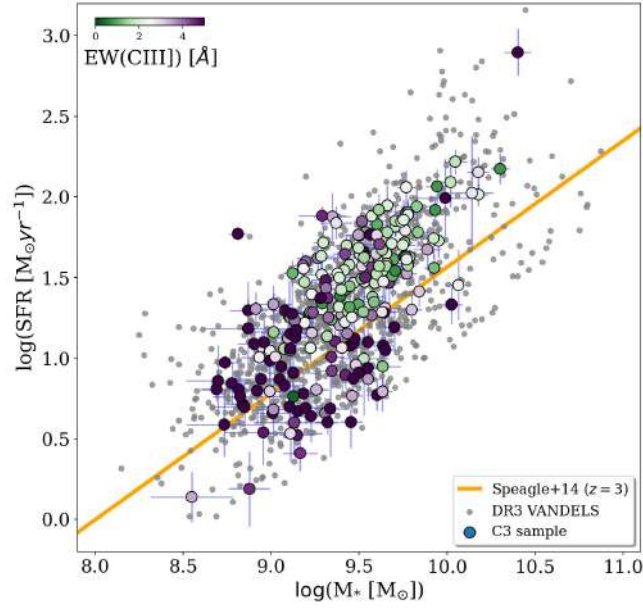


Figure 3.2.4:  $M_*$ -SFR relation with our sample color-coded by EW (CIII]). The orange solid line is the main sequence at  $z = 3$  according to Speagle et al. (2014). Gray points are as in Fig. 3.2.3.

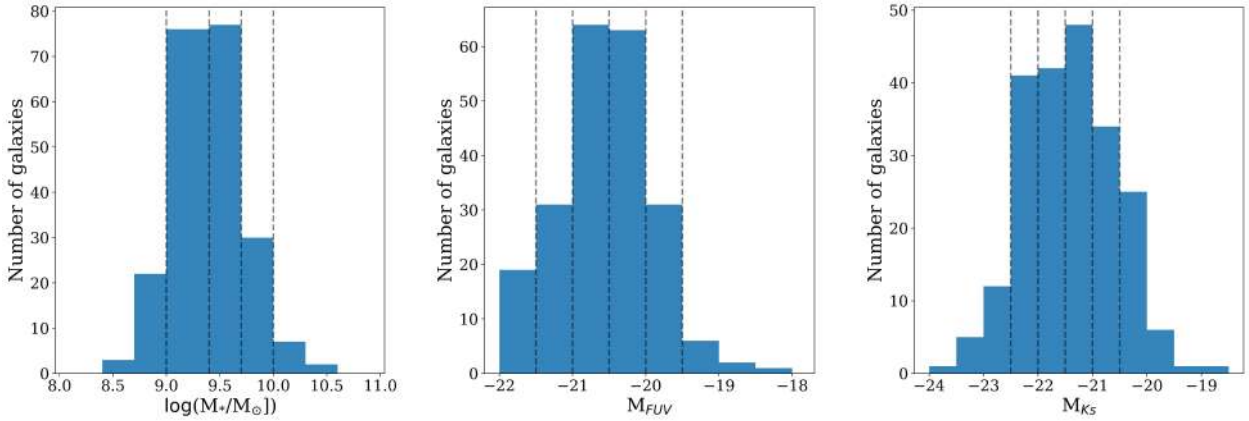


Figure 3.2.5: Distribution of the resulting BAGPIPES parameters in the C3 sample, *from left to right*: stellar mass, FUV and Ks band luminosity. The vertical dashed lines represent the ranges of each bin for stacking according to Table 3.2.1.

tween  $-24.16$  and  $-18.90$  mag, with a mean value of  $\langle M_{K_s} \rangle = -21.44$  mag ( $\sigma = 0.85$ ). As expected, the rest  $K_s$ -band luminosity is a good tracer of the stellar mass of the galaxies, showing little scatter in Fig. 3.2.3. Fig. 3.2.4 demonstrates that the C3 sample is mainly located along the  $M_*$ -SFR main-sequence followed by the parent sample. Only a few galaxies at the higher stellar mass end ( $\gtrsim 10^{10} M_\odot$ ) appear offset to higher SFR. The C3 sample is therefore fairly representative of the VANDELS DR3 parent sample in this redshift range. The parameters shown in Fig. 3.2.3 are thus used for the stacking analysis of the global properties of the sample and their distributions are displayed in the histograms in Figure 3.2.5.

Besides the physical parameters obtained from BAGPIPES, we also measure the EW(CIII]) and

Table 3.2.1: Bin ranges used for the stack analysis with BAGPIPES parameters.

Bin	Bin range $\log M_*/M_\odot$	$N_{gal}^{(a)}$	Bin range FUV luminosity	$N_{gal}^{(a)}$	Bin range $K_s$ luminosity	$N_{gal}^{(a)}$
1	8.4 - 9.0	25	-22.0 : -21.5	19	-24.0 : -22.5	19
2	9.0 - 9.4	76	-21.5 : -21.0	31	-22.5 : -22.0	41
3	9.4 - 9.7	77	-21.0 : -20.5	64	-22.0 : -21.5	42
4	9.7 - 10.0	30	-20.5 : -20.0	63	-21.5 : -21.0	48
5	10.0 - 10.6	9	-20.0 : -19.5	31	-21.0 : -20.5	34
6			-19.5 : -18.0	9	-20.5 : -18.5	33

<sup>(a)</sup> Number of galaxies in each bin.

EW(Ly $\alpha$ ) in all galaxies of the C3 sample. For CIII], we use *slinefit*<sup>‡</sup> following a similar scheme to the one that will be explained in detail in Sec. 3.2.3 for the stacked spectra. The EW(CIII]) distribution is presented in the left panel in Fig. 3.2.6. The EW(CIII]) has a mean value of  $\langle \text{EW}(\text{CIII])} \rangle = 3.98 \text{ \AA}$  ( $\sigma = 3.12 \text{ \AA}$ ). While most galaxies show low EW(CIII])  $< 5 \text{ \AA}$ , we find a small number of strong CIII] emitters with EW(CIII]) up to  $\sim 20 \text{ \AA}$  ( $\sim 11\%$  of the C3 sample with EW(CIII])  $> 8 \text{ \AA}$ ). The EW(CIII]) values are shown in the color code of Fig. 3.2.4, where the  $M_*$ -SFR plane is shown. It can be noticed that the intense and faint CIII] emitters are above and below the main sequence, with some trend suggesting that the more intense CIII] emitter have lower stellar masses and then lower star formation rates.

About half of our C3 sample is at  $z > 2.9$  with Ly $\alpha$  observable in the spectral range. For these 105 galaxies, we use the EW(Ly $\alpha$ ) obtained by Cullen et al. (2020). The distribution of such values is presented in Fig. 3.2.6. We find that the EW(Ly $\alpha$ ) span a wide range from  $-48.37$  to  $99.79 \text{ \AA}$ , with a mean value of  $12.69 \text{ \AA}$  ( $\sigma = 28.78$ ). These values are significantly higher than the mean EW(Ly $\alpha$ )  $\sim 2 \text{ \AA}$  of the parent sample. Thus, the C3 sample includes both strong Ly $\alpha$  emitting galaxies and galaxies with weak or absent Ly $\alpha$  emission. About 34% of the C3 sample with Ly $\alpha$  included in the spectral range are considered LAEs (i.e., EW(Ly $\alpha$ )  $> 20 \text{ \AA}$ ) consistent with what is commonly found for LGBs at these redshifts (e.g., Cassata et al., 2015; Ouchi et al., 2020). A smaller fraction of LAEs ( $\sim 23\%$ ) is found for galaxies with non-detections ( $S/N < 3$ ) of CIII] in the parent sample.

### 3.2.3 Stacking procedure

In this Chapter, we are interested in the characterization of the mean physical properties of the CIII] emitters in VANDELS. For this reason, we perform a stacking analysis, binning the C3 sample by stellar mass and rest-frame luminosity and EW. This allows us to increase the S/N of the data and probe properties, such as stellar metallicity, which would not be possible in individual objects.

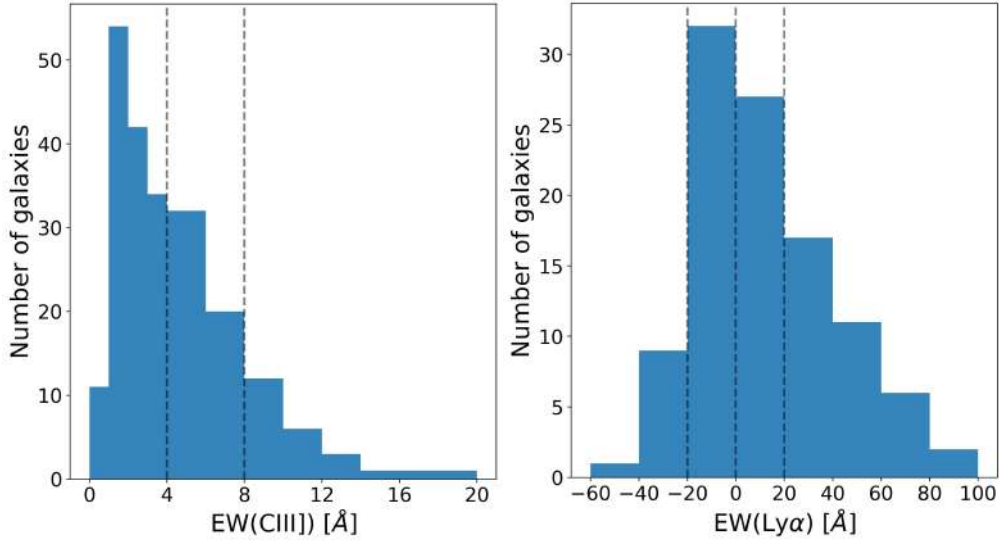
For this aim, we separate the selected galaxies into five stellar mass bins of width  $\sim 0.3$  dex and six bins of luminosity of 0.5 dex each. This way, we have a significant number of galaxies per bin, as shown in Table 3.2.1 and marked by the vertical dashed lines in Fig. 3.2.5. As shown in Fig. 3.2.3,

<sup>‡</sup><https://github.com/cschreib/slinefit>

Table 3.2.2: Bin ranges used for the stack analysis with EW.

Bin	Bin range EW(CIII)] [Å]	$N_{gal}^{(a)}$	Bin range EW(Ly $\alpha$ ) [Å]	$N_{gal}^{(a)}$
1	0 : 4	141	-60 : -20	10
2	4 : 8	52	-20 : 0	32
3	8 : 20	24	0 : 20	27
4			20 : 100	36

(a) Number of galaxies in each bin

Figure 3.2.6: EW(CIII)] (*left*) and EW(Ly $\alpha$ ) (*right*) distributions of the galaxies in the C3 sample. The vertical dashed lines are the limits of the bins used for stacking according to Table 3.2.2

stellar mass and  $K_s$  luminosity are correlated, as the latter is a good tracer of the former. While we expect stacks in these two quantities to produce similar results, we decided to use both of them to evaluate any possible difference due to the larger dynamic range of the  $K_s$  luminosity.

We also separate the sample in bins of EW(CIII)] and EW(Ly $\alpha$ ). For the former, we separate them into 3 bins of 4Å. And for Ly $\alpha$ , the C3 sample is restricted to the subsample of galaxies with  $z_{sys} > 2.9$  where Ly $\alpha$  is observable, either in absorption or emission. We choose bins of  $\sim 20\text{Å}$  for the EW(Ly $\alpha$ ), which are presented in Table 3.2.2 and are marked by vertical dashed lines in Fig. 3.2.6.

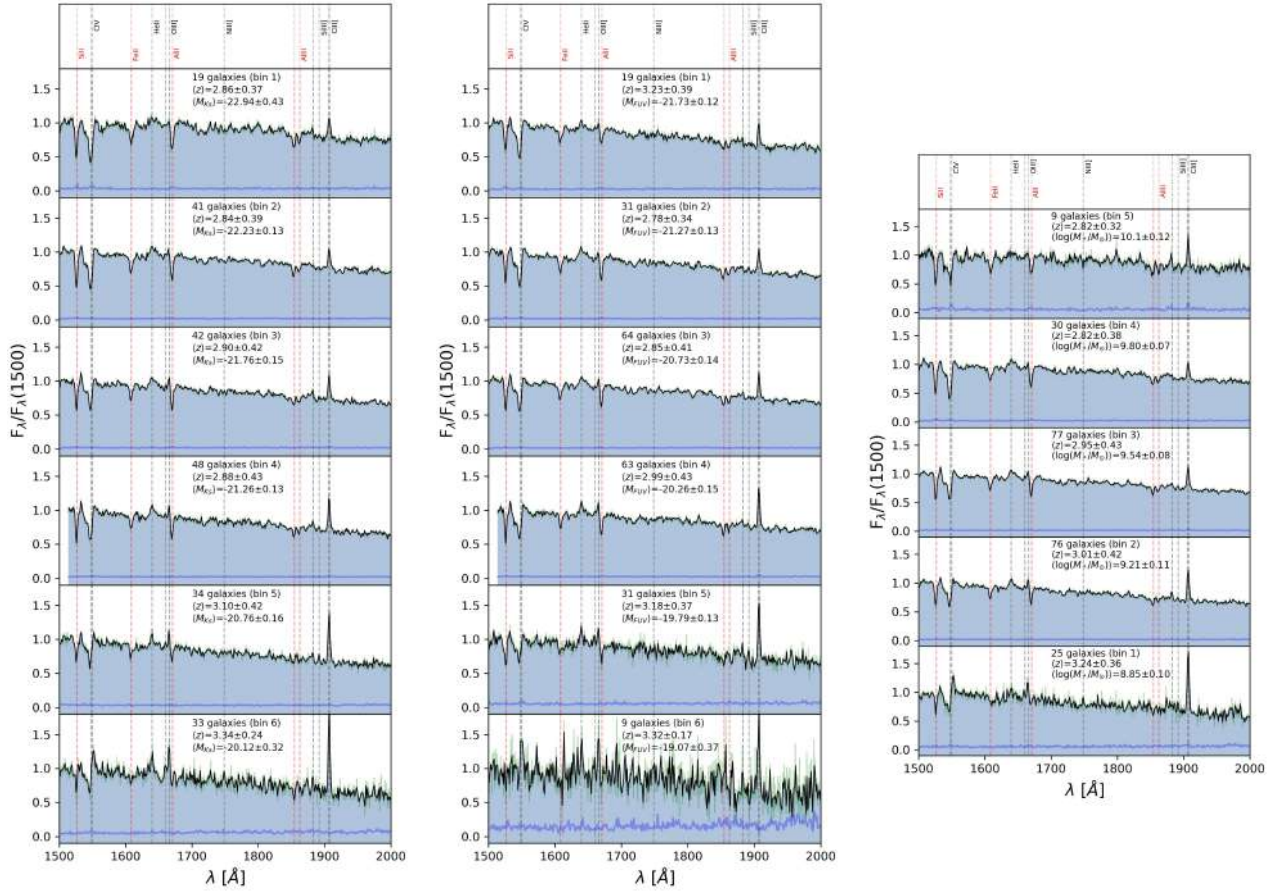


Figure 3.2.7: Resulting stacked spectra for each physical parameter with the C3 sample (what we call Stack A, see text for more details). *From left to right:*  $M_{K_s}$ ,  $M_{FUV}$ , and stellar mass. In each panel, the green faint line is the stack spectrum with the  $\sim 0.6 \text{\AA}/\text{pixel}$  sampling, while the black one is with  $\sim 1.2 \text{\AA}/\text{pixel}$ . The blue line is the  $1-\sigma$  error spectrum. The vertical lines mark known UV lines (in black: emission lines, in red: ISM absorption lines). Information about the number of galaxies, the mean redshift, and the mean parameter are included in each panel.

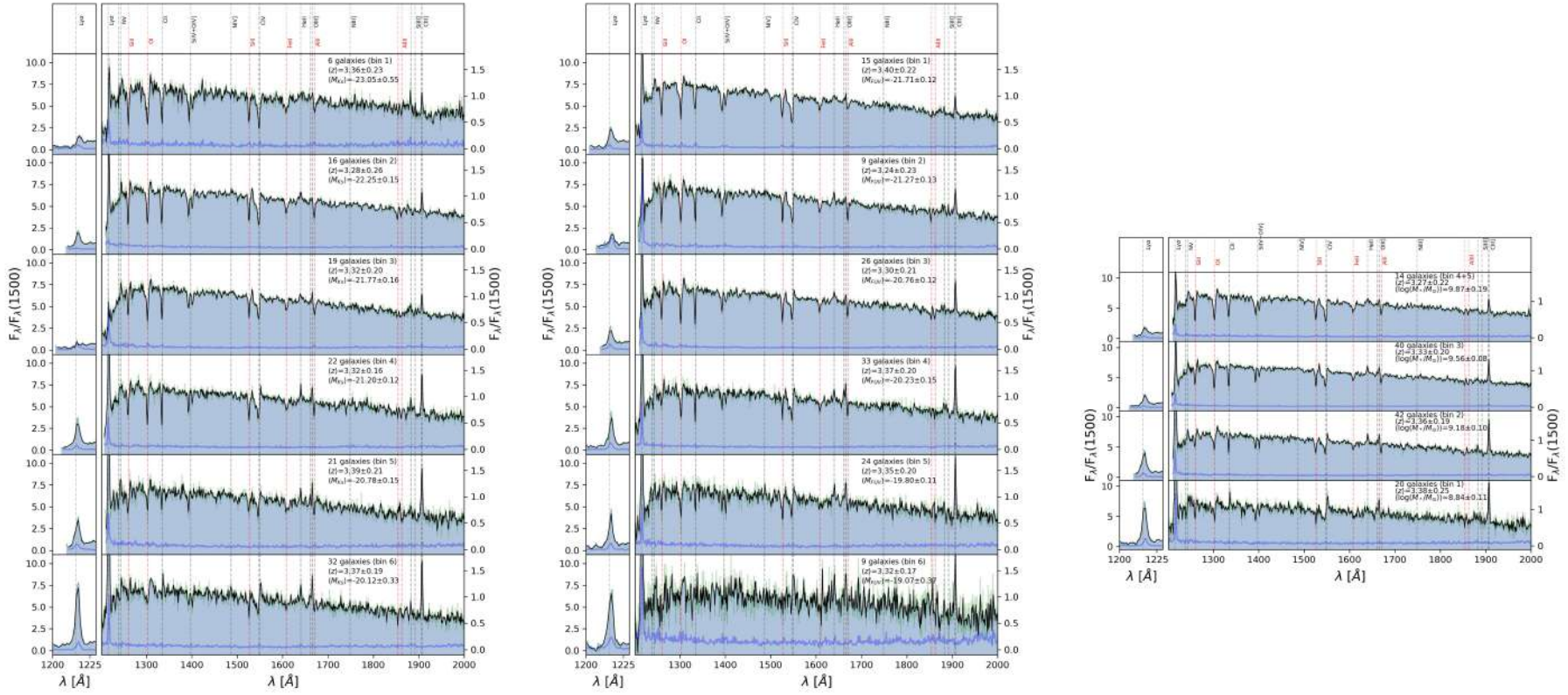


Figure 3.2.8: Resulting Stack B for each physical parameter. *From left to right:*  $M_{K_s}$ ,  $M_{FUV}$ , and stellar mass. In each panel, the green faint line is the stack spectrum with the  $\sim 0.6 \text{\AA}/\text{pixel}$  sampling, while the black one is with  $\sim 1.2 \text{\AA}/\text{pixel}$ . The blue line in the  $1\text{-}\sigma$  error spectrum. The vertical lines mark known UV lines. Information about the number of galaxies, the mean redshift, and the mean parameter are included in each panel.

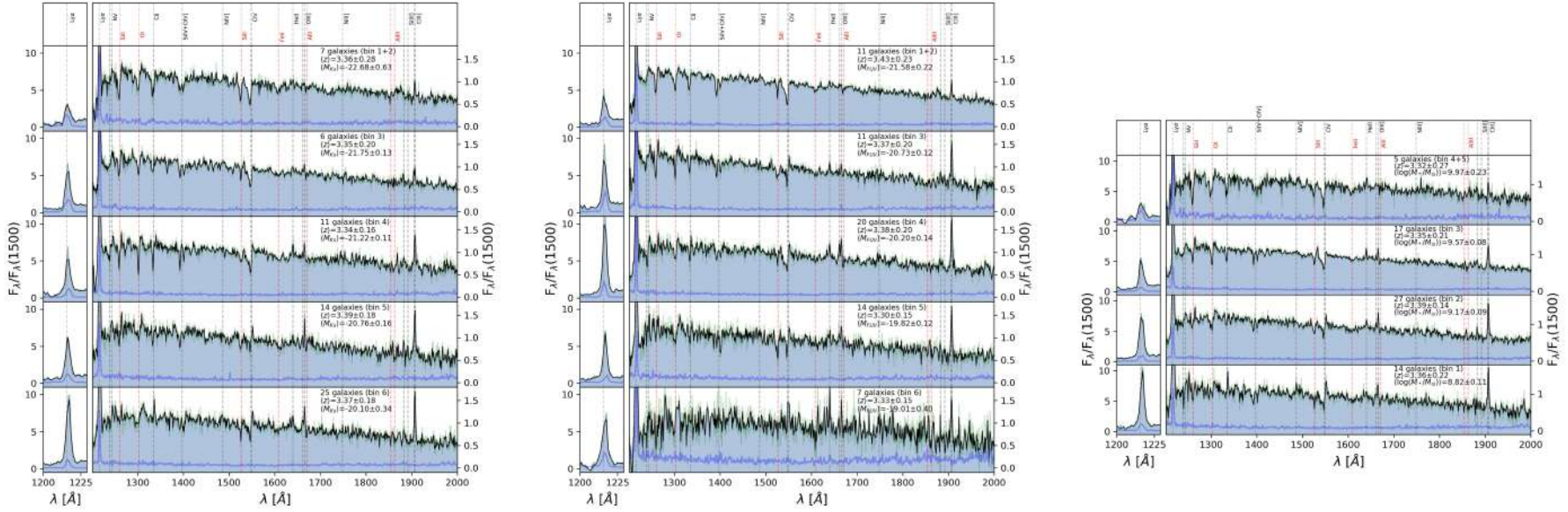


Figure 3.2.9: Resulting Stack C for each physical parameter. *From left to right:*  $M_{K_s}$ ,  $M_{FUV}$ , and stellar mass. In each panel, the green faint line is the stack spectrum with the  $\sim 0.6 \text{ \AA}/\text{pixel}$  sampling, while the black one is with  $\sim 1.2 \text{ \AA}/\text{pixel}$ . The blue line in the  $1\text{-}\sigma$  error spectrum. The vertical lines mark known UV lines. Information about the number of galaxies, the mean redshift, and the mean parameter are included in each panel.

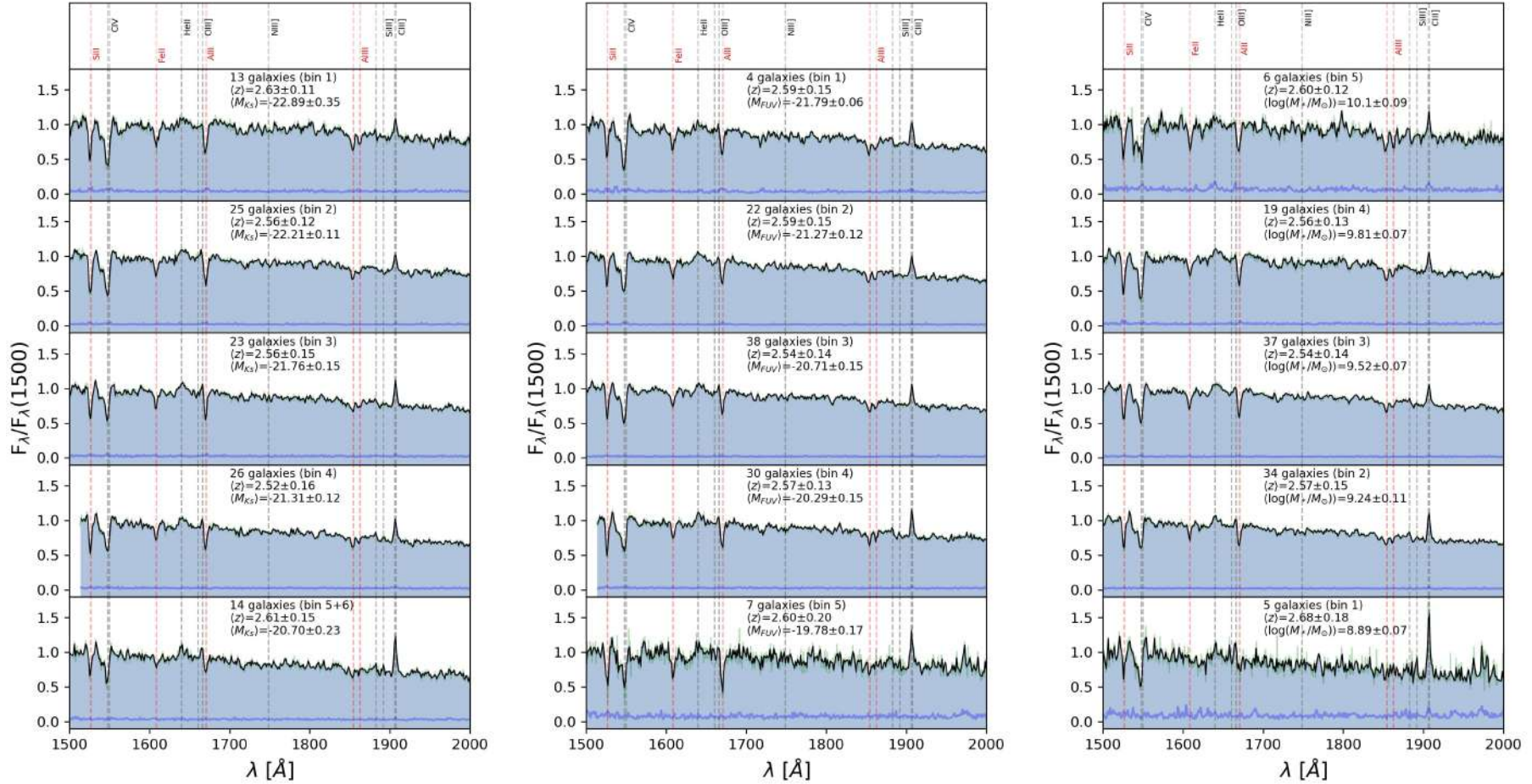


Figure 3.2.10: Resulting Stack D for each physical parameter. *From left to right:*  $M_{K_s}$ ,  $M_{FUV}$ , and stellar mass. In each panel, the green faint line is the stack spectrum with the  $\sim 0.6\text{\AA}/\text{pixel}$  sampling, while the black one is with  $\sim 1.2\text{\AA}/\text{pixel}$ . The blue line in the  $1\text{-}\sigma$  error spectrum. The vertical lines mark known UV lines. Information about the number of galaxies, the mean redshift, and the mean parameter are included in each panel.

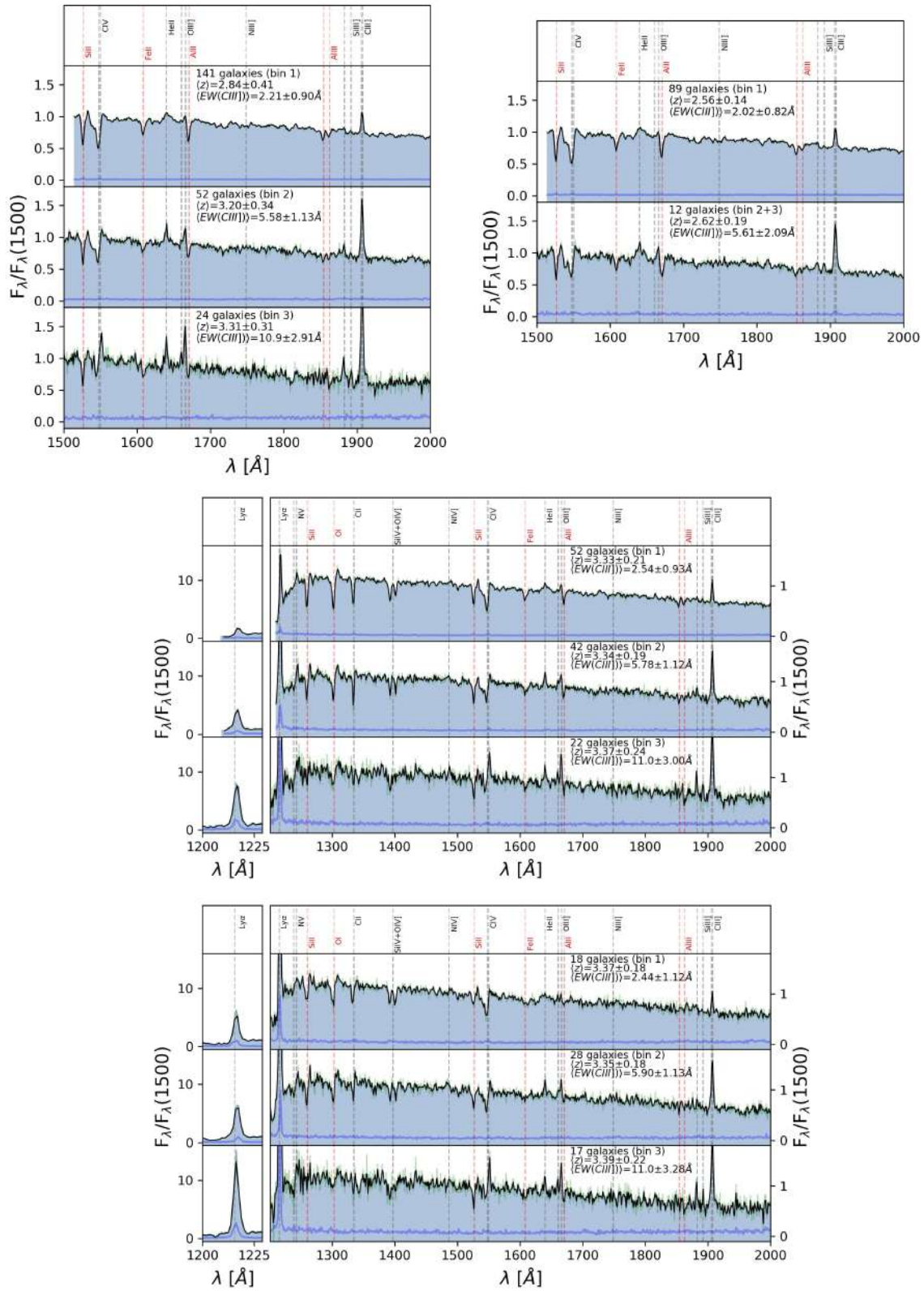


Figure 3.2.11: Stacks by  $EW(CIII])$ . From the left to the right on top row: Stack A, Stack D, Middle row: Stack B, and Bottom row: Stack C. In each panel, the green faint line is the stack spectrum with the  $\sim 0.6\text{\AA}/\text{pixel}$  sampling, while the black one is with  $\sim 1.2\text{\AA}/\text{pixel}$ . The blue line in the 1- $\sigma$  error spectrum. The vertical lines mark known UV lines. Information about the number of galaxies, the mean redshift, and the mean parameter are included in each panel.

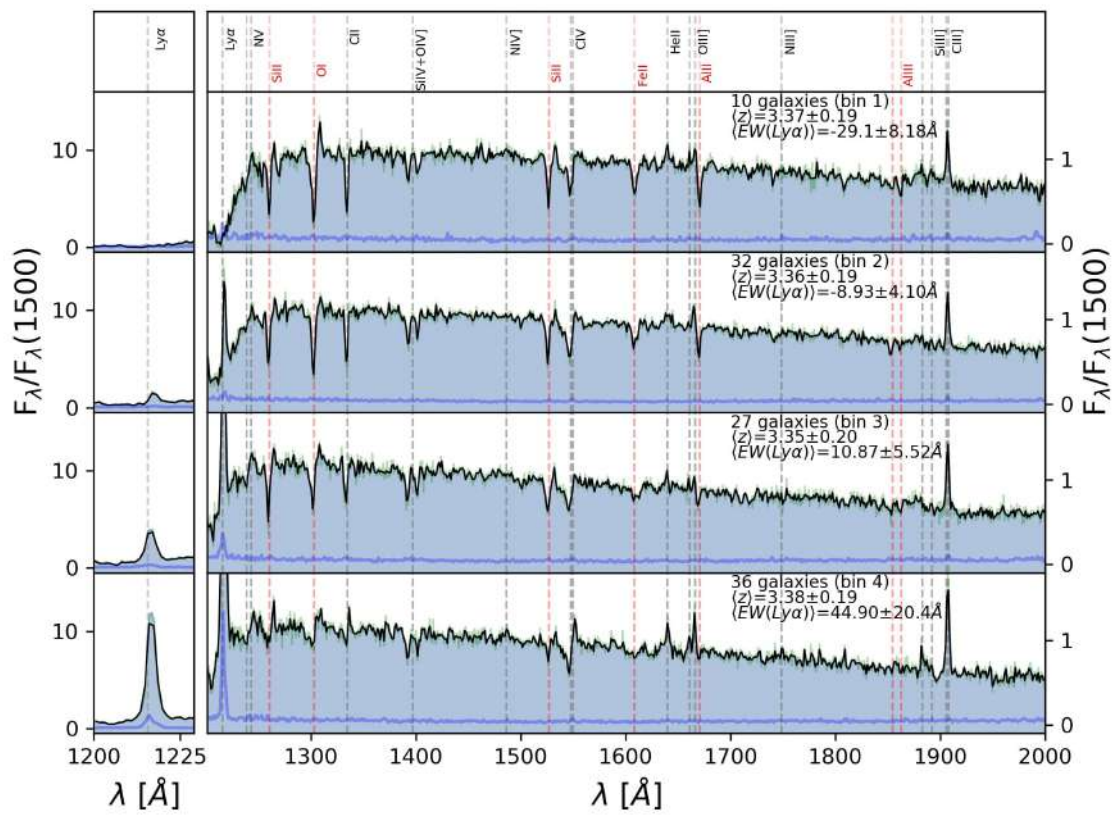


Figure 3.2.12: Resulting stacks by  $EW(\text{Ly}\alpha)$ . Same as in Fig. 3.2.7. Information about the number of galaxies, the mean redshift, and the mean  $EW(\text{Ly}\alpha)$  are included in each panel. The left panels show the relative Ly $\alpha$  strength in each bin.

For the stacking, we use a non-weighted scheme following [Marchi et al. \(2017\)](#). All the individual spectra in the sample are first shifted into the rest-frame using the systemic redshift and then they are resampled onto a common grid according to the mean systemic redshift of the sample ( $z_{\text{sys}} \sim 2.98$ ) and normalized to the mean flux between 1460 and 1540Å. The final flux at each wavelength was taken as the median of all the individual flux values after a  $3\text{-}\sigma$  clipping for rejecting outliers. The final wavelength range is where all spectra overlap and the spectral binning is 0.64Å. The  $1\text{-}\sigma$  error spectrum is estimated by a bootstrap re-sampling of the individual fluxes for each wavelength and the standard deviation of the resulting median stacked spectra. Changing the range of normalization to  $\sim 1800\text{Å}$  does not affect the shape of the stacked spectra.

We also tested alternative weighted schemes for stacking, similar to the one presented in [Marchi et al. \(2017\)](#) and used in [Saxena et al. \(2020\)](#) with a  $1/\sigma^2$  weight, where  $\sigma$  is estimated as the flux error along the normalization range in each spectrum. The error spectra with the weighted scheme were larger compared with the median stacking. For this reason, we consider the median stacking for this work, as they are a better representation of the global properties of the galaxies in each bin.

Four different median stacking schemes were performed depending on the redshifts included in each bin. In the remaining of this work, they are named as follows:

- Stack A: All the galaxies in the bin are stacked, considering the entire C3 sample. These stacks for each physical parameter are presented in Fig. [3.2.7](#).
- Stack B: Only galaxies with  $z > 2.93$  are considered for stacking in each bin. These galaxies have Ly $\alpha$  included in the spectral range. The stacks for each physical parameter are presented in Fig. [3.2.8](#).
- Stack C: Only galaxies with  $z > 2.93$  and with  $\text{EW}(\text{Ly}\alpha) > 0$  (i.e. Ly $\alpha$  in emission) are stacked. These stacks for each physical parameter are presented in Fig. [3.2.9](#).
- Stack D: We stack only galaxies with  $z < 2.93$ . In this subset, Ly $\alpha$  is not covered by the VANDELS spectra. Thus we ignore whether these galaxies are Ly $\alpha$  emitters or not. The stacks for each physical parameter are displayed in Fig. [3.2.10](#).

An additional subset of stacks A, B, C, and D by  $\text{EW}(\text{CIII])}$  are presented in Fig. [3.2.11](#). In the case of the stacks by  $\text{EW}(\text{Ly}\alpha)$ , only Stack B is performed. The resulting stacks are presented in Fig. [3.2.12](#).

The above redshift dependence reduces the number of galaxies in each bin. In these cases, we adapt the binning for stacking to have at least four galaxies in each bin. This ensures the stack spectrum will gain at least a factor of 2 in the S/N ratio. The final number of galaxies for each stacked spectrum is included in labels in Fig. [3.2.7](#), [3.2.8](#), [3.2.9](#), [3.2.10](#), [3.2.11](#), and [3.2.12](#). We find the composite spectrum of a bin to be representative of the median properties of the galaxies in each bin. Small changes in the bin sizes used for the stacking may change the error bars in the derived parameters in the least populated bins but they do not affect our results significantly. We discuss possible caveats related to the stacking analysis in Section [3.4.3](#).

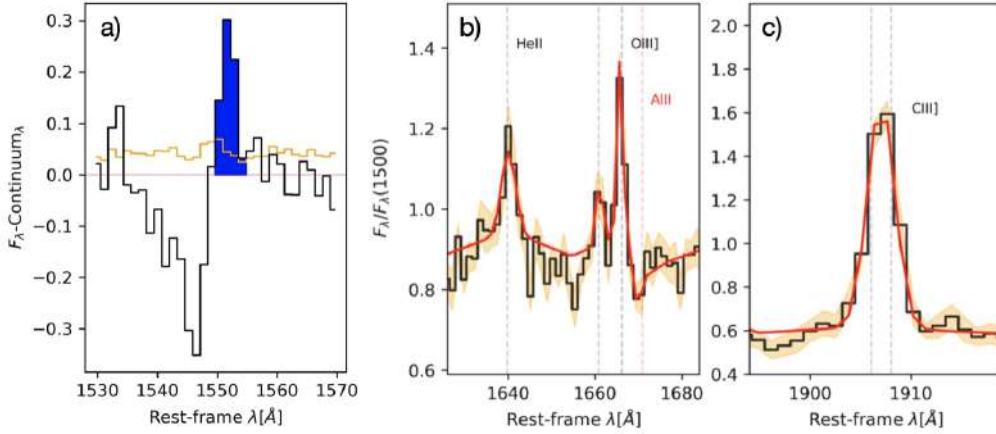


Figure 3.2.13: Emission-line flux and EW measurements in the stack by  $\text{EW}(\text{Ly}\alpha) > 20$ . *Panel a)* Continuum-subtracted spectrum. The orange line shows the error spectrum ( $1\sigma$ ). The blue shaded region is the pixel integrated for the CIV line. *b) and c)* The red line is the *slinefit* fitting for the spectrum. The orange-shaded region shows  $1\sigma$  uncertainty of the stacked spectrum.

### 3.2.4 Line measurements

Emission-line fluxes and EWs of the lines in each stacked spectrum were measured using *slinefit*, which is a software capable of simultaneously measuring emission and absorption lines and the UV-NIR continuum. For this purpose, *slinefit* uses templates built with the Bruzual & Charlot (2003) stellar population models. For our measurements, we include rest-frame UV emission and absorption lines at  $\lambda_{\text{rest}} > 1500\text{\AA}$  from Shapley et al. (2003). Rest-frame UV lines at  $\lambda_{\text{rest}} < 1500\text{\AA}$  were not included in the measurements. In particular, the Ly $\alpha$  line is instead measured following the same fitting technique presented in Cullen et al. (2020). In all the *slinefit* fitting runs, we allow that lines other than CIII] may have a small offset with respect to the systemic velocity and the minimum width of the lines to be 100 km/s.

In the first set of measurements, we only measure simultaneously CIII] and closer lines (AlIII $\lambda$ 1855 $\text{\AA}$ , SiIII $\lambda$ 1883,1892 $\text{\AA}$ , MgII $\lambda$ 2799 $\text{\AA}$ ). We obtain the width of CIII] to be  $\sim 300\text{-}350$  km/s in all stacked spectra. We use this value to constrain the maximum width for the other emission lines. After that, in a second set of measurements, we measure HeII $\lambda$ 1640 $\text{\AA}$ , OIII] $\lambda$ 1666,1660 $\text{\AA}$ , and CIV $\lambda$ 1548,1550 $\text{\AA}$  (hereafter HeII, OIII], and CIV, respectively), with the constraint in the maximum width. In these cases, the maximum offset allowed is 100km/s, except for CIV for which a maximum of 1000km/s is allowed because larger offsets are observed. The P-Cygni profile of CIV is fitted assuming the same intensity for both components. Both components of OIII] are fitted with their ratio unconstrained.

Due to the complex CIV profile, the measurements with *slinefit* are found to slightly underestimate the continuum. For this reason, a more detailed continuum determination is performed. First, the continuum is fitted with a linear function between 1400 and 2000 $\text{\AA}$ , masking out regions with emission and absorption lines detected. Then, the spectrum is continuum-subtracted. Finally, the CIV flux is found by direct integration of the emission line profile after imposing a maximum baseline width of 4 $\text{\AA}$  (or  $\sim 390$ km/s), which is the typical value obtained for CIII]. The EW is estimated using the mean continuum flux in the same integrated range.

All the above measurements are performed for all the stacked spectra with the  $0.6\text{\AA}/\text{pixel}$  sampling, but the S/N in the case of faint emission lines is low and then the measurements are additionally performed in the resampled spectra by a factor of 2. For the resampling, we use *SpectRes*<sup>§</sup> that is a software that efficiently resamples spectra and their associated uncertainties, preserving the integrated flux. An example of the measurements can be seen in Fig. 3.2.13. Hereafter, we consider the resampled spectra measurements for the emission lines which are presented in Tables 3.2.3, 3.2.4, 3.2.5, 3.2.6, and 3.2.7.

In the same tables, the mean color excess  $E(B-V)$  is reported for each stack. They are estimated from the individual  $E(B-V)$  values for each galaxy in each bin, which are obtained by BAGPIPES fitting. In the C3 sample,  $E(B-V)$  ranges from  $\sim 0.01$ - $0.43$  mag, with a mean value of  $0.098 \pm 0.014$  mag. The mean  $E(B-V)$  of the stacks are used to compute the reddening correction<sup>¶</sup> using the Calzetti et al. (2000) extinction curve for simplicity and assuming that the color excess of the stellar continuum is the same that the color excess for the nebular gas emission lines. Despite the evidence that this assumption could not be true (e.g. Calzetti et al., 2000; Reddy et al., 2015) and the ionized gas  $E(B-V)$  could be larger than a factor of 2.2 the stellar  $E(B-V)$  (in particular, galaxies with high SFR), we assume it for simplicity. However, we note that the results of this Chapter are not affected if we change this prescription to more extreme assumptions. Using the calibration presented in Sanders et al. (2021) to correct the gas extinction from the SED extinction, we obtain a factor up to  $\sim 3$  of difference between gas and stellar extinction, but even with those values, the trends found in this Chapter are not altered significantly.

Line fluxes are presented uncorrected by extinction in Tables 3.2.3, 3.2.4, 3.2.5, 3.2.6, and 3.2.7. However, results and figures shown in subsequent sections consider dereddened quantities.

## 3.3 Results

### 3.3.1 Identification of UV absorption and emission lines

The high S/N spectra of the stacks allow us to identify several interesting features both in absorption and emission in the rest-frame UV spectra. Among these features, low-ionization interstellar lines such as  $\text{SiII}\lambda 1260\text{\AA}$ ,  $\text{OI}+\text{SiII}\lambda 1303\text{\AA}$ ,  $\text{CII}\lambda 1334\text{\AA}$ ,  $\text{SiII}\lambda 1526\text{\AA}$ ,  $\text{FeII}\lambda 1608\text{\AA}$ , and  $\text{AlII}\lambda 1670\text{\AA}$  are found. In Fig. 3.2.7, where the stacks A (redshift-independent) by stellar mass and luminosities are shown, we find that the stronger ISM absorption lines are in the stacks built with higher stellar masses (or more luminous at a given broadband). This is expected since these lines are saturated in low-resolution spectra and then their width increases with dynamical mass. The same trend is shown in Fig. 3.2.8, 3.2.9, 3.2.10 for the stacks B, C, and D by stellar mass and luminosities.

We find a similar trend when considering the stacks by  $\text{EW}(\text{Ly}\alpha)$  in Fig. 3.2.12. We find the stronger low-ionization ISM absorption lines in the stacks with smaller  $\text{EW}(\text{Ly}\alpha)$ , i.e. when  $\text{Ly}\alpha$  is in absorption, while the ISM absorption lines are barely identified in the stack with the larger  $\text{EW}(\text{Ly}\alpha)$ . This is consistent with previous observations (e.g. Shapley et al., 2003). Regarding the stacks by

<sup>§</sup><https://github.com/ACcarnall/spectres>. More details on Carnall (2017)

<sup>¶</sup>Using the *extinction* code at <http://github.com/kbarbary/extinction>

Table 3.2.3: Parameters estimated for the stacks by stellar mass

Bin	$\log(M_*/M_\odot)^a$	$E(B-V)^b$	$CIV/CIII]^c$	$HeII/CIII]^c$	$OIII]/CIII]^c$	$EW(CIV)^d$	$EW(CIII)]^d$	$\log(C/O)^e$	$\log(Z_*/Z_\odot)^f$
Stack A									
1	$8.85 \pm 0.10$	0.06	$0.32 \pm 0.05$	$0.14 \pm 0.05$	$0.11 \pm 0.02$	$1.18 \pm 0.17$	$5.24 \pm 0.38$	$-0.24 \pm 0.10$	$-0.77 \pm 0.20$
2	$9.21 \pm 0.11$	0.07	$0.20 \pm 0.02$	$0.38 \pm 0.03$	$0.18 \pm 0.01$	$0.40 \pm 0.05$	$2.66 \pm 0.12$	$-0.50 \pm 0.10$	$-0.76 \pm 0.03$
3	$9.54 \pm 0.08$	0.10	$0.18 \pm 0.03$	$0.45 \pm 0.04$	$0.19 \pm 0.03$	$0.23 \pm 0.03$	$1.73 \pm 0.09$	$-0.54 \pm 0.13$	$-0.67 \pm 0.02$
4	$9.80 \pm 0.07$	0.13	$0.26 \pm 0.05$	$0.54 \pm 0.06$	$0.08 \pm 0.03$	$0.28 \pm 0.05$	$1.42 \pm 0.07$	$-0.10 \pm 0.21$	$-0.58 \pm 0.02$
5	$10.1 \pm 0.12$	0.21	$< 0.03$	$< 0.12$	$< 0.15$	$< 0.06$	$2.33 \pm 0.41$	$> -0.58$	$-0.72 \pm 0.06$
Stack B									
1	$8.84 \pm 0.11$	0.05	$0.38 \pm 0.06$	$< 0.12$	$0.20 \pm 0.06$	$1.45 \pm 0.21$	$5.69 \pm 0.39$	$-0.52 \pm 0.19$	$-0.95 \pm 0.07$
2	$9.18 \pm 0.10$	0.06	$0.19 \pm 0.03$	$0.25 \pm 0.04$	$0.13 \pm 0.02$	$0.59 \pm 0.10$	$4.65 \pm 0.24$	$-0.33 \pm 0.10$	$-0.96 \pm 0.04$
3	$9.56 \pm 0.08$	0.08	$0.23 \pm 0.04$	$0.33 \pm 0.05$	$0.20 \pm 0.04$	$0.45 \pm 0.07$	$2.76 \pm 0.19$	$-0.57 \pm 0.13$	$-0.93 \pm 0.03$
4	$9.87 \pm 0.19$	0.16	$0.15 \pm 0.05$	$0.40 \pm 0.07$	$0.18 \pm 0.05$	$0.19 \pm 0.07$	$1.86 \pm 0.14$	$-0.51 \pm 0.20$	$-0.64 \pm 0.03$
Stack C									
1	$8.82 \pm 0.11$	0.04	$0.34 \pm 0.07$	$< 0.09$	$0.22 \pm 0.06$	$1.22 \pm 0.22$	$5.75 \pm 0.46$	$-0.52 \pm 0.16$	$-0.74 \pm 0.18$
2	$9.17 \pm 0.09$	0.05	$0.22 \pm 0.05$	$0.20 \pm 0.05$	$0.22 \pm 0.04$	$0.77 \pm 0.18$	$5.55 \pm 0.31$	$-0.61 \pm 0.13$	$-1.05 \pm 0.05$
3	$9.57 \pm 0.08$	0.05	$0.24 \pm 0.06$	$0.23 \pm 0.05$	$0.22 \pm 0.04$	$0.56 \pm 0.12$	$3.39 \pm 0.34$	$-0.54 \pm 0.1$	$-0.96 \pm 0.02$
4	$9.97 \pm 0.23$	0.22	$< 0.10$	$0.41 \pm 0.20$	$< 0.21$	$< 0.13$	$1.96 \pm 0.69$	$> -0.66$	$-0.48 \pm 0.08$
Stack D									
1	$8.89 \pm 0.07$	0.07	$0.28 \pm 0.08$	$0.22 \pm 0.10$	$0.12 \pm 0.03$	$0.98 \pm 0.26$	$4.59 \pm 0.69$	$-0.30 \pm 0.13$	$< -0.982$
2	$9.24 \pm 0.11$	0.08	$0.30 \pm 0.05$	$0.46 \pm 0.05$	$0.20 \pm 0.03$	$0.43 \pm 0.07$	$1.94 \pm 0.11$	$-0.55 \pm 0.09$	$-0.75 \pm 0.04$
3	$9.52 \pm 0.07$	0.12	$0.18 \pm 0.03$	$0.49 \pm 0.06$	$0.09 \pm 0.04$	$0.18 \pm 0.03$	$1.35 \pm 0.08$	$-0.18 \pm 0.19$	$-0.63 \pm 0.02$
4	$9.81 \pm 0.07$	0.14	$0.24 \pm 0.07$	$0.59 \pm 0.09$	$< 0.20$	$0.22 \pm 0.06$	$1.17 \pm 0.09$	$> -0.58$	$-0.50 \pm 0.04$
5	$10.1 \pm 0.09$	0.19	$< 0.06$	$< 0.60$	$< 0.46$	$< 0.07$	$1.71 \pm 0.43$	$> -1.02$	$-0.64 \pm 0.06$

Panels depending on the kind of stack according to Subsection 3.2.3

(a) Bin mean  $\log(M_*/M_\odot)$  according to Table 3.2.1

(b) Mean  $E(B-V)$  in mag

(c) Flux normalized to CIII] not corrected by extinction.

(d) Equivalent width in units of  $\text{\AA}$ .

(e) Estimated using Pérez-Montero & Amorín (2017)

(f) Estimated using Cullen et al. (2019)

Table 3.2.4: Parameters estimated for the stacks by  $K_s$ -band luminosity

Bin	Mean $M_{K_s}$ <sup>a</sup>	E(B-V) <sup>b</sup>	CIV/CIII] <sup>c</sup>	HeII/CIII] <sup>c</sup>	OIII]/CIII] <sup>c</sup>	EW(CIV) <sup>d</sup>	EW(CIII] <sup>d</sup>	log(C/O) <sup>e</sup>	log( $Z_*/Z_\odot$ ) <sup>f</sup>
Stack A									
1	$-22.94 \pm 0.43$	0.18	< 0.03	$0.37 \pm 0.07$	$0.08 \pm 0.03$	< 0.03	$1.25 \pm 0.10$	> -0.56	$-0.61 \pm 0.04$
2	$-22.23 \pm 0.13$	0.14	$0.26 \pm 0.04$	$0.53 \pm 0.05$	< 0.14	$0.26 \pm 0.04$	$1.33 \pm 0.06$	> -0.38	$-0.60 \pm 0.02$
3	$-21.76 \pm 0.15$	0.09	$0.22 \pm 0.04$	$0.38 \pm 0.05$	$0.17 \pm 0.03$	$0.28 \pm 0.05$	$1.70 \pm 0.12$	$-0.46 \pm 0.11$	$-0.75 \pm 0.02$
4	$-21.26 \pm 0.13$	0.08	$0.25 \pm 0.04$	$0.44 \pm 0.04$	$0.20 \pm 0.02$	$0.42 \pm 0.06$	$2.29 \pm 0.12$	$-0.55 \pm 0.09$	$-0.82 \pm 0.10$
5	$-20.76 \pm 0.16$	0.06	$0.20 \pm 0.03$	$0.24 \pm 0.04$	$0.16 \pm 0.02$	$0.53 \pm 0.08$	$3.66 \pm 0.19$	$-0.44 \pm 0.08$	$-1.00 \pm 0.04$
6	$-20.12 \pm 0.32$	0.04	$0.27 \pm 0.04$	$0.26 \pm 0.05$	$0.24 \pm 0.03$	$1.04 \pm 0.14$	$5.71 \pm 0.26$	$-0.62 \pm 0.13$	< -0.932
Stack B									
1	$-23.05 \pm 0.55$	0.18	< 0.06	$0.46 \pm 0.22$	< 0.30	< 0.04	$1.09 \pm 0.37$	> -0.85	$-0.79 \pm 0.08$
2	$-22.25 \pm 0.15$	0.15	$0.14 \pm 0.03$	$0.35 \pm 0.06$	< 0.09	$0.21 \pm 0.05$	$2.06 \pm 0.10$	> -0.28	$-0.77 \pm 0.10$
3	$-21.77 \pm 0.16$	0.08	$0.21 \pm 0.07$	$0.27 \pm 0.08$	$0.18 \pm 0.06$	$0.31 \pm 0.09$	$2.13 \pm 0.23$	$-0.53 \pm 0.18$	$-0.91 \pm 0.04$
4	$-21.20 \pm 0.12$	0.07	$0.26 \pm 0.04$	$0.19 \pm 0.03$	$0.20 \pm 0.03$	$0.73 \pm 0.10$	$4.07 \pm 0.24$	$-0.56 \pm 0.11$	$-0.70 \pm 0.07$
5	$-20.78 \pm 0.15$	0.06	$0.14 \pm 0.05$	$0.14 \pm 0.04$	$0.23 \pm 0.04$	$0.48 \pm 0.16$	$5.11 \pm 0.36$	$-0.59 \pm 0.10$	< -0.962
6	$-20.12 \pm 0.33$	0.04	$0.29 \pm 0.04$	$0.25 \pm 0.05$	$0.23 \pm 0.04$	$1.14 \pm 0.18$	$5.87 \pm 0.26$	$-0.57 \pm 0.12$	< -0.992
Stack C									
1	$-22.68 \pm 0.63$	0.19	< 0.12	< 0.28	< 0.17	< 0.15	$1.88 \pm 0.43$	> -0.57	$-0.42 \pm 0.06$
2	$-21.75 \pm 0.13$	0.05	$0.23 \pm 0.07$	$0.25 \pm 0.11$	$0.19 \pm 0.09$	$0.36 \pm 0.10$	$2.35 \pm 0.43$	$-0.45 \pm 0.24$	$-0.75 \pm 0.06$
3	$-21.22 \pm 0.11$	0.07	$0.24 \pm 0.05$	$0.18 \pm 0.03$	$0.19 \pm 0.06$	$0.70 \pm 0.15$	$4.24 \pm 0.37$	$-0.52 \pm 0.15$	$-0.73 \pm 0.20$
4	$-20.76 \pm 0.16$	0.06	$0.21 \pm 0.06$	$0.10 \pm 0.04$	$0.26 \pm 0.03$	$0.73 \pm 0.21$	$5.48 \pm 0.36$	$-0.64 \pm 0.12$	$-1.05 \pm 0.05$
5	$-20.10 \pm 0.34$	0.03	$0.25 \pm 0.04$	$0.14 \pm 0.04$	$0.22 \pm 0.04$	$0.95 \pm 0.17$	$5.97 \pm 0.34$	$-0.59 \pm 0.11$	< -0.982
Stack D									
1	$-22.89 \pm 0.35$	0.19	< 0.07	$0.28 \pm 0.08$	< 0.21	< 0.07	$1.39 \pm 0.13$	> -0.68	$-0.66 \pm 0.05$
2	$-22.21 \pm 0.11$	0.13	$0.24 \pm 0.07$	$0.58 \pm 0.09$	< 0.20	$0.21 \pm 0.06$	$1.12 \pm 0.09$	> -0.56	$-0.54 \pm 0.04$
3	$-21.76 \pm 0.15$	0.11	$0.15 \pm 0.05$	$0.41 \pm 0.06$	$0.19 \pm 0.03$	$0.20 \pm 0.07$	$1.78 \pm 0.14$	$-0.54 \pm 0.13$	$-0.66 \pm 0.03$
4	$-21.31 \pm 0.12$	0.08	$0.40 \pm 0.08$	$0.50 \pm 0.07$	$0.29 \pm 0.05$	$0.41 \pm 0.07$	$1.44 \pm 0.13$	$-0.64 \pm 0.11$	$-0.94 \pm 0.02$
5	$-20.70 \pm 0.23$	0.07	$0.15 \pm 0.06$	$0.28 \pm 0.05$	$0.14 \pm 0.02$	$0.29 \pm 0.12$	$2.66 \pm 0.18$	$-0.43 \pm 0.12$	$-1.01 \pm 0.05$

Same as in 3.2.3 but <sup>a</sup>Bin mean  $K_s$ -band luminosity according to Table 3.2.1.

Table 3.2.5: Parameters estimated for the stacks by FUV luminosity

Bin	Mean $M_{FUV}^a$	E(B-V) <sup>b</sup>	CIV/CIII] <sup>c</sup>	HeII/CIII] <sup>c</sup>	OIII]/CIII] <sup>c</sup>	EW(CIV) <sup>d</sup>	EW(CIII)] <sup>d</sup>	log(C/O) <sup>e</sup>	log( $Z_*/Z_\odot$ ) <sup>f</sup>
Stack A									
1	$-21.73 \pm 0.12$	0.08	$0.24 \pm 0.05$	$0.31 \pm 0.07$	$0.13 \pm 0.06$	$0.28 \pm 0.06$	$1.70 \pm 0.10$	$-0.34 \pm 0.28$	$-0.64 \pm 0.03$
2	$-21.27 \pm 0.13$	0.09	$0.25 \pm 0.04$	$0.52 \pm 0.05$	$0.11 \pm 0.02$	$0.28 \pm 0.05$	$1.54 \pm 0.07$	$-0.28 \pm 0.13$	$-0.61 \pm 0.03$
3	$-20.73 \pm 0.14$	0.10	$0.12 \pm 0.03$	$0.35 \pm 0.03$	$0.14 \pm 0.02$	$0.17 \pm 0.04$	$1.82 \pm 0.08$	$-0.46 \pm 0.11$	$-0.76 \pm 0.02$
4	$-20.26 \pm 0.15$	0.10	$0.21 \pm 0.04$	$0.42 \pm 0.04$	$0.20 \pm 0.02$	$0.40 \pm 0.07$	$2.49 \pm 0.15$	$-0.57 \pm 0.13$	$-0.65 \pm 0.02$
5	$-19.79 \pm 0.13$	0.08	$0.14 \pm 0.05$	$0.26 \pm 0.06$	$0.14 \pm 0.03$	$0.43 \pm 0.17$	$4.08 \pm 0.25$	$-0.38 \pm 0.16$	$-0.70 \pm 0.09$
6	$-19.07 \pm 0.37$	0.13	$0.52 \pm 0.10$	$0.27 \pm 0.08$	$0.30 \pm 0.06$	$2.13 \pm 0.40$	$6.24 \pm 0.46$	$-0.68 \pm 0.12$	$< -0.862$
Stack B									
1	$-21.71 \pm 0.12$	0.07	$0.18 \pm 0.06$	$0.25 \pm 0.05$	$0.16 \pm 0.06$	$0.23 \pm 0.07$	$1.88 \pm 0.10$	$-0.50 \pm 0.17$	$-0.69 \pm 0.02$
2	$-21.27 \pm 0.13$	0.08	$0.25 \pm 0.08$	$0.21 \pm 0.05$	$0.15 \pm 0.05$	$0.41 \pm 0.13$	$2.37 \pm 0.22$	$> -0.73$	$-0.56 \pm 0.04$
3	$-20.76 \pm 0.12$	0.08	$0.20 \pm 0.03$	$0.24 \pm 0.04$	$0.15 \pm 0.03$	$0.41 \pm 0.06$	$2.84 \pm 0.22$	$-0.40 \pm 0.13$	$-0.93 \pm 0.04$
4	$-20.23 \pm 0.15$	0.07	$0.20 \pm 0.04$	$0.21 \pm 0.04$	$0.18 \pm 0.03$	$0.69 \pm 0.12$	$4.88 \pm 0.35$	$-0.53 \pm 0.12$	$-0.79 \pm 0.12$
5	$-19.80 \pm 0.11$	0.06	$0.25 \pm 0.06$	$0.26 \pm 0.06$	$0.23 \pm 0.04$	$0.91 \pm 0.21$	$5.21 \pm 0.30$	$-0.60 \pm 0.11$	$-0.88 \pm 0.08$
6	$-19.07 \pm 0.37$	0.13	$0.52 \pm 0.10$	$0.27 \pm 0.08$	$0.30 \pm 0.06$	$2.13 \pm 0.40$	$6.24 \pm 0.46$	$-0.66 \pm 0.13$	$< -0.862$
Stack C									
1	$-21.58 \pm 0.22$	0.07	$0.21 \pm 0.07$	$0.17 \pm 0.07$	$< 0.13$	$0.27 \pm 0.08$	$1.87 \pm 0.16$	$> -0.35$	$-0.76 \pm 0.09$
2	$-20.73 \pm 0.12$	0.05	$0.21 \pm 0.05$	$0.11 \pm 0.04$	$< 0.13$	$0.74 \pm 0.16$	$5.21 \pm 0.48$	$> -0.37$	$< -1.002$
3	$-20.20 \pm 0.14$	0.06	$0.16 \pm 0.04$	$0.21 \pm 0.04$	$0.18 \pm 0.03$	$0.68 \pm 0.20$	$6.30 \pm 0.47$	$-0.54 \pm 0.10$	$-1.00 \pm 0.06$
4	$-19.82 \pm 0.12$	0.05	$0.32 \pm 0.07$	$0.13 \pm 0.05$	$0.23 \pm 0.05$	$1.14 \pm 0.23$	$5.10 \pm 0.42$	$-0.63 \pm 0.15$	$-0.91 \pm 0.09$
5	$-19.01 \pm 0.40$	0.11	$0.54 \pm 0.14$	$0.45 \pm 0.14$	$0.31 \pm 0.08$	$1.85 \pm 0.47$	$5.56 \pm 0.49$	$-0.57 \pm 0.21$	$< -0.792$
Stack D									
1	$-21.79 \pm 0.06$	0.09	$0.29 \pm 0.10$	$0.36 \pm 0.08$	$0.08 \pm 0.02$	$0.42 \pm 0.15$	$2.10 \pm 0.22$	$-0.06 \pm 0.24$	$-0.38 \pm 0.04$
2	$-21.27 \pm 0.12$	0.09	$0.26 \pm 0.06$	$0.49 \pm 0.06$	$0.08 \pm 0.03$	$0.27 \pm 0.06$	$1.48 \pm 0.07$	$-0.09 \pm 0.19$	$-0.59 \pm 0.03$
3	$-20.71 \pm 0.15$	0.10	$0.15 \pm 0.04$	$0.42 \pm 0.06$	$0.12 \pm 0.04$	$0.15 \pm 0.05$	$1.42 \pm 0.10$	$-0.33 \pm 0.13$	$-0.69 \pm 0.04$
4	$-20.29 \pm 0.15$	0.13	$0.20 \pm 0.06$	$0.57 \pm 0.08$	$0.13 \pm 0.03$	$0.25 \pm 0.07$	$1.64 \pm 0.13$	$-0.37 \pm 0.14$	$-0.64 \pm 0.03$
5	$-19.78 \pm 0.17$	0.16	$< 0.16$	$0.33 \pm 0.11$	$0.17 \pm 0.06$	$< 0.28$	$2.14 \pm 0.24$	$-0.44 \pm 0.18$	$-0.68 \pm 0.10$

Same as in 3.2.3 but <sup>a</sup>Bin mean FUV luminosity according to Table 3.2.1.

Table 3.2.6: Parameters estimated for the stacks by EW(Ly $\alpha$ )

Bin	EW(Ly $\alpha$ ) <sup>a</sup>	E(B-V) <sup>b</sup>	CIV/CIII] <sup>c</sup>	HeII/CIII] <sup>c</sup>	OIII]/CIII] <sup>c</sup>	EW(CIV) <sup>d</sup>	EW(CIII)] <sup>d</sup>	log(C/O) <sup>e</sup>	log( $Z_*/Z_\odot$ ) <sup>f</sup>
1	$-29.1 \pm 8.18$	0.09	$< 0.14$	$0.34 \pm 0.08$	$0.22 \pm 0.05$	$< 0.24$	$2.51 \pm 0.33$	$-0.68 \pm 0.11$	$-0.87 \pm 0.02$
2	$-8.93 \pm 4.10$	0.10	$0.15 \pm 0.04$	$0.23 \pm 0.04$	$0.19 \pm 0.04$	$0.31 \pm 0.08$	$2.84 \pm 0.20$	$-0.54 \pm 0.13$	$-0.71 \pm 0.04$
3	$10.87 \pm 5.52$	0.06	$0.12 \pm 0.05$	$0.12 \pm 0.03$	$0.09 \pm 0.03$	$0.30 \pm 0.12$	$3.73 \pm 0.33$	$-0.22 \pm 0.26$	$-0.97 \pm 0.04$
4	$44.90 \pm 20.4$	0.06	$0.25 \pm 0.03$	$0.26 \pm 0.04$	$0.22 \pm 0.03$	$0.95 \pm 0.12$	$5.82 \pm 0.24$	$-0.60 \pm 0.14$	$-1.06 \pm 0.04$

Same as in 3.2.3 but <sup>a</sup>Bin mean EW(Ly $\alpha$ ) according to Table 3.2.2

Table 3.2.7: Parameters estimated for the stacks by EW(CIII])

Bin	EW(CIII)] <sup>a</sup>	E(B-V) <sup>b</sup>	CIV/CIII] <sup>c</sup>	HeII/CIII] <sup>c</sup>	OIII]/CIII] <sup>c</sup>	EW(CIV) <sup>d</sup>	EW(CIII)] <sup>d</sup>	log(C/O) <sup>e</sup>	log( $Z_*/Z_\odot$ ) <sup>f</sup>
Stack A									
1	2.21 ± 0.90	0.10	0.21 ± 0.03	0.58 ± 0.03	0.15 ± 0.02	0.23 ± 0.03	1.48 ± 0.04	-0.44 ± 0.10	-0.72 ± 0.02
2	5.58 ± 1.13	0.07	0.17 ± 0.02	0.29 ± 0.03	0.14 ± 0.01	0.52 ± 0.08	4.40 ± 0.15	-0.4 ± 0.08	-0.75 ± 0.04
3	10.9 ± 2.91	0.07	0.26 ± 0.03	0.13 ± 0.02	0.19 ± 0.02	1.40 ± 0.19	8.21 ± 0.35	-0.50 ± 0.1	-1.09 ± 0.04
Stack B									
1	2.54 ± 0.93	0.09	0.22 ± 0.04	0.28 ± 0.04	0.13 ± 0.03	0.32 ± 0.06	2.08 ± 0.09	-0.38 ± 0.10	-0.76 ± 0.04
2	5.78 ± 1.12	0.07	0.16 ± 0.03	0.26 ± 0.03	0.13 ± 0.02	0.58 ± 0.11	5.05 ± 0.20	-0.30 ± 0.12	-0.91 ± 0.05
3	11.0 ± 3.00	0.07	0.36 ± 0.04	0.12 ± 0.02	0.22 ± 0.02	1.88 ± 0.21	7.98 ± 0.39	-0.56 ± 0.10	-1.03 ± 0.06
Stack C									
1	2.44 ± 1.12	0.06	0.31 ± 0.09	0.27 ± 0.09	< 0.13	0.42 ± 0.11	2.03 ± 0.18	> -0.33	-0.99 ± 0.03
2	5.90 ± 1.13	0.06	0.19 ± 0.03	0.24 ± 0.04	0.15 ± 0.03	0.69 ± 0.13	5.41 ± 0.23	-0.40 ± 0.12	-1.02 ± 0.04
3	11.0 ± 3.28	0.07	0.33 ± 0.04	0.12 ± 0.03	0.19 ± 0.02	1.56 ± 0.18	7.64 ± 0.43	-0.49 ± 0.1	-1.01 ± 0.07
Stack D									
1	2.02 ± 0.82	0.12	0.20 ± 0.03	0.56 ± 0.04	0.17 ± 0.02	0.22 ± 0.04	1.47 ± 0.06	-0.48 ± 0.10	-0.69 ± 0.02
2	5.61 ± 2.09	0.08	0.14 ± 0.05	0.31 ± 0.05	0.13 ± 0.02	0.39 ± 0.13	4.03 ± 0.30	-0.36 ± 0.10	-0.64 ± 0.05

Same as in 3.2.3 but <sup>a</sup>Bin mean EW(CIII]) according to Table 3.2.2

EW(CIII]), we note the same trend as we show in Fig. 3.2.11. The stronger low-ionization ISM absorption lines are found in the stacks with smaller EW(CIII]).

In addition to the low-ionization features associated with neutral outflowing gas, we identify high-ionization interstellar absorption lines such as SiIV $\lambda\lambda$ 1393,1402Å, CIV, and NV $\lambda\lambda$ 1238,1242Å. While SiIV $\lambda\lambda$ 1393,1402Å and NV $\lambda\lambda$ 1238,1242Å are only identified in all the stacks B and C, and in the stacks by EW(Ly $\alpha$ ) due to the spectral range, CIV is identified in all the stacks. We note in Figs. 3.2.7, 3.2.8, 3.2.9, 3.2.10, 3.2.12, 3.2.11 that the stronger absorption lines are in the stacks of higher stellar mass, brighter in any luminosity, lower EW(Ly $\alpha$ ), and lower EW(CIII]), i.e. similar to the trend observed in low-ionization ISM features.

In our stacks, we also identify fine structure emission lines of SiII that have been observed in the rest-UV spectrum of star-forming galaxies (e.g., Shapley et al., 2003). SiII\* $\lambda$ 1533Å is in the spectral range of all the stacks. This faint line is between two ISM absorption lines and is identified in most of the stacks. This line is particularly more intense in the more massive and luminous galaxies showing both lower EW(Ly $\alpha$ ) and lower EW(CIII]), but the trend is less clear than the one we find in the ISM absorption lines (see Fig. 3.2.7, 3.2.8, 3.2.9, 3.2.10, 3.2.12, 3.2.11). Other fine structure lines, such as SiII\* $\lambda$ 1265Å and SiII\* $\lambda$ 1309Å are also identified in stacks B and C, and in the stack by EW(Ly $\alpha$ ) (see Fig. 3.2.8, 3.2.9, 3.2.12, 3.2.11). These lines are identified in all the stacks, irrespective of stellar mass, luminosity, or EW bin, suggesting they are a more common feature in the UV spectra of CIII] emitters.

In addition to CIII], we identify nebular emission lines such as OIII], CIV, and HeII, which are central to the main goals of this Chapter. We observe that the strength of the nebular lines depends on the stellar mass and luminosity. We find that in general, the less massive (and fainter in any band) stacks show the more intense Ly $\alpha$ , CIV, HeII, OIII] and CIII] nebular lines. In the case of more massive (and brighter in any band), we find that the same set of nebular lines tends to be fainter. In particular for CIV and HeII, they show a stellar wind component as suggested by the P-Cygni profile (in the former) or broad profile (in the latter). In particular, CIV shows a P-Cygni type profile in all stacks with the emission being more intense in the less massive (or faintest) stacks and the ones with lowest EWs, either CIII] or Ly $\alpha$  (see Fig. 3.2.7, 3.2.8, 3.2.9, 3.2.10, 3.2.12, 3.2.11).

In Fig. 3.2.12 it is worth noticing that the nebular features appear less dependent of the  $\text{EW}(\text{Ly}\alpha)$  than the ISM absorption features, for which clearer differences are seen. We also note that comparing stacks B and C, which differ by the inclusion of galaxies with  $\text{Ly}\alpha$  in absorption or not, we find no strong difference in nebular emission lines or ISM absorption, but there are differences in the strength of  $\text{Ly}\alpha$ .

### 3.3.2 Relation of $\text{EW}(\text{CIII])}$ with luminosity and stellar mass

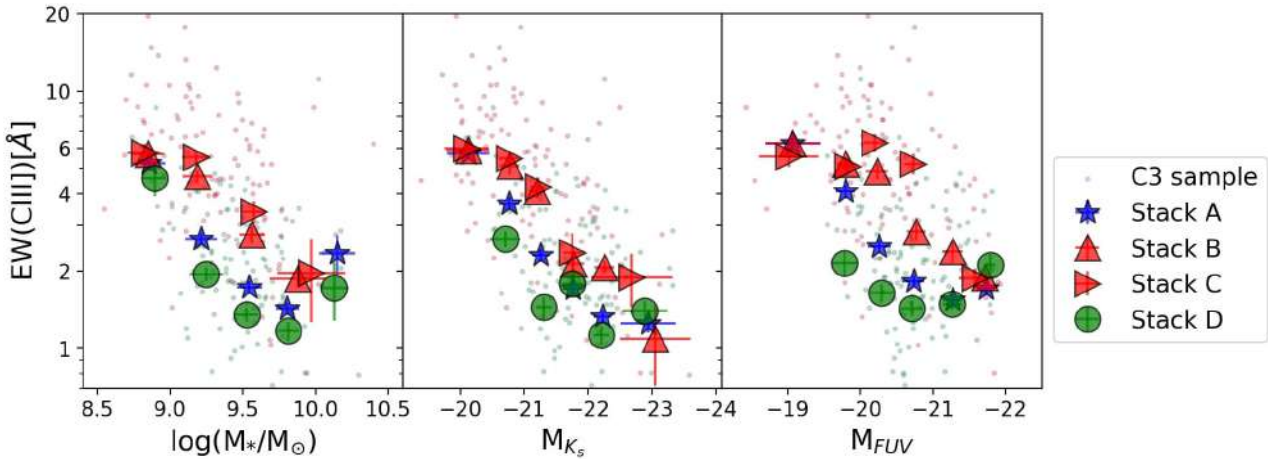


Figure 3.3.1: Relation of  $\text{EW}(\text{CIII])}$  with (from left to right) stellar mass,  $K_s$ -band luminosity, and FUV luminosity, for the stacks A, B, C, and D for each parameter, and for the individual galaxies in the C3 sample (small circles). In green, galaxies at  $z \lesssim 3$ , and in red, galaxies at  $z \gtrsim 3$ . In the  $x$ -axis, the parameters correspond to mean values for stacks, while for the C3 sample, the parameters correspond to the SED fitting values.

In this section, we present a qualitative description of the relation of  $\text{EW}(\text{CIII])}$  with the physical parameters used for stacking, which are shown in Fig. 3.3.1. We find a trend in which the stacks with more massive galaxies have lower  $\text{EW}(\text{CIII])}$ , while the more intense CIII] emitters correspond to the ones built with the lowest stellar mass, but the scatter is large when we consider individual objects (small circles) and the relation is weak, especially for stacks A and D, which are those containing galaxies at  $z \lesssim 3$  (small green circles). Something similar is observed with the broad-band luminosities, where the stacks of fainter objects tend to have higher  $\text{EW}(\text{CIII])}$ . The scatter follows the one observed for the luminosity of the individual galaxies of the C3 sample. We note that galaxies in the C3 sample at  $z \lesssim 3$  (included in stack D) show a mean  $\text{EW}(\text{CIII])}=2.4\text{\AA}$  and tend to have lower  $\text{EW}(\text{CIII])}$  than galaxies at  $z \gtrsim 3$  (included in stack B and C) which show a mean  $\text{EW}(\text{CIII])}=5.3\text{\AA}$ . This is related to the overlap of VANDELs targets with slightly different selection criteria around  $z \sim 3$ . For instance, galaxies selected as LBGs tend to show lower stellar masses than those selected as bright SFGs. We refer to Garilli et al. (2021) for a more detailed discussion on the effect of the VANDELs selection criteria on the galaxies physical properties.

Comparing the different schemes of stacking, it can be noticed that Stack B and C, i.e. the stacks that only include galaxies at  $z \gtrsim 3$ , have larger  $\text{EW}(\text{CIII])}$  than Stacks A and D for a given stellar mass or luminosity. On the other hand, Stack D, including only galaxies at  $z \lesssim 3$ , tends to have lower  $\text{EW}(\text{CIII])}$  for a given mass or luminosity than all the other stacking schemes. Except for the stack

with the lowest stellar mass,  $\text{EW}(\text{CIII])} \gtrsim 3\text{\AA}$  are not observed in Stack D. In addition, comparing Stack B and C, i.e. the effect of including or not galaxies with  $\text{Ly}\alpha$  in absorption, we note that slightly high  $\text{EW}(\text{CIII])}$  is observed when only  $\text{Ly}\alpha$  in emission is included.

A similar brief analysis is presented in Section 3.4.4 for the non-detected CIII] emitters from the parent sample. We find they are consistent with these results and they are intrinsically faint CIII] emitters with  $\text{EW}(\text{CIII])} \lesssim 2\text{\AA}$  for any FUV luminosity.

### 3.3.3 Diagnostic diagrams based on UV emission lines

Different diagnostic diagrams using rest-frame EWs of CIII], CIV, OIII] and the line ratios of CIII], CIV, and HeII have been proposed to identify the main source of ionizing photons in distant galaxies (e.g., Nakajima et al., 2018b; Hirschmann et al., 2019). These diagnostics are useful for determining the nature of the dominant ionizing source of galaxies. However, they need to be constrained using large samples of galaxies where these lines are detected. Given that the C3 sample is drawn from a parent sample of photometrically-selected SFGs, they can be used to probe and constrain these models using nebular flux ratios and EWs of systems that are not particularly extreme in their properties.

In this subsection, we explore the ionization properties of the C3 sample using different diagnostic diagrams proposed by Nakajima et al. (2018b), which are presented in Fig. 3.3.2 and 3.3.3. These diagnostic diagrams consider equivalent widths and line ratios of UV nebular lines to classify star-forming and AGN-dominated galaxies, respectively. They are based on the prediction of photoionization models showing that UV lines are sensitive to the shape of the incident radiation field and can be used to distinguish the nature of the dominant ionizing source –pure star formation or AGNs (cyan and red circles in Fig. 3.3.3, respectively). We include also the results from synthetic emission lines from Hirschmann et al. (2019) that take into account composite galaxies classified by BPT diagram (Baldwin et al., 1981) for the limits in the diagnostic diagrams and the criteria for defining a composite galaxy depends on the ratio of black hole accretion rate and star-formation rate.

In Fig. 3.3.2, we present the diagrams  $\text{EW}(\text{CIII])}$  versus  $\text{CIII]}/\text{HeII}$ ,  $\text{EW}(\text{CIV})$  versus  $\text{CIV}/\text{HeII}$ , and  $\text{EW}(\text{OIII])}$  versus  $\text{OIII]}/\text{HeII}$ . Our results are color-coded by the physical parameter used for stacking and with symbols representing each type of stack (see Fig. 3.3.2). As a reference for comparison, we include in Fig. 3.3.2, 3.3.3 similar results for stacks of CIII]-emitters from the VUDS survey (Le Fèvre et al., 2015). The black dashed lines are the limits between star-forming galaxies (on the right of the lines) and AGNs (on the left of the lines). The gray shaded region in the first diagram is where the models overlap and the classification may be ambiguous. In stacks where one of the lines in the diagnostic ratios is not detected at  $2\sigma$ ,  $2\sigma$ -limits are taken into account. Instead, if two lines involved in a given diagnostic are undetected, then the stack is not considered.

Overall, the main result from Fig. 3.3.2 is that all the stacks explored in our VANDELS sample lay within the region dominated by ionization driven by star formation. In the upper panel, stacks with lower stellar mass and fainter broad-band luminosity tend to show higher  $\text{EW}(\text{CIII])}$  and higher  $\text{CIII]}/\text{HeII}$  ratios. Similar results are found in the middle panel of Fig. 3.3.2 which shows a similar trend with  $\text{EW}(\text{CIV})$  and  $\text{CIV}/\text{HeII}$ . Finally, the bottom panel of Fig. 3.3.2 shows the  $\text{EW}(\text{OIII])}$  as a function of the  $\text{OIII]}/\text{HeII}$  ratio. Similar trends are found but with few stacks closer to the demarcation lines. Besides being consistent with the region dominated by star formation, all the stacks lay in the

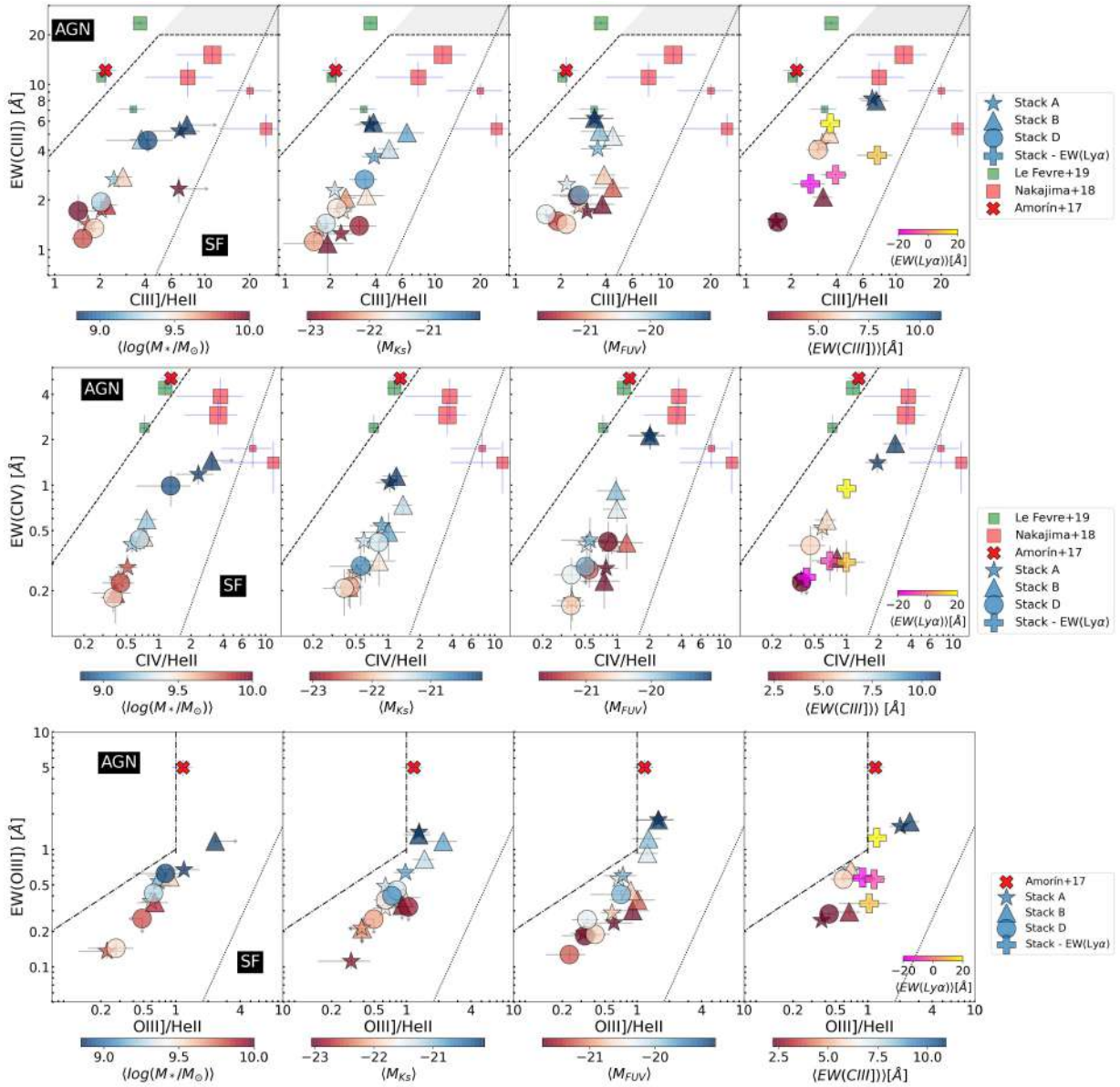


Figure 3.3.2: Diagnostic diagrams with EW of UV emission lines for the different stack sets, colored by the parameter used for stacking. The black dashed lines separate AGNs and star-forming galaxies as proposed in [Nakajima et al. \(2018b\)](#). The dotted and dotted-dashed lines are from [Hirschmann et al. \(2019\)](#) to separate between SFGs and composite, and composite and AGNs, respectively. *Top row*: Diagnostic of  $\text{EW}(\text{CIII])}-\text{CIII]}/\text{HeII}$  ratio. The gray-shaded region is where the models overlap. *Middle row*: Diagnosis of  $\text{EW}(\text{CIV})-\text{CIV}/\text{HeII}$  ratio. *Bottom row*: Diagnosis of  $\text{EW}(\text{OIII])}-\text{OIII]}/\text{HeII}$  ratio. The green boxes are the composites from [Le Fèvre et al. \(2019\)](#) and the bigger the size, the higher the  $\text{EW}(\text{CIII])}$ . The red X mark is the composite from [Amorín et al. \(2017\)](#). The red rectangles are the stacks from ([Nakajima et al., 2018a](#)) with the brightest  $M_{UV}$  (smallest rectangle), smaller  $\text{EW}(\text{Ly}\alpha)$ , faintest  $M_{UV}$ , and larger  $\text{EW}(\text{Ly}\alpha)$  (largest rectangle).

region of composite galaxies according to [Hirschmann et al. \(2019\)](#) in all diagnostic diagrams by EW.

We note that our stacks with stronger CIII] emission have consistent line ratios to the stack of CIII] emitters of similar EW in VUDS ( $5 < \text{EW}(\text{CIII])} < 10 \text{ \AA}$ ), the smaller green rectangle in the top

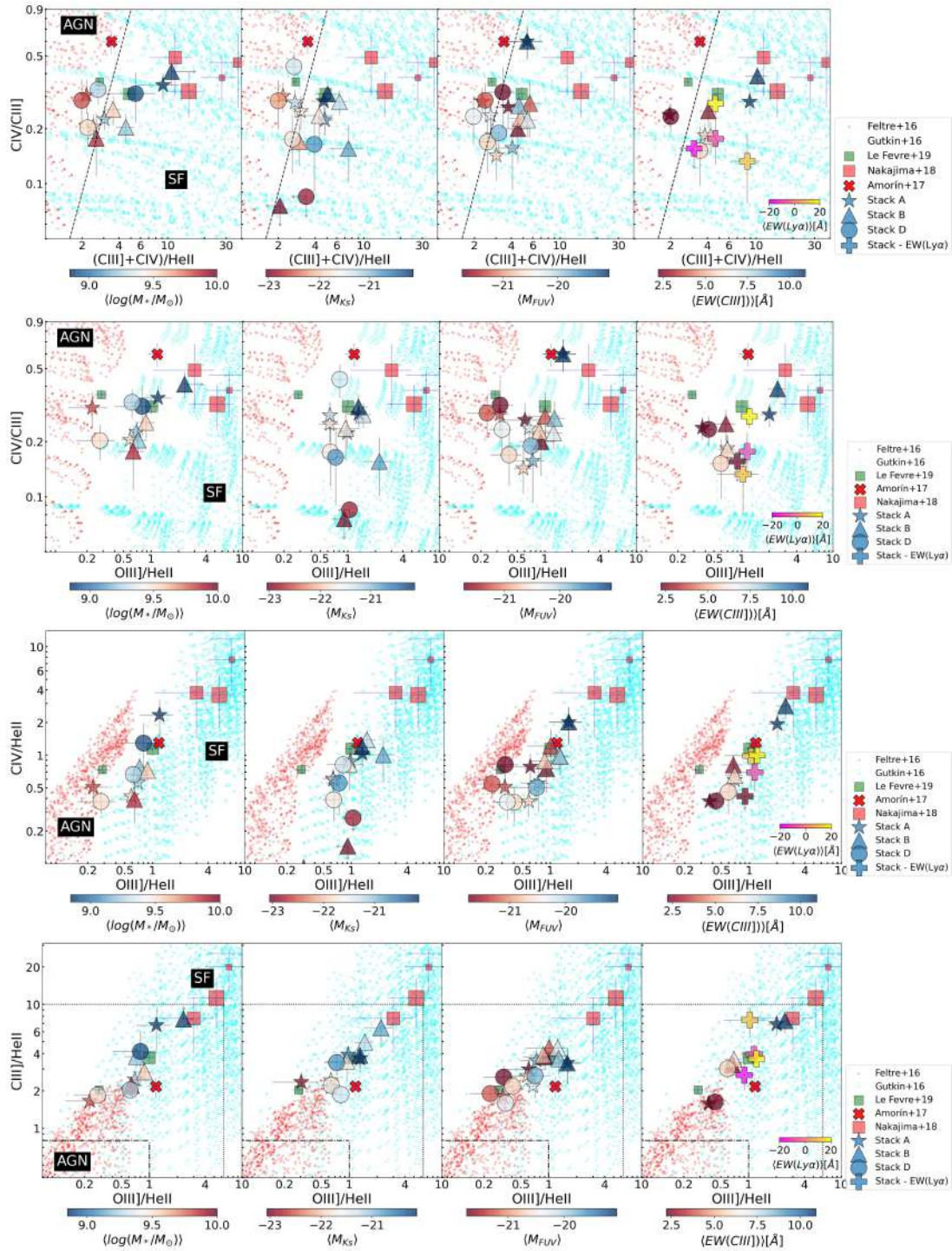


Figure 3.3.3: Diagnostic diagrams with fluxes of UV emission lines for the different stack sets, color-coded by the parameter used for stacking. Symbols are the same as in Fig. 3.3.2. The red and cyan points are the photoionization models for AGN (Feltre et al., 2016) and SF (Gutkin et al., 2016) for metallicity  $Z=0.0001, 0.0002, 0.0005, 0.001, 0.002$ , and for ionization parameter  $\log(U)=-4, -3, -2, -1$ . The dotted-dashed lines in the bottom panel separate composite and AGNs according to Hirschmann et al. (2019).

panel in Fig. 3.3.2) presented in Le Fèvre et al. (2019). Bigger green symbols show VUDS galaxies with  $EW(CIII]) > 10 \text{ \AA}$ , which are closer to the demarcation lines. Therefore, our stacks explore a

region in the emission line parameter space of photoionization models that are poorly explored in previous surveys and is occupied by the weak CIII] emitters.

In order to complement the above diagnostics with EW, we also explore diagnostic diagrams using only UV emission-line flux ratios. We compare them with the [Feltre et al. \(2016\)](#) and [Gutkin et al. \(2016\)](#) photoionization models to probe the dominant ionizing source in our C3 sample. For the OIII] fluxes, we consider the sum of the OIII] $\lambda$ 1661Å and OIII] $\lambda$ 1666Å lines by adopting a theoretical ratio of OIII] $\lambda$ 1661Å/OIII] $\lambda$ 1666Å=0.41 from [Gutkin et al. \(2016\)](#) for a  $\log U = -2$ .

In the panels of Fig. 3.3.3 from top to bottom, we present CIV/CIII] as a function of (CIV+CIII])/HeII ratio, and CIV/CIII], CIV/HeII and CIII]/HeII as a function of OIII]/HeII, respectively. Overall, the C3 stacks are fully consistent with diagnostics shown in Fig. 3.3.2, and point to pure star formation as the dominant source of ionization. Moreover, given that the galaxies in the C3 sample are selected to be star-forming and X-ray sources were excluded, these results lead to constraining photoionization models at  $z \sim 3$ .

A few stacks in these diagnostic diagrams lie close to the demarcation lines. As shown in previous studies ([Feltre et al. \(2016\)](#); [Gutkin et al. \(2016\)](#); [Nakajima et al. \(2018b\)](#)) these diagnostics may have some overlapping regions in which both star-forming and AGN-driven ionization may coexist. Only a few points lie at low OIII]/HeII and low CIII]/HeII (or CIV/HeII), a region where some contribution from AGNs might be expected according to models. Also Fig. 3.3.3 shows that the less massive galaxies tend to have higher OIII]/HeII ratios. In the bottom panel of Fig. 3.3.3, demarcation lines from [Hirschmann et al. \(2019\)](#) are shown. The stacks lay consistently in the region of composite galaxies.

As shown in [Hirschmann et al. \(2019\)](#), the demarcation lines between composite and SFGs are clearer at  $z = 0 - 1$ . At higher redshifts, the models overlap in this zone. This could be an effect of the evolution of the criteria for defining a composite galaxy with redshift, or the change of the demarcation lines in the BPT diagram depending on the ionization parameter, electron density, or extreme UV ionization field ([Kewley et al., 2019](#)) which are likely to change due to the evolution of mass-metallicity relation with redshift. The higher electron temperatures at low metallicity can enhance the strengths of collisionally excited lines. It is also possible to find some pure SFGs with higher C/O in the composite region because the demarcation lines are based on fixed C/O at a given metallicity.

### 3.3.4 An apparent EW(Ly $\alpha$ )-EW(CIII]) correlation

Previous studies have reported a positive correlation between EW(Ly $\alpha$ ) and EW(CIII]) (e.g. [Shapley et al., 2003](#); [Stark et al., 2014](#); [Le Fèvre et al., 2019](#); [Cullen et al., 2020](#)). Such a relation is potentially useful for using CIII] to identify galaxies in the epoch of reionization where Ly $\alpha$  is strongly attenuated by the IGM.

In Figure 3.3.4, we explore the possible correlation between EW(Ly $\alpha$ ) and EW(CIII]) for our C3 sample. We consider spectra from Stack B by stellar mass, FUV,  $K_s$  luminosity, EW(CIII]), and EW(Ly $\alpha$ ). We also include data from the literature, both stacks ([Shapley et al., 2003](#); [Amorín et al., 2017](#); [Nakajima et al., 2018a](#); [Cullen et al., 2020](#); [Feltre et al., 2020](#)) and individual galaxies at similar

redshifts (Stark et al., 2014), for which the existence of such correlation has been confirmed. We fit a linear regression to all the above data, which gives

$$EW(Ly\alpha) = (10.67 \pm 0.89) \times EW(CIII]) - (26.38 \pm 5.72). \quad (3.3.1)$$

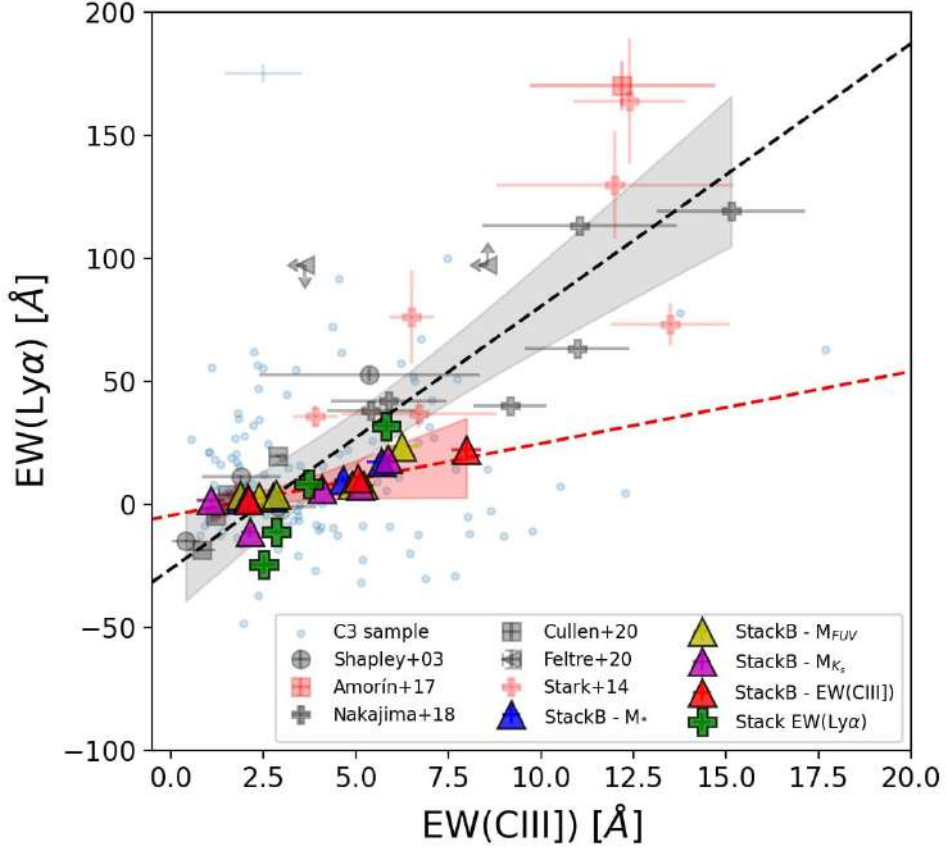


Figure 3.3.4:  $EW(Ly\alpha)$ - $EW(CIII])$  relation. The results from stacks B are represented by the triangle symbols, with different colors depending on the parameter used for stacking: blue for stellar mass, yellow for FUV luminosity, magenta for  $K_s$  luminosity, red for  $EW(CIII])$ , and green for  $EW(Ly\alpha)$ . Individual galaxies with measured  $Ly\alpha$  from the C3 sample are the small blue circles with their typical errors on the upper left. Previous results from literature at similar redshift are also displayed (Stacking: Shapley et al. (2003); Amorín et al. (2017); Nakajima et al. (2018a); Cullen et al. (2020); Feltre et al. (2020). Individual objects: Stark et al. (2014)). The dashed black line is the best fit in Eq. 3.3.1 including our stacks and the sample from the literature. The red dashed line is the best fit in Eq. 3.3.2 including only our stacks.

The linear fit is performed using LMFIT (Newville et al., 2016) with a least-squared method weighted by  $1/\sigma$ , where  $\sigma$  is the uncertainty in the parameter used for fitting. We use the same method for linear fitting in the following sections. When the linear fit is displayed in figures, the shaded region is the  $3\text{-}\sigma$  uncertainty band of the fitting and it covers the range where the fit is performed and valid.

The relation in Eq. 3.3.1 fits the data with a relatively large scatter, which is shown at the  $3\sigma$  level by the grey band in Fig. 3.3.4. If we only include our stacks in the linear fit, we find that the best fit is

$$EW(Ly\alpha) = (2.92 \pm 0.85) \times EW(CIII]) - (4.65 \pm 2.36), \quad (3.3.2)$$

which has a lower slope. The shallower relation can be an effect for the low EW(CIII]) of our stacks and because most of the literature sample is selected by Ly $\alpha$  or by strong CIII] emission. If we compare our stacks built by EW(Ly $\alpha$ ) (green symbols in Fig. 3.3.4), we find that they are in better agreement with Eq. 3.3.1.

Our VANDELS data allow us to probe the low EW end of this relation. Fig. 3.3.4 shows that there is a clear trend that seems to hold even in the absence of very strong CIII] emitters in our stacks. We caution, however, that the functional form in Eq. 3.3.1 and Eq. 3.3.2 is representative of the average population of star-forming galaxies at  $z \sim 2 - 4$  and that strong deviations for individual galaxies can exist, especially at low EW. This is illustrated in Fig. 3.3.4 where we show the distribution of individual galaxies in the C3 sample. We note that these objects are not included in the linear fit in Eq. 3.3.1 and Eq. 3.3.2. The scatter shown by the individual galaxies is larger than the typical uncertainties. A similar diagram was presented in Marchi et al. (2019) for a few individual VANDELS sources.

Based on Cloudy photoionization models, Jaskot & Ravindranath (2016) show that at a given EW(Ly $\alpha$ ), the scatter in EW(CIII]) can be as high as 10-20Å, comparable to the observed level of scatter among galaxies, depending on the different metallicities, ionization parameters, and ages considered for the models. In general, higher EW(CIII]) for a given EW(Ly $\alpha$ ) indicates higher ionization parameters, younger ages, and lower stellar metallicity. In a future work, we will address this point by using our large sample of CIII] emitters to constrain different photoionization models with their individual measurements.

Overall, the correlation found in Fig. 3.3.4 suggests that CIII] emitters are good markers of LAEs, especially for galaxies with low stellar mass, low luminosity, and high star formation rates. This confirms the potential use of CIII] to identify and study galaxies at the epoch of reionization, for which Ly $\alpha$  emission is strongly attenuated due to IGM opacity. However, this could be challenging due to the lower EWs of CIII] compared to that of Ly $\alpha$  in SFGs. A similar stacking approach will be useful with large enough samples at  $z > 6$  for studying their global properties, but CIII] may be the only robust and high S/N emission that may be observed to have individual detections from the ground.

### 3.3.5 A relation between stellar metallicity and the CIII] and Ly $\alpha$ equivalent widths

The rest-frame UV spectrum is dominated by the continuum light from young, massive stars that contains features of the chemistry of stellar photospheres and expanding stellar winds. The strength of these features has a strong dependence on the total photospheric metallicity. The full UV-spectrum fitting uses the strength of these faint photospheric features to estimate the stellar metallicity. We study the stellar metallicity (tracing the Fe/H abundance) of the C3 sample following two complementary approaches. First, we follow the full spectrum fitting method described in Cullen et al. (2019). In short, the high S/N stacked spectra are fitted using a Bayesian approach with Starburst99 (SB99) high-resolution WM-Basic theoretical models with constant star-formation rates (Leitherer et al., 2014). As a result, for some stacked spectra the stellar metallicity is an upper limit because the model parameter space does not extend below  $Z_{\star}=0.001$  ( $0.07 Z_{\odot}$ ). In these cases, a 2- $\sigma$  upper limit is reported.

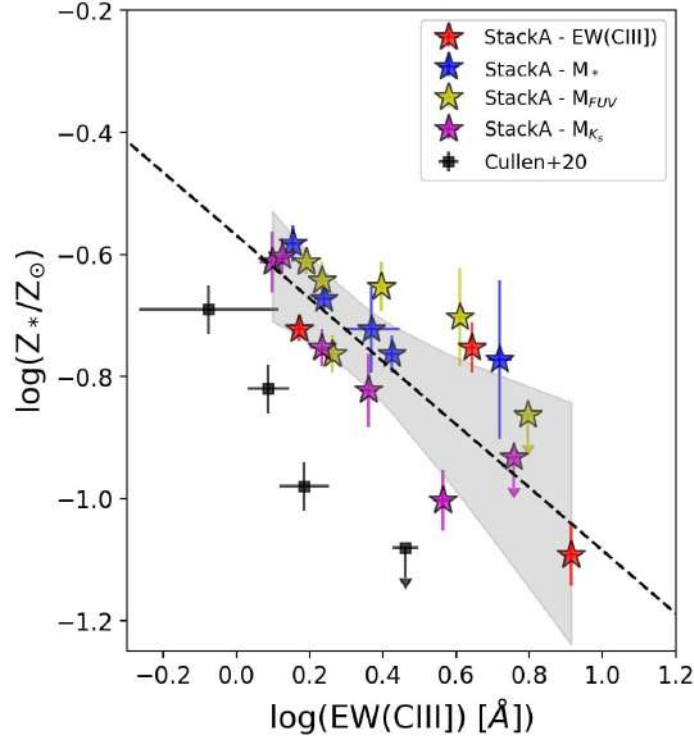


Figure 3.3.5: EW(CIII)]-stellar metallicity relation. The results from our stacks A are represented by star symbols. Colors for our stacks are the same as in Fig. 3.3.4. Black dashed line is the best fit in Eq. 3.3.3 and the gray shaded region is the  $3\text{-}\sigma$  band uncertainty.

A second set of stellar metallicity estimates is performed using the method presented in Calabrò et al. (2021). This method is based on stellar photospheric absorption features at  $1501\text{\AA}$  and  $1719\text{\AA}$ , which are calibrated with SB99 models and are largely unaffected by stellar age, dust, IMF, nebular continuum or interstellar absorption. These estimations were only possible in stacks A and B, which are the ones with the highest S/N ( $\sim 20\text{-}30$ ). Using this method, we find consistent stellar metallicity values with those obtained with the full spectral fitting. However, the stellar metallicities based on the two photospheric indices show larger uncertainties (up to  $\sim 0.6$  dex). Hereafter, we use the results from the first approach.

The stellar metallicity of the C3 sample ranges from  $\log(Z_*/Z_\odot) = -1.09$  ( $\sim 8\%$  solar) to  $-0.38$  ( $\sim 40\%$  solar), with a mean value of  $\log(Z_*/Z_\odot) = -0.8$  ( $\sim 16\%$  solar). All stellar metallicities for stacks are reported in Tables 3.2.3, 3.2.4, 3.2.5, 3.2.6, and 3.2.7.

We explore the relation of the stellar metallicity with the EW(CIII)], which is shown in Fig. 3.3.5. For this, we use the spectra from Stack A, which include the entire C3 sample of galaxies, irrespective of redshift. We include the stacks by stellar mass, FUV luminosity,  $K_s$  luminosity, and EW(CIII)] for the fitting. The best linear fit to data is

$$\log(Z_*/Z_\odot) = (-0.51 \pm 0.08) \times \log(\text{EW}(\text{CIII}]) - (0.57 \pm 0.03), \quad (3.3.3)$$

with EW(CIII)] in  $\text{\AA}$ . We find a decrease of EW(CIII)] with stellar metallicity. Comparing these results with Cullen et al. (2020), we find an offset towards higher EW(CIII)] for a given stellar metallicity. We find three reasons for such offset. Firstly, the two samples only overlap in a narrow redshift range, as the Cullen et al. (2020) sample include galaxies between  $z = 3$  and  $z = 5$ , thus excluding

galaxies at  $z < 3$  which are numerous in our sample. Secondly, the selection criteria for our sample is based on CIII], leading to stacks with higher EW(CIII)]. Finally, the use of accurate systemic redshifts based on CIII] line profile fitting lead to stacks with higher EW(CIII)] than stacks for the entire parent sample using the VANDELS spectroscopic redshift. We find the latter can explain up to a difference of  $\log(\text{EW}(\text{CIII}])) \sim 0.2$  dex in the stacks of lower stellar mass and luminosity.

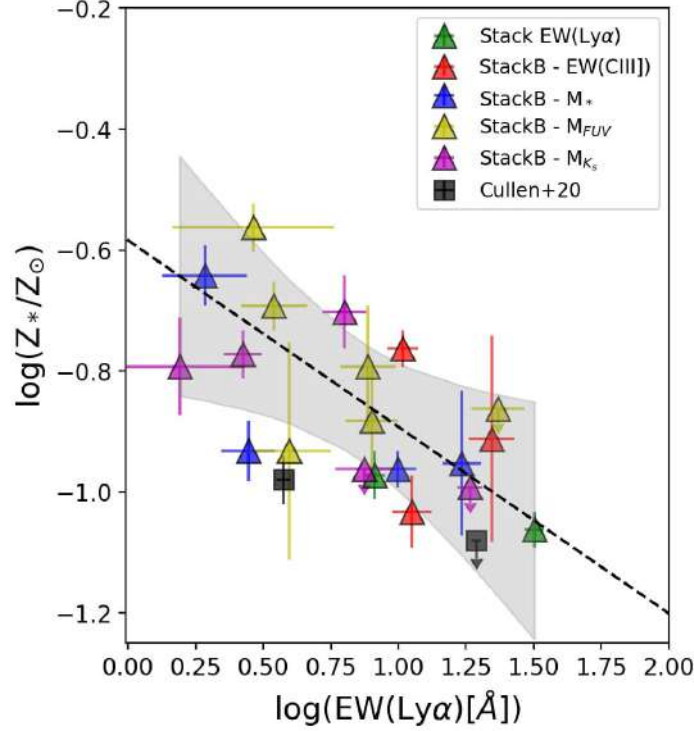


Figure 3.3.6: EW(Ly $\alpha$ )-stellar metallicity relation. The symbols and colors for our stacks are the same as in Fig. 3.3.4. Black dashed line is the best fit to the stacked data (triangles) presented in Eq. 3.3.4, with the gray shaded regions at  $3\text{-}\sigma$ , respectively. The black symbols are the stacks in Cullen et al. (2020) with Ly $\alpha$  in emission.

In Figure 3.3.6, we show stellar metallicities as a function of EW(Ly $\alpha$ ) for the set of spectra from Stack B using different colors for stacks by stellar mass, EW(CIII)], and FUV,  $K_s$  luminosity, and EW(Ly $\alpha$ ). We perform a linear fitting to only our stack data, excluding two bins for which the EW(Ly $\alpha$ ) is negative (i.e. Ly $\alpha$  is in absorption). Our best fit is

$$\log(Z_*/Z_\odot) = (-0.30 \pm 0.07) \times \log(\text{EW}(\text{Ly}\alpha)) - (0.58 \pm 0.06) \quad (3.3.4)$$

with EW(Ly $\alpha$ ) in  $\text{\AA}$ . We find a decrease of EW(Ly $\alpha$ ) with stellar metallicity. The relation in Eq. 3.3.4 provide larger metallicities at fixed EW(Ly $\alpha$ ) compared to the one presented by Cullen et al. (2020) which is based on stacking of galaxies at  $z > 3$  and include spectra with Ly $\alpha$  in absorption. In our fit, instead, we only consider stacks with Ly $\alpha$  in emission. We note, however, that despite the difference in redshift, the two stacks from Cullen et al. (2020) (black rectangles in Fig. 3.3.6 and built by binning in EW(Ly $\alpha$ )) with Ly $\alpha$  in emission show a trend that is consistent with our stacks based on EW(Ly $\alpha$ ) (green triangles).

Overall, the relation found in Fig. 3.3.6 confirms and adds robustness to the anticorrelation found for VANDELS galaxies out to  $z \sim 5$  in Cullen et al. (2020). We demonstrate in Fig. 3.3.5 and Fig. 3.3.6

that galaxies with stronger CIII] emission show larger Ly $\alpha$  EW and lower stellar metallicities of  $\lesssim 10\%$  solar. In correlations involving Ly $\alpha$ , it is important to note that the Ly $\alpha$  emission is resonantly scattered and the correlations are not easily interpreted as for the CIII] or other nebular emission lines. As shown in Cullen et al. (2020), Eq. 3.3.4 indicates that harder ionizing continuum spectra emitted by low metallicity stellar populations play a role in modulating the Ly $\alpha$  emission in star-forming galaxies.

### 3.3.6 C/O ratio and its relation with EW and physical parameters

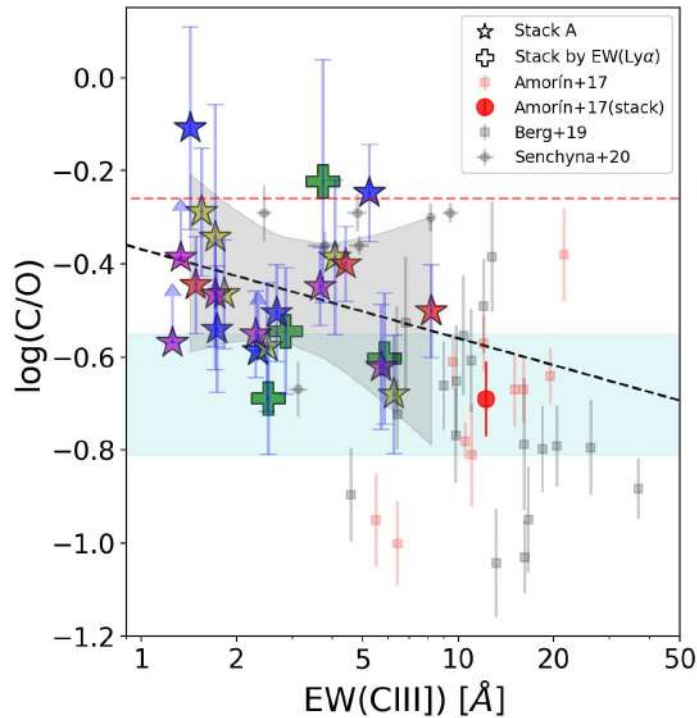


Figure 3.3.7: Relation between the EW(CIII]) and C/O ratio as derived using HCM-UV. The red dashed line corresponds to the solar value. The cyan-shaded region is the average C/O for Lyman-break galaxies in Shapley et al. (2003) and the red circle is the result for a composite spectrum of CIII]-emitters in Amorín et al. (2017). Individual CIII] emitters at high- $z$  (red squares, Amorín et al., 2017) and low- $z$  (black squares and circles Berg et al., 2019; Senchyna et al., 2021) are also included. Colors for our stacks are the same as in Fig. 3.3.4. The black dashed line is the best linear fit to our stacks, as displayed in Eq. 3.3.5.

The relative abundances of carbon, nitrogen and other alpha elements to oxygen may provide insight not only on the origin of carbon in galaxies but also in their chemical evolution. However, constraining the C/O abundance is often difficult. For local galaxies, the emission lines often used to derive C/O are exceedingly faint carbon recombination lines (e.g. Esteban et al., 2014) or the CIII] collisionally excited line, which is accessible for low-metallicity objects only from space (e.g. Senchyna et al., 2017; Berg et al., 2019). At  $z \gtrsim 1$ , the required emission lines lie in the optical range but even for low-metallicity objects their faintness require very deep observations or stacking (e.g. Shapley et al., 2003; Amorín et al., 2017). While this makes the C/O difficult to constrain, this abundance ratio is essential to understand different emission-line diagnostics (e.g. Feltre et al., 2016; Jaskot &

Ravindranath, 2016; Nakajima et al., 2018b; Byler et al., 2018) and more generally the origin of carbon and the chemical evolution of star-forming galaxies. Here we explore the C/O ratio, which can be derived from the observed C and O lines in the UV.

We estimate the C/O abundance using the code HII-CHI-mistry in its version for the UV (Pérez-Montero & Amorín, 2017) (hereafter HCM-UV<sup>‡</sup>) considering PopStar stellar atmospheres (Mollá et al., 2009), for the photoionization models used by the code. This PYTHON code derives the carbon-to-oxygen ratio (i.e.  $\log(C/O)$ ) from a set of observed UV emission-line intensities, which are also used to estimate ionization parameter and gas metallicity in a consistent framework with results provided by the direct Te-method. More details on this methodology can be found in Pérez-Montero & Amorín (2017). For C/O, we use as an input the CIV, CIII], OIII] fluxes (and their errors) which are reported in Tables 3.2.3, 3.2.4 and 3.2.5, after extinction correction (as explained in Sec. 3.2.4). In most of the stacks, the OIII] $\lambda$ 1660Å is not detected at  $3\sigma$ . For this reason, we consider the theoretical ratio of OIII] $\lambda$ 1660Å/OIII] $\lambda$ 1666Å $\sim$ 0.4 from photoionization models with an ionization parameter of -3 and -2 (Gutkin et al., 2016). In the code, 25 Monte Carlo iterations are performed to estimate the uncertainties in the C/O calculations. In the cases where OIII] $\lambda$ 1666Å is detected with a  $<2\sigma$  level or when the C/O uncertainties are larger than 0.9 dex, C/O is estimated as a lower limit. Results are reported in Tables 3.2.3, 3.2.4, 3.2.5, 3.2.6, and 3.2.7. We find  $\log(C/O)$  values ranging from -0.68 (38% solar) to -0.06 ( $\sim$ 150% solar) with a mean value of -0.50 (60% solar).

Alternatively to HCM-UV, we used the empirical calibration between C3O3 ( $\equiv \log((CIII]+CIV)/OIII]$ ) and C/O found by Pérez-Montero & Amorín (2017) using a control sample with C/O and metallicities obtained from UV and optical lines. Using this calibration  $\log(C/O) = -1.07 + 0.80 \times C3O3$ , which essentially provides an accurate fit to models predictions for the C3O3 index, we find consistent results, within the typical error of  $\sim 0.2$  dex, with those of HCM-UV. Small differences can be attributed to slight changes in the ionization parameter (see Fig. 2 in Pérez-Montero & Amorín, 2017), which is constrained by HCM-UV using CIV and CIII]. All C/O results presented in subsequent analysis and figures are derived with HCM-UV but they are fully consistent with the C3O3 calibration.

We explore the relation of  $\log(C/O)$  with  $EW(CIII]$  in Fig. 3.3.7. We only include the results from stack A by stellar mass, luminosities and  $EW(CIII]$ , and the stacks by  $EW(Ly\alpha)$ . A linear regression to data gives

$$\log(C/O) = -(0.19 \pm 0.14) \times \log(EW(CIII])) - (0.36 \pm 0.07), \quad (3.3.5)$$

with a Pearson correlation coefficient  $r_p = -0.30$ . This relation suggests a decrease of C/O abundance ratio with  $EW(CIII]$ , i.e. the more extreme CIII] emitters tend to have lower  $\log(C/O)$ . We showed in Eq. 3.3.3 that strong CIII] emitters also have low stellar metallicities, which lead to less cooling and higher nebular temperatures that enhance the CIII] emission. Therefore, Eq. 3.3.5 suggests a change in stellar metallicity. The relation between C/O and stellar and gas metallicities will be discussed in Section 3.4.2.

We also observe a weak relation ( $r_p = -0.29$ ) between C/O with  $EW(Ly\alpha)$ , where LAEs tend to have lower C/O, thus suggesting higher  $EW(CIII]$  and lower metallicity, i.e. a younger chemical age. For  $EW(Ly\alpha)=20\text{Å}$ , a  $\log(C/O) \sim -0.5$  is found ( $\sim$ 60% solar) and a corresponding  $EW(CIII]) \sim 10\text{Å}$  (from Eq. 3.3.5). We stress, however, that the relation between both C/O and  $EW(Ly\alpha)$  could not be physically motivated and it relies on previous correlations found between EWs in Eq. 3.3.2.

<sup>‡</sup>We used the version 3.2 publicly available at <https://www.iaa.csic.es/~epm/HII-CHI-mistry-UV.html>

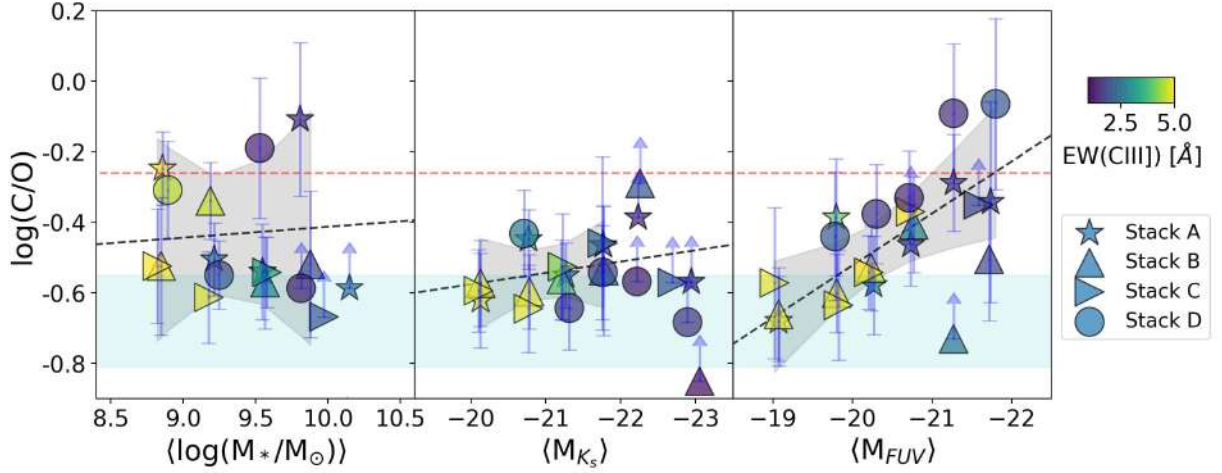


Figure 3.3.8: Relation between the different physical properties used for the stacks and  $C/O$  ratio using as derived using HCM-UV. The red dashed line corresponds to the solar value. The cyan shaded region is from Shapley et al. (2003). The results of the stacks are color coded by  $EW(CIII])$ . The black dashed line is the best linear fit for each parameter in Eq. 3.3.6, 3.3.7, and 3.3.8, respectively.

On the other hand, in Figure 3.3.8 we present the results of  $C/O$  for the C3 sample as a function of the physical parameter used for stacking and color-coded by  $EW(CIII])$ . We find an apparent mild increase of  $C/O$  with stellar mass (left panel on Fig. 3.3.8). A linear fit to data after excluding lower limits gives

$$\log(C/O) = (0.03 \pm 0.12) \times \log(M_*/M_\odot) - (0.72 \pm 1.20), \quad (3.3.6)$$

with  $r_p = 0.07$ . This relation is weak and of limited use due to the lack of reliable  $C/O$  estimations in the high mass end for which OIII] is barely detected in our stacks. This makes the dynamical range of stellar mass too small to provide a more robust relation.

In the  $K_s$  band (middle panel on Fig. 3.3.8), we perform a linear fitting excluding the lower limits, which gives

$$\log(C/O) = -(0.03 \pm 0.03) \times M_{K_s} - (1.21 \pm 0.72), \quad (3.3.7)$$

with  $r_p = -0.37$ . We find an increase of  $C/O$  with  $K_s$  luminosity, but again the relation is weak mostly due to the lower limits for high-luminosity stacks.

On the other hand, the FUV luminosity (right panel of Fig. 3.3.8) has a stronger correlation with  $C/O$ . A linear regression excluding lower limits gives

$$\log(C/O) = -(0.14 \pm 0.03) \times M_{FUV} - (3.47 \pm 0.63), \quad (3.3.8)$$

with  $r_p = -0.74$ . This correlation clearly shows an increase of  $C/O$  in galaxies with higher FUV luminosity and can be used to estimate a mean  $C/O$  value from a galaxy luminosity. Assuming the FUV luminosity is a tracer of the recent SFR and that more evolved stellar populations may have a larger contribution in the  $C/O$  relation with stellar mass and  $K_s$  luminosity, the above differences might be explained invoking a strong dependence of  $C/O$  with star formation histories. However, larger samples and deeper spectra, especially for high mass galaxies, would be needed to provide better insight.

We note that our results suggest that stacking by FUV luminosity results in a more homogeneous distribution of C/O within the bins, compared to the stellar mass and  $K_s$  luminosity. In the short dynamical range for stellar mass ( $\sim 1$  dex where C/O was estimated) there is no clear trend for this sample.

In summary, the C/O abundance of CIII] emitters increases from less than half solar for fainter (low-mass) galaxies to about solar abundance for our brighter (high-mass) objects. The stronger CIII] emitters, i.e. higher EWs, are found in low luminosity, low C/O galaxies.

### 3.3.7 On the relation of SFR with EW(CIII]) and C/O

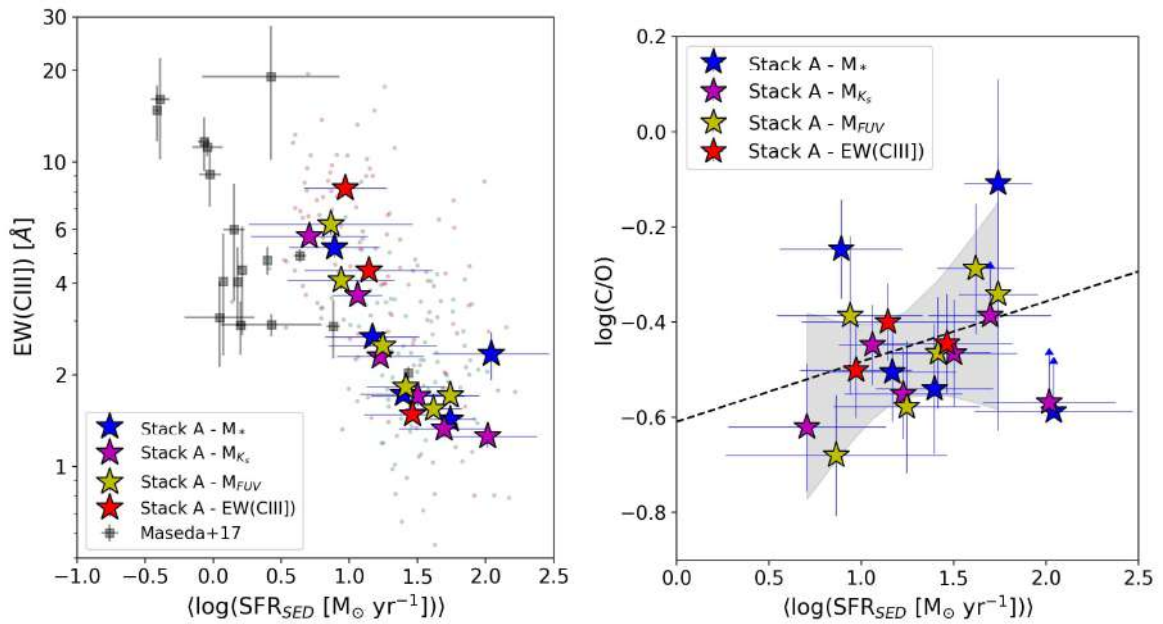


Figure 3.3.9: Relation between SFR-EW(CIII]) (*left panel*) and SFR-C/O (*right panel*). Stars symbols are Stack A color-coded depending on the parameter used for stacking, according to legend, as in Fig. 3.3.4. *On the left panel*: The black squares are results from CIII] emitters in Maseda et al. (2017). The small dots are the C3 sample with the same colors as in Fig. 3.3.1. *On the right panel*: The dashed black line is the best fit for the SFR-CO relation in Eq. 3.3.9.

We explore the relation between EW(CIII]) and C/O abundance ratio with SFR. In both cases, we illustrate these findings using the sample of Stack A by stellar mass, FUV and  $K_s$  luminosities, and EW(CIII]). We estimate the SFR with the mean value of the SED-based SFR of individual galaxies in each bin. In Fig. 3.3.9 we present these results. Overall, we find that EW(CIII]) decreases with SFR, as we also find for individual galaxies in the C3 sample. This is consistent with the trend observed in Maseda et al. (2017) for a smaller sample of strong CIII] emitters. Our stacks show that galaxies with  $\text{SFR} \gtrsim 30 M_\odot/\text{yr}$  have  $\text{EW}(\text{CIII])} \lesssim 3 \text{ \AA}$ . Instead, for galaxies with  $\text{SFR} \lesssim 30 M_\odot/\text{yr}$ , the relation becomes steeper and shows more dispersion on the EW(CIII]) values, with the more intense CIII] emitters having lower SFRs. Stacks with average  $\text{SFR} \lesssim 10 M_\odot/\text{yr}$  show all EW(CIII]) larger than  $\sim 3 \text{ \AA}$ . We note that the result in Fig. 3.3.9 does not imply that higher SFR tends to suppress CIII] emission, as this relation hides an underlying metallicity dependence that is key for interpreting the CIII] emission (see Section 3.4.1 for a discussion on stellar mass-metallicity relation). Higher SFR

implies a larger number of ionizing photons, which tend to enhance CIII] emission. However, since our sample lies in the star-forming main sequence, galaxies with higher SFR have higher stellar mass and also higher metallicity, which imply more efficient cooling and weaker collisionally-excited lines such as CIII].

Finally, we do not find a correlation of  $EW(CIII)]$  with specific SFR ( $sSFR = SFR/M_*$ ). For the stacks shown in Fig. 3.3.9 and based on the mean values of stellar mass and SFR from the SED fitting, we find values for  $\log(sSFR [yr^{-1}])$  ranging between  $-8.3$  and  $-7.9$  with no clear correlation with  $EW(CIII)]$ . Note, however, that the dynamical range in  $sSFR$  probed by the C3 sample appears too small compared with the uncertainties to probe possible correlations with other observables.

On the other hand, Fig. 3.3.9 shows a trend between SFR and C/O abundance. The C/O tends to increase with the average SFR. This relation shows a large scatter and appears mainly driven by the stacks by  $M_{FUV}$ . This result shows consistency with the relation found between C/O and  $M_{FUV}$  in Fig. 3.3.8, as  $M_{FUV}$  is a good tracer of SFR. A linear fit to this relation, excluding upper limits, gives

$$\log(C/O) = (0.12 \pm 0.11) \times \log(SFR_{SED}) - (0.61 \pm 0.13), \quad (3.3.9)$$

where SFR is in  $M_{\odot}/yr$  ( $r_p = 0.51$ ). Considering that our C3 sample is representative of main-sequence galaxies, this relation shows the limitation of Eq. 3.3.6 because faint OIII] lines are not detected in stacks with high-mass galaxies.

It is worth noting that in Fig. 3.3.5, 3.3.6, 3.3.7, and 3.3.9, different dynamic ranges in stellar metallicity and C/O are obtained depending on the parameter used for stacking. Overall, the trends found in these and other relations are mainly driven by the stacks binned by luminosity, which are more uniformly populated. In Section 3.4.3, we show that our results remain unchanged if we restrict the fitting to only those stacks binned by luminosity.

## 3.4 Discussions

### 3.4.1 On the stellar mass-metallicity relation of CIII] emitters at $z \sim 3$

Scaling relations, such as the stellar MZR, are important diagnostics to understand the evolution of galaxies. In particular, the MZR is shaped by different physical processes such as strong outflows produced by stellar feedback, infall of metal-poor gas, the so-called stellar mass downsizing for which high-mass galaxies evolve more rapidly and at higher redshifts than low-mass ones, or by the shape of the high-mass end of the IMF (see Maiolino & Mannucci, 2019, for a review). Thus, the MZR of a galaxy population in a determined redshift may provide clues on the dominant processes that affect its evolution in that period.

The gas-phase MZR (hereafter MZRg) has been explored in the local universe, exploiting the methods based on optical emission lines applied to large samples of galaxies (e.g. Tremonti et al., 2004; Andrews & Martini, 2013). In the same way, the MZRg has been explored at higher redshifts (e.g. Erb et al., 2006; Mannucci et al., 2010; Pérez-Montero et al., 2013; Troncoso et al., 2014; Lian et al., 2015; Sanders et al., 2021) thus providing a clear evolutionary picture up to  $z \sim 3.5$  (e.g. Maiolino et al., 2008; Mannucci et al., 2010). The MZRg is found to evolve with redshift, with

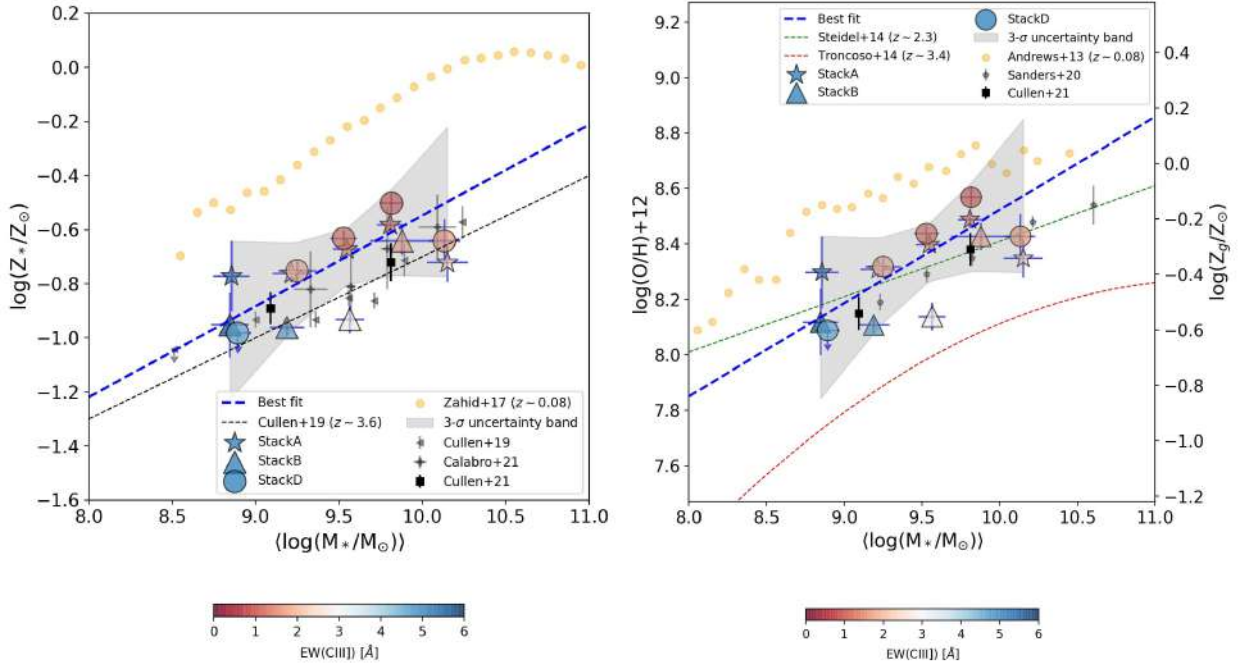


Figure 3.4.1: *Left panel*: MZR with the stacks A, B, D by stellar mass with star, triangle and circle symbols, respectively, and color-coded by  $EW(CIII])$ . The black symbols are stacks from Cullen et al. (2019); Calabrò et al. (2021); Cullen et al. (2021). The orange circles is the local MZR from Zahid et al. (2017). The blue dashed line is the best fit with the shaded region at  $3\text{-}\sigma$  in Eq. 3.4.1, and the black dashed line is the MZR from Cullen et al. (2019). *Right panel*: MZRg with the same stacks as left panel but re-scaled with the  $\alpha$ -enhancement. Green dashed line from Steidel et al. (2014). Red dashed line from Troncoso et al. (2014). Black symbols are values from literature (Sanders et al., 2021; Cullen et al., 2021). The orange points are the local MZRg from Andrews & Martini (2013). The  $Z_g$  scale in the y-axes corresponds to the gas-phase metallicity obtained from Eq. 3.4.2 (see text for more details).

metallicity declining with redshift at a given stellar mass. In one of the latest works, Sanders et al. (2021) use  $T_e$ -consistent metallicity calibrations to derive O/H for star-forming galaxies out to  $z \sim 3.3$  and explore the MZRg evolution. They find similar slopes at all redshifts for  $\log(M_*/M_\odot) \lesssim 10$  and a nearly constant offset of about 0.2-0.3 dex towards lower metallicities compared to local galaxies at a given stellar mass. After comparing with chemical evolution models, the authors argue that this is driven by both higher gas fraction (leading to stronger dilution of ISM metals) and higher metal removal efficiency, e.g. by feedback.

On the other hand, studying the redshift evolution of the stellar MZR (hereafter MZR) has been historically more challenging due to the required high S/N continuum spectra. In the local universe, the first studies of the MZR by Gallazzi et al. (2005) and subsequent work via stacking of SDSS optical spectra for statistical samples of galaxies (Zahid et al., 2017), found stellar metallicity increasing over a large range of  $\log(M_*/M_\odot) \sim 9$ -11. At higher redshifts, however, the lack of high S/N optical spectra for statistical samples precludes similar analyses. Estimates of stellar metallicity are found, instead, from metallicity-sensitive indices or full spectral modeling of deep rest-frame UV spectra sampling young, massive stars (e.g. Sommariva et al., 2012; Cullen et al., 2019; Calabrò et al., 2021). Therefore, they provide  $Z_*$  values expected to be similar to those derived for the ISM out of which young stars have recently formed. Recent studies have shown an evolving MZR up to  $z \sim 3$ , decreas-

ing  $Z_*$  at fixed  $M_*$  by more than a factor of 2 from  $z = 0$  to  $z = 3.5$ , similarly to what is found for the MZRg (e.g. Cullen et al., 2019, 2020; Calabrò et al., 2021).

Here, we explore the position of normal galaxies with detected CIII] emission in the MZR at  $z \sim 2-4$ , while comparing with some of the above results from the literature. Using the results presented in previous sections, we probe the stellar mass-metallicity relation MZR<sub>s</sub> on the left panel in Fig. 3.4.1. In this figure, we use stacks A, B, and D computed by stellar mass. Our best linear fit to these points gives the following relation,

$$\log(Z_*/Z_\odot) = (0.33 \pm 0.10) \times [\log(M_*/M_\odot) - 10] - (0.54 \pm 0.05), \quad (3.4.1)$$

which is represented by the blue dashed line in Fig. 3.4.1. The MZR<sub>s</sub> of CIII] emitters at  $2 < z < 4$  have a nearly constant offset of  $\sim 0.4$  dex compared with the local MZR<sub>s</sub> from Zahid et al. (2017) over more than one decade in  $M_*$ . Compared to other MZR<sub>s</sub> at similar redshift from Cullen et al. (2019, 2020) and Calabrò et al. (2021), we find a relatively good agreement in slope and normalization thus suggesting that CIII] emitters are not different from their parent sample of star-forming galaxies in the MZR<sub>s</sub>. While stacks A and D are slightly shifted to high  $Z_*$ , stacks B appear more consistent with the MZR<sub>s</sub> derived in the above previous VANDELS studies. These small differences may arise from the different selection criteria. In particular, redshift selection used in these works only include galaxies at  $z > 3$ , while our stacks D include only galaxies at  $z < 2.9$  and stacks A include a mix of galaxies below and above  $z = 2.9$ . We also find that for a given stellar mass, the intense CIII] emitters tend to lie below the MZR<sub>s</sub>, while the faint emitters, tend to lie above the MZR<sub>s</sub> (see Fig. 3.4.1). On the other hand, the offset between Eq. 3.4.1 and the MZR<sub>s</sub> reported in Cullen et al. (2020) is explained in part due to the difference in the redshift range covered by the samples and differences in the assumptions leading to stellar mass derivations. In Cullen et al. (2020), stellar masses are derived from SED fitting assuming solar metallicity and models that do not account for nebular emission. These assumptions lead to an offset of around  $\sim 0.2$  dex towards higher stellar masses compared with our updated catalog.

If we assume that stellar and gas-phase metallicity are the same, our results are consistent with the MZRg derived from Troncoso et al. (2014) (at  $1-\sigma$ ) for the range of stellar mass covered by our stacks. However, this assumption is not necessarily true, especially at high- $z$ .

Sommariva et al. (2012) found a small difference ( $\sim 0.16$  dex) between  $Z_g$  and  $Z_*$ , but their conclusion was not robust given their large reported uncertainties. One might expect small differences because we are measuring stellar metallicity using UV absorption features driven by massive stars with short lifetimes and similar properties of the interstellar gas where they were formed. However, larger differences can be found for galaxies whose ISM has been enriched primarily by core-collapse supernovae with highly super-solar O/Fe, as discussed in other works (e.g., Steidel et al., 2016; Topping et al., 2020). Such conclusion has been recently reached in a work by Cullen et al. (2021) where it was found that a subset of galaxies in VANDELS at  $z \sim 3.4$  are  $\alpha$ -enhanced (i.e., their O/Fe ratios are more than two times solar) from a direct comparison of their stellar and gas metallicities.

Studies of the MZRg using exclusively the rest-UV spectrum has strong limitations due to the lack of hydrogen lines besides Ly $\alpha$ . While this line has been used in galaxies with extremely high EWs (Amorín et al., 2017), we avoid the use of Ly $\alpha$  in our VANDELS sample because it is generally affected by resonant scattering and absorption by the IGM. An alternative method to constrain gas-phase metallicity is using nebular HeII instead of Ly $\alpha$ . This possibility has been implemented, for instance, in HCM-UV (version 4) and in Byler et al. (2020) using a He2-O3C3 calibration. However,

HeII is generally weak in most stacks and it may include both nebular and stellar origin, which being difficult to disentangle is thus an additional source of error.

We estimate gas-phase metallicities for our stacks using the above two methods. When we compare them with the derived stellar metallicities we find a mean difference of  $\log Z_* - \log Z_g \sim 0.16$  dex for the stacks by stellar mass, FUV luminosity, and EW(CIII]). However, the dispersion is larger ( $\Delta(\log Z_* - \log Z_g) \sim 0.25$  dex) and since the uncertainties for the metallicities are also larger (up to  $\sim 0.4$  dex), the above comparison does not provide a robust assessment of the true difference between stellar and gas-phase metallicities, which are proxies of the Fe/H and O/H abundances, respectively.

For this reason, we follow an alternative approach to estimate gas-phase metallicities in our stacks. Following Cullen et al. (2021), we consider that

$$\log(Z_g/Z_\odot) = \log(Z_g/Z_*) + \log(Z_*/Z_\odot), \quad (3.4.2)$$

where  $\log(Z_g/Z_*) \sim [\text{O}/\text{Fe}]$  is a proxy of the  $\alpha$ -enhancement, which depends on stellar mass. Then, adopting the difference found by Cullen et al. (2021) for MZR and MZRg, we infer that  $[\text{O}/\text{Fe}] \sim 0.37$ - $0.40$  dex for the range of stellar masses of our sample. Thus, we use  $[\text{O}/\text{Fe}] \sim 0.38$ , the value corresponding to the mean stellar mass, to convert our  $Z_*$  into  $Z_g$  values. In the right panel of Fig. 3.4.1 we show the MZRg obtained following the above approach. Despite our C3 sample is a subsample of the one used by Cullen et al. (2021), the assumed  $[\text{O}/\text{Fe}]$  appears reasonable, as the C3 stacks shown in Fig. 3.4.1 follow a consistent trend with the results found by Cullen et al. (2021) using a different stacking procedure.

In order to obtain an independent value for gas metallicity, we also probed the Si3-O3C3 calibration presented by Byler et al. (2020). For our stacks, the values obtained with the assumed  $[\text{O}/\text{Fe}]$  are consistent within 0.15 dex with the gas-phase metallicities obtained using the Si3-O3C3 calibration. We note that the latter is found to have a median offset of 0.35 dex when compared to other well-known metallicity calibrations based on optical indices. Acknowledging these differences and the relatively good agreement between these two methods, we choose to use the re-scaled values with the mean  $[\text{O}/\text{Fe}]$  in the following sections. Clearly, follow up studies probing bright optical lines of CIII] emitters are necessary to provide more reliable gas-phase metallicity determinations.

On the right panel in Fig. 3.4.1, our best fit with the assumed mean  $[\text{O}/\text{Fe}]$  is fully consistent with the MZRg at  $z \sim 2.3$  from Steidel et al. (2014). Our results are also consistent with most data points in the MZRg estimates obtained at  $z \sim 3$  from Onodera et al. (2016) and Sanders et al. (2021), which are also included for comparison. Our results are thus consistent with the reported redshift evolution of the MZRg, illustrated here using a comparison with the local relation found by Andrews & Martini (2013). The larger differences are found with respect to the MZRg found by Troncoso et al. (2014), which could be explained by systematic differences in the excitation conditions and metallicities between the samples, as suggested in Sanders et al. (2021). Indeed, the Troncoso et al. (2014) sample is likely to be biased towards lower metallicities. But the agreement of our relation with the previous MZRg depends on the  $\alpha$ -enhanced assumed in our transformation between metallicity phases.

To better constrain the gas-phase metallicity of CIII] emitters at these redshifts, we need NIR follow-up observations to obtain the rest-optical spectra of these objects. In Chapter 4, this analysis based on individual galaxies will be presented. Finally, we use the gas-phase metallicity of the C3 sample to probe the Fundamental Metallicity Relation (FMR, Mannucci et al., 2010), which describes an invariant dependence with SFR of the MZRg metallicity of galaxies out to  $z \sim 2.5$ . Recent work

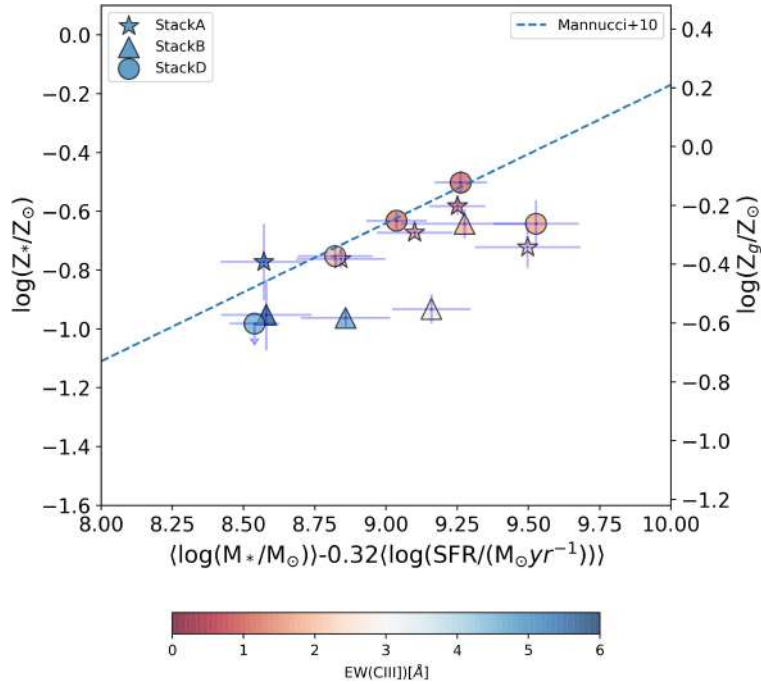


Figure 3.4.2: FMR with the stacks A, B, D by stellar mass, color-coded by  $EW(CIII)]$ . Blue dashed line is the relation shown in Mannucci et al. (2010). The right scale is the  $[O/H] \sim \log(Z_g/Z_\odot)$  assuming the  $\alpha$ -enhanced in Eq. 3.4.2.

by Sanders et al. (2021) suggest this lack of evolution extends out to  $z \sim 3.3$ . In our work, exploring this relation is highly dependent on the adopted  $Z_g$ . For example, if we assume that  $Z_* = Z_g$  our results would show an offset to low metallicity of  $\sim 0.5$  dex. However, assuming the average  $\alpha$ -enhancement derived by Cullen et al. (2021) and used in Fig. 3.4.1, we find a trend that appears in agreement with the slope of the FMR, as shown in Fig. 3.4.2. While two stacks in the B scheme (i.e. only galaxies with  $z \geq 2.9$ ), appear offset towards lower metallicity, stacks D (i.e. only galaxies with  $z < 2.9$ ) and stacks A (stars, representing all galaxies at  $2.4 \lesssim z \lesssim 3.9$ ) find a relatively good agreement with the slope of local FMR. Considering the typical large uncertainties involved both in the data measurements and metallicity derivation, especially inherent to the different spectral features and methodologies applied in this and previous works, this result is surprisingly robust. In agreement with recent results (Sanders et al., 2021), this favors the scenario where the FMR does not evolve significantly up to  $z \sim 3$ .

### 3.4.2 On the stellar metallicity - C/O relation at $z \sim 3$

The C/O ratio may provide us general trends in the evolutionary state of a galaxy and its ISM. In evolved, metal-enriched galaxies an increase of C/O with increasing metallicity has been observed (Garnett et al., 1995; Berg et al., 2016, 2019) and also reproduced by models (e.g. Henry et al., 2000; Mollá et al., 2015; Mattsson, 2010). This trend can be explained because carbon is primarily produced by the triple- $\alpha$  process in both massive and low- to intermediate-mass stars but, in massive stars, carbon arises almost exclusively from the production due to metallicity-dependent stellar winds, mass loss and ISM enrichment which are greater at higher metallicities (Henry et al., 2000). An evolutionary effect due to the delayed release of carbon (which is mostly produced by low- and

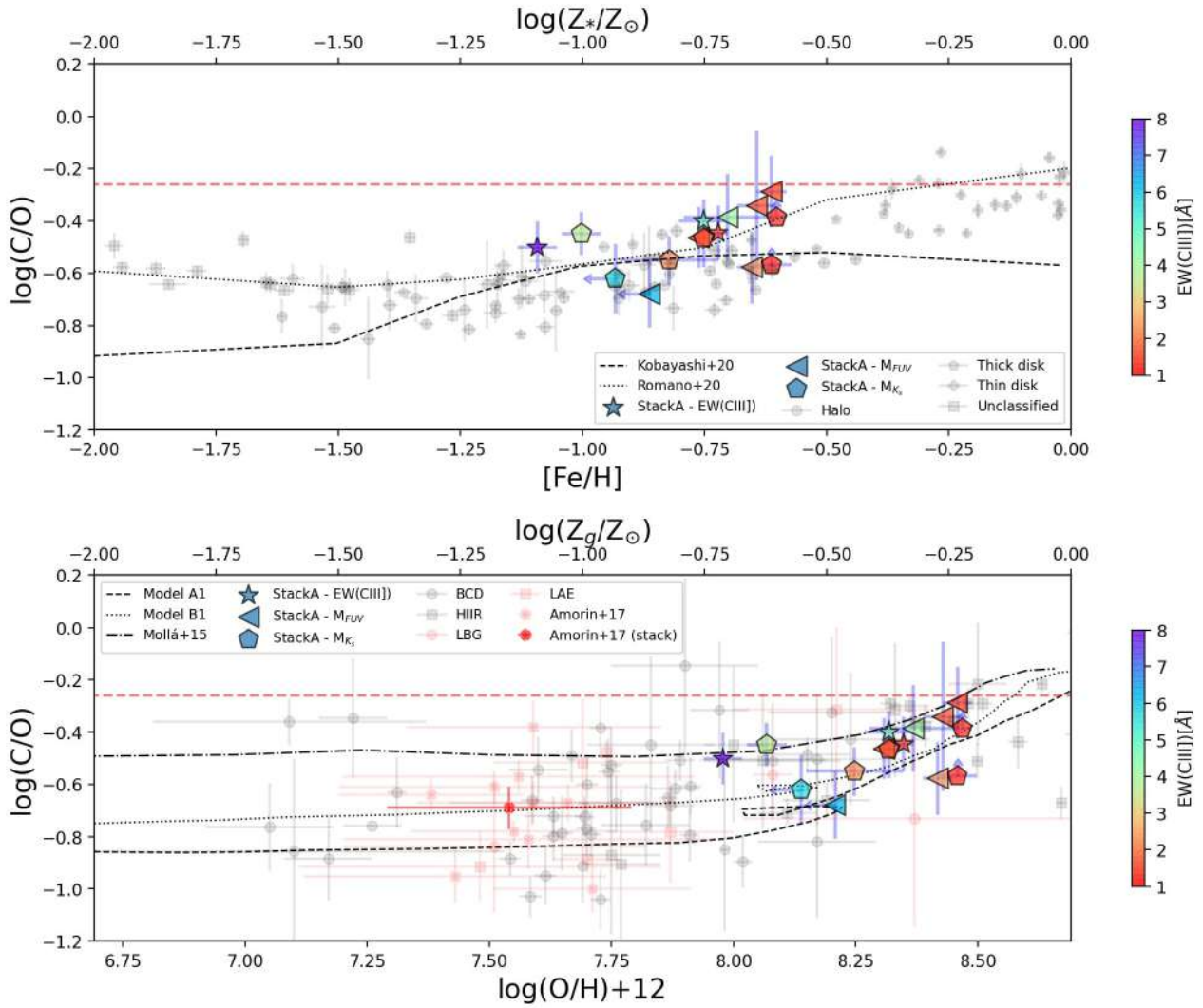


Figure 3.4.3: *Top panel:*  $C/O-Z_*$  relation. Black symbols are values of stars from the Galactic thin, thick disk, halo and unclassified from the literature (Amarsi et al., 2019). The dashed black line is the K20 model in Kobayashi et al. (2020) and the dotted line is the model MWG-11 in Romano et al. (2020). *Bottom panel:*  $C/O-Z_g$  relation. The red markers are high-redshift galaxies from literature and black markers are local galaxies and HII regions (see text for references). The multi-zone chemical evolution models from Mattsson (2010) are also shown by black lines. The black dotted-dashed line is the chemical model from Mollá et al. (2015). *In both panels:* The red dashed line is the  $C/O$  solar value. The stack A by  $EW(CIII)]$  and broadband luminosities are shown by markers according to legend and color-coded by  $EW(CIII)]$ .

intermediate-mass) relative to oxygen (which is produced almost exclusively by massive stars) in younger and less metal-rich systems is an alternative explanation for this trend (Garnett et al., 1995).

In this section, we discuss the position of the C3 sample in the  $Z_*$ - $C/O$  plane, which provide new insights into their chemical enrichment. On the top panel in Fig. 3.4.3, we present the  $Z_*$ - $C/O$  relation for our C3 sample in VANDELS along with the predictions from a chemical evolution model (model MWG-11 in Romano et al. (2020) and model K20 in Kobayashi et al. (2020)) and stellar metallicities  $[Fe/H]$  estimations of local Milky Way stars in the halo, thick and thin disk (Amarsi

et al., 2019). We show results from stack A, which include the entire C3 sample. Symbols are color-coded by EW(CIII]) and their marker depends on the parameter used for stacking, i.e stacks by EW(CIII]), FUV and  $K_s$  bands in stars, left-triangle and pentagon, respectively. Our results indicate that C/O increases with stellar metallicity for  $Z_\star \gtrsim 10\%$  solar, in agreement with the trends of chemical evolution models and of metal-rich stars in the Galactic thick disk. Our results show higher values than the ones predicted by Kobayashi et al. (2020) for a given stellar metallicity, but this also occurs with most of the thin disk stars. According to these authors, the latter can be partially explained by an under-prediction of carbon yields by AGB stars on the models. More generally, we note that our results are found in better agreement with the model prediction by Romano et al. (2020).

For the gas-phase metallicity, we present results on the bottom panel of Fig. 3.4.3. The stacks are the same on the top panel but re-scaled assuming Eq. 3.4.2. We include four different predictions from chemical evolution models by Mattsson (2010) and Mollá et al. (2015). We also include comparison samples from literature: LAEs (Bayliss et al., 2014; Christensen et al., 2012; Erb et al., 2010; James et al., 2014; Villar-Martín et al., 2004) and LGBs (de Barros et al., 2016; Vanzella et al., 2016; Steidel et al., 2016) at  $z \sim 2-4$ , and local analogs such as Blue Compact Dwarfs (BCD) (Garnett et al., 1995, 1997; Kobulnicky et al., 1997; Kobulnicky & Skillman, 1998; Izotov et al., 1999; Thuan et al., 1999; Berg et al., 2016; Senchyna et al., 2021) and HII regions (Garnett et al., 1995; Kurt et al., 1995; Garnett et al., 1999; Mattsson, 2010; Senchyna et al., 2021) at  $z \sim 0$ . We note that metallicities for these objects are derived from nebular lines. Our points in Fig. 3.4.3, instead, assume Eq. 3.4.2 with a fixed [O/Fe]. However, this assumption might not be accurate and significant (and probably different) levels of  $\alpha$ -enhancement in individual galaxies may generate systematic offsets between  $Z_\star$  and  $Z_g$  (Cullen et al., 2021). Such effect will tend to increase the dispersion of data in the x-axis. With these caveats in mind, the trends shown in Fig. 3.4.3 are yet useful to discuss the different levels of chemical enrichment traced by the C/O ratio, particularly for our C3 sample.

Despite the large scatter shown by observations, Fig. 3.4.3 shows a trend of increasing C/O with stellar metallicity for our VANDELS C3 sample. This trend is strongly driven by the low mass (low luminosity) stacks, which show lower C/O and metallicities. Particularly, the stack by EW(CIII]) with the highest EW(CIII]) (purple star in Fig. 3.4.3) has the lowest stellar metallicity and a lower C/O ratio, which suggests that this population with extreme EW(CIII]) have indeed a young stellar population still dominated by massive stars.

The comparison of the VANDELS C3 sample with the sample of galaxies at similar redshift (red symbols), shows that our stacks have higher metallicity (even assuming  $Z_\star = Z_g$ ) and higher C/O ratios than that of most CIII] emitters in the comparison sample. This suggests that, on average, we are probing galaxies that are chemically more evolved. Compared to the local sample, the C/O ratios of our VANDELS C3 sample are comparable to those of local HII regions at similar metallicity, for which the C/O abundances increase toward solar values due to a mix of young and aged stellar populations contributing to C production. Local BCDs, instead, show similar C/O but lower metallicities, i.e. compatible with our results if we assume a lower  $\alpha$ -enhancement.

Several mechanisms can affect the position of galaxies in Fig. 3.4.3. This includes variations in the star formation histories (i.e. shape, duration of bursts and star formation efficiency), gas fraction and inflow rates that may affect the gas metallicity and even potential changes in the initial mass function, may contribute to the scatter (e.g. Mattsson, 2010; Mollá et al., 2015; Berg et al., 2016; Vincenzo & Kobayashi, 2018; Kobayashi et al., 2020; Palla et al., 2020). High values of C/O at low metallicity could be due to the effects of a massive inflow of pristine gas, which may lower the gas

metallicity of an otherwise more chemically evolved system, without altering C/O (Nakajima et al., 2018b). This is another caveat to consider when there is not a direct measurement of the gas-phase metallicity.

In models, C/O is sensitive to the prescriptions for yields, the initial mass function, star formation efficiencies, inflow rates that are not fully understood that make difficult to interpret observations and may also produce variable levels of C/O at low metallicity, as suggested in Mattsson (2010) and Berg et al. (2016). Although models can reproduce some observations, they do not explain the large scatter observed and the precise values completely. Moreover, the large observational and methodological uncertainties involved makes the interpretation of the C/O abundances challenging.

In this work, we find that our results are consistent with the trend of increasing C/O seen in the models for the range of gas-phase metallicities probed by the stacks (around 20 to 60% solar), assuming a constant  $\alpha$ -enhancement. In particular, we compare our data with the multi-zone chemical evolution models from Mattsson (2010). Case A1 (black dashed line in Fig. 3.4.3) represents a case where the low and intermediate mass stars are producing most of the carbon, while case B1 (black dotted line in Fig. 3.4.3) represents a case where the carbon is to a large extent produced in high mass stars. Other models such as those in Mollá et al. (2015) (see also Berg et al., 2016), which predict higher values of  $\log(C/O)$  for a given O/H, find a good agreement especially for our stacks at higher EW(CIII]).

Based on a detailed comparison with models, Berg et al. (2019) discuss the sensitivity of the C/O ratio to both the detailed star formation history and supernova (SNe) feedback. In models, lower C/O values are found at lower star formation efficiencies and burst with longer duration. On the other hand, larger C/O ratios are more related with the presence of SNe feedback that ejects oxygen and reduces the effective yields. The rapid C/O enrichment found for the C3 sample could be thus related to a more bursty star formation history. Given that our C3 sample are mostly main-sequence galaxies, we speculate that a recent star formation history with multiple bursts could have enhanced the C/O to their observed levels.

More detailed observations are needed for both local and high redshift galaxies to fully understand the C/O enrichment history through cosmic time. The HST CLASSY survey (Berg et al., 2022), which has obtained high S/N UV nebular spectra for a representative sample of local galaxies, will certainly contribute to clarify this scenario in the local universe and future observations with JWST will enable more detailed studies of the C/O evolution of star-forming galaxies at intermediate and high redshift.

### 3.4.3 Caveats related with stacking methods

In this section, we discuss possible effects of stacking and the binning choice in the relations shown in Fig. 3.3.1. For this aim, in Fig. 3.4.4 we compare the EW(CIII]) measured on the stacked spectra with the median EW(CIII]) of the galaxies in each bin as measured in individual spectra. We do this comparison with stacks A, which are obtained after binning by stellar mass and FUV luminosity. The error bars for the median EWs represent the standard deviation in the bin. We notice that the trends are consistent between both methods, with some differences in the actual value of EW(CIII]), but consistent within the large errors. Therefore, measurements of the stacks are representative of the median properties of the galaxies in each bin and we do not expect strong biases due to bin size or the

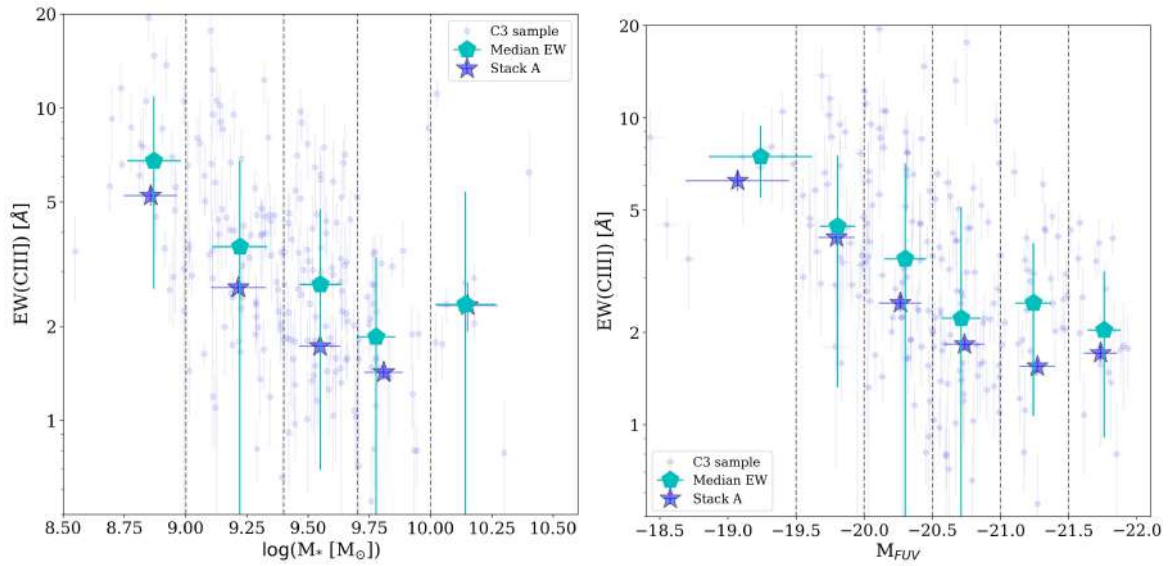


Figure 3.4.4: Relation between  $\text{EW}(\text{CIII])}$  and stellar mass (*left panel*) and FUV (*right panel*) luminosity, similar as shown in Fig. 3.3.1 for stack A (blue stars) and C3 sample (small blue circles). The cyan pentagons are the median values for the individual galaxies in the bin and their errorbars correspond to the standard deviation in the bin (boundaries marked by vertical dashed line).

particular choice of limits.

On the other hand, we note that the parameter used for stacking may result in different ranges in stellar metallicity and C/O (e.g. Fig. 3.3.5, 3.3.6, 3.3.7, and 3.3.9). This is the result of the distribution of the galaxies in the bins depending on their physical properties. As shown in Fig. 3.2.3, the relations between stellar mass and luminosities show scatter, and then the same galaxies are not in the corresponding same bin for each parameter. However, the trends are still found if we use only one set of stacking. For instance, in Fig. 3.4.5 we show by the cyan dashed line the relations found if we only considered the stacks by luminosity. We note the the cyan lines follow the same trend that the black lines, which are the relations reported in the Chapter including the other set of stacks in the legends. They also are within the  $3\text{-}\sigma$  uncertainty of the reported relations. In the  $\text{EW}(\text{Ly}\alpha)\text{-}Z_*$  relation (top-right panel in Fig. 3.4.5), we note that the dynamical range in  $\text{EW}(\text{Ly}\alpha)$  is shorter compared with the entire set of stacks, because only upper limits in stellar metallicity are determined due to the lower S/N of the stacks with higher EWs in this set of stacks. The inclusion of additional sets of stacks binned by different parameters allows the exploration of a larger dynamical space, generally at the cost of a larger variance, but without affecting the trends found in the relations.

### 3.4.4 Analysis of non-detected CIII] emitters in the parent sample

The results presented in this Chapter are based on the selection of a sample of galaxies with the CIII] line detected with  $S/N > 3$ . This S/N threshold is motivated by the need of having reliable systematic redshifts, which are obtained fitting this nebular line –the most intense UV metal line in the parent sample. In this section, we study whether this selection criterion has any effect on our results. We analyze the 521 star-forming galaxies from the VANDELS parent sample with non-detections in the CIII] line, i.e. those objects excluded from our C3 sample. We perform the same stacking

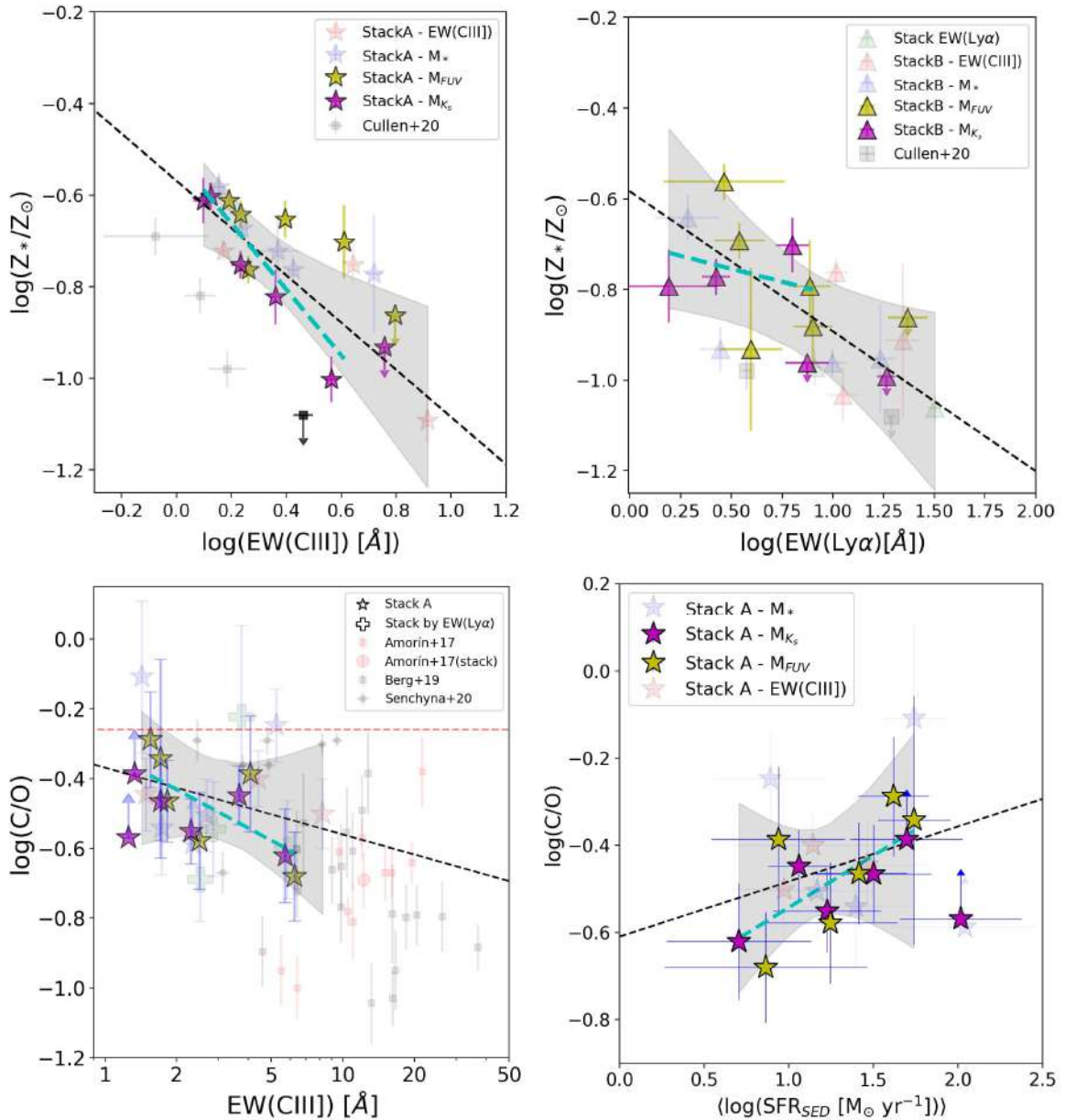


Figure 3.4.5: Same as in Fig. 3.3.5, 3.3.6, 3.3.7, and 3.3.9. The cyan dashed line shows the best fit including only the stacks A binned by luminosity. The stacks excluded in the fit are shown using transparent symbols.

analysis done for the C3 sample, following schemes A and B in bins of FUV luminosity and using the same bin distribution and methodology explained in Section 3.2. Because of the lack of accurate systemic redshifts for this sample, stacks are performed using the spectroscopic redshift reported by the VANDELS DR3 catalog, which is mostly based on template fitting of ISM absorption features by the tool PANDORA/EZ (McLure et al., 2018). We find that the resulting stacks show similar features compared to the stacks in the C3 sample, showing detections of multiple ISM absorption lines and nebular emission lines. Overall, the effect of using spectroscopic instead of systemic redshifts in the stacking is to broaden emission line profiles in the stacks due to small velocity shifts. As a result, the S/N ratio of the detected lines tends to be lower and their line fluxes are more uncertain than that of the C3 sample, despite the number of galaxies averaged in each stack being generally higher.

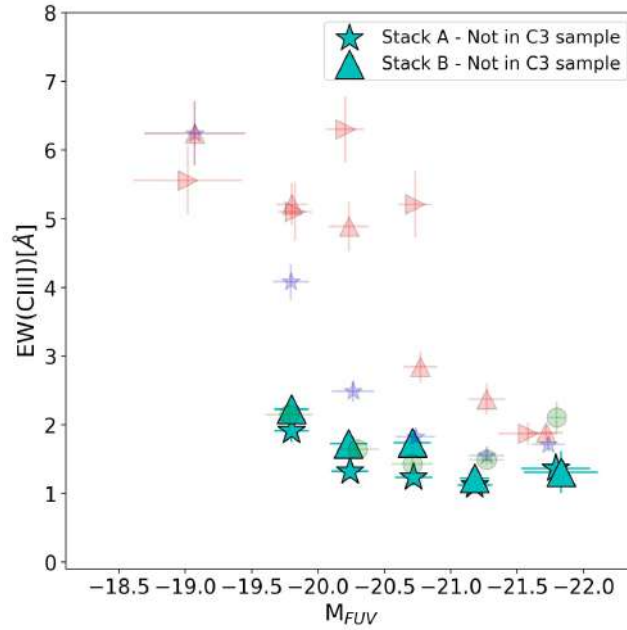


Figure 3.4.6:  $M_{FUV}$ -EW(CIII]) relation for the stacks by FUV luminosity with the non-detected CIII] sample (in cyan symbols). Faint symbols are the same as in Fig. 3.3.1.

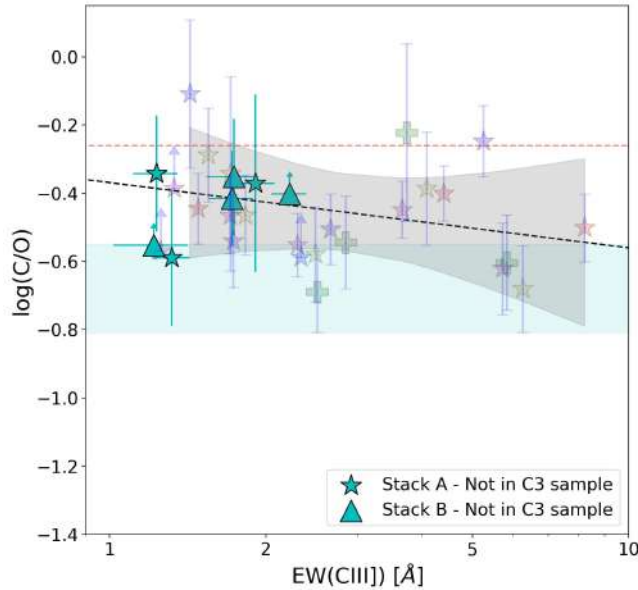


Figure 3.4.7: EW(CIII])-C/O relation for the stacks by FUV luminosity with the non-detected CIII] sample (in cyan symbols). Faint symbols, shaded regions and dashed lines are the same as in Fig. 3.3.7

In all the stacks but the one at lower luminosity, we detect CIII] with a  $S/N > 3$ . However, their fluxes are fainter than their counterparts in the C3 sample. In Fig. 3.4.6 we present the resulting EW(CIII]) as a function of the mean FUV luminosity for the stacks A and B with detected CIII]. Their trend is in good agreement with the same relations found using the C3 sample, showing a very mild increase of EW(CIII]) from  $\sim 1\text{\AA}$  to  $\sim 2\text{\AA}$  towards lower FUV luminosity. This suggest that including these galaxies without individual detection of CIII] in the stacks for the C3 sample will not change the resulting EWs and their relations with luminosity. Similar conclusion is found when

comparing line ratios of UV metal lines. Although not all the stacks in this test have good detections ( $S/N > 3$ ) in all the relevant emission lines, the position of their line ratios in the diagnostic diagrams presented in Fig. 3.3.2 and 3.3.3 are consistent with those of the faintest CIII] emitters, i.e. fully consistent with pure stellar photoionization.

Finally, we also test the possible effects in the C/O abundances. Following the same methods described in Section 3.3.6 for the C3 sample, we estimate C/O in the non-C3 stacks where we have at least  $S/N \geq 2$  detections of OIII]. We find consistent C/O values with those of the C3 sample, with  $\log(C/O)$  ranging from  $-0.6$  to  $-0.34$  (i.e. 45% to 80% solar, respectively). These values show good agreement with the relation between C/O and  $EW(CIII])$  found in Eq. 3.3.5 for the C3 sample, as illustrated in Fig. 3.4.7. Again, this result suggests that the non-detected CIII] emitters in the parent sample that were excluded from the stacking analysis of the C3 sample include intrinsically faint CIII] emitters, which are well represented by the results found for the C3 sample throughout this Chapter. We can therefore conclude that CIII] emission should be a common feature in UV faint galaxies at  $z \sim 3$ . This result is relevant for reionization studies because the number of UV faint galaxies increase significantly at higher redshift (e.g. Bouwens et al., 2016; Yue et al., 2018).

## 3.5 Conclusions

We study a large representative sample of 217 galaxies with CIII] detection at  $2 < z < 4$  covering a range of  $\sim 2$  dex in stellar mass. These CIII] emitters have a broad range of UV luminosities, thus allowing a stacking analysis to characterize their mean physical properties. We consider stacking by different bins of stellar mass, rest-frame FUV and  $K_S$  luminosities, and rest-frame  $EW(CIII])$  and  $EW(Ly\alpha)$ . We derive stellar metallicity and the C/O abundance from stack spectra and discuss several relations found between these parameters. We summarize our conclusions as follows:

- i) Reliable ( $S/N > 3$ ) CIII] emitters represent  $\sim 30\%$  of the VANDELS parent sample at  $z \sim 2-4$ . They show  $EW(CIII])$  between  $0.3$  and  $20\text{\AA}$  with a mean value of  $\sim 4\text{\AA}$ . However, stacked spectra of galaxies with marginal or non detection of CIII] ( $S/N < 3$ ) in individual spectra show weak ( $EW \lesssim 2\text{\AA}$ ) CIII] emission, suggesting this line is common in normal star-forming galaxies at  $z \sim 3$ . On the other hand, extreme emitters ( $EW(CIII]) \gtrsim 8\text{\AA}$ ) are exceedingly rare ( $\sim 3\%$ ) in VANDELS, which is expected as the C3 sample is drawn from a parent sample of main sequence galaxies.
- ii) Stacking reveals that faint UV nebular lines of OIII], SiIII, CIV and HeII, and fine structure emission lines of SiII are ubiquitous in CIII] emitters. We find that the strength of the nebular lines depends on the stellar mass and luminosity. Overall, less massive (and fainter in any band) stacks show more intense  $Ly\alpha$ , CIV, HeII, OIII] and CIII] than more massive (and brighter in any band), which tend to have fainter UV emission lines.
- iii) According to UV diagnostic diagrams, nebular lines in VANDELS CIII] emitters are powered by stellar photoionization, suggesting no other ionization source than massive stars. These results add new constraints to models on the flux ratios and EWs of nebular emission lines in main sequence SF regions for the faint CIII] regime at  $z \sim 2 - 4$ .

- iv) The  $\text{EW}(\text{Ly}\alpha)$  and  $\text{EW}(\text{CIII])}$  appear correlated in our C3 sample but a large scatter is found for individual galaxies. Stacks with larger  $\text{EW}(\text{CIII])}$  show larger  $\text{EW}(\text{Ly}\alpha)$ , but not all CIII] emitters are  $\text{Ly}\alpha$  emitters.
- v) Galaxies with higher  $\text{EW}(\text{CIII])}$  show lower stellar metallicities. This result suggests that extremely low metallicities ( $<10\%$  solar) should be expected for the most extreme galaxies in terms of their  $\text{EW}(\text{CIII])}$ . Our results (Eq. 3.3.3) show that galaxies with stellar metallicity  $Z_{\star} < 0.1Z_{\odot}$  are typically strong CIII] emitters ( $\text{EW}(\text{CIII])} > 7\text{\AA}$ ).
- vi) The stellar metallicities of CIII] emitters are not significantly different from that of the parent sample, increasing from  $\sim 10\%$  to  $\sim 40\%$  solar for stellar masses  $\log(M_{\star}/M_{\odot}) \sim 9-10.5$ . The stellar mass-metallicity relation of the CIII] emitters is consistent with previous works showing strong evolution from  $z = 0$  to  $z \sim 3$ , both using stellar (Fe/H) and nebular (O/H) metallicities inferred from the UV spectra and assuming an average  $[\text{Fe}/\text{O}] = 0.38$ , recently found for a subsample of VANDELs galaxies at  $z \sim 3$  (Cullen et al., 2021).
- vii) We find the C/O abundances of CIII] emitters ranging 35%-150% solar, with a noticeable increase with FUV luminosity, and a smooth decrease with CIII] EWs. Fainter FUV galaxies have lower C/O, higher  $\text{EW}(\text{CIII])}$ , and lower  $Z_{\star}$ , which suggest a UV spectrum dominated by massive stars and a bright nebular component which is still chemically unevolved.
- viii) We discuss for the first time the C/O-Fe/H and the C/O-O/H relations for star-forming galaxies at  $z \sim 3$ . They show stellar and nebular abundances consistent with the trends observed in Milky Way halo and thick disc stars and local HII galaxies, respectively. We find a good agreement with modern chemical evolution models, which suggest that CIII] emitters at  $z \sim 3$  are experiencing an active phase of chemical enrichment.

Our results provide new insight into the nature of UV line emitters at  $z \sim 3$ , paving the way for future studies at higher- $z$  using the JWST.

# Ionized kinematics of low-mass star-forming galaxies at $z \sim 3$ \*

In this Chapter, we present our study of the impact of stellar feedback on the chemical abundances of the ISM in a sample of SFGs with strong emission lines at  $z \sim 3$ . We selected 35 low-mass SFGs ( $7.9 < \log(M_*/M_\odot) < 10.3$ ) from deep spectroscopic surveys based on their CIII] $\lambda$ 1908 emission. We used new follow-up NIR observations to examine their rest-optical emission lines and identify ionized outflow signatures through broad emission line wings detected after Gaussian modeling of [OIII] $\lambda\lambda$ 4959,5007 profiles. We characterized the galaxies' gas-phase metallicity and C/O abundance using a Te-based method via the OIII] $\lambda$ 1666/[OIII] $\lambda$ 5007 ratio and photoionization models.

This Chapter is organized as follows. In Sec. 4.2 we present the sample selection and the optical and NIR spectroscopy used in this work. In Sec. 4.3 we present the physical properties of the sample and the narrow+broader Gaussian modeling of the [OIII] $\lambda\lambda$ 4959,5007 profiles. Then, we present the results of our study in Sec. 4.4 describing the main source of ionization of our sample, their chemical abundances (basically, gas phase metallicity (O/H) and C/O abundance) and the properties of ionized gas kinematics based on the outflow component. Then, we present the discussion of our results in Sec. 4.5 based on how outflows and SFHs may affect the chemical properties of their host galaxy. Finally, in Sec. 4.6, we present our conclusions.

## 4.1 Context

Understanding the last phase transition of the Universe, known as the EoR, is one of the longstanding goals of extragalactic astronomy. The massive stars residing in the high- $z$  SFGs are suspected to be the dominant ionizing agents that drive reionization (e.g., Robertson et al., 2015; Finkelstein et al., 2019). However, some studies suggest that low luminosity AGN may play a significant role in reionization (e.g., Madau & Haardt, 2015; Dayal et al., 2020). From recent high-resolution cosmological simulations of Lyman continuum (LyC,  $\lambda < 912\text{\AA}$ ) emitting sources in the EoR,  $z > 5$  simulated galaxies

---

\*Based on Llerena et al. (2023) “Ionized gas kinematics and chemical abundances in low-mass SFGs at  $z \sim 3$ ”, accepted for publication in *Astronomy & Astrophysics*.

are studied with a detailed treatment of the multiphase ISM and stellar-feedback. For example, with the Feedback in Realistic Environments (FIRE: Hopkins et al., 2018) project, it has been found that a majority of LyC escape comes from the very young ( $< 10$  Myr), kpc-scale star-forming regions of a galaxy, with negligible contribution from an older ( $> 10$  Myr) stellar population. These ISM structures clear out the neutral gas column to allow the escape of ionizing photons at very low escape fractions ( $f_{\text{esc}}$ ) that can reach 10–20% only for a small amount of time since the ionizing photon production from massive stars begins to decline after 3 Myr (e.g., Ma et al., 2015, 2020). At the same time, most of the ionizing photons are consumed by surrounding neutral gas clouds (e.g., Ma et al., 2015; Kakiichi & Gronke, 2021). Also, the reionization phase is estimated to be a fast epoch where the Universe goes from 90% neutral at  $z \sim 8.22$  to 10% neutral at  $z \sim 6.25$  in  $\sim 300$  Myr by massive starburst galaxies (Naidu et al., 2020). Understanding the mechanisms that facilitate the escape remains crucial.

On the other hand, deep rest-frame UV spectra ( $\lambda \sim 1200 - 2000 \text{ \AA}$ ) of several high- $z$  galaxies ( $z \sim 5 - 7$ ; e.g., Stark et al., 2015; Mainali et al., 2018; Hutchison et al., 2019; Castellano et al., 2022; Tang et al., 2023) reveal prominent high-ionization nebular emission lines, such as He II  $\lambda 1640$ , O III]  $\lambda \lambda 1661, 66$ , C III]  $\lambda \lambda 1907, 09$  (C III] hereafter) and C IV  $\lambda \lambda 1548, 51$  (C IV hereafter). To unveil their nature, the rest-frame UV is crucial, and analogs to these reionization sources at lower redshifts are key. The rest-UV spectra can foster our understanding of SFGs in terms of the stellar populations hosting massive stars and their impact on ISM physical conditions, chemical evolution, feedback processes, and reionization. This is important since JWST instruments such as NIRSpec (Jakobsen et al., 2022) will cover blueward of  $\sim 4500 \text{ \AA}$  only in objects  $z < 10$ . As such, understanding the ISM properties from UV spectra will be essential for characterizing and interpreting the spectroscopic observations of high- $z$  systems. Large and deep surveys such as the LBG survey of  $z \sim 3$  (Steidel et al., 2003), VUDS (Le Fèvre et al., 2015; Tasca et al., 2017), MUSE Hubble Ultra Deep Survey (Bacon et al., 2017), and VANDELS (McLure et al., 2018; Pentericci et al., 2018a; Garilli et al., 2021), have targeted SFGs at mainly  $z \sim 2 - 4$  to study the physical properties of SFGs with intense rest-UV emission lines. From an observational point of view at  $z \sim 3$ , the escape fraction depends on galaxy properties such as EW of Ly $\alpha$ , stellar mass, and color excess by dust extinction (e.g., Steidel et al., 2018; Saxena et al., 2022a; Begley et al., 2022; Pahl et al., 2022). Moreover, the profile shape of Ly $\alpha$  is an essential predictor of the LyC escape fraction as this gives information about the covering fraction of neutral gas at the systemic velocity (Izotov et al., 2020; Flury et al., 2022b). Such indirect probes are essential since ionizing fluxes cannot be measured at  $z > 6$  due to the large opacity of the IGM (Inoue et al., 2014) and the measurement of the escape fraction of ionizing photons will heavily rely on indirect probes at high redshift (e.g., Xu et al., 2022a; Naidu et al., 2022) or work on analogs at lower redshift (e.g., Schaerer et al., 2016; Flury et al., 2022a).

One of the main suspects in aiding the escape of ionizing photons is galaxy scale outflows (e.g., Chisholm et al., 2017; Kim et al., 2020; Hogarth et al., 2020, and references therein). These outflows are expected to remove surrounding neutral gas, thus clearing a pathway for ionizing photons to efficiently escape. However, it is often challenging to reconcile the timescales of such strong galactic outflows with the timescale of production and escape of ionizing photons in a galaxy. Outflowing gas of SFGs at  $z \sim 2$  has been reported both from optical emission lines such as [OIII]  $\lambda 5007$  (hereafter [OIII]) or H $\alpha$  (e.g., Förster Schreiber et al., 2019; Übler et al., 2022) as well as UV absorption lines (e.g., Steidel et al., 2010; Jones et al., 2018; Calabrò et al., 2022). Optical rest-frame emission lines are able to trace denser outflowing gas, providing an instantaneous snapshot of the ongoing ejective feedback; therefore, in principle, they are less contaminated by tenuous gas around galaxies (Concas et al., 2022). These emission lines are typically modeled with one narrow and one broad Gaussian

component. The latter is considered the outflow component. The properties of the outflows are probed to depend on the properties of the host galaxy. For example, it is observed that the velocity of outflows increases as a function of SFR and galaxy stellar mass ( $M_*$ ) (e.g., [Weiner et al., 2009](#)), which is also seen in simulations (e.g., [Muratov et al., 2015](#)). In [Freeman et al. \(2019\)](#), with the MOSFIRE Deep Evolution Field survey (MOSDEF, [Kriek et al., 2015](#)), they found that the broad-to-narrow flux ratio increases with stellar mass. Understanding how the presence of highly ionized gas outflows affects the properties of host galaxies gives insights into how the stellar feedback from young stars plays a vital role in the escape of ionizing photons.

Finally, analytic models explain that scaling relations such as the MZR ([Tremonti et al., 2004](#)) and the FMR ([Mannucci et al., 2010](#); [Curti et al., 2020](#); [Sanders et al., 2021](#)) arise due to an interplay between star formation, the infall of metal-poor IGM gas and the ejection of metal-rich ISM gas. The FMR is a signature of the smooth, long-lasting equilibrium between gas flows and secular evolution (e.g., [Bouché et al., 2010](#); [Lilly et al., 2013](#)). Based on the FMR, less massive galaxies ( $M_* < 10^{11} M_\odot$ ) with smaller SFR produce less heavy elements that are more efficiently ejected due to their shallow potential wells; as a result, for a given  $M_*$ , the gas metallicity decreases with SFR ([Dayal et al., 2013](#)). On the other hand, the lack of any correlation between the ratio of a secondary element, like C or N, to a primary one, like O, with SFR (e.g., [Pérez-Montero & Contini, 2009](#)) could indicate how stellar winds eject metals, leaving their proportions unaffected in the remaining gas. The role of outflows in shaping the chemical properties of galaxies is another critical feature to understand in galaxy evolution.

## 4.2 Data and sample selection

Our strategy is based on the combined analysis of the rest-UV+optical spectra of a diverse sample of SFGs at  $z = 2 - 4$ . Our main selection criteria (the detection of CIII]) depends on the rest-UV emission lines that are obtained by optical spectrographs. Our parent sample is a combination of two large surveys carried out with the VIMOS spectrograph ([Le Fèvre et al., 2003](#)): the VUDS ([Le Fèvre et al., 2015](#); [Tasca et al., 2017](#)) and the VANDELS ([McLure et al., 2018](#); [Pentericci et al., 2018a](#)) surveys. From this parent sample, we select galaxies with NIR spectroscopy targeting their rest-optical emission lines.

Our final sample contains 17 VANDELS galaxies (hereafter, C3-VANDELS) and 18 VUDS galaxies (hereafter, C3-VUDS). We describe the selection of the final sample and the NIR observations in the next sections.

### 4.2.1 Sample selection from rest-frame UV spectroscopy

#### 4.2.1.1 VANDELS parent sample

We use spectroscopic data from VANDELS ([McLure et al., 2018](#); [Pentericci et al., 2018a](#)) – a deep VIMOS survey of the CANDELS fields – which is a completed ESO public spectroscopic survey carried out using the VLT. VANDELS covers two well-studied extragalactic fields, the UDS and the

CDFS. See more details in Sec. 2.1.2. Briefly, the final VANDELS data release, DR4, contains spectra of  $\sim 2100$  galaxies in the redshift range  $1.0 < z < 7.0$ , with on-source integration times ranging from 20 to 80 hours, where  $> 70\%$  of the targets have at least 40 hours of integration time (Garilli et al., 2021). The spectral resolution of VANDELS spectra is  $R \sim 600$  in the wavelength range  $480 < \lambda_{obs} < 980\text{nm}$ . At the redshift range  $2 < z < 4$  of our interest due to CIII] selection, 887 galaxies were observed with reliable redshift. From them, we select a parent sample of 280 SFGs that show  $S/N > 3$  in CIII] with  $EW(\text{CIII])} > 0$ . Most of them (74%) show  $EWs < 5\text{\AA}$  while only  $\sim 5\%$  shows  $EWs > 10\text{\AA}$ . To select this parent sample, we follow the methodology presented in Llerena et al. (2022) for the VANDELS DR3.

#### 4.2.1.2 VUDS parent sample

We also use observations from the VUDS survey (Le Fèvre et al., 2015; Tasca et al., 2017), a massive 640-hour ( $\sim 80$  nights) spectroscopic campaign reaching extreme depths ( $i' < 25$  mag) over three well-studied extragalactic fields: COSMOS, ECFDS, and VVDS-02h. Spectroscopic observations consisted of approximately 50400s of integration across the wavelength range  $365 < \lambda_{obs} < 935\text{nm}$  at a spectral resolution of  $R = 230$ . More details of the survey in Sec. 2.1.1. At  $2 < z < 3.8$ , where the instrumental setup allows following the CIII] line reliably, 3899 SFGs were observed. Our parent sample is described in Le Fèvre et al. (2019) and is selected with  $2 < z < 3.8$  and  $S/N > 3$  in CIII]. They selected 1763 SFGs with  $EW(\text{CIII])} > 0$ , most of them (75%) show  $EWs < 5\text{\AA}$  while only  $\sim 8\%$  shows  $EWs > 10\text{\AA}$ .

## 4.2.2 Rest-frame optical spectroscopy

We describe the NIR spectroscopy available which was used to select the final sample to be analyzed in this Chapter. In summary, the rest-optical spectra for VANDELS targets are obtained from the NIR-VANDELS survey (Cullen et al., 2021) using Keck/MOSFIRE (McLean et al., 2012). While for the VUDS targets, we obtained the rest-optical spectra from different instruments. First, from the public MOSDEF survey (Kriek et al., 2015) using Keck/MOSFIRE. We also considered NIR spectroscopy observations with X-Shooter (Vernet et al., 2011) for a subsample selected from Amorín et al. (2017). Finally, we also considered NIR spectroscopy observations with Magellan/FIRE (Simcoe et al., 2010). More details on the selection are presented in the following subsections.

### 4.2.2.1 MOSFIRE spectroscopy

From the parent sample of CIII] emitters selected in the VANDELS survey with reliable spectroscopic redshift, we cross-match with the catalog of sources in the NIRVANDELS survey (Cullen et al., 2021). This is a Keck/MOSFIRE VANDELS follow-up survey for 35 sources at  $2.95 \leq z \leq 3.8$  and 10 sources at  $2.09 \leq z \leq 2.61$ . The details of the observations and the data reduction are described in Cullen et al. (2021). The slitwidth was  $0.7''$ , yielding a spectral resolution of  $\sim 3650$  in H and  $\sim 3600$  in K band, respectively. 19 galaxies in NIRVANDELS show  $S/N > 3$  in CIII]. Two objects were discarded because they do not show optical emission lines, particularly [OIII]. Our final C3-VANDELS sample contains 17 galaxies in both CDFS and UDS fields.

Table 4.2.1: Coordinates and spectroscopic redshift of the final sample.

ID	RA <sup>(a)</sup> deg	DEC <sup>(a)</sup> deg	$z_{\text{CIII]}}$ <sup>(b)</sup>	Note <sup>(c)</sup>
C3-VANDELS sample				
UDS020394	34.54	-5.16	3.308	1
CDFS020954	53.02	-27.73	3.496	1
CDFS023527	53.08	-27.71	3.110	1
UDS021601	34.55	-5.16	3.344	1
CDFS022563	53.04	-27.72	3.003	1
UDS022487	34.48	-5.15	3.064	1
CDFS015347	53.06	-27.78	3.516	1
CDFS019276	53.02	-27.75	3.400	1
UDS020928	34.51	-5.16	3.137	1
CDFS019946	53.06	-27.74	2.437	1
UDS020437	34.52	-5.16	3.207	1
CDFS018182	53.01	-27.76	2.317	1
CDFS018882	53.03	-27.75	3.403	1
CDFS025828	53.05	-27.69	3.350	1
CDFS022799	53.06	-27.72	2.544	1
UDS021398	34.53	-5.16	2.492	1
UDS015872	34.52	-5.19	2.301	1
C3-VUDS sample <sup>(d)</sup>				
5100998761	150.16	2.26	2.453	3
5101444192	150.16	2.61	3.420	3
510994594	150.07	2.28	3.297	1
5101421970	150.34	2.61	2.470	3
510838687	149.86	1.98	2.557	2
5100556178	150.16	1.89	2.537	2
511229433	150.11	2.41	3.256	1
511245444	150.15	2.30	3.038	1
530048433	53.10	-27.76	2.312	1
510583858	150.05	1.86	2.417	3
511451385	150.15	2.57	2.370	2
511025693	150.06	2.25	3.256	1
5100997733	150.14	2.27	3.003	1
511228062	150.07	2.41	3.354	1
5101001604	150.18	2.24	3.157	1
510996058	150.11	2.28	2.493	1
511001501	150.12	2.24	2.227	1
530053714	53.04	-27.73	2.436	1

<sup>(a)</sup> Right Ascension and Declination.

<sup>(b)</sup> Spectroscopic redshift based on CIII].

<sup>(c)</sup> NIR instrument used as: (1)Keck/MOSFIRE, (2)Magellan/FIRE, (3)VLT/X-Shooter

<sup>(d)</sup> The ID starts with 51 (53) for targets in the COSMOS (ECDFS) field.

To build our sample of VUDS galaxies, we use the publicly available MOSDEF survey (Kriek et al., 2015) which is also a Keck/MOSFIRE survey that comprises NIR spectra of  $\sim 1500$  K-band selected galaxies targeted to lie within three distinct redshift intervals  $1.37 \leq z \leq 1.70$ ,  $2.09 \leq z \leq 2.61$  and  $2.95 \leq z \leq 3.80$ . The details of the observations and the data reduction are described in Kriek et al. (2015). The  $0.7''$ -width slit results in a spectral resolution of  $R = 3000$  for J band. For H and K bands, the resolution is the same as in the NIRVANDELS survey. The MOSDEF survey covers well-studied HST extragalactic legacy fields by the CANDELS and 3D-HST surveys: AEGIS, COSMOS, GOODS-N, GOODS-S, and UDS. We crossmatch the MOSDEF and our VUDS parent sample catalogs to increase the number of galaxies. We prioritized galaxies with  $S/N_{\text{CIII]} > 3$  and

Table 4.2.2: Main physical properties of the sample based on SED fitting.

ID	$\log(M_*)$ $M_\odot$	$\log(\text{SFR})$ $M_\odot \text{ yr}^{-1}$	$E(B-V)_{\text{SED}}$ mag	$E(B-V)_g^{(a)}$ mag
C3-VANDELS sample				
UDS020394	$8.92 \pm 0.17$	$0.84 \pm 0.10$	$0.08 \pm 0.02$	...
CDFS020954	$8.82 \pm 0.08$	$1.72 \pm 0.03$	$0.21 \pm 0.01$	...
CDFS023527	$9.54 \pm 0.11$	$1.53 \pm 0.09$	$0.14 \pm 0.02$	...
UDS021601	$9.34 \pm 0.10$	$1.01 \pm 0.10$	$0.11 \pm 0.02$	...
CDFS022563	$8.75 \pm 0.14$	$1.19 \pm 0.07$	$0.14 \pm 0.01$	...
UDS022487	$9.09 \pm 0.11$	$1.34 \pm 0.15$	$0.14 \pm 0.03$	...
CDFS015347	$9.11 \pm 0.15$	$1.18 \pm 0.08$	$0.12 \pm 0.01$	...
CDFS019276	$10.26 \pm 0.07$	$2.27 \pm 0.07$	$0.25 \pm 0.01$	...
UDS020928	$9.48 \pm 0.09$	$1.78 \pm 0.05$	$0.24 \pm 0.01$	...
CDFS019946	$8.96 \pm 0.08$	$1.21 \pm 0.06$	$0.14 \pm 0.01$	$0.53 \pm 0.31$
UDS020437	$9.61 \pm 0.09$	$1.42 \pm 0.11$	$0.11 \pm 0.02$	...
CDFS018182	$9.33 \pm 0.09$	$1.34 \pm 0.07$	$0.08 \pm 0.01$	$0.18 \pm 0.06$
CDFS018882	$9.81 \pm 0.08$	$1.80 \pm 0.08$	$0.24 \pm 0.01$	...
CDFS025828	$9.57 \pm 0.12$	$2.03 \pm 0.05$	$0.17 \pm 0.01$	...
CDFS022799	$9.14 \pm 0.05$	$1.86 \pm 0.04$	$0.14 \pm 0.01$	$0.07 \pm 0.05$
UDS021398	$9.25 \pm 0.07$	$1.41 \pm 0.05$	$0.12 \pm 0.01$	$0.49 \pm 0.35$
UDS015872	$9.71 \pm 0.04$	$1.66 \pm 0.04$	$0.23 \pm 0.01$	$0.30 \pm 0.11$
C3-VUDS sample				
5100998761	$7.86 \pm 0.03$	$0.84 \pm 0.04$	$0.04 \pm 0.01$	$0.17 \pm 0.24$
5101444192	$8.76 \pm 0.03$	$1.77 \pm 0.03$	$0.13 \pm 0.01$	...
510994594	$9.89 \pm 0.08$	$1.31 \pm 0.12$	$0.15 \pm 0.03$	...
5101421970	$9.78 \pm 0.05$	$1.08 \pm 0.07$	$0.07 \pm 0.02$	$0.21 \pm 0.11$
510838687	$8.87 \pm 0.14$	$1.22 \pm 0.09$	$0.11 \pm 0.01$	...
5100556178	$8.91 \pm 0.12$	$1.16 \pm 0.08$	$0.11 \pm 0.01$	...
511229433	$9.43 \pm 0.09$	$1.25 \pm 0.16$	$0.17 \pm 0.03$	...
511245444	$9.24 \pm 0.12$	$1.31 \pm 0.12$	$0.11 \pm 0.02$	...
530048433	$9.24 \pm 0.07$	$0.95 \pm 0.06$	$0.06 \pm 0.01$	$0.28 \pm 0.30$
510583858	$9.83 \pm 0.03$	$1.09 \pm 0.06$	$0.09 \pm 0.01$	$0.34 \pm 0.11$
511451385	$8.63 \pm 0.06$	$1.46 \pm 0.05$	$0.20 \pm 0.00$	...
511025693	$9.18 \pm 0.12$	$1.07 \pm 0.13$	$0.15 \pm 0.02$	...
5100997733	$10.07 \pm 0.08$	$1.72 \pm 0.14$	$0.23 \pm 0.03$	...
511228062	$9.56 \pm 0.06$	$1.53 \pm 0.05$	$0.19 \pm 0.01$	...
5101001604	$9.03 \pm 0.05$	$2.00 \pm 0.03$	$0.22 \pm 0.01$	...
510996058	$9.11 \pm 0.07$	$1.88 \pm 0.06$	$0.17 \pm 0.01$	$0.31 \pm 0.31$
511001501	$9.21 \pm 0.09$	$1.41 \pm 0.09$	$0.13 \pm 0.01$	$0.34 \pm 0.06$
530053714	$9.72 \pm 0.05$	$0.97 \pm 0.05$	$0.09 \pm 0.01$	$0.12 \pm 0.25$

<sup>(a)</sup> Color excess based on Balmer decrement as explained in 4.3.2.

with [OIII] detected. We ended up with a subsample of 11 galaxies in the COSMOS and ECDFS fields.

#### 4.2.2.2 X-shooter Spectroscopy and data reduction

Four additional VUDS galaxies were observed in a follow-up program (Program: 0101.B-0779, PI: Amorín R.) with VLT/X-shooter (Vernet et al., 2011) which is a wide-band echelle spectrograph where two dichroic split the light into three arms (UVB, VIS, and NIR), and simultaneously exposures. In this Chapter, we only used the spectra from the NIR arm. These galaxies were selected from Amorín et al. (2017) for their intense CIII] emission in deep VUDS spectra. Due to their redshift (at  $z \sim 2.4$  and  $\sim 3.4$ ), bright optical emission lines fall within good transmission windows. Observations

were done in echelle mode from 2018 May to 2019 March with 900s integrations using 1.0,0.9,0.9" (UVB/VIS/NIR) slits for a resolution  $R=5400, 8900, 5600$ , respectively in seeing conditions of  $\sim 0.6$  arcsec. Each observing block (OB) is  $\sim 3600$ s of integration time, and each galaxy has 2-3 OBs. One of the galaxies (VUDS 5101421970) has an additional observing block of 3600s from the program 0103.B-0446(A) (PI: Nakajima, K.) to complete a total of 3 hours of exposure. The NIR region of the X-shooter spans the combined Y, J, H, and K regions from 1024–2048 nm. The reduction of each OB is performed using the EsoReflex (Freudling et al., 2013) X-shooter pipeline (Modigliani et al., 2010), which provides merged, 2D NIR, visible, and UVB spectra. With the pipeline, we performed dark subtraction, flat-fielding, flexure correction and 2D mapping, wavelength calibration, and flux calibration with standard stars. This is the same methodology used in Matthee et al. (2021) where 3 out of 4 of our X-shooter sample are analyzed. To combine the OBs, we use the IRAF (Tody, 1986) task `imcombine` with median and  $\sigma$ -clipping. To extract the 1D spectrum, we use the trace by `[OIII] $\lambda\lambda$ 4959,5007+H $\beta$`  that is clearly detected, but the continuum is undetected in any galaxies.

#### 4.2.2.3 FIRE Spectroscopy and data reduction

A follow-up with Magellan/Folded Port Infrared Echellette (FIRE, Simcoe et al., 2010) was carried out for 3 galaxies selected from the VUDS parent sample to have CIII] detection and at  $z < 3$  so that bright emission lines do not overlap with strong skylines. Observations were conducted on 2022 April/May. FIRE was used in the high-resolution echelle mode. The observations were conducted as follows: the J-band acquisition camera was used to locate a nearby star from which a blind offset was applied to position the science target in the slit. The slits used were either 0.75", or 1.0" in width, depending on the seeing ( $< 1''$ ), yielding a spectral resolution of  $R \sim 5200$ . The slits were oriented at the parallactic angle to minimize differential atmospheric refraction. Exposure times of 900s were used for ABBA dither sequences with total integrations ranging from 3 to 4 hr. The readouts were performed with the Sample Up The Ramp mode to minimize overheads. For each science target, one A0V star was observed at a similar airmass for telluric correction. Data were reduced using the publicly available pipeline<sup>†</sup> developed by the instrument team. Unfortunately, the bright emission lines in this subsample were affected by sky emission lines which preclude the kinematic analysis explained in the following sections. We use this subsample to estimate the flux of emission lines, which are included in the chemical analysis, and to estimate EWs of bright observed lines. For the VUDS targets, our final C3-VUDS sample is made of 18 galaxies.

In summary, our final sample combining C3-VANDELS and C3-VUDS samples with different NIR instruments contains 35 CIII] emitters, whose physical properties are described in the following section. In Table 4.2.1, the coordinates and spectroscopic redshifts based on CIII] of the individual galaxies in our sample are listed with notes on which NIR instrument was used.

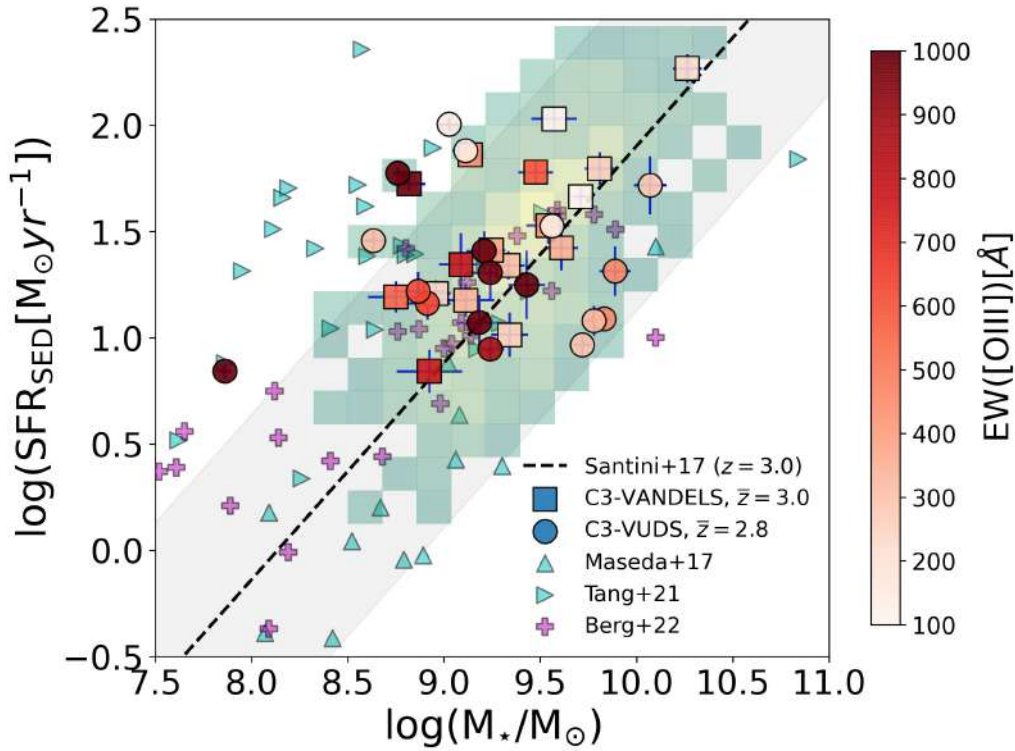


Figure 4.3.1: Sample distributed along the star-forming main-sequence at  $z \sim 3$  color-coded by  $EW([OIII])$ . The 2D histogram corresponds to the VANDELS parent sample at the same redshift range, while the black dashed line is the main sequence according to [Santini et al. \(2017\)](#). The magenta crosses, and cyan triangles are reference samples at low ([Berg et al., 2022](#)) and intermediate redshifts ([Maseda et al., 2017](#); [Tang et al., 2021](#)), respectively (see Section 4.3.1).

## 4.3 Physical parameters of the final sample

### 4.3.1 Spectral Energy Distribution modeling

We perform a SED fitting to the entire final sample using BAGPIPES ([Carnall et al., 2018](#)). The photometric catalog for the C3-VANDELS sample comes from the CANDELS team ([Galametz et al., 2013](#); [Guo et al., 2013](#)) and is the same used for the VANDELS team for targets with HST imaging that are described in ([McLure et al., 2018](#); [Garilli et al., 2021](#)). For the galaxies in the CDFS field, we used the following bands: U-VIMOS, HST: F435W, F606W, F775W, F814W, F850LP, F098M, F105W, F125W, F160W, Ks-ISAAC, Ks-HAWKI,  $3.6\mu\text{m}$ -IRAC,  $4.5\mu\text{m}$ -IRAC. For the galaxies in the UDS field, we used the bands: U-CFHT, Subaru: B, V, R, i, z, HST: F606W, F125W, F160W, HAWKI: Y, Ks, WFCAM: J, H, K,  $3.6\mu\text{m}$ -IRAC,  $4.5\mu\text{m}$ -IRAC.

For the C3-VUDS sample, we use the photometric catalog from COSMOS2015 ([Laigle et al., 2016](#)) for targets in the COSMOS field, while for galaxies in the ECDFS field, we used the photometric catalog used by the VUDS team (e.g., [Calabrò et al., 2017](#); [Ribeiro et al., 2017](#); [Lemaux et al., 2022](#)) that is obtained from [Cardamone et al. \(2010\)](#); [Grogin et al. \(2011\)](#). For the galaxies in the

<sup>†</sup><https://github.com/rasimcoe/FIREHOSE>

Table 4.3.1: Observed fluxes and rest-frame EWs of the rest-UV emission lines of our sample

ID	Ly $\alpha^a$	CIV <sup>a</sup>	HeII $\lambda$ 1640 <sup>a</sup>	OIII] $\lambda$ 1666 <sup>a</sup>	CIII] <sup>a</sup>	EW(Ly $\alpha^b$ )	EW(CIII)] <sup>b</sup>
C3-VANDELS sample							
UDS020394	12.11 $\pm$ 1.15	1.41 $\pm$ 0.41	<0.74	1.25 $\pm$ 0.37	4.13 $\pm$ 0.64	23.7 $\pm$ 2.3	13.6 $\pm$ 2.1
CDFS020954	4.24 $\pm$ 1.5	0.61 $\pm$ 0.26	1.12 $\pm$ 0.5	1.42 $\pm$ 0.3	4.25 $\pm$ 0.77	19.8 $\pm$ 7.0	9.7 $\pm$ 1.8
CDFS023527	120.45 $\pm$ 4.62	<0.94	1.92 $\pm$ 0.29	2.38 $\pm$ 0.44	8.83 $\pm$ 1.33	56.6 $\pm$ 2.2	6.9 $\pm$ 1.0
UDS021601	8.7 $\pm$ 1.27	<0.5	0.67 $\pm$ 0.31	<0.58	2.73 $\pm$ 0.73	12.5 $\pm$ 1.8	6.2 $\pm$ 1.6
CDFS022563	29.88 $\pm$ 4.73	<0.5	0.95 $\pm$ 0.38	0.73 $\pm$ 0.21	3.13 $\pm$ 0.47	19.8 $\pm$ 3.1	6.0 $\pm$ 0.9
UDS022487	8.61 $\pm$ 2.76	<0.76	<0.75	2.25 $\pm$ 0.44	3.77 $\pm$ 0.84	8.5 $\pm$ 2.7	4.4 $\pm$ 1.0
CDFS015347	13.04 $\pm$ 1.47	<0.6	1.44 $\pm$ 0.38	1.33 $\pm$ 0.28	2.38 $\pm$ 0.93	37.2 $\pm$ 4.2	4.1 $\pm$ 1.6
CDFS019276	<2.69	1.66 $\pm$ 0.65	<1.8	<1.11	7.17 $\pm$ 2.03	<1.1	3.6 $\pm$ 1.0
UDS020928	<2.24	1.83 $\pm$ 0.47	0.78 $\pm$ 0.31	0.57 $\pm$ 0.28	3.05 $\pm$ 0.68	<11.4	3.1 $\pm$ 0.7
CDFS019946	...	<1.49	<1.2	<0.75	3.02 $\pm$ 0.53	...	3.0 $\pm$ 0.5
UDS020437	<4.46	<1.84	<0.81	1.91 $\pm$ 0.58	3.82 $\pm$ 1.39	<2.3	3.0 $\pm$ 1.1
CDFS018182	...	3.94 $\pm$ 1.56	5.77 $\pm$ 1.07	1.82 $\pm$ 0.78	8.41 $\pm$ 1.31	...	2.9 $\pm$ 0.5
CDFS018882	-0.88 $\pm$ 0.33	0.75 $\pm$ 0.21	<0.45	0.8 $\pm$ 0.23	2.77 $\pm$ 0.58	-3.9 $\pm$ 1.5	2.7 $\pm$ 0.6
CDFS025828	10.86 $\pm$ 3.08	<1.1	2.11 $\pm$ 0.72	<1.79	4.98 $\pm$ 1.15	4.7 $\pm$ 1.3	2.5 $\pm$ 0.6
CDFS022799	...	<2.23	2.74 $\pm$ 1.21	<2.78	8.95 $\pm$ 1.1	...	2.5 $\pm$ 0.3
UDS021398	...	<1.39	1.66 $\pm$ 0.79	<1.14	2.95 $\pm$ 0.64	...	1.7 $\pm$ 0.4
UDS015872	...	<1.92	1.82 $\pm$ 0.69	<0.65	2.7 $\pm$ 0.66	...	1.2 $\pm$ 0.3
C3-VUDS sample							
5100998761	334.39 $\pm$ 8.23	7.08 $\pm$ 1.33	5.91 $\pm$ 1.66	5.02 $\pm$ 0.75	18.53 $\pm$ 1.56	151.5 $\pm$ 3.7	15.3 $\pm$ 1.3
5101444192	184.78 $\pm$ 2.78	3.98 $\pm$ 0.44	2.4 $\pm$ 0.82	3.02 $\pm$ 0.46	10.22 $\pm$ 1.05	327.5 $\pm$ 4.9	13.1 $\pm$ 1.3
510994594	103.4 $\pm$ 3.24	1.92 $\pm$ 0.69	4.22 $\pm$ 0.76	<0.46	8.68 $\pm$ 0.92	118.2 $\pm$ 3.7	11.5 $\pm$ 1.2
5101421970	715.43 $\pm$ 21.66	24.77 $\pm$ 2.91	11.76 $\pm$ 1.59	5.39 $\pm$ 1.37	22.83 $\pm$ 2.11	243.8 $\pm$ 7.4	10.6 $\pm$ 1.0
510838687	19.16 $\pm$ 2.33	2.71 $\pm$ 1.24	<2.44	3.69 $\pm$ 0.87	11.18 $\pm$ 1.52	23.8 $\pm$ 2.9	10.2 $\pm$ 1.4
5100556178	266.96 $\pm$ 5.41	<1.48	3.36 $\pm$ 0.78	<0.94	8.88 $\pm$ 0.99	89.3 $\pm$ 1.8	8.7 $\pm$ 1.0
511229433	47.41 $\pm$ 2.03	0.81 $\pm$ 0.39	4.61 $\pm$ 0.45	2.01 $\pm$ 0.39	8.8 $\pm$ 1.28	55.9 $\pm$ 2.4	7.8 $\pm$ 1.1
511245444	81.83 $\pm$ 2.15	4.47 $\pm$ 0.88	1.25 $\pm$ 0.42	1.61 $\pm$ 0.32	7.34 $\pm$ 1.96	67.9 $\pm$ 1.8	6.2 $\pm$ 1.7
530048433	165.55 $\pm$ 8.43	5.82 $\pm$ 2.28	2.88 $\pm$ 1.23	2.01 $\pm$ 0.96	13.3 $\pm$ 2.29	40.7 $\pm$ 2.1	5.2 $\pm$ 0.9
510583858	126.63 $\pm$ 5.55	3.96 $\pm$ 1.56	11.56 $\pm$ 3.69	2.17 $\pm$ 0.58	7.03 $\pm$ 1.4	102.6 $\pm$ 4.5	4.8 $\pm$ 1.0
511451385	62.34 $\pm$ 3.72	<1.91	<1.93	1.41 $\pm$ 0.38	5.28 $\pm$ 1.36	78.2 $\pm$ 4.7	4.7 $\pm$ 1.2
511025693	15.24 $\pm$ 2.22	<1.71	3.27 $\pm$ 0.86	2.22 $\pm$ 0.63	6.92 $\pm$ 1.16	7.3 $\pm$ 1.1	4.4 $\pm$ 0.7
5100997733	7.71 $\pm$ 2.88	<1.68	<2.26	<1.38	5.35 $\pm$ 1.41	4.0 $\pm$ 1.5	4.3 $\pm$ 1.1
511228062	<1.34	<1.23	<0.74	<0.45	3.97 $\pm$ 1.56	<1.6	3.9 $\pm$ 1.5
5101001604	1.93 $\pm$ 0.81	<0.91	<1.37	<1.17	3.46 $\pm$ 1.56	9.2 $\pm$ 3.8	3.4 $\pm$ 1.5
510996058	18.45 $\pm$ 2.31	<2.19	<1.05	<0.65	1.28 $\pm$ 0.3	18.8 $\pm$ 2.4	2.2 $\pm$ 0.5
511001501	<4.67	<1.53	<1.28	<1.01	4.59 $\pm$ 0.88	<1.6	2.1 $\pm$ 0.4
530053714	<2.46	<3.31	3.17 $\pm$ 1.16	1.91 $\pm$ 0.73	3.35 $\pm$ 1.22	<1.2	1.5 $\pm$ 0.6

(a) Flux in units  $10^{-18}$  erg s $^{-1}$  cm $^{-2}$ .(b) Rest-frame equivalent width in units  $\text{\AA}$ .

COSMOS field, we considered the following bands: u-CFHT, VISTA: Y, J, H, Ks, Subaru: B, V, R, i, z, Y, 3.6 $\mu$ m-IRAC, 4.5 $\mu$ m-IRAC. For the galaxies in the ECDFS field, we considered the following bands: MUSYC: U38, U, B, V, R, I, z, J, H, K, Subaru: IA427, IA464, IA484, IA505, IA527, IA574, IA624, IA679, IA709, IA738, IA767, IA827, 3.6 $\mu$ m-IRAC, 4.5 $\mu$ m-IRAC.

We assume an exponentially declining  $\tau$ -model for the SFH. We obtain values for the timescale  $\tau > 5$ Gyr, which implies a constant SFH at the redshift range covered by our sample. For the metallicity, we allow it to vary up to  $0.25Z_{\odot}$ , in agreement with the stellar metallicities observed in star-forming galaxies at  $z \sim 3$  (e.g., Cullen et al., 2019; Calabrò et al., 2021; Llerena et al., 2022). We include a nebular component which includes emission lines and nebular continuum emission in the model given the emission lines that are observed in these galaxies. The nebular component depends on the ionization parameter ( $\log U$ ) and can vary between  $-3$  and  $-2$  in our model. We use Calzetti law for the dust reddening determination (Calzetti et al., 2000) with the total extinction  $A_V$  free to

Table 4.3.2: Observed fluxes and rest-frame EWs of the rest-optical emission lines of our sample

ID	[OII] $\lambda$ 3727 <sup>a</sup>	[OII] $\lambda$ 3729 <sup>a</sup>	H $\beta$ <sup>a</sup>	[OIII] $\lambda$ 5007 <sup>a</sup>	H $\alpha$ <sup>a</sup>	EW(H $\beta$ ) <sup>b</sup>	EW([OIII] $\lambda$ 5007) <sup>b</sup>
C3-VANDELS sample							
UDS020394	<3.4	3.73 $\pm$ 1.7	9.06 $\pm$ 1.37	60.77 $\pm$ 3.2	...	112.8 $\pm$ 17.1	779.0 $\pm$ 41.1
CDFS020954	11.22 $\pm$ 1.57	9.51 $\pm$ 1.5	18.15 $\pm$ 0.97	112.83 $\pm$ 12.9	...	153.5 $\pm$ 8.2	984.4 $\pm$ 112.6
CDFS023527	8.94 $\pm$ 1.57	<13.6	...	122.12 $\pm$ 21.4	...	...	437.6 $\pm$ 76.7
UDS021601	...	8.46 $\pm$ 1.87	6.1 $\pm$ 1.44	32.2 $\pm$ 1.2	...	48.5 $\pm$ 11.5	260.3 $\pm$ 9.7
CDFS022563	3.78 $\pm$ 1.12	7.01 $\pm$ 1.12	5.67 $\pm$ 1.1	43.17 $\pm$ 1.61	...	68.9 $\pm$ 13.4	551.4 $\pm$ 20.6
UDS022487	17.66 $\pm$ 1.81	18.21 $\pm$ 1.82	13.32 $\pm$ 1.4	122.76 $\pm$ 24.63	...	82.4 $\pm$ 8.6	786.9 $\pm$ 157.9
CDFS015347	3.03 $\pm$ 0.86	<2.44	3.35 $\pm$ 0.92	35.4 $\pm$ 1.66	...	30.9 $\pm$ 8.5	336.5 $\pm$ 15.8
CDFS019276	22.7 $\pm$ 3.61	30.3 $\pm$ 3.6	37.17 $\pm$ 2.15	151.27 $\pm$ 24.9	...	53.1 $\pm$ 3.1	222.8 $\pm$ 36.7
UDS020928	13.49 $\pm$ 1.8	19.33 $\pm$ 2.06	13.96 $\pm$ 2.42	136.21 $\pm$ 13.19	...	59.8 $\pm$ 10.4	601.1 $\pm$ 58.2
CDFS019946	...	...	6.77 $\pm$ 1.99	48.73 $\pm$ 7.83	31.68 $\pm$ 1.94	31.5 $\pm$ 9.3	234.4 $\pm$ 37.7
UDS020437	18.54 $\pm$ 3.04	26.44 $\pm$ 3.05	15.1 $\pm$ 1.0	105.11 $\pm$ 10.72	...	48.9 $\pm$ 3.2	348.3 $\pm$ 35.5
CDFS018182	...	...	26.53 $\pm$ 1.35	157.75 $\pm$ 11.43	88.82 $\pm$ 3.24	49.8 $\pm$ 2.5	305.6 $\pm$ 22.1
CDFS018882	7.67 $\pm$ 1.25	7.53 $\pm$ 1.24	7.53 $\pm$ 0.88	60.3 $\pm$ 3.03	...	31.4 $\pm$ 3.7	257.9 $\pm$ 12.9
CDFS025828	11.67 $\pm$ 2.25	15.87 $\pm$ 2.42	4.47 $\pm$ 1.62	38.66 $\pm$ 1.29	...	11.9 $\pm$ 4.3	108.2 $\pm$ 3.6
CDFS022799	...	...	43.35 $\pm$ 2.07	235.67 $\pm$ 35.94	129.48 $\pm$ 2.95	79.6 $\pm$ 3.8	451.6 $\pm$ 68.9
UDS021398	...	...	16.52 $\pm$ 5.61	125.81 $\pm$ 11.47	74.42 $\pm$ 3.97	47.8 $\pm$ 16.2	377.7 $\pm$ 34.4
UDS015872	...	...	16.7 $\pm$ 1.64	66.21 $\pm$ 7.38	62.61 $\pm$ 2.68	25.4 $\pm$ 2.5	102.2 $\pm$ 11.4
C3-VUDS sample							
5100998761	3.78 $\pm$ 1.89	<5.13	10.66 $\pm$ 1.64	103.76 $\pm$ 6.6	35.09 $\pm$ 6.2	153.1 $\pm$ 23.6	1549.8 $\pm$ 98.5
5101444192	5.66 $\pm$ 2.83	...	23.19 $\pm$ 4.1	241.86 $\pm$ 4.59	...	144.7 $\pm$ 25.5	1560.8 $\pm$ 29.6
510994594	<9.93	...	13.04 $\pm$ 1.4	122.7 $\pm$ 8.85	...	49.5 $\pm$ 5.3	463.0 $\pm$ 33.4
5101421970	8.24 $\pm$ 3.37	7.91 $\pm$ 3.37	25.89 $\pm$ 1.57	168.87 $\pm$ 16.98	89.04 $\pm$ 7.73	49.7 $\pm$ 3.0	322.4 $\pm$ 32.4
510838687	40.52 $\pm$ 8.34	<16.7	<34.38	125.5 $\pm$ 3.1	30.18 $\pm$ 5.72	<6.7	630.6 $\pm$ 15.6
5100556178	<11.95	25.47 $\pm$ 5.98	<24.09	126.42 $\pm$ 4.44	93.04 $\pm$ 12.51	<4.9	642.8 $\pm$ 22.6
511229433	20.92 $\pm$ 6.06	23.49 $\pm$ 6.06	39.02 $\pm$ 2.06	271.06 $\pm$ 14.51	...	245.1 $\pm$ 13.0	1715.7 $\pm$ 91.8
511245444	...	...	...	201.06 $\pm$ 45.9	...	...	978.9 $\pm$ 223.5
530048433	20.35 $\pm$ 2.89	39.34 $\pm$ 6.38	37.35 $\pm$ 10.95	243.88 $\pm$ 5.66	137.42 $\pm$ 3.94	130.4 $\pm$ 38.2	870.6 $\pm$ 20.2
510583858	17.77 $\pm$ 8.05	<16.1	33.75 $\pm$ 2.33	233.86 $\pm$ 22.94	131.38 $\pm$ 11.18	64.9 $\pm$ 4.5	445.5 $\pm$ 43.7
511451385	10.2 $\pm$ 5.01	<10.02	<14.6	53.19 $\pm$ 1.17	<67.08	<1.9	304.0 $\pm$ 6.7
511025693	16.4 $\pm$ 2.38	16.96 $\pm$ 2.4	34.89 $\pm$ 1.25	239.5 $\pm$ 18.03	...	146.1 $\pm$ 5.2	1002.9 $\pm$ 75.5
5100997733	<4.71	14.79 $\pm$ 2.33	11.58 $\pm$ 2.22	96.32 $\pm$ 6.97	...	33.9 $\pm$ 6.5	279.9 $\pm$ 20.3
511228062	22.09 $\pm$ 2.15	17.35 $\pm$ 2.15	27.23 $\pm$ 2.15	107.34 $\pm$ 7.94	...	34.1 $\pm$ 2.7	134.3 $\pm$ 9.9
5101001604	<3.52	6.41 $\pm$ 1.76	8.37 $\pm$ 1.01	33.14 $\pm$ 1.12	...	38.3 $\pm$ 4.6	155.9 $\pm$ 5.3
510996058	10.7 $\pm$ 1.99	9.12 $\pm$ 1.99	10.38 $\pm$ 2.8	26.61 $\pm$ 2.07	39.28 $\pm$ 5.86	50.6 $\pm$ 13.6	133.4 $\pm$ 10.4
511001501	42.27 $\pm$ 3.24	53.89 $\pm$ 3.24	34.88 $\pm$ 1.89	185.02 $\pm$ 31.48	136.42 $\pm$ 2.87	197.6 $\pm$ 10.7	1060.6 $\pm$ 180.4
530053714	10.59 $\pm$ 3.43	<6.86	27.96 $\pm$ 6.69	113.72 $\pm$ 2.05	87.52 $\pm$ 5.02	74.0 $\pm$ 17.7	299.5 $\pm$ 5.4

(a) Flux in units  $10^{-18}$  erg s $^{-1}$  cm $^{-2}$ .(b) Rest-frame equivalent width in units  $\text{\AA}$ .

vary between 0 and 2 mag. We constrain the ages from 100Myr up to 1Gyr. Our SED fitting leads to differences of  $\sim 0.3$  dex towards lower stellar mass and  $\sim 0.1$  dex towards higher SFR compared with a model with similar SFH but with fixed solar metallicity and without a nebular model. The larger effect on the SFR offset is the assumption of subsolar metallicity, while the larger effect on the stellar mass offset is due to the inclusion of the nebular model. The stellar masses and SFRs obtained with the SED fitting are displayed in Fig. 4.3.1 and reported in Table 4.2.2. We highlight that the SFR is calculated over a timescale of 100Myr. Our sample ranges  $\sim 2.4$  dex in stellar mass from  $10^{7.9}$  to  $10^{10.3}M_{\odot}$  and  $\sim 1.4$  dex in SFR from 6.9 to 185  $M_{\odot}$  yr $^{-1}$ . The physical parameters are reported in Table 4.2.2, including the color excess (E(B-V)<sub>SED</sub>) from the SED model, which ranges from 0.04 to 0.25 mag. The photometry used, and the resulting SED model are displayed in Fig. 4.3.2 and 4.3.3 for C3-VANDELS and C3-VUDS samples, respectively.

We perform a SED fitting following the same constraints to our VANDELS parent sample (2D

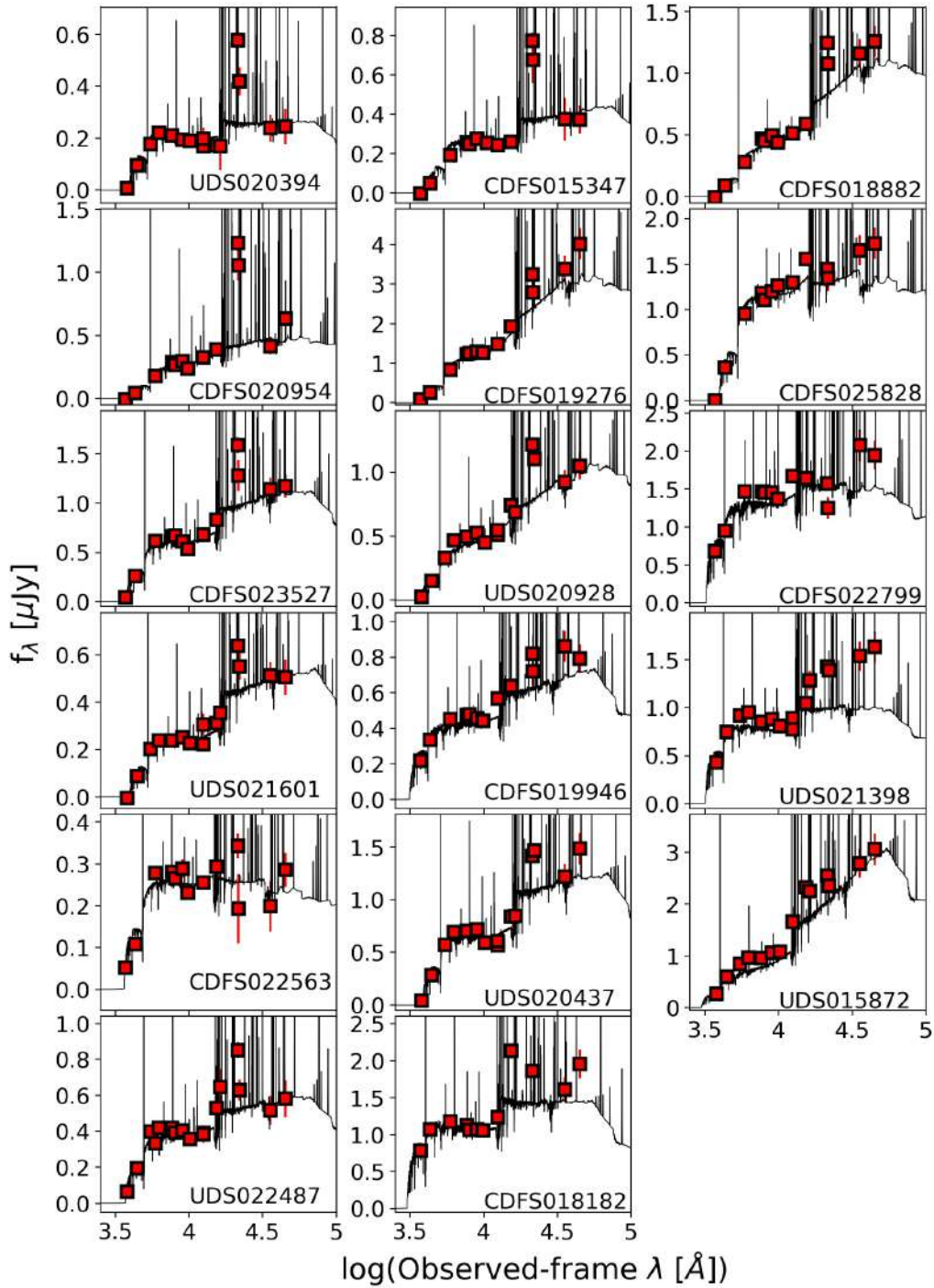


Figure 4.3.2: SED model for the galaxies in the C3-VANDELS sample. The red squares are the photometric points, and the solid black line is the resulting spectrum from the SED fitting using BAGPIPES as described in Sec. 4.3.1.

histogram in Fig. 4.3.1), and we note that they follow the main-sequence (MS) at  $z \sim 3$  according to Santini et al. (2017) with stellar mass corrected by a factor of 0.6 (Madau & Dickinson, 2014) by adopting the same assumed IMF in this Thesis.

Regarding our combined samples, we note that most are distributed along the MS, with 7 (5 of

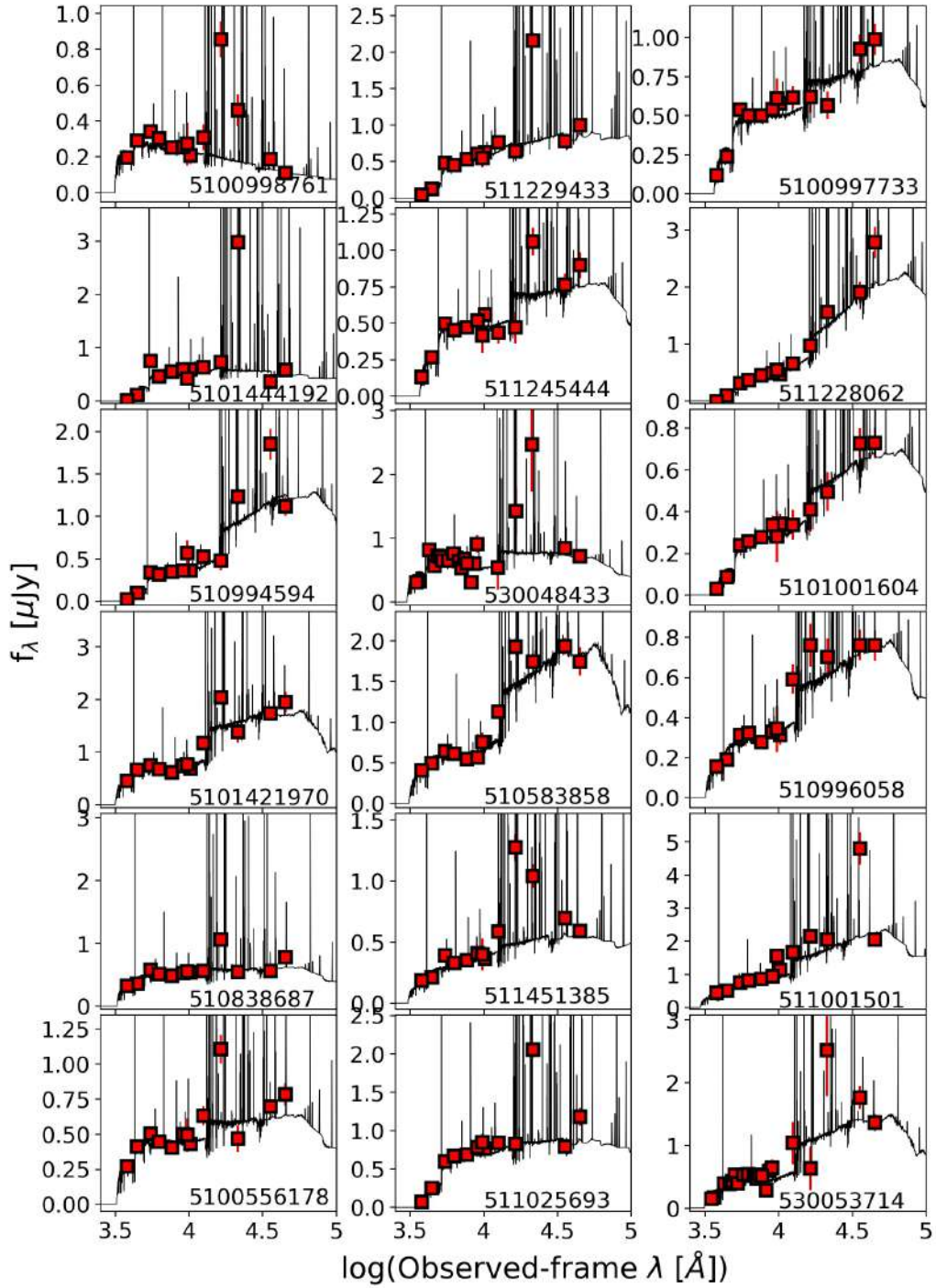


Figure 4.3.3: Same as in Fig. 4.3.2 but for the galaxies in the C3-VUDS sample.

which are VUDS galaxies) slightly above 3 times the observed 0.37 dex scatter of the relation. We compare our sample with other works at similar intermediate redshifts (Maseda et al., 2017; Tang et al., 2021) and with local metal-poor SFGs (Berg et al., 2022) that will be used in the following sections.

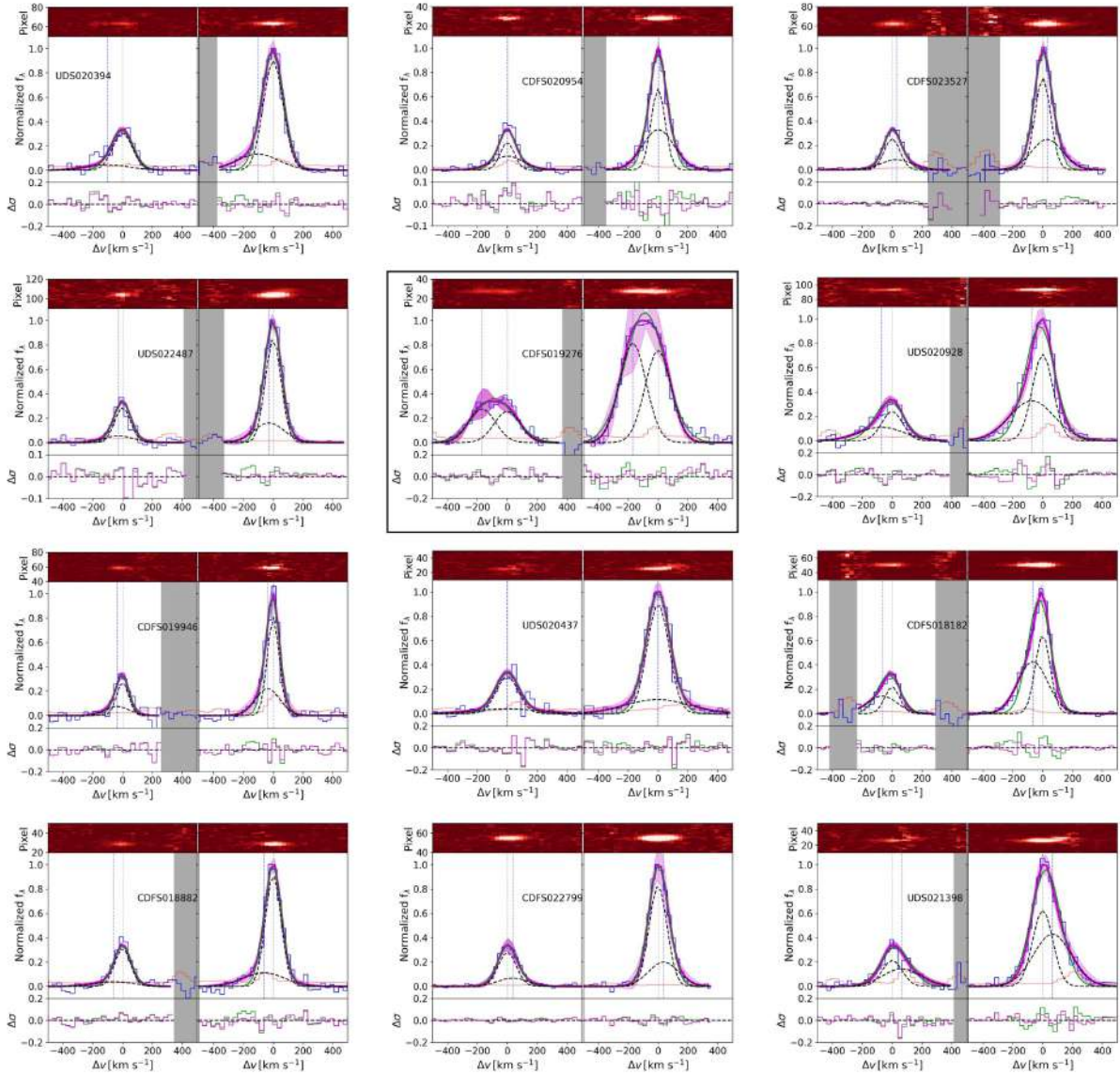


Figure 4.3.4: Best-fit of the [OIII] profiles from the C3-VANDELS sample with  $\Delta\text{BIC} > 2$ . The panels show single galaxies ordered by  $\text{EW}(\text{CIII})$  from left-right and top-bottom. *In each panel:* *Top:* The 2D spectrum showing the detected lines. *Middle:* Models for [OIII] $\lambda$ 4959 (left) [OIII] $\lambda$ 5007 (right). The blue line is the observed spectrum, while the red line is the error spectrum. The Gaussian lines are normalized to the intensity peak of [OIII] $\lambda$ 5007. The black dashed lines are the narrow and broad components, and the magenta line is the global fit considering both components. The magenta-shaded region is the  $3\sigma$  uncertainty of the fit. The green line is the single-gaussian fit. The vertical gray line marks the systemic velocity traced by the peak intensity of the narrow component. Meanwhile, the vertical blue line marks the peak intensity of the broad component. *Bottom:* The residuals ( $\Delta\sigma$ ) for each model are shown with the same colors as described. The gray-shaded regions are masked regions due to sky residuals. The galaxies in the black square show two narrow components.

### 4.3.2 Emission-line fluxes and EWs

Line flux and EW were measured individually in each galaxy. We measure the fluxes of UV lines using single Gaussians and a linear component to include the local continuum. We consider Ly $\alpha$ , CIV,

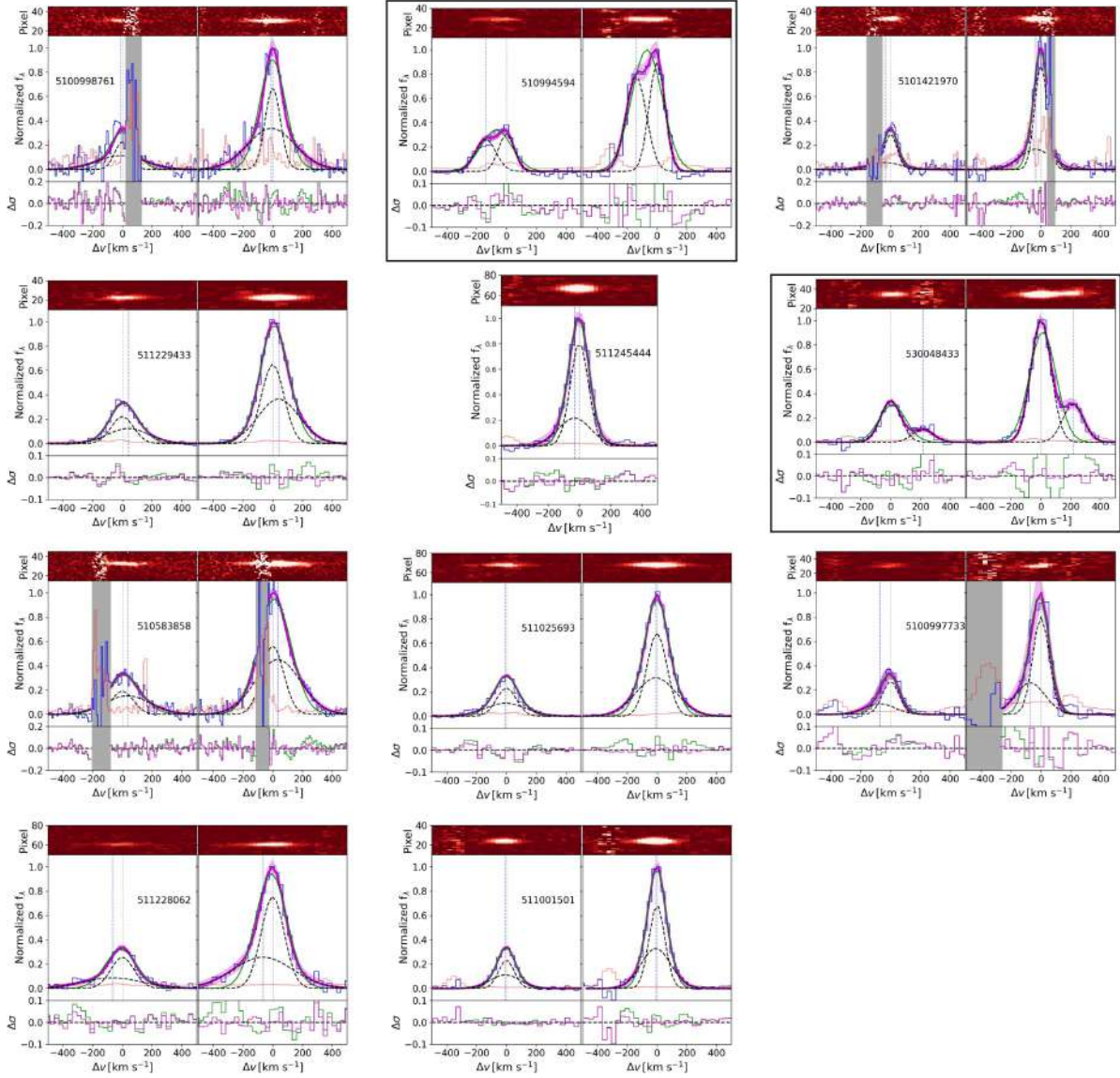


Figure 4.3.5: Same as in Fig. 4.3.4 but for the C3-VUDS sample with  $\Delta\text{BIC} > 2$ .

$\text{HeII}\lambda 1640$ ,  $\text{OIII]}\lambda 1666$ , and  $\text{CIII]}$  in the set of lines to be measured. We considered the  $\text{CIII]}$  width as the maximum width of the lines, which is in the range of  $\sim 250 - 300 \text{ km s}^{-1}$  ( $\text{FWHM} \sim 15 - 18 \text{ \AA}$ ) and depends on each galaxy. The systemic redshift is based on the  $\text{CIII]}$  peak. Given that the  $\text{CIII]}$  doublet is not resolved in our observations, we assume an air wavelength of  $1907.05 \text{ \AA}$  for the average peak. The observed fluxes and rest-frame EW of the observed lines are reported in Table 4.3.1. The uncertainties are estimated directly from the Gaussian fitting based on the covariance matrix using non-linear least squares. For galaxies in the C3-VANDELS sample at  $z < 3$ ,  $\text{Ly}\alpha$  is not measured since it is not included in the VANDELS spectral range.

On the other hand, the observed fluxes of rest-optical lines are reported in Table 4.3.2. The fluxes are computed from a single Gaussian component (except for  $\text{[OIII]}\lambda\lambda 4959, 5007$ , which is explained later). A local continuum is set to zero because it is undetected above  $1 \sigma$ . We consider  $\text{[OII]}\lambda 3727$ ,  $\text{[OII]}\lambda 3729$ ,  $\text{H}\beta$ ,  $\text{[OIII]}\lambda\lambda 4959, 5007$ ,  $\text{H}\alpha$ , and  $\text{[NII]}\lambda 6583$  to be measured. The spectra of the galaxies in the C3-VANDELS and C3-VUDS samples are displayed in Fig. 4.3.10 and 4.3.11, respectively.

Table 4.3.3: Kinematic properties of the ionized gas based on [OIII] modeling

ID	$\sigma_N^a$ km s <sup>-1</sup>	$\sigma_B^a$ km s <sup>-1</sup>	$\Delta v_B$ km s <sup>-1</sup>	$f_B^b$	$\Delta BIC$	$r_H$ kpc	$\Sigma_{SFR}$ M <sub>⊙</sub> yr <sup>-1</sup> kpc <sup>-2</sup>	$\dot{M}_{out}$ M <sub>⊙</sub> yr <sup>-1</sup>	log η dex
C3-VANDELS sample									
UDS020394	55.8±2.2	135.46±25.61	-102.27±2.76	0.24±0.04	15.69	0.19±0.05	91.17±64.14	20.08±7.98	-0.01±0.25
CDFS020954	30.61±3.24	98.41±9.74	1.44±1.2	0.53±0.1	45.47	2.94±0.48	0.71±0.38	4.62±1.27	-0.92±0.22
CDFS023527	38.27±3.95	96.72±14.37	29.03±14.29	0.39±0.14	11.69	3.06±0.34	...	...	...
UDS021601	78.34±3.71	...	...	0.0±0.0	-3.29	1.51±0.27	1.38±0.77	...	...
CDFS022563	75.24±3.61	...	...	0.0±0.0	-2.96	0.76±0.09	4.27±2.06	...	...
UDS022487	39.02±3.65	95.38±22.64	-28.53±22.38	0.27±0.15	4.58	1.59±0.12	1.72±0.79	2.21±1.37	-1.09±0.33
CDFS015347	72.95±4.4	...	...	0.0±0.0	-2.52	0.37±0.05	14.6±7.96	...	...
CDFS019276	80.31±8.39	82.76±8.76 <sup>x</sup>	-169.59±26.17	0.53±0.15	34.27	2.14±0.06	2.79±1.36	22.32±6.67	-0.56±0.25
UDS020928	60.09±4.3	145.78±9.67	-72.53±15.9	0.5±0.08	46.37	1.36±0.19	2.21±1.15	10.94±3.15	-0.37±0.23
CDFS019946	18.67±3.0	72.98±10.86	-37.17±17.53	0.36±0.13	13.92	1.59±0.15	0.84±0.46	1.37±0.68	-0.99±0.31
UDS020437	64.94±3.91	210.37±52.76	-2.53±2.02	0.27±0.08	9.86	3.55±0.3	0.41±0.17	2.31±0.9	-1.15±0.24
CDFS018182	34.8±2.53	93.54±3.4	-66.83±8.34	0.57±0.07	142.25	3.64±0.19	0.14±0.06	1.76±0.25	-0.83±0.19
CDFS018882	38.69±1.53	131.58±19.81	-61.91±1.47	0.24±0.04	21.75	0.55±0.04	13.76±5.77	7.78±1.94	-0.52±0.2
CDFS025828	58.65±2.64	...	...	0.0±0.0	-9.4	2.48±0.23	0.43±0.24	...	...
CDFS022799	48.45±2.39	93.54±19.68	36.5±15.84	0.29±0.12	15.53	2.99±0.06	0.52±0.21	1.41±0.63	-1.31±0.26
UDS021398	57.33±5.16	121.47±11.32	64.37±6.62	0.56±0.08	7.57	2.21±0.16	0.68±0.38	6.0±2.31	-0.54±0.29
UDS015872	67.91±4.24	...	...	0.0±0.0	0.63	1.59±0.1	1.49±0.6	...	...
C3-VUDES sample									
5100998761	45.11±3.41	145.77±9.99	-10.85±6.69	0.63±0.06	95.07	0.25	10.94±5.2	14.56±3.18	0.51±0.21
5101444192	67.05±2.68	...	...	0.0±0.0	-4.64	0.16 <sup>+</sup>	495.88±225.56	...	...
510994594	39.8±3.08	58.13±5.15 <sup>x</sup>	-139.76±8.79	0.53±0.06	120.65	0.41	20.67±9.37	23.97±4.75	0.05±0.2
5101421970	36.7±2.55	100.95±14.48	-36.99±15.61	0.33±0.08	19.38	0.88 <sup>+</sup>	4.71±2.07	4.84±1.44	-0.68±0.21
510838687	68.4±1.78	...	...	0.0±0.0	-99.9	2.06 <sup>+</sup>	0.52±0.24	...	...
5100556178	102.02±2.32	...	...	0.0±0.0	-99.9	0.53 <sup>+</sup>	23.66±10.41	...	...
511229433	66.73±2.15	133.06±5.44	39.32±2.12	0.51±0.05	83.19	0.91	12.88±5.57	36.84±5.52	-0.26±0.18
511245444	45.3±4.44	97.24±18.26	-31.17±20.5	0.32±0.18	4.34	0.74	...	...	...
530048433	57.91±1.6	60.4±5.27 <sup>x</sup>	216.22±5.44	0.24±0.02	247.42	1.14	4.67±2.39	5.81±1.86	-0.82±0.25
510583858	70.44±5.52	147.27±7.68	34.21±7.45	0.62±0.09	82.54	0.71 <sup>+</sup>	7.22±3.53	27.85±5.49	0.09±0.21
511451385	93.53±2.7	...	...	0.0±0.0	-99.9	0.24 <sup>+</sup>	...	...	...
511025693	56.55±2.48	132.1±7.66	-6.84±3.68	0.49±0.06	113.15	0.84	13.71±6.01	29.49±5.27	-0.31±0.19
5100997733	42.17±2.86	93.54±15.86	-72.62±72.62	0.37±0.06	16.57	2.45	0.63±0.29	2.36±0.96	-1.0±0.26
511228062	69.14±3.92	196.84±15.86	-66.15±16.49	0.47±0.06	68.67	0.64	22.25±9.85	57.25±11.52	0.01±0.19
5101001604	36.05±5.07	...	...	0.0±0.0	-11.88	0.95	5.29±2.31	...	...
510996058	52.0±11.9	...	...	0.0±0.0	-1.1	2.71	0.4±0.2	...	...
511001501	38.92±3.82	92.89±10.82	-7.75±5.2	0.48±0.14	27.75	0.95	4.75±2.39	7.95±2.72	-0.53±0.25
530053714	91.19±2.04	...	...	0.0±0.0	-5.97	2.1	0.98±0.47	...	...

(a) Intrinsic velocity dispersion of the narrow (N) and broad (B) component from the [OIII] line.

(b) Broad-to-narrow flux ratio.

(<sup>+</sup>) For this galaxy, we constrained the size using the i-band HST/F814W image.

(<sup>x</sup>) Best-fit with 2 narrow components.

We highlight the spectral regions including the emission-lines used that includes Ly $\alpha$ , CIV $\lambda\lambda$ 1548,51, HeII $\lambda$ 1640, OIII] $\lambda\lambda$ 1661,66, CIII] $\lambda\lambda$ 1907,09, [OII] $\lambda\lambda$ 3727,29, H $\beta$ , [OIII] $\lambda\lambda$ 4959,5007 and H $\alpha$ .

For [OIII] $\lambda\lambda$ 4959,5007 we consider a more detailed modeling. We fit the [OIII] $\lambda\lambda$ 4959,5007 profiles with two Gaussian components. In the other rest-optical lines, unfortunately, the S/N is lower, and a similar analysis can not be performed. We fit the doublet [OIII] $\lambda\lambda$ 4959,5007 simultaneously using LMFIT (Newville et al., 2016), considering a wavelength range from 4939 to 5027Å to include only the doublet. We fix the ratio between both components to 1:2.98 (Storey & Zeippen, 2000). We mask the region in the spectra between both lines and the regions with strong sky residuals. As an initial guess, we include one narrow (100km s<sup>-1</sup>) and one broad component (150km s<sup>-1</sup>), and both

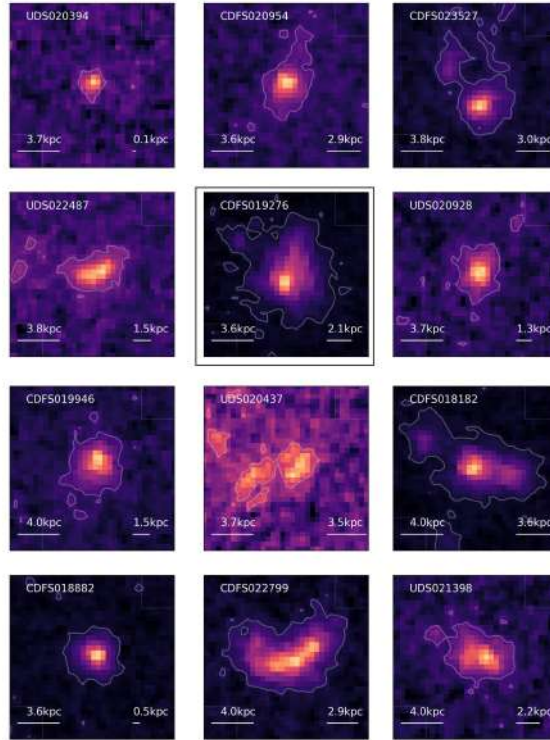


Figure 4.3.6: HST/F160W images [Koekemoer et al. \(2011\)](#) of the C3-VANDELS sample with  $\Delta\text{BIC} > 2$ , i.e., the subsample with a broad component in their [OIII] profile. The images are tracing the rest-optical. The white contour is the  $3\sigma$  level. The physical scale of 0.5 arcsec at their redshift is shown on the left of each image, while on the right, the effective radius is shown. The galaxy marked with a black square shows two narrow components in its [OIII] profile.

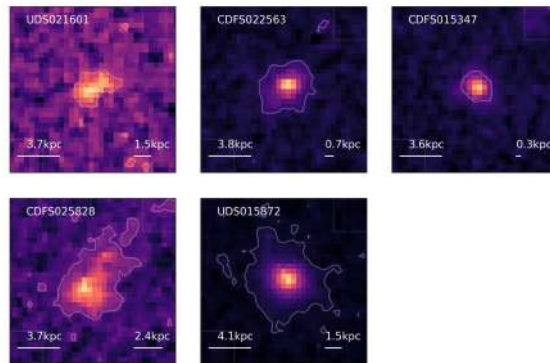


Figure 4.3.7: The same as in Fig. 4.3.6 but for the C3-VANDELS sample without features of a broad component in their [OIII] profile.

widths are free to vary. We constrain the kinematics, assuming that the width of the components in each line is the same, as well as their peak velocities and ratios. We also perform a single Gaussian model to compare with and to test the improvement of the model with two Gaussians based on the Bayesian Information Criterion (BIC), which is a statistical measure used to compare models based on their fit to the data and complexity. According to this criterion, the model having the lowest BIC is the preferred model. When the difference between the BIC values of the two models is greater than 2, it is rated as positive evidence against the significance of the model with the higher BIC ([Fabozzi](#)

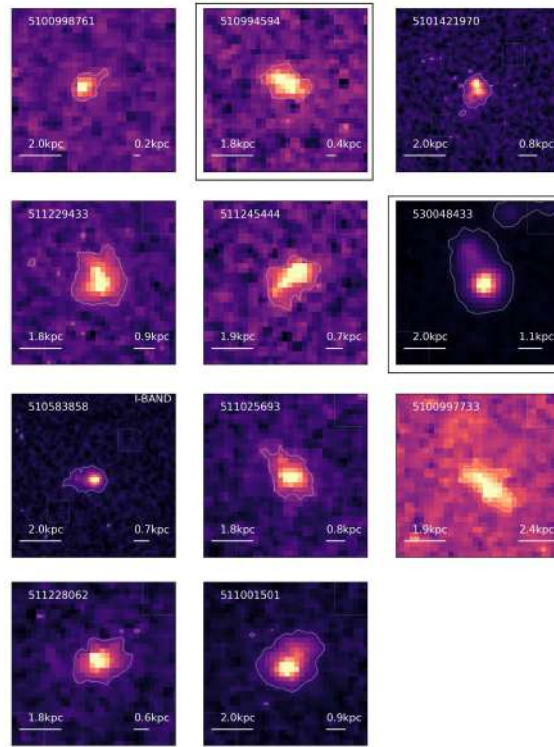


Figure 4.3.8: HST/F160W images [Koekemoer et al. \(2011\)](#) of the C3-VUDS sample with  $\Delta\text{BIC} > 2$ , i.e., the subsample with a broad component in their [OIII] profile. The images are tracing the rest-optical. The white contour is the  $3\sigma$  level. The physical scale of 0.5 arcsec at their redshift is shown on the left of each image, while on the right, the effective radius is shown. The galaxies with only i-band HST/F814W have a label. The galaxies marked with a black square show two narrow components in their [OIII] profile.

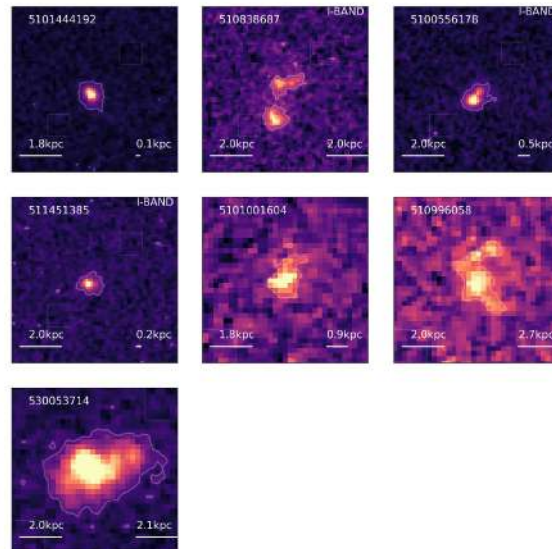


Figure 4.3.9: The same as in Fig. 4.3.8 but for the C3-VUDS sample without features of a broad component in their [OIII] profile.

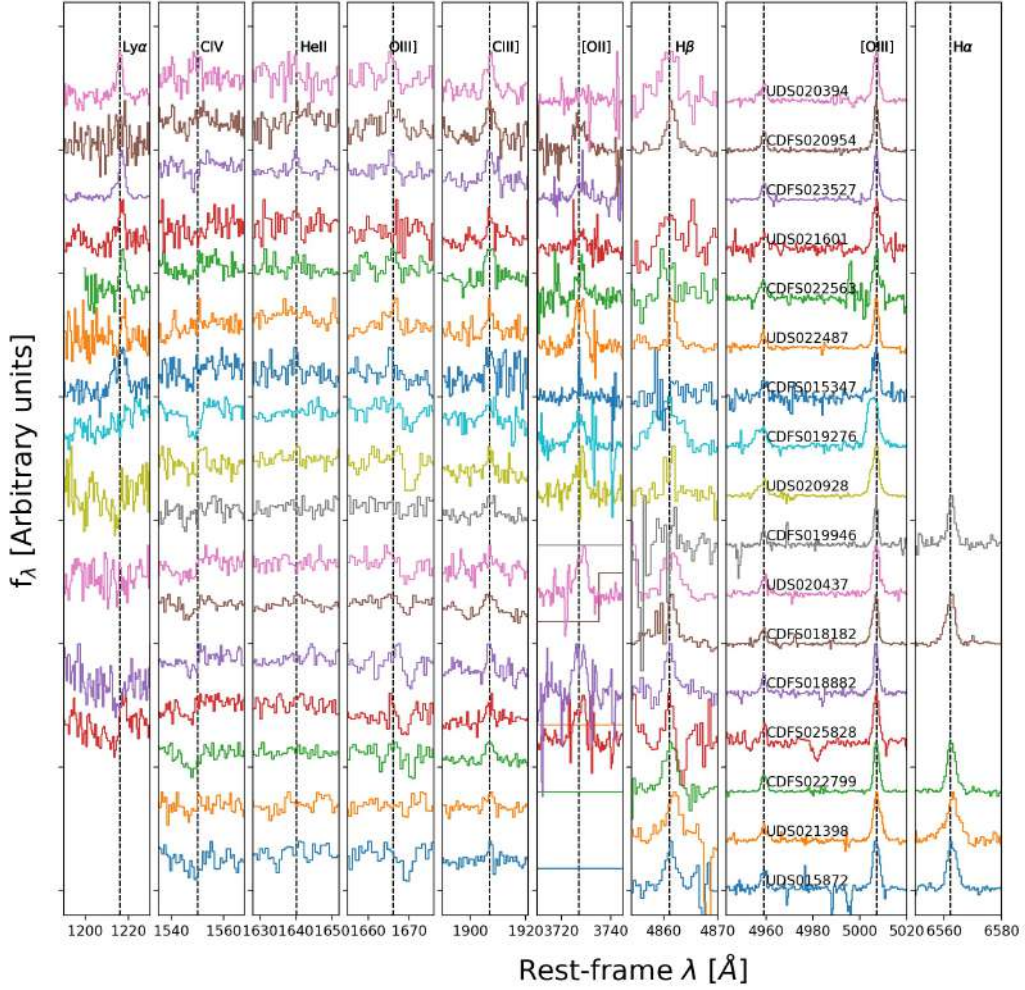


Figure 4.3.10: Rest-frame spectra of the galaxies in the C3-VANDELS subsample. From left to right panels, we highlight the following emission-lines (which are marked with the black dashed line): Ly $\alpha$ , C IV  $\lambda\lambda$ 1548,51, He II  $\lambda$ 1640, O III]  $\lambda\lambda$ 1661,66, C III]  $\lambda\lambda$ 1907,09, [O II]  $\lambda\lambda$ 3727,3729, H $\beta$ , [O III]  $\lambda\lambda$ 4959,5007 and H $\alpha$ . The flux density is in arbitrary units. Each galaxy is shown with the same color in each panel and its ID is in the [O III]  $\lambda\lambda$ 4959,5007 panel.

et al., 2014). We choose the BIC criterion as it prevents the selection of an over-fit model because it penalizes models with more free parameters. To compare, we estimate the  $\Delta\text{BIC} = \text{BIC}_{\text{single-gaussian}} - \text{BIC}_{\text{double-gaussian}}$  and consider that the second component is statistically needed if  $\Delta\text{BIC} > 2$  (Fabozzi et al., 2014). A similar criterion is adopted for the complex line profiles of strong LAEs (Matthee et al., 2021) and GP galaxies (Bosch et al., 2019; Hogarth et al., 2020) based on  $\chi^2$  minimization. We find that 23 (65%) out of the 35 galaxies in the sample show two kinematic components in their [O III]  $\lambda\lambda$ 4959,5007 profiles. In the remaining 12 galaxies, only one single component is statistically justified. We only consider that the second component is broad if there is a difference of one spectral resolution element between the widths of the two Gaussian components. Otherwise, we consider that there are two narrow components in the double Gaussian model. The results from the fitting are shown in Fig. 4.3.4 and 4.3.5 for the subsample with two components in the C3-VANDELS and C3-VUDS samples, respectively. For [O III], we report in Table 4.3.2 the global flux (double Gaussian model) or the flux of the single-gaussian model if the second component is not justified. The kinematic information of the fits is reported in Table 4.3.3. We consider the intensity peak of the

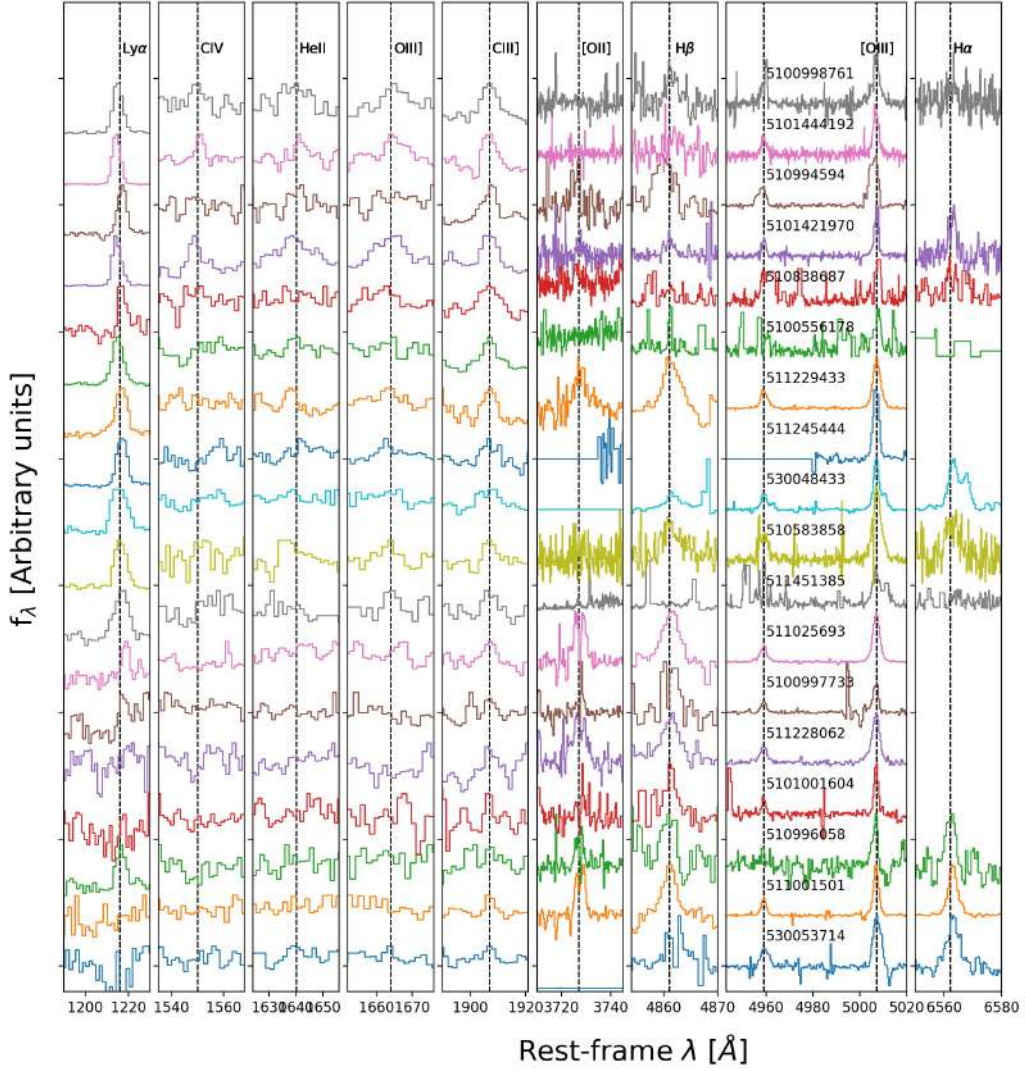


Figure 4.3.11: Same as in Fig. 4.3.10 but for the galaxies in the C3-VUDS sample.

narrower component as the systemic velocity.

Regarding the rest-EW, the SED model obtained from photometry is used to determine the continuum of the rest-optical emission lines of our sample. Since we are interested in qualitative trends with the EWs, we do not perform an additional aperture correction for the continuum. For a particular line with intensity peak at  $\lambda_{\text{peak}}$ , the continuum is obtained as the average between the continuum at  $\lambda_{\text{peak}} - 20 [\text{\AA}]$  and  $\lambda_{\text{peak}} + 20[\text{\AA}]$ . The measured EWs for  $H\beta$  and  $[\text{OIII}]$  are reported in Table 4.3.2. For the rest-UV lines, we use the local continuum measured directly from the spectra, which is detected in all galaxies in the final sample. We check that the UV continuum from the SED fitting model is consistent with the continuum measured in the spectra. For example, for the C3-VANDELS sample, the difference for the continuum for  $\text{CIII]}$  between the SED model and the local continuum measured directly from the spectra is, on average,  $\sim 14\%$ . This difference implies a difference in the EW of  $\sim 0.6\text{\AA}$ , on average, which is smaller than the typical error of  $0.93\text{\AA}$  in the EWs.

Most of the targets (20 out of 35) in our sample are at  $z > 3$ , which means that  $H\alpha$  is not included in the observed NIR spectral range. For this reason, we can not determine the nebular extinction

( $E(B-V)_g$ ) based on Balmer decrement for the entire sample. For the galaxies (12 out of 35) with detected  $H\alpha$  and  $H\beta$  ( $S/N > 2$ ), we estimated the nebular attenuation assuming  $H\alpha/H\beta = 2.79$  under Case B Approximation for  $T_e = 15000\text{K}$  and  $n_e = 100\text{ cm}^{-3}$  (Pérez-Montero, 2017) and considering the Cardelli law (Cardelli et al., 1989). The obtained  $E(B-V)_g$  values are reported in Table 4.2.2. On the other hand, we have an estimation of the stellar extinction, which is obtained from the SED fitting. Most of our galaxies have low dust content with  $E(B-V)_{\text{SED}} < 0.25\text{ mag}$  (see Table 4.2.2). From this subsample, we extrapolate the nebular extinction for the entire sample based on their SED extinction. The best linear fit leads to  $E(B-V)_g = 0.75 \times E(B-V)_{\text{SED}} + 0.19$ . We use this extrapolation only where  $E(B-V)_g$  is not determined directly by the Balmer decrement. We correct the observed fluxes (reported in Tables 4.3.1 and 4.3.2) assuming the Reddy et al. (2015) law with  $R_V = 2.505$ , based on other works with UV emission lines (e.g., Mingozi et al., 2022).

### 4.3.3 SFR surface density

We also estimate the instantaneous  $\text{SFR}(H\alpha)$  using the relation  $\log \text{SFR}(H\alpha) = \log(L(H\alpha)[\text{ergs}^{-1}]) - 41.27$  which assumes the Chabrier (2003) IMF (Kennicutt & Evans, 2012) and the luminosities are corrected by dust reddening as explained in Sec. 4.3.2. For the cases where  $H\alpha$  is not available, we use  $H\beta$  assuming the same theoretical ratio  $H\alpha/H\beta = 2.79$ . Since  $H\alpha$  is only available for a small subsample, and  $H\beta$  is fainter and has lower  $S/N$  compared to [OIII], a multiple Gaussian components analysis is not possible for the entire sample. For this reason, we assume the same broad-to-narrow flux ( $f_B$ ) ratio from [OIII] to take into account only the flux from the narrow  $H\alpha$  (or  $H\beta$ ) to estimate the SFR, excluding the contribution from the broad component.

We use the above values to derive the instantaneous SFR surface density ( $\Sigma_{\text{SFR}}$ ) defined as  $\Sigma_{\text{SFR}} = \frac{\text{SFR}(H\alpha)}{2\pi r_H^2}$ , where  $r_H$  is the effective radius of the galaxy measured in the H-band. We obtained the effective radius directly from the literature based on HST imaging. For the C3-VANDELS sample, they are obtained directly from the CANDELS catalog (van der Wel et al., 2012), while for the VUDS sample, they are obtained from Ribeiro et al. (2016). In both cases, they used GALFIT (Peng et al., 2002, 2010a) and HST/F160W images to fit Sérsic profiles to obtain the effective radius. For the C3-VUDS subsample, there are 6 out of 18 galaxies for which the H-band HST image is not available. They are identified in Table 4.3.3. In those cases, we consider the effective radius using HST/F814W images from the same Ribeiro et al. (2016) catalog following consistent methodology.

We note that at the redshift range covered for our sample, the F814W images trace the rest-frame UV-continuum by mostly massive stars, while the F160W images trace the rest-frame optical, which includes older stars and extended gas. From the C3-VUDS galaxies with both images available (12 galaxies), we find that the effective radius from the H-band image is typically a factor 1.4 greater than in the i-band. Still, in a few cases (3 out of 12), the differences can be up to a factor of  $\sim 3$ . When only HST/F814W is available, we correct the effective radius by a factor of 1.4.

In Fig. 4.3.6, we display the HST/F160W images of the C3-VANDELS sample with two components in their [OIII] profile. While in Fig. 4.3.7, we show the same but for the C3-VANDELS sample with a single Gaussian model. The images for the C3-VUDS sample are shown in Fig. 4.3.8 and 4.3.9 for the galaxies with and without broad component, respectively. We note that in both cases, most of the galaxies (25 out of 35) tend to be compact, i.e., they show smaller sizes compared with

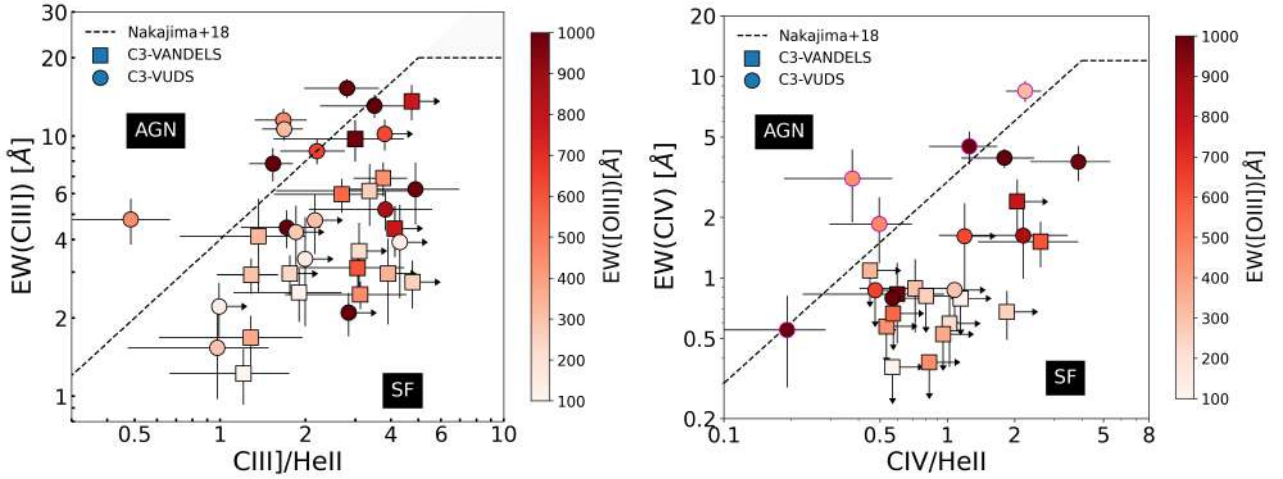


Figure 4.4.1: UV diagnostic diagrams for our sample based on the EWs of CIII] (*left*) and CIV (*right*). In both panels, our sample is color-coded by EW([OIII]), and the black dashed lines are the demarcation between AGN (on the left) and SF (on the right) according to Nakajima et al. (2018b). On the right panel, the symbols with magenta edges are galaxies classified as AGN according to the EW(CIII)]-CIII]/HeII diagram.

the Size-Mass Relation at  $z \sim 2.75$  of late-type galaxies (van der Wel et al., 2014). They do not show clear evidence of mergers.

## 4.4 Results

### 4.4.1 Ionizing sources: Diagnostic diagrams

In this section, we analyze the ionization source of the galaxies in our sample. First, we use the UV diagnostic diagram based on the EW(CIII)] vs CIII]/HeII $\lambda$ 1640 flux ratio and EW(CIV)] vs CIV/HeII $\lambda$ 1640 flux ratio. The results are shown in Fig. 4.4.1. It is shown that most of the galaxies in the sample are consistent with being ionized by massive stars according to the demarcation lines in Nakajima et al. (2018b). For some galaxies, these ratios are lower limits due to the fact that HeII $\lambda$ 1640 (or CIV) is not detected in their spectra, and then  $2\sigma$  upper limits are determined. It can be seen that the more extreme [OIII] emitters tend to fall in the upper right of the diagrams, suggesting high EW(CIII)] and EW(CIV) but not very strong HeII $\lambda$ 1640 that could be an indication of AGN contribution.

We find that all the galaxies in the C3-VANDELS sample are consistent with pure stellar photoionization, but there are few (5 galaxies in each diagram) C3-VUDS galaxies that are in the AGN region or near the boundary between both regions (symbols with magenta edges on the right panel in Fig. 4.4.1). In particular, two of these galaxies (5100998761 and 5101421970) show also unusually high  $T_e > 20000\text{K}$  (see Section 4.4.4), and some non-thermal contribution cannot be ruled out according to these diagnostics. Such high  $T_e$  are now observed in young SFGs in the EoR ( $z = 5.33 - 6.93$ ) with intense EW([OIII] $\lambda$ 4959,5007+H $\beta$ ) $\sim 1000\text{\AA}$  (Matthee et al., 2022) and have been previously reported in extremely metal-poor starbursts in the local Universe (Kehrig et al., 2016).

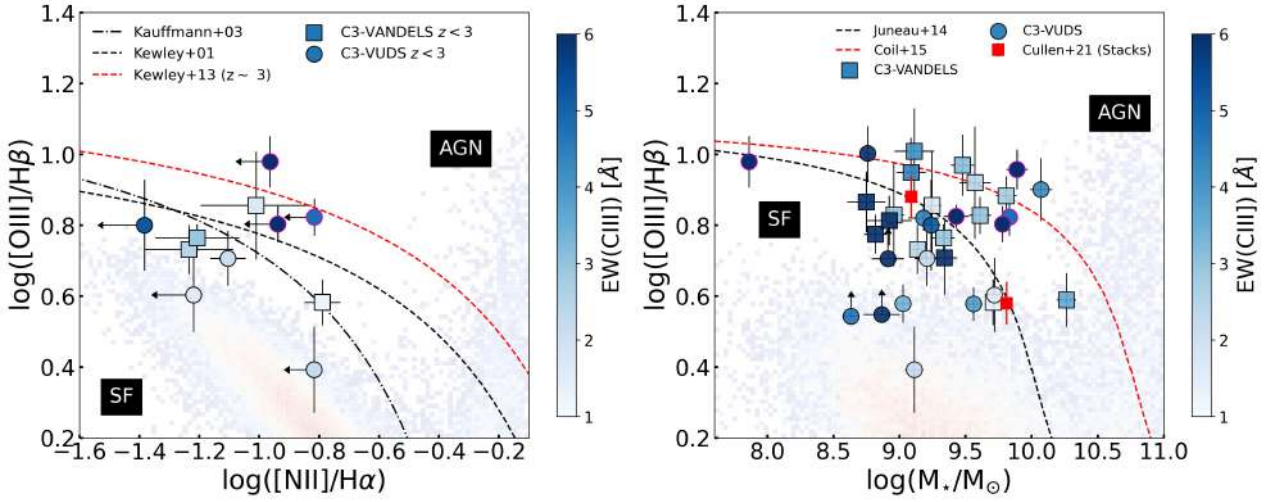


Figure 4.4.2: *Left*: Classical BPT diagram (Baldwin et al., 1981) for our subsample at  $z < 3$ , color-coded by  $\text{EW}(\text{CIII})$ . The black dashed lines are the typical local AGN/SF demarcation lines from Kewley et al. (2001); Kauffmann et al. (2003). The red dashed line is the demarcation at  $z \sim 3$  according to Kewley et al. (2013). *Right*: Mass-Excitation diagram for our entire sample color-coded by  $\text{EW}(\text{CIII})$ . The black and red dashed lines are the AGN/SF demarcation at low- $z$  (Juneau et al., 2014) and  $z \sim 2.3$  (Coil et al., 2015), respectively. As a reference, we include the stacks from Cullen et al. (2021), from which our VANDELs subsample is a subset. On both panels, the symbols with magenta edges are galaxies classified as AGN according to UV diagnostic diagrams in Fig. 4.4.1.

Recently, the C IV/C III] ratio has been proposed as a potential indirect indicator to constrain the LyC escape fraction (Schaerer et al., 2022a; Saxena et al., 2022b). We also find that most of the galaxies are consistent within the errors with  $\text{CIV}/\text{CIII}] < 0.7$ , which indicates they are not strong LyC leakers and are likely to show  $f_{\text{esc}} < 0.1$ . Only one VUDS galaxy (5101421970) shows  $\text{CIV}/\text{CIII}] > 0.7$ , which in the UV diagnostic diagrams is classified as AGN.

We also explore Baldwin, Phillips & Terlevich (BPT, Baldwin et al., 1981) optical diagnostics to verify the SF nature of these galaxies. In Fig. 4.4.2 (left panel) we show the classical BPT diagram ( $[\text{NII}]\lambda 6583/\text{H}\alpha$  vs  $[\text{OIII}]/\text{H}\beta$ ) for the subsample of galaxies at  $z < 3$  for which  $\text{H}\alpha$  is included in K band. It can be seen that this subsample falls within demarcation lines for SF regions and is broadly offset from the typical excitation of local SFGs. We notice that the subsample at  $z < 3$  are among the fainter CIII] emitters in the entire sample with  $\text{EW}(\text{CIII}) < 3\text{\AA}$ , in particular the ones with  $[\text{NII}]\lambda 6584$  detected. The more extreme CIII] emitters (with  $\text{EW}_s > 4\text{\AA}$ ) tend to show upper limits in  $[\text{NII}]$  and high  $[\text{OIII}]/\text{H}\beta$  ratios.

Finally, in Fig. 4.4.2 (right panel), we explore the Mass-Excitation (MEx, Juneau et al., 2014) diagram for the entire sample (except for the galaxies that do not have  $\text{H}\beta$  in the spectral range). Similarly to the BPT diagram, we find that they are also consistent with SF. The more extreme CIII] emitters tend to fall in the low mass region (roughly  $< 10^{9.5} M_{\odot}$ ) and high  $[\text{OIII}]/\text{H}\beta > 4$ , which indicates a highly excited ISM. The two particular extreme galaxies with possible AGN contribution are in the SF region in this diagram (one of them shows the smaller stellar mass in the sample). The above analysis suggests that combining UV and optical lines may give us more clues on their nature, particularly for extremely metal-poor SF galaxies, which may display very high electron temperatures. Hereafter, we consider that the galaxies in our sample are dominated by SF with a highly excited ISM

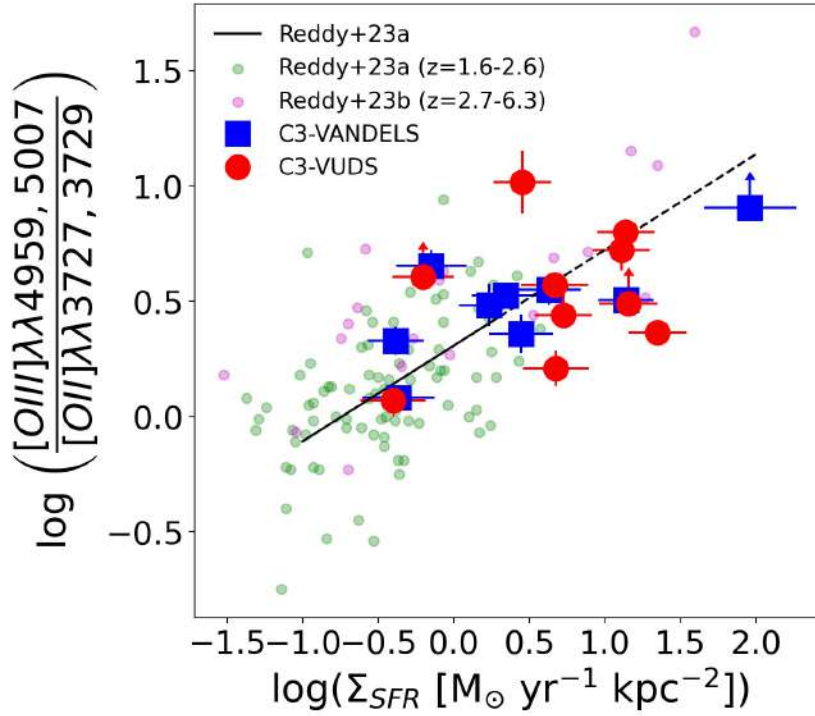


Figure 4.4.3: Variation of  $[\text{OIII}]/[\text{OII}]$  with  $\Sigma_{\text{SFR}}$ . Individual galaxies with detected  $[\text{OII}]$  are shown with red and blue symbols for the C3-VUDS and C3-VANDELS samples, respectively. We also include lower limits based on upper limits on  $[\text{OII}]$ . The green and magenta small circles are galaxies from Reddy et al. (2023a) at  $z = 1.6 - 2.6$  and Reddy et al. (2023b) at  $z = 2.7 - 6.3$ , respectively. The black solid line is the relation presented in Reddy et al. (2023a) and its extrapolation up to  $\Sigma_{\text{SFR}} = 100 \text{ M}_{\odot} \text{ yr}^{-1} \text{ kpc}^{-2}$  is in dashed black line.

and do not show clear evidence of AGN contribution based on their emission lines.

## 4.4.2 Ionization parameter

We also study the ionization properties of our sample of galaxies by means of a tracer of the ionization parameter  $\log U$ . Given the limited wavelength coverage of our spectra, we use the  $\frac{[\text{OIII}]\lambda\lambda 4959, 5007}{[\text{OII}]\lambda\lambda 3727, 3729}$  ratio as a proxy for  $\log U$  (Kewley et al., 2019). We find  $[\text{OIII}]/[\text{OII}]$  values within 1 and 10, which imply a high ionization parameter between roughly  $\log U = -3$  and  $\log U = -2$  (Reddy et al., 2023a).

In Fig. 4.4.3, we present the relation for  $[\text{OIII}]/[\text{OII}]$  and  $\Sigma_{\text{SFR}}$  found by Reddy et al. (2023a,b) for SFGs in the MOSDEF survey and others at higher redshift, suggesting that galaxies with more compact and violent star formation show more extreme ionization conditions. We find that our VANDELS and VUDS galaxies follow the same trend and lie closer to the  $z > 3$  galaxies than the ones at  $z < 2.6$  in the above works. Despite our sample galaxies lying mostly in the SF main sequence at  $z \sim 3$  (Fig. 4.3.1), their ionization properties and emission line EWs appear more extreme than their counterparts at lower redshift.

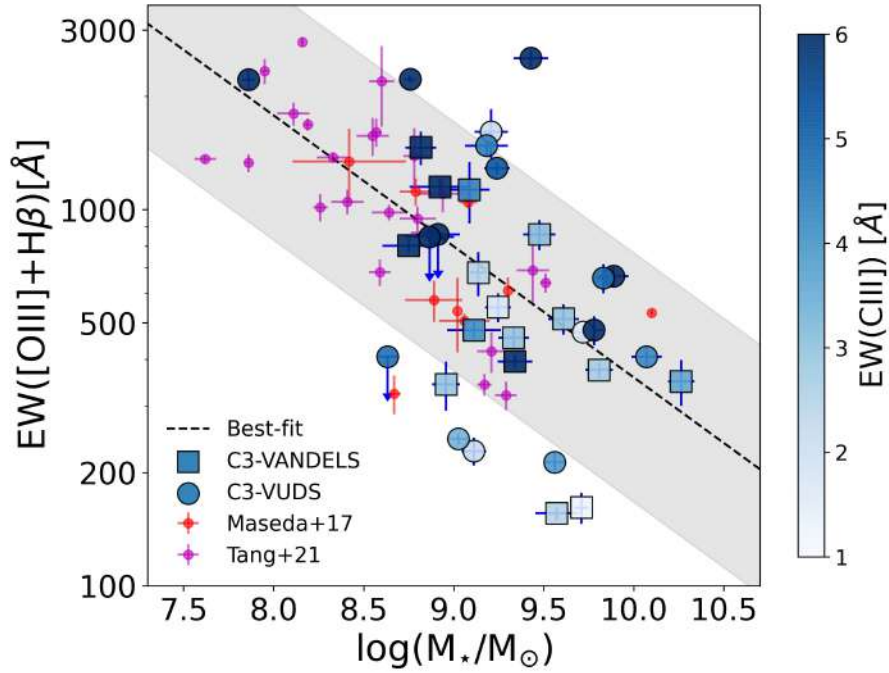


Figure 4.4.4: Relation between  $EW([\text{OIII}]\lambda\lambda 4959,5007+\text{H}\beta)$  and stellar mass. Our sample is color-coded by  $EW(\text{CIII])}$ . The small red and magenta circles are literature samples at intermediate redshifts from Maseda et al. (2017) and Tang et al. (2021), respectively. The black dashed line is the best fit (slope  $-0.34$ ) with our data and the gray shaded region is the  $1\sigma$  observed scatter of  $0.33$  dex.

### 4.4.3 EW relations

For UV lines, we find that our sample covers a range of  $EW(\text{CIII])}$  from  $\sim 1\text{\AA}$  to  $\sim 15\text{\AA}$  with a mean value of  $5.6\text{\AA}$  ( $\sigma = 3.7\text{\AA}$ ). Six galaxies (17%) show  $EW(\text{CIII])} > 10\text{\AA}$ , similar to the EW values observed in galaxies at  $z > 6$  (e.g., Stark et al., 2017; Hutchison et al., 2019). Our sample includes 14 galaxies at  $z \gtrsim 3$  with  $\text{Ly}\alpha$  included in our spectral range and with  $EW(\text{Ly}\alpha) > 20\text{\AA}$ , five of them reaching  $EW(\text{Ly}\alpha) > 100\text{\AA}$ .

For optical lines, we find strong  $[\text{OIII}]\lambda\lambda 4959,5007$  emission, with  $EW([\text{OIII}])$  spanning from  $102\text{\AA}$  to  $1715\text{\AA}$  with a mean value of  $563\text{\AA}$  ( $\sigma = 420\text{\AA}$ ), well within the typical EWs defined for EELGs at lower redshifts (e.g., Amorín et al., 2014, 2015; Calabrò et al., 2017; Pérez-Montero et al., 2021). Only 5 galaxies (14%) of the sample show  $EW([\text{OIII}]) > 1000\text{\AA}$ , which are typical values found for  $z > 6$  EoR galaxies from photometric data (e.g., Endsley et al., 2021) and more recently with JWST spectroscopy (Matthee et al., 2022).

We explore the correlation between stellar mass and  $[\text{OIII}]+\text{H}\beta$  EWs in Fig. 4.4.4. We find that low-mass galaxies tend to show higher EWs, following a similar trend found in the literature, both at  $z \sim 2-3$  (e.g., Maseda et al., 2017; Tang et al., 2021) and in reionization galaxies (Endsley et al., 2021). The most extreme EWs in our sample correspond to galaxies with  $EW(\text{CIII])} > 5\text{\AA}$  and  $EW([\text{OIII}]\lambda\lambda 4959,5007+\text{H}\beta) > 500\text{\AA}$ , as shown in Fig. 4.4.5, which are still rare at  $z \sim 3$  but becomes the norm towards reionization (e.g., Smit et al., 2014; De Barros et al., 2019; Endsley et al., 2021; Sun et al., 2022a,b; Matthee et al., 2022). The trend in Fig. 4.4.5 also shows that the strong  $[\text{OIII}]$  and  $\text{CIII]}$  emitters at  $z > 3$  are typically those with larger EW in  $\text{Ly}\alpha$  ( $\gtrsim 20\text{\AA}$ ). However, a

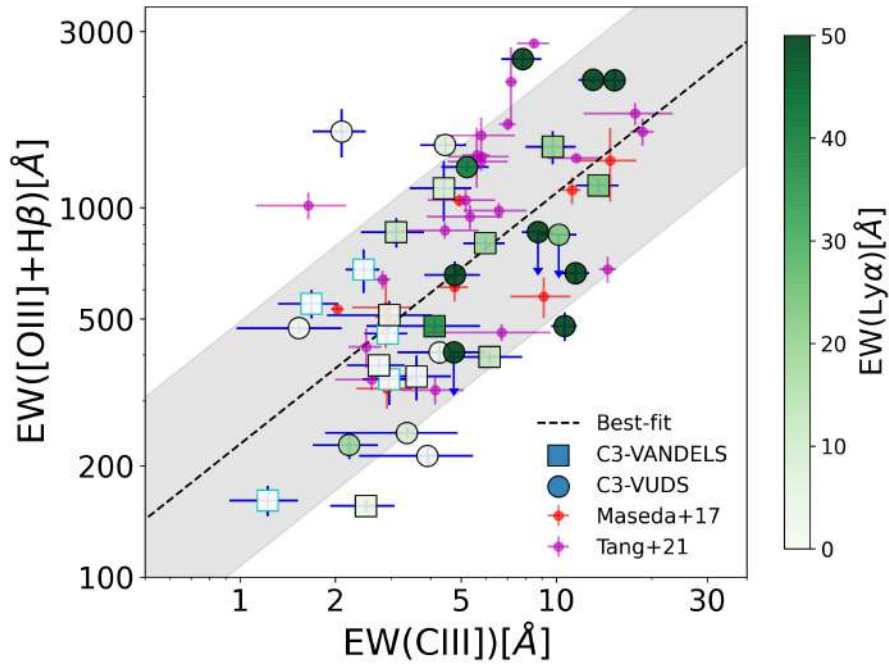


Figure 4.4.5: Relation between  $\text{EW}([\text{OIII}]\lambda\lambda 4959, 5007 + \text{H}\beta)$  and  $\text{EW}(\text{CIII})$ . Our sample is color-coded by  $\text{EW}(\text{Ly}\alpha)$ . The square symbols with cyan edges are galaxies in the C3-VANDELS at  $z < 3$ , for which  $\text{Ly}\alpha$  is not in the spectral range. The small red and magenta circles are literature samples at intermediate redshifts from Maseda et al. (2017) and Tang et al. (2021), respectively. The black dashed line is the best fit (slope 0.68) with our data and the gray shaded region is the  $1\sigma$  observed scatter of 0.33 dex.

few galaxies with weak  $\text{Ly}\alpha$  emission are found among the strong  $[\text{OIII}]$  emitters, in agreement with previous works (Le Fèvre et al., 2019; Du et al., 2020).

The above results can be interpreted in the context of the galaxies ionizing photon production efficiency, which correlates with  $\text{H}\alpha$  and  $[\text{OIII}]$  EWs (Tang et al., 2019). Even for extreme  $[\text{OIII}] + \text{H}\beta$  emitters that efficiently produce ionizing photons, the emerging  $\text{Ly}\alpha$  line will not be necessarily intense due to its resonant nature, which makes it sensitive to dust content, neutral hydrogen column density and their spatial distribution (e.g., Hayes, 2015). Indeed, our subsample of strong  $[\text{OIII}]$  emitters with lower  $\text{EW}(\text{Ly}\alpha)$  are found to show higher dust extinction. These objects are likely found in a very early phase after the onset of star formation where the young ( $< 2\text{-}3\text{Myr}$ ) massive stars are still embedded in their dense and dusty birth clouds and did not have enough time to clear channels through the ISM via feedback (e.g., winds, supernovae), and then  $\text{Ly}\alpha$  photons are trapped while  $\text{LyC}$  photons are absorbed (Naidu et al., 2022).

#### 4.4.4 Electron densities and temperatures

The two components of the doublet  $[\text{OII}]\lambda\lambda 3727, 3729$  are detected and unaffected by strong sky residuals in 15 galaxies of our entire sample. For this subsample, we estimate the electron density using the `getTemDen` task in `PyNeb`<sup>‡</sup> (Luridiana et al., 2012, 2015), which is a modern python tool

<sup>‡</sup><http://research.iac.es/proyecto/PyNeb//>

to compute emission line emissivities of recombination and collisionally excited lines and for given density and temperature, the code solves the equilibrium equations and determines the level populations. In our calculations, we assumed  $T_e = 15000\text{K}$  and performed 100 Monte Carlo simulations in order to include the uncertainties of the observed fluxes. We find a wide range of electron densities from  $\sim 47$  to  $\sim 1261\text{ cm}^{-3}$ , with a mean value of  $560\text{ cm}^{-3}$ . These values are within the range of values reported at similar redshifts (e.g., [Sanders et al., 2016](#); [Reddy et al., 2023a](#)). Given the uncertainties (we obtained a mean value of  $327\text{ cm}^{-3}$ ) in the estimated  $n_e$  values due to the low S/N of  $[\text{OII}]\lambda\lambda 3727, 3729$ , we report densities as upper limits in Table 4.4.1 and in the following sections we use only the mean value of the entire sample.

In order to estimate the electron temperature we used the  $\text{OIII}\lambda 1666/[\text{OIII}]\lambda 5007$  ratio where available.  $\text{OIII}\lambda 1666$  is detected with  $\text{S/N} > 2$  in 21 galaxies in our sample. We use the `getTemDen` task in `PyNeb` assuming  $n_e = 560\text{ cm}^{-3}$ . Given that an offset between the  $T_e([\text{OIII}])$  found using this ratio and the commonly used ratio  $[\text{OIII}]\lambda 4363/[\text{OIII}]\lambda 5007$  has been found in local galaxies, we correct downwards the obtained temperature by the typical difference of  $-0.025$  dex obtained for CLASSY SFGs in [Mingozzi et al. \(2022\)](#), which leads to differences of  $\sim -1000\text{K}$ . We report these temperatures in Table 4.4.1. As discussed in [Mingozzi et al. \(2022\)](#), one of the intrinsic reasons that may explain the offset between both methods is that the ISM is patchy. The UV light is visible only through the less dense (and/or less reddened) regions along the line of sight, while the optical may be arising also from denser (and/or more reddened regions). We find  $T_e([\text{OIII}]) > 1.3 \times 10^4\text{K}$  with some objects having very high temperatures but not exceeding  $2.5 \times 10^4\text{K}$ , as reported in Table 4.4.1. We find a mean value of  $1.77 \times 10^4\text{K}$  for the entire sample with typical errors of  $0.2 \times 10^4\text{K}$ , which were calculated with 100 Monte Carlo simulations taking into account a normal distribution of the fluxes of the used lines to estimate  $T_e([\text{OIII}])$ . Our results are consistent with the early results from the JWST/NIRSpec, based on the first direct detection of the faint auroral line  $[\text{OIII}]\lambda 4363$  at  $z \sim 8$ , where  $T_e$  from  $1.2 \times 10^4$  and up to  $2.8 \times 10^4\text{K}$  are estimated, with the  $T_e$ -based metallicities ranging from extremely metal-poor ( $12 + \log(\text{O}/\text{H}) < 7$ ) to about one-third solar ([Schaerer et al., 2022b](#); [Trump et al., 2022](#); [Curti et al., 2023](#); [Nakajima et al., 2022](#)).

We note that the  $\text{OIII}\lambda 1666/[\text{OIII}]\lambda 5007$  ratio is obtained from two different instruments, which may result in possible systematic errors due to flux calibration and dust attenuation corrections, given the large wavelength separation of the lines. First, we checked that the spectra are consistent with the photometry based on the SED model to avoid flux-matching issues. For example, we find that the difference between the mean continuum between  $1450$  and  $1500\text{\AA}$  in the SED model and the observed spectrum is on average  $\sim 10\%$  of the observed flux which is lower than the scatter in this spectral region, which is on average  $25\%$  of the observed flux. Additionally, we check that changing the dust attenuation law does not affect our results. For instance, if we consider the [Calzetti et al. \(2000\)](#) law, the mean  $T_e$  changes by only  $76\text{ K}$ , which is negligible compared with the typical uncertainties.

#### 4.4.5 Oxygen and Carbon abundance

The study of the abundances of heavy elements in the ISM of galaxies provides precious insights into the physical processes responsible for their formation and how the relative importance of such processes has changed across cosmic time (see the review by [Maiolino & Mannucci, 2019](#)). Due to the line production mechanisms, nebular UV emission can be used to also directly calculate the physical and chemical conditions under which emission lines are produced. For instance, while the

Table 4.4.1: Electron density, temperature and chemical abundances estimated for our sample

ID	$n_e$ [ $\text{cm}^{-3}$ ]	$t_e$ [ $10^4\text{K}$ ]	$\log(\text{O}/\text{H})_{\text{PyNeb}}+12^{\text{a}}$ (1)	$\log(\text{O}/\text{H})_{\text{SLC}}+12^{\text{b}}$ (2)	$\log(\text{O}/\text{H})_{\text{SLC-UV}}+12^{\text{c}}$ (3)	$\log(\text{O}/\text{H})_{\text{HCM-UV}}+12^{\text{d}}$ (4)	$\log(\text{C}/\text{O})$
C3-VANDELS sample							
UDS020394	...	$1.85 \pm 0.2$	$7.74 \pm 0.1$	...	...	$7.74 \pm 0.1$	$-0.49 \pm 0.19$
CDFS020954	$<1048.0$	$1.83 \pm 0.15$	$7.78 \pm 0.13$	$8.08 \pm 0.12$	$7.61 \pm 0.06$	$7.78 \pm 0.13$	$-0.69 \pm 0.17$
CDFS023527	...	$1.93 \pm 0.16$	...	...	$7.65 \pm 0.04$	$7.39 \pm 0.09$	$-0.66 \pm 0.12$
UDS021601	...	$<1.81$	...	...	...	$7.85 \pm 0.32$	$-0.44 \pm 0.35$
CDFS022563	$<272.0$	$1.82 \pm 0.18$	$7.85 \pm 0.14$	$8.11 \pm 0.12$	$7.64 \pm 0.05$	$7.85 \pm 0.14$	$-0.51 \pm 0.2$
UDS022487	$<570.0$	$1.89 \pm 0.2$	$7.96 \pm 0.17$	$8.14 \pm 0.12$	...	$7.96 \pm 0.17$	$-0.9 \pm 0.15$
CDFS015347	...	$2.47 \pm 0.27$	$7.78 \pm 0.18$	...	$7.46 \pm 0.11$	$7.78 \pm 0.18$	$-0.92 \pm 0.14$
CDFS019276	$<259.0$	$<1.59$	...	$8.18 \pm 0.12$	...	$7.84 \pm 0.29$	$-0.31 \pm 0.2$
UDS020928	$<179.0$	$1.29 \pm 0.2$	$8.31 \pm 0.12$	$8.12 \pm 0.12$	$7.67 \pm 0.07$	$8.31 \pm 0.12$	$-0.34 \pm 0.15$
CDFS019946	...	$<2.81$	...	...	...	$7.76 \pm 0.08$	$-0.48 \pm 0.23$
UDS020437	$<239.0$	$1.79 \pm 0.2$	$7.9 \pm 0.18$	$8.19 \pm 0.12$	...	$7.9 \pm 0.18$	$-0.73 \pm 0.23$
CDFS018182	...	$1.38 \pm 0.15$	...	...	$7.59 \pm 0.05$	$8.23 \pm 0.23$	$-0.4 \pm 0.22$
CDFS018882	$<830.0$	$1.88 \pm 0.23$	$7.89 \pm 0.16$	$8.13 \pm 0.12$	...	$7.89 \pm 0.16$	$-0.64 \pm 0.18$
CDFS025828	$<328.0$	$<3.02$	...	$8.28 \pm 0.12$	...	$7.94 \pm 0.3$	$-0.73 \pm 0.21$
CDFS022799	...	$<1.22$	...	...	...	$8.4 \pm 0.18$	$-0.67 \pm 0.14$
UDS021398	...	$<2.03$	...	...	...	$7.78 \pm 0.2$	$-0.57 \pm 0.29$
UDS015872	...	$<1.54$	...	...	...	$7.92 \pm 0.32$	$-0.33 \pm 0.22$
C3-VUDS sample							
5100998761	...	$2.15 \pm 0.12$	$7.75 \pm 0.09$	...	$7.64 \pm 0.03$	$7.75 \pm 0.09$	$-0.49 \pm 0.09$
5101444192	...	$1.64 \pm 0.06$	$7.99 \pm 0.08$	...	$7.64 \pm 0.04$	$7.99 \pm 0.08$	$-0.56 \pm 0.11$
510994594	...	$<1.22$	...	...	...	$8.36 \pm 0.16$	$0.02 \pm 0.18$
5101421970	$<1201.0$	$1.98 \pm 0.21$	$7.64 \pm 0.08$	$7.95 \pm 0.13$	$7.6 \pm 0.03$	$7.64 \pm 0.08$	$-0.27 \pm 0.08$
510838687	...	$2.14 \pm 0.24$	...	...	...	$7.59 \pm 0.14$	$-0.69 \pm 0.16$
5100556178	...	$<1.38$	...	...	...	$8.11 \pm 0.27$	$-0.24 \pm 0.14$
511229433	$<468.0$	$1.46 \pm 0.08$	$7.99 \pm 0.09$	$8.05 \pm 0.12$	$7.59 \pm 0.04$	$7.99 \pm 0.09$	$-0.58 \pm 0.09$
511245444	...	$1.42 \pm 0.12$	...	...	$7.7 \pm 0.06$	$8.07 \pm 0.21$	$-0.35 \pm 0.1$
530048433	$<47.0$	$1.41 \pm 0.2$	$8.05 \pm 0.17$	$8.11 \pm 0.12$	$7.71 \pm 0.06$	$8.05 \pm 0.17$	$-0.21 \pm 0.22$
510583858	...	$1.61 \pm 0.14$	$7.88 \pm 0.1$	...	$7.45 \pm 0.06$	$7.88 \pm 0.1$	$-0.53 \pm 0.16$
511451385	...	$2.44 \pm 0.32$	...	...	...	$7.73 \pm 0.62$	$-0.6 \pm 0.17$
511025693	$<510.0$	$1.52 \pm 0.13$	$7.94 \pm 0.09$	$8.03 \pm 0.12$	$7.56 \pm 0.06$	$7.94 \pm 0.09$	$-0.65 \pm 0.17$
5100997733	...	$<1.94$	...	...	...	$7.83 \pm 0.19$	$-0.52 \pm 0.32$
511228062	$<1261.0$	$<1.29$	...	$8.18 \pm 0.12$	...	$8.24 \pm 0.16$	$-0.29 \pm 0.17$
5101001604	...	$<2.83$	...	...	...	$7.7 \pm 0.14$	$-0.62 \pm 0.28$
510996058	$<1061.0$	$<2.14$	...	$8.28 \pm 0.12$	...	$7.51 \pm 0.21$	$-0.41 \pm 0.29$
511001501	$<195.0$	$<1.39$	...	$8.23 \pm 0.12$	...	$8.1 \pm 0.39$	$-0.43 \pm 0.35$
530053714	...	$1.39 \pm 0.15$	$7.85 \pm 0.14$	...	$7.45 \pm 0.12$	$7.85 \pm 0.14$	$-0.68 \pm 0.2$

(a) Metallicity from PyNeb method

(b) Metallicity from Strong-Line Calibration method with O32 parameter (Pérez-Montero et al., 2021)

(c) Metallicity from corrected UV Strong-Line Calibration method with He2-O3C3 parameter (Mingozzi et al., 2022)

(d) Metallicity from HCM-UV corrected according by a factor 0.3 dex when  $\log(\text{O}/\text{H})_{\text{PyNeb}}$  is not available.

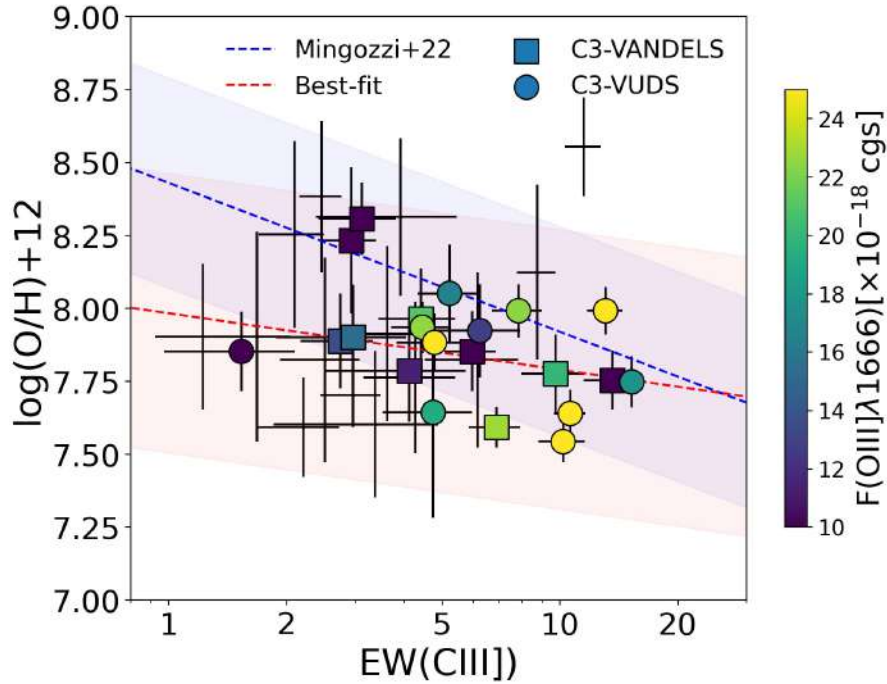


Figure 4.4.6: Relation between gas-phase metallicity and  $\text{EW}(\text{C III]})$  for our sample. The blue dashed line and blue shaded region corresponds to the relation found in Mingozi et al. (2022) at low  $z$  and their observed  $2\sigma$  scatter. The red dashed line is our best fit and the observed  $2\sigma$  scatter is the red shaded region. The sample is color-coded by  $\text{O III]}$  flux in the cases where this line is detected at  $S/N > 2$ . In the other cases, only errorbars are shown.

oxygen abundance ( $\text{O}/\text{H}$ ) is the standard measure of a gas-phase metallicity in galaxies,  $\text{C III]}$  provides a path to estimate the C abundance, which is a non- $\alpha$  element. Because C is primarily produced in lower mass stars than O, the injection of C and O to the ISM occurs on different time scales, providing a probe of the duration, history, and burstiness of the star formation (e.g., Berg et al., 2019). Also, the relative abundance of C and O can be relatively unaffected by hydrodynamical processes, like outflows of enriched gas (e.g., Edmunds, 1990). In particular, the line intensity ratio  $\text{C III]}/\text{O III]}\lambda 1666$  has been used to estimate the relative C/O abundances at different redshifts (e.g., Garnett et al., 1995; Shapley et al., 2003; Erb et al., 2010; Steidel et al., 2016; Berg et al., 2016; Pérez-Montero & Amorín, 2017; Berg et al., 2019; Amorín et al., 2017; Llerena et al., 2022). Moreover, the combination of UV+optical emission lines has been explored to constrain  $T_e$  using the  $\text{O III]}\lambda 1666/[\text{O III]}\lambda 5007$  ratio (Pérez-Montero & Amorín, 2017), and then to estimate gas-phase metallicity, in particular for those cases where the optical auroral line  $[\text{O III]}\lambda 4363$  is not available due to weakness or spectral coverage.

We derive the C/O abundance based on photoionization models using the public version 4.23<sup>§</sup> of HCM-UV (Pérez-Montero & Amorín, 2017) using as an ionizing source for the models the POP-STAR synthetic SEDs (Mollá et al., 2009) and assuming the relations between metallicity and excitation for EELGs assumed by the code when no auroral emission line is provided. The code HCM-UV performs a Bayesian-like calculation that compares extinction-corrected UV emission line fluxes and their uncertainties with the prediction of a grid of models covering a wide range of values in  $\text{O}/\text{H}$ ,  $\text{C}/\text{O}$ , and  $\log U$ . The code calculates C/O as the average of the  $\chi^2$ -weighted distribution of the C/O values in the models. Then, C/O is fixed in the grid of models, and both  $\text{O}/\text{H}$  and  $\log U$  are calculated

<sup>§</sup><http://home.iaa.csic.es/~epm/HII-CHI-mistry-UV.html>

as the mean of the model input values in the  $\chi^2$ -weighted distribution. The  $\chi^2$  values for each model are derived from the quadratic relative differences between the observed and predicted emission-line ratios. The uncertainties of the derived parameters are calculated as the quadratic addition of the weighted standard deviation and the dispersion of the results after a Monte Carlo simulation.

As input, we use CIII], OIII] $\lambda\lambda$ 1661,1666, H $\beta$ , and [OIII]. We do not include CIV in the input since CIV is only detected in 42% of our sample. We consider the ratio OIII] $\lambda$ 1661/OIII] $\lambda$ 1666=0.44, based on photoionization models (Gutkin et al., 2016). Due to the spectral resolution of  $\sim 7\text{\AA}$  at 1666 $\text{\AA}$  for the C3-VUDS sample, the OIII] $\lambda\lambda$ 1661,1666 is blended, and then the measured flux corresponds to the doublet. On the other hand, for the C3-VANDELS sample, the spectral resolution is  $\sim 3\text{\AA}$  at 1666 $\text{\AA}$ , we multiplied by a factor 1.44 the measured OIII] $\lambda$ 1666 flux to account for the doublet. We include the flux of the doublet OIII] $\lambda\lambda$ 1661,1666 in the input in the cases where the line is detected with  $S/N > 2$ . For the other lines, in the case of an upper limit, the  $2\sigma$  limit is considered as input in the code with an error of  $1\sigma$ , following the methodology described in Pérez-Montero et al. (2023). The obtained C/O values are, on average,  $\sim 0.11$  dex higher than that obtained if using the C3O3 calibration proposed by Pérez-Montero & Amorín (2017).

We find a mean value of  $\log(C/O) = -0.52$  ( $\sim 54\%$  solar) with a typical error of 0.15 dex which is consistent with the typical value of SFGs at  $z \sim 3$  based on stacking (Shapley et al., 2003; Llerena et al., 2022). Our results of  $\log(C/O)$  range from  $-0.90$  (23% solar) to  $-0.15$  (128% solar) and are consistent with the wide range of C/O values observed in local Blue Compact Dwarf (BCD) galaxies (Garnett et al., 1995, 1997; Kobulnicky et al., 1997; Kobulnicky & Skillman, 1998; Izotov et al., 1999; Thuan et al., 1999; Berg et al., 2016; Senchyna et al., 2021) and Giant HII regions (Garnett et al., 1995; Kurt et al., 1995; Garnett et al., 1999; Mattsson, 2010; Senchyna et al., 2021). The lowest values in our sample are also within the range of values reported of  $\log(C/O) = -0.83 \pm 0.38$  at metallicity  $< 2\%$  solar for EoR galaxies at  $z \sim 8$  from JWST spectra and is consistent with the large dispersion in  $\log(C/O)$  observed in  $z \sim 0 - 2$  low-metallicity dwarf galaxies without evidence of an evolution in the C/O versus O/H relationship (Arellano-Córdova et al., 2022). Even a lower value  $\log(C/O) = -1.01 \pm 0.22$  has been reported at  $z = 6.23$  which is consistent with the expected yield from core-collapse supernovae, indicating negligible carbon enrichment from intermediate-mass stars (Jones et al., 2023).

For the gas-phase metallicity derivation, we first use the HCM-UV code with the same input as described before. We then compare these results with the results obtained from an alternative methodology using PyNeb (Luridiana et al., 2012, 2015). To derive the total oxygen abundance we use the approximation  $O/H = \frac{O^+}{H^+} + \frac{O^{2+}}{H^+}$ . To estimate  $O^{2+}/H^+$ , we use the `getIonAbundance` task in PyNeb assuming the corrected electron temperature, the global [OIII] flux and  $n_e = 560 \text{ cm}^{-3}$ . To estimate  $O^+/H^+$  we use the same task with [OII] $\lambda$ 3727 where available (otherwise, we used [OII] $\lambda$ 3729 if available). To estimate  $T_e[\text{OII}]$ , we assume the relation  $T_e([\text{OII}]) = \frac{2}{T_e([\text{OIII}])^{-1} + 0.8}$  based on photoionization models to infer  $T_e([\text{OII}])$  from  $T_e([\text{OIII}])$  (Pérez-Montero, 2017). The total oxygen abundance  $\log(O/H)_{\text{PyNeb}}$  with this method is reported in Table 4.4.1.

A comparison of the above two methods finds an offset of  $\sim 0.4$  dex (a factor of 2.5) towards lower metallicity for the results based on HCM-UV. For the galaxies where the lack of detected lines the PyNeb method is not possible, we correct upwards the gas-phase metallicity from HCM-UV by a factor 0.4 dex. These values are reported in column 4 in Table 4.4.1. We find a mean value

of  $\log(O/H)_{\text{HCM-UV}} + 12 = 7.91$  (17% solar) with values ranging from 7 to 73% solar. Finally, we compare our metallicity derivation with the expected values using the EW(CIII)-metallicity calibration proposed by [Mingozi et al. \(2022\)](#) for local analogs, which is displayed in Fig. 4.4.6. For most galaxies in our sample, our results are consistent within  $2\sigma$  with the local relation (blue dashed line), which has an observed scatter of 0.18 dex. Our best fit (red dashed line) shows an offset towards lower values compared to the local relation and the observed scatter is 0.24 dex.

We compare our estimations with the results using Strong-Line Calibration (SLC) from pure optical and UV lines. For example, if we use the  $O32 = \log\left(\frac{[\text{OIII}]\lambda\lambda 4959, 5007}{[\text{OII}]\lambda 3727}\right)$  calibration from [Pérez-Montero et al. \(2021\)](#), we find that the obtained metallicities tend to be  $\sim 0.19$  dex offset towards higher metallicities. The values found using this calibrator are reported in column 2 in Table 4.4.1. A slightly higher mean offset of  $\sim 0.30$  dex is found using the [Bian et al. \(2018\)](#) O32 calibration. Moreover, if we use calibrations based only on UV lines, for instance, He2-O3C3 ([Byler et al., 2020](#)) based on the ratios  $\log\left(\frac{[\text{OIII}]\lambda 1666}{\text{CIII}}\right)$  and  $\log\left(\frac{[\text{HeII}]\lambda 1640}{\text{CIII}}\right)$ , we find metallicities that tend to be  $\sim 0.42$  dex lower than our estimated metallicities. This mean offset towards lower metallicities is reduced to  $\sim 0.30$  dex if we used the proposed corrected He2-O3C3 calibration in [Mingozi et al. \(2022\)](#) where offsets between UV and optical methods have been observed in local galaxies ([Mingozi et al., 2022](#)). The values found using this calibrator are reported in column 3 in Table 4.4.1.

Hereafter, we consider for our discussions the metallicities derived combining UV and optical emission lines in Table 4.4.1 column (4) since this method allows us to estimate gas-phase metallicities for the entire sample of galaxies.

#### 4.4.6 Ionized gas kinematics

In this Chapter, we interpret the narrow component in the [OIII] profile as the warm gas tracing virial motions within SF regions while the broad component is interpreted as the turbulent outflowing gas with a velocity in reference to the systemic velocity (cf, e.g., [Amorín et al., 2012a](#); [Arribas et al., 2014](#); [Freeman et al., 2019](#); [Hogarth et al., 2020](#)). The outflowing gas can be SF- or AGN-driven depending on the source of energy. From observations, SF-driven winds are closely coupled to SF properties such as  $\Sigma_{\text{SFR}}$  whereas AGN-driven winds are strongly correlated with stellar mass and are rare in low-mass galaxies ([Förster Schreiber et al., 2019](#)). In the literature, broad components have been observed in AGN with large velocity dispersion  $> 200\text{km s}^{-1}$  ([Rodríguez del Pino et al., 2019](#); [Förster Schreiber et al., 2019](#)).

In order to obtain the intrinsic velocity dispersion of the [OIII] lines we subtracted the instrumental ( $\sigma_{\text{ins}}$ ) and thermal ( $\sigma_{\text{ther}}$ ) widths in quadrature. For the former, we considered the resolution in the H-band of  $R = 3600$  (for MOSFIRE) and  $R = 5600$  (for X-shooter) which corresponds to  $\sigma_{\text{ins}} \sim 35\text{km s}^{-1}$  and  $\sim 23\text{km s}^{-1}$ , respectively. For the latter, we assume the same formula as in [Hogarth et al. \(2020\)](#) and assume the mean  $T_e$  value obtained for the sample of  $1.77 \times 10^4\text{K}$ , which leads to  $\sigma_{\text{ther}} \sim 0.8\text{km s}^{-1}$ . As described in Sec. 4.3.2, we assume that the second component is broad if there is a difference greater than  $35\text{km s}^{-1}$  with respect to the narrower component which coincides with the global peak of the profile. From the 23 galaxies with two kinematic components, we find that 3 of them do not show a broad component but they show two narrow instead. These galaxies are

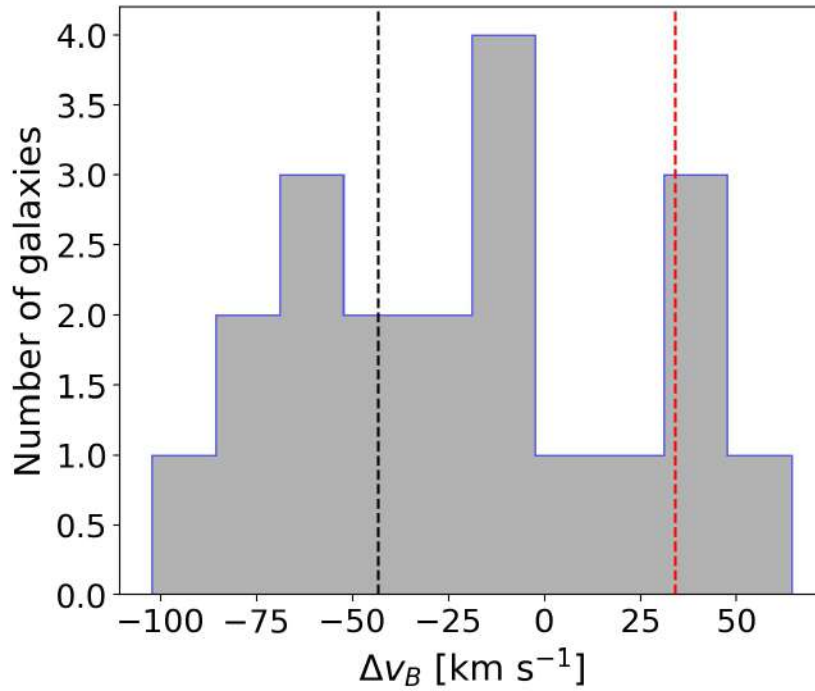


Figure 4.4.7: Distribution of the velocity shift  $\Delta v_B$  of the broad component in our sample. The black and red dashed lines mark the mean values when the broad component is blue- and red-shifted, respectively.

marked in Table 4.3.3. In these cases, the complex profile is more likely to be tracing a merger instead of a turbulent outflowing gas but it is not totally clear from HST images where obvious companions are not observed (see images marked by the black square in Fig. 4.3.6 and 4.3.8). We exclude these 3 galaxies from the interpretation of outflowing gas.

Regarding the intrinsic velocity dispersion ( $\sigma_{\text{vel}}$ ) of the components, we find that the narrow component shows values ranging from  $\sim 19$  to  $\sim 102$  km s<sup>-1</sup>, with a mean value of 57 km s<sup>-1</sup> (typical error of 3.7 km s<sup>-1</sup>) for the entire sample. If we consider only the galaxies that show broad components, the  $\sigma_{\text{vel}}$  of the narrow component are up to 70 km s<sup>-1</sup> with a mean value of 48 km s<sup>-1</sup>. Meanwhile, the broad components range from 73 to 210 km s<sup>-1</sup> with a mean value of 121 km s<sup>-1</sup> (typical error of 34 km s<sup>-1</sup>). The uncertainties are estimated directly from the Gaussian fitting based on the covariance matrix using non-linear least squares. We note that the continuum non-detection implies that the true intensity and width of the broader components fit in [OIII] should be considered as possible lower limits.

In 14 of these galaxies, the broad component is blue-shifted from the systemic velocity while in 6 of them, this component is redshifted, with a mean velocity shift ( $\Delta v_B$ ) of  $-43$  and  $34$  km s<sup>-1</sup>, respectively as shown in Fig. 4.4.7. The velocity shift shows typical errors of 7 km s<sup>-1</sup>. In 5 of these galaxies, the velocity shift is  $< 10$  km s<sup>-1</sup> that is lower than the NIR resolution, then they may show outflows very close to the systemic velocity. We find that in both cases, the broad component shows a mean velocity dispersion  $\sigma_B = 118 - 124$  km s<sup>-1</sup> which is in the range of typical widths for ionized outflows from SFGs at similar redshifts with comparable EWs (e.g., Matthee et al., 2021) and in local analogs (e.g., Amorín et al., 2012a; Bosch et al., 2019; Hogarth et al., 2020). We highlight that none of the galaxies in our sample show the extremely broad wings ( $\sigma \sim 255$  km s<sup>-1</sup>) observed

in local giant HII regions dominated by supernovae feedback (Castaneda et al., 1990). Regarding the broad-to-narrow flux ratio ( $f_B$ ), our sample covers values from 24% to 63% with a mean value of 43% ( $\sigma = 0.13$ ).

For the three galaxies of the C3-VUDS sample observed with X-shooter, we find consistent results with the kinematic analysis presented in Matthee et al. (2021), in which the authors considered only our 3 galaxies with  $z < 3$ . Additionally, the resolved Ly $\alpha$  profiles of these galaxies were analyzed in Naidu et al. (2022). For example, in the Ly $\alpha$  profile of 510583858, an intense blue peak is reported, which suggests the presence of an inflow of gas (Yang et al., 2014). This interpretation is in line with that from the kinematics of the ionized gas, where we find a redshifted broad component for the optical lines. For the other two galaxies included in Naidu et al. (2022), they show Ly $\alpha$  profiles with weaker blue peaks compared with the dominant red peak, which is indicative of outflowing material.

#### 4.4.6.1 Outflow interpretation for the broad emission

Here we note that the blueshifted broad component can be interpreted as an outflow on the near side of the galaxy or as an inflow on the far side, and the opposite for the redshifted components. Moreover, the dust distribution may also play a role in the interpretation given that dust may be blocking the flowing (Arribas et al., 2014). Given the low dust content in our sample galaxies, we assume that in both cases, blue or redshifted, the broad component is primarily tracing outflowing material, and the shift depends on the geometry and the particular line of sight.

In order to derive the maximum velocity ( $v_{\max}$ ) of the unresolved outflow, we follow the same approach as in Hogarth et al. (2020); Avery et al. (2021); Concas et al. (2022) and references therein. We consider  $v_{\max} = |\Delta v| + 2 \times \sigma_B$ , in order to include both blue or redshifted cases as outflowing gas where the maximum velocity will be in the line profile wings dominated by the outflow (see for instance Rodríguez del Pino et al., 2019; Lutz et al., 2020). We find a mean maximum velocity of  $283 \text{ km s}^{-1}$ , ranging from 183 to  $460 \text{ km s}^{-1}$ .

For the C3-VANDELS sample, we also perform a qualitative comparison with the kinematics analysis based on rest-UV absorption lines described in Calabrò et al. (2022). They found that the bulk ISM velocity along the line of sight is  $60 \pm 10 \text{ km s}^{-1}$  for low ionization gas, consistent with the mean value found in our sample. However, for the maximum velocity, they find a mean value of  $500 \text{ km s}^{-1}$ . The higher value compared with our results may be explained by the low resolution of the VANDELS spectra, which leads to higher unresolved line widths. Another possible explanation is that nebular emission lines may trace denser gas than ISM absorption lines (e.g., Marasco et al., 2023). In this case, the emission lines would trace smaller-scale outflows near the star cluster and with lower velocities, while the UV absorption lines would trace large-scale outflows with a galactic extent and with larger velocities (Chisholm et al., 2016, and references therein).

In a galaxy-by-galaxy comparison using the bulk velocity traced by the combined fit of low-ionization lines (SiII $\lambda$ 1260, SiII $\lambda$ 1526, CII $\lambda$ 1334, and AlII $\lambda$ 1670), we find that in 8 (out of the 11 C3-VANDELS galaxies with detected broad component) the bulk velocity and the offset of the broad component agrees in the direction of the flow (i.e., if they are blue or redshifted). In 2 cases, we find a broad component that is blueshifted while the bulk velocity is redshifted but they are consistent within the uncertainties. Only in one case, did we find a redshifted broad component and a negative bulk velocity. Our results suggest that the broad component of [OIII] is indeed tracing flowing material

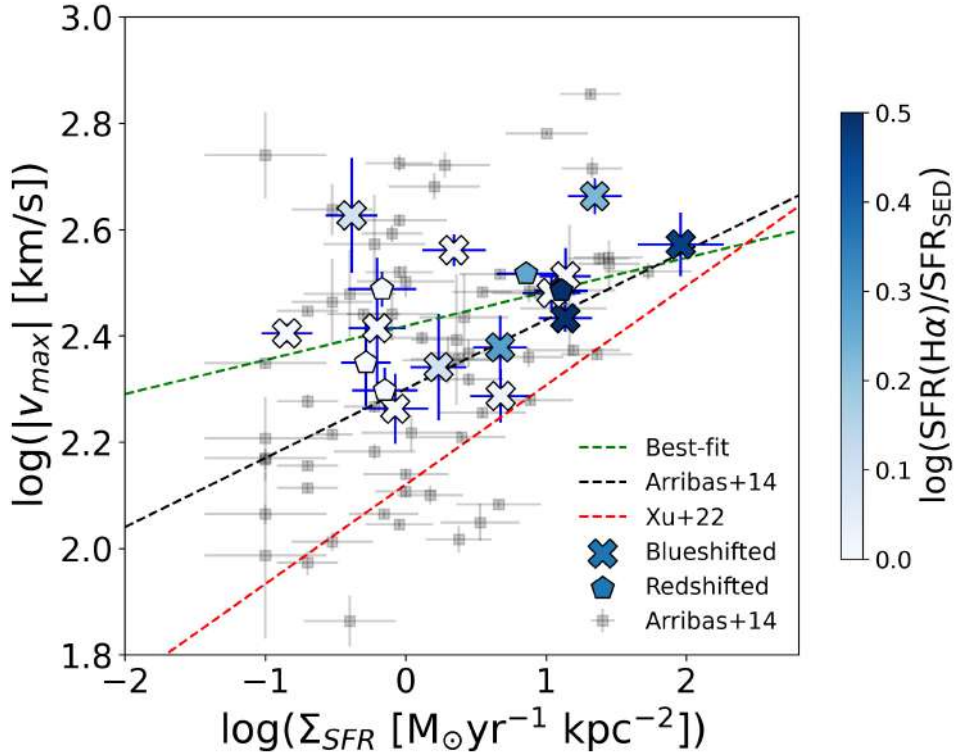


Figure 4.4.8: Relation between outflow velocity and  $\Sigma_{SFR}$ . Our sample is color-coded by the  $\text{SFR}(\text{H}\beta)/\text{SFR}_{\text{SED}}$  ratio. Our sample is divided by galaxies with blue (cross symbol) and redshifted (pentagon symbol) broad components. The black dashed line corresponds to the best slope from [Arribas et al. \(2014\)](#), and the black squares are their observed data. The green dashed line is our best fit. The red dashed line is the best fit from [Xu et al. \(2022b\)](#). Two galaxies with broad components (CDFS023527 and 511245444) are excluded from this plot since  $\text{H}\alpha$  and  $\text{H}\beta$  are not included in the observed spectral range.

that roughly agrees to be blue or redshifted in both absorption and emission lines.

#### 4.4.6.2 Outflow velocities and star formation properties

Now, we relate the maximum velocity of the outflow with the global properties of our sample. We find a weak positive correlation between the maximum velocity and the galaxy stellar mass (Pearson correlation coefficients  $\rho:0.22$ ,  $0.91\sigma$  significance). This trend suggests that more massive galaxies can power faster outflows compared with less massive galaxies. Regarding the relation with SED-derived SFR, we find no correlation ( $\rho \sim 0$ ,  $0.36\sigma$  significance). The correlation is stronger ( $\rho=0.16$ ,  $0.66\sigma$  significance) when we consider the instantaneous SFR traced by  $\text{H}\beta$  (or  $\text{H}\alpha$ ). The slope of the best fit is 0.06, which is in agreement with the trend found in [Arribas et al. \(2014\)](#) for a sample of local luminous and ultra-luminous infrared galaxies (U/LIRGs) at galactic and sub-galactic (i.e., star-forming clumps) scales. This suggests that longer timescale SFR is not tracing the actual outflow, while the instantaneous SFR is a more real tracer of the outflow and the maximum velocity that is reachable. This might be the reason why only a marginal (at  $2\sigma$  level) correlation was found between maximum velocity and SFR in [Calabrò et al. \(2022\)](#).

In Fig. 4.4.8, we explore the relationship between the maximum velocity of the outflow and the

$\Sigma_{\text{SFR}}$ . A relation between both properties is expected as explained by simple models (e.g., Heckman et al., 2015; Xu et al., 2022b). The warm ionized outflow is described by a collection of clouds or filaments driven outward by the momentum transferred by the very hot gas of the stellar ejecta from the starburst, which creates a fast-moving wind that accelerates the ambient gas. We find a weak positive correlation ( $\rho=0.40$ ,  $1.69\sigma$  significance) which is consistent with what was also found from absorption lines (e.g., Calabrò et al., 2022). This suggests that even though they might trace different regions, they might be triggered by the exact mechanisms and with a similar origin. Interestingly, we find that our best fit shows a shallower slope of  $0.06 \pm 0.03$  (green dashed line) compared to the slope of 0.13 (scaled black dashed line) found in Arribas et al. (2014). Here, we use the instantaneous SFR traced by the narrow component of  $\text{H}\beta$  (or  $\text{H}\alpha$ ), assuming the same ratio observed in  $[\text{OIII}]$ . Based on UV absorption lines, a similar trend is observed with a steeper slope of 0.18 (red dashed line) found in the CLASSY survey with local metal-poor galaxies (Xu et al., 2022b).

Additionally, we use the  $\text{SFR}(\text{H}\beta)/\text{SFR}_{\text{SED}}$  ratio as a proxy of the burstiness of the galaxy since both SFR estimators trace different timescales, with  $\text{SFR}(\text{H}\beta)$  more sensitive to younger ages. We find a mean  $\text{SFR}(\text{H}\beta)/\text{SFR}_{\text{SED}}$  ratio of 1.4 with values ranging from 0.4 to 5.1. Half of the sample shows  $\text{SFR}(\text{H}\beta)$  higher than  $\text{SFR}_{\text{SED}}$ . We find that the galaxies with the larger burstiness tend to show also high  $\Sigma_{\text{SFR}}$ , which is displayed in the color-codes in Fig. 4.4.8.

## 4.5 Discussions

### 4.5.1 Mass-Metallicity and Fundamental Metallicity relations

The gas-phase metallicity of galaxies encodes information on how physical processes drive the evolution of galaxies. The emergence of scaling relations, such as MZR, plays a fundamental role in understanding galaxy formation processes and constraining physical models of galaxy evolution. As galaxies grow, feedback processes are responsible for shaping the MZR, as they promote the dispersion and removal of a significant fraction of metals from the star-forming regions into the CGM. The selective loss of newly synthesized heavy elements could be particularly important in low-mass galaxies due to their shallow potential wells (e.g., Tremonti et al., 2004; Andrews & Martini, 2013). Besides, the slope and normalization of the MZR may evolve with redshift, with high- $z$  galaxies showing lower metallicity for a given stellar mass (e.g., Sanders et al., 2021). Simulations explain this evolution invoking the higher gas fractions of galaxies at higher redshifts (Torrey et al., 2019).

In Figure 4.5.1, we show that our subset of galaxies with reliable  $\text{H}\beta$  luminosities follow the MZR built using MOSDEF main-sequence galaxies at similar redshift by Sanders et al. (2021) and the  $z \sim 0$  relation for local analogs of similar stellar mass in the CLASSY survey (Berg et al., 2022). Our sample is mostly within  $3\sigma$ , the intrinsic scatter of these relations, with a few galaxies showing lower metallicity. We interpret this apparent offset as a likely selection effect, i.e., our sample includes strong emission-line galaxies which tend to have higher SFR, more extreme ionization conditions, and lower metallicity than the sample used to establish the MZR we are using for reference. Indeed, the high  $\log([\text{OIII}]/\text{H}\beta) > 0.6$  of our sample is roughly the higher excitation in the lower-mass bin used for the MZR in Sanders et al. (2021). This is also evident from Fig. 4.4.3, showing that our sample has larger  $[\text{OIII}]/[\text{OII}]$  ratios than MOSDEF galaxies used for the determination of the MZR at  $z \sim 3$ . Compared to strong  $[\text{OIII}]$  emitters at higher redshifts, we find our galaxies following a similar trend to that found for a more extreme subset of EoR galaxies (Matthee et al., 2022; Heintz et al., 2022).

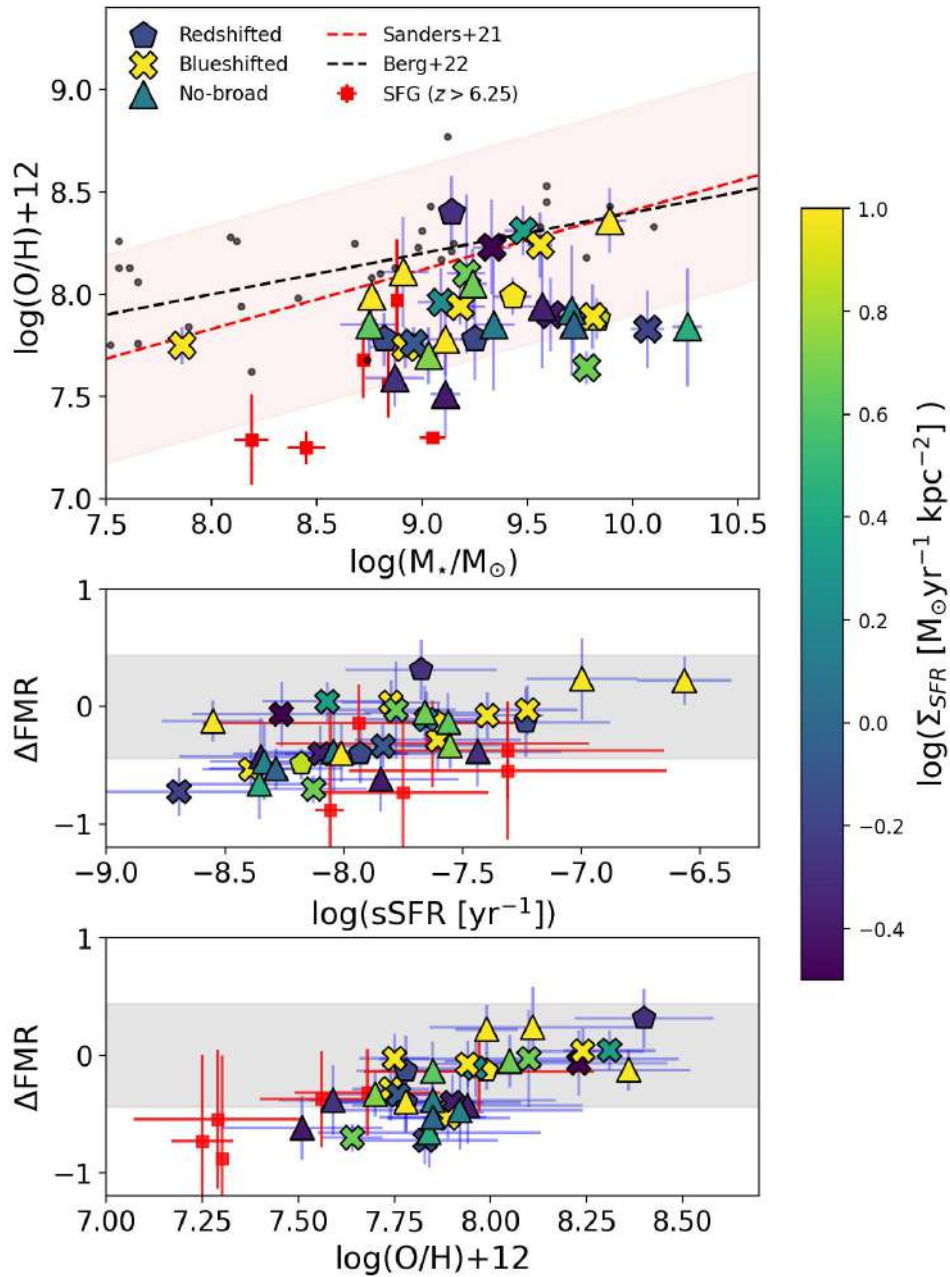


Figure 4.5.1: *Top*: Mass-Metallicity relation: The red dashed line is the MZR of SFGs at  $z \sim 3.3$  from Sanders et al. (2021) and the red shaded region is the observed  $3\sigma$  scatter. For comparison, metal-poor local galaxies from Berg et al. (2022) are included as black circles and the corresponding MZR as the black dashed line. The red squares are SFGs at  $z > 6.25$  from Matthee et al. (2022) (stack) and Heintz et al. (2022) (single lensed galaxies). *Middle (Bottom)*: Differences between the metallicity from FMR and our metallicity estimations as a function of sSFR (metallicity). The gray shaded region is the  $2\sigma$  observed scatter of 0.22 dex for the FMR at  $z \sim 3.3$  (Sanders et al., 2021). In all panels, our sample is color-coded by  $\Sigma_{\text{SFR}}$ , and the triangle symbols are the galaxies that do not show broad components. At the same time, pentagons and crosses are galaxies in our sample that show red- and blue-shifted broad components, respectively.

The scatter of galaxies around the median MZR correlates with SFR, i.e the FMR (Mannucci et al., 2010; Curti et al., 2020), which implies that at fixed stellar mass, galaxies with higher SFR show

lower metallicities. Observationally, the FMR appears invariant with redshift up to  $z \sim 3.5$  (e.g., [Curti et al., 2020](#); [Sanders et al., 2021](#)), although low-mass starbursting galaxies may show clear deviations ([Amorín et al., 2014](#); [Calabrò et al., 2017](#)). The shape of the FMR is found modulated by the age of the stellar populations, with younger ( $< 150$  Myr) and more bursty SF showing lower metallicity ([Duarte Puertas et al., 2022](#)). Models and simulations find that the FMR results from the smooth evolution of galaxies in a quasi-equilibrium state, which is regulated by inflows and outflows over time ([Lilly et al., 2013](#); [Nelson et al., 2019a](#)). The strength of the implied SFR-metallicity relation is found dependent on feedback via the shape of the star formation history, particularly for low-mass starbursting galaxies ([Torrey et al., 2018](#)).

In order to explore the position of our sample in the FMR, we compare gas-phase metallicities obtained with the expected FMR values. We define the parameter  $\Delta\text{FMR} = \log(\text{O}/\text{H}) - \log(\text{O}/\text{H})_{\text{FMR}}$ , where  $\log(\text{O}/\text{H})_{\text{FMR}}$  is the relation found in [Sanders et al. \(2021\)](#) that depends on the stellar mass and SFR. While most of the galaxies in our sample are consistent (within the uncertainties in the gas-phase metallicity) with the observed  $2\sigma$  scatter of the relation (middle and bottom panel in [Fig. 4.5.1](#)), we find a weak negative trend between  $\Delta\text{FMR}$  and specific SFR ( $\text{sSFR} = \text{SFR}/M_*$ ) similar to that shown in galaxies at  $z > 6.25$  with comparable sSFR (e.g., [Matthee et al., 2022](#); [Heintz et al., 2022](#)). However, no dependence is found with  $\Sigma_{\text{SFR}}$ . Although we find the above trend appears independent of the method used to estimate the metallicity, we should take this result with caution as the uncertainties in metallicity are still large.

Indeed, it is worth noticing that some caveats may affect the above comparisons. First, stellar masses in our work are obtained assuming sub-solar stellar metallicities, which could lead to differences of up to  $\sim 0.3$  dex compared to assuming solar values as in [Sanders et al. \(2021\)](#), as mentioned in [Sec. 4.3.1](#). Second, the different methods used to derive metallicities may lead to possible systematic differences. We use a Te-consistent method based on the comparison of UV and optical emission line ratios with predictions from photoionization models. As described in [Section 4.4.5](#), metallicity differences of up to  $\sim 0.3$  dex can be found when a sole strong-line calibration is used instead. Acknowledging these caveats, rather than absolute values we are interested in the emerging trends of such comparisons.

In conclusion, we find that our sample follows the MZR at  $z \sim 3$  with a subset of them showing slightly lower metallicities. These galaxies also show lower metallicities than expected from the FMR, which could be due to the relatively extreme ionization properties of their young and intense SF regions. Recent gas accretion fueling a compact starburst and the intense stellar feedback it produces, i.e., inflows and outflows, respectively, are physical mechanisms that could naturally drive the observed offset in the MZR and FMR towards lower metallicities. Probing relative abundances (such as C/O or N/O) which depend on the SF history of galaxies (e.g., [Vincenzo & Kobayashi, 2018](#); [Berg et al., 2019](#)) can be a useful tool to explore this hypothesis.

## 4.5.2 The C/O-O/H relation

The C/O abundance may provide us with general trends in the evolutionary state of a galaxy and its ISM. Models (e.g., [Henry et al., 2000](#); [Mollá et al., 2015](#); [Mattsson, 2010](#)) and observations of local galaxies ([Garnett et al., 1995](#); [Berg et al., 2016, 2019](#)) show that C/O increases with metallicity for galaxies with  $Z \gtrsim 20\%$  solar. This trend can be explained because C is primarily produced by the

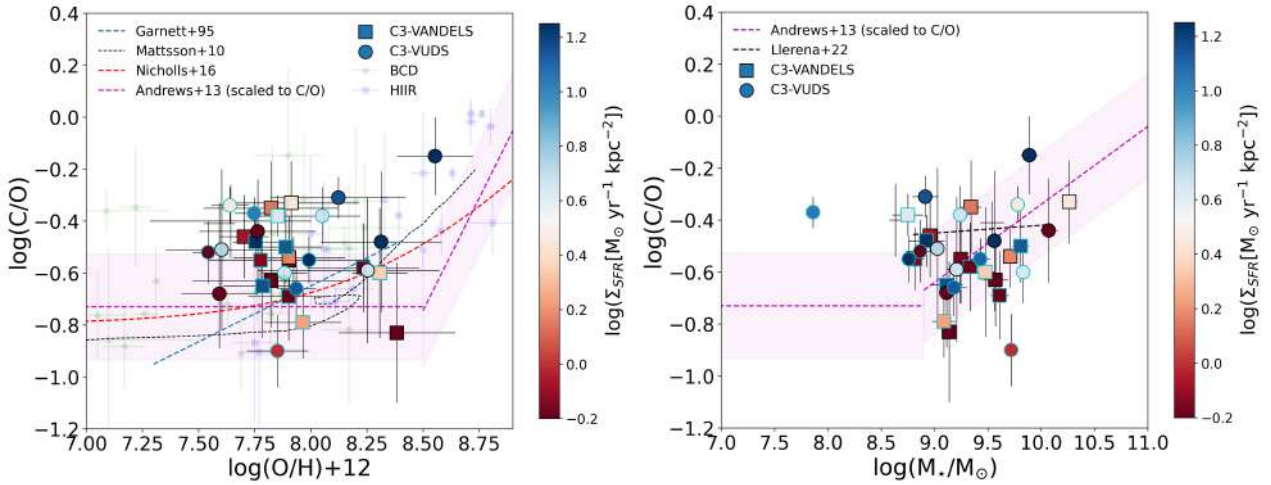


Figure 4.5.2: Left panel:  $C/O$ - $O/H$  relation. Our sample is color-coded by  $\Sigma_{\text{SFR}}$ . The symbols with cyan edges are galaxies with limits in  $\text{OIII}\lambda 1666$ . We compare our results with local BCD galaxies (small green circles, Garnett et al., 1995, 1997; Kobulnicky et al., 1997; Kobulnicky & Skillman, 1998; Izotov et al., 1999; Thuan et al., 1999; Berg et al., 2016; Senchyna et al., 2021) and HII regions (small blue squares Garnett et al., 1995; Kurt et al., 1995; Garnett et al., 1999; Mattsson, 2010; Senchyna et al., 2021). We also show chemical evolution models from the literature as dashed lines with colors described in the legend (Garnett et al., 1995; Mattsson, 2010; Nicholls et al., 2017). The magenta dashed line is the scaled  $N/O$ -mass relation in Andrews & Martini (2013) assuming a constant  $C/N$  factor based on Berg et al. (2019). The magenta-shaded region is the  $1\sigma$  uncertainty considering the observed scatter in the relation and the conversion factor. *Right panel*: Relation between  $C/O$  and stellar mass. Symbols are the same as in the left panel. In this panel, the black dashed line is the relation presented in Llerena et al. (2022) at  $z \sim 3$  based on stacking.

triple- $\alpha$  process in both massive and low- to intermediate-mass stars but, in massive stars, carbon arises almost exclusively from metallicity-dependent stellar winds, mass loss, and ISM enrichment, which are larger at higher metallicities (Henry et al., 2000). Instead, in younger metal-poor systems the delayed release of C (mostly produced by low- and intermediate-mass) relative to O (produced almost exclusively by massive stars) appears as the driver of the observed trend (Garnett et al., 1995). However, the large dispersion of  $C/O$  values over a large range in metallicity found for galaxies at  $z \sim 0-2$  ( $\sim 0.2$  dex) suggests that the  $C/O$  abundance is largely sensitive to other factors, such as the detailed SFH, with longer burst durations and lower star formation efficiencies corresponding to low  $C/O$  ratios (Berg et al., 2019).

In Figure 4.5.2 (left panel), we show our galaxy sample in the  $C/O$ - $O/H$  plane. We find no apparent increase of  $C/O$  with metallicity, as models predict (e.g., Mattsson, 2010; Nicholls et al., 2017), but a large scatter of  $C/O$  values around metallicity  $\sim 10-20\%$  solar. Despite the uncertainties in both  $C/O$  and  $O/H$ , part of this scatter could be physical, as discussed in previous works showing similar findings at low and high redshifts (e.g., Amorín et al., 2017; Berg et al., 2019; Llerena et al., 2022). In Fig. 4.5.2, we do not find a clear correlation of the  $C/O$  scatter with  $\Sigma_{\text{SFR}}$  or  $s\text{SFR}$ , which may suggest a more local effect affecting the  $C/O$ - $O/H$  relation at low metallicity, a topic that will be addressed in a future, more specific study. Finally, these results also suggest some caution in using  $C/O$  as an indicator of metallicity, as it may be subject to large uncertainty and possible selection effects.

On the other hand, the right panel in Fig. 4.5.2 shows that our galaxies appear consistent with an increase of C/O with stellar mass. In order to compare with local galaxies, we re-scaled the N/O-stellar mass relation reported in Andrews & Martini (2013) and assumed a constant C/N conversion (Berg et al., 2019) to obtain the relation shown by the magenta dashed line. Our sample shows a large scatter in C/O for a given stellar mass, roughly consistent with Llerena et al. (2022) for CIII] emitters at  $z \sim 3$  using stacking. However, they appear to follow the trend expected for their stellar mass, suggesting that a fraction of their C/O may have a secondary origin. This is not seen in the O/H-C/O plane. While we do not find a correlation with outflow velocities and  $\Sigma_{\text{SFR}}$ , one possible interpretation for these trends is that a recent metal-poor inflow may produce a dilution of O/H while keeping the C/O as large as expected for their stellar mass. To explore further this and other possible interpretations larger representative samples over a wide range of mass and metallicity are needed. JWST spectroscopy will certainly help to reduce uncertainties in the chemical abundance of high- $z$  galaxies, thus providing a more robust interpretation of the C/O-O/H relation for samples at  $z \gtrsim 4$  (e.g., Arellano-Córdova et al., 2022).

In conclusion, the low metallicity and relatively large C/O abundance of our sample suggest that these galaxies are in a relatively active and early phase of chemical enrichment. The complex interplay between metal content and stellar feedback will be discussed in the following sections.

### 4.5.3 Outflow properties and their relation with star formation rate density

One important parameter in understanding the effects of outflows in the properties of galaxies is the mass-loading factor ( $\eta = \dot{M}_{\text{out}}/\text{SFR}$ ) which measures how efficiently outflows remove gas from the galaxy relative to the formation of stars. To be consistent with previous works, we follow the same models in Concas et al. (2022) to calculate the mass loading factor  $\eta$ . In the case of a multiconical or spherical outflow and a constant outflow velocity, the mass outflow rate  $\dot{M}_{\text{out}}$  from the H $\alpha$  line is given by

$$\dot{M}_{\text{out}} = 1.02 \times 10^{-9} \left( \frac{v_{\text{max}}}{\text{kms}^{-1}} \right) \left( \frac{M_{\text{out}}^{\text{H}\alpha}}{M_{\odot}} \right) \left( \frac{\text{kpc}}{R_{\text{out}}} \right) C [\text{M}_{\odot} \text{yr}^{-1}], \quad (4.5.1)$$

where the factor  $C$  depends on the assumed outflow history,  $R_{\text{out}}$  is the radius of the outflow,  $v_{\text{max}}$  is the maximum outflow velocity defined in Sec. 4.4.6 and  $M_{\text{out}}^{\text{H}\alpha}$  is the mass outflow which is given by

$$M_{\text{out}}^{\text{H}\alpha} = 3.2 \times 10^5 \left( \frac{L_B^{\text{H}\alpha}}{10^{40} \text{ergs}^{-1}} \right) \left( \frac{100 \text{cm}^{-3}}{n_e} \right) M_{\odot}, \quad (4.5.2)$$

where  $L_B^{\text{H}\alpha}$  is the dust-corrected luminosity of the outflow (broad) component of H $\alpha$ . To estimate  $L_B^{\text{H}\alpha}$  we use the dust-corrected H $\beta$  luminosity and assumed the broad-to-narrow flux ratio from [OIII]. We do not use the model-based [OIII] since it depends on the metallicity (see Concas et al., 2022) and we prefer to keep the mass outflow rate independent of the method used to derive metallicity. However, we checked that the values obtained by using the two lines differ by 0.28 dex, with higher  $\dot{M}_{\text{out}}$  values when using the [OIII] line. This difference is also discussed in Concas et al. (2022) and they find agreement only when a higher metallicity of 50% solar is assumed.

From Eq. 4.5.2, we find the outflow mass ranging from  $10^{7.0}$  to  $10^{8.03} M_{\odot}$ , with a mean value of  $10^{7.58} M_{\odot}$ . Since our data do not allow a reliable estimate of  $n_e$  for the outflow component (i.e., using only the broad emission of [OII] $\lambda\lambda 3727, 3729$ ), we assumed an outflow mean electron density of 380

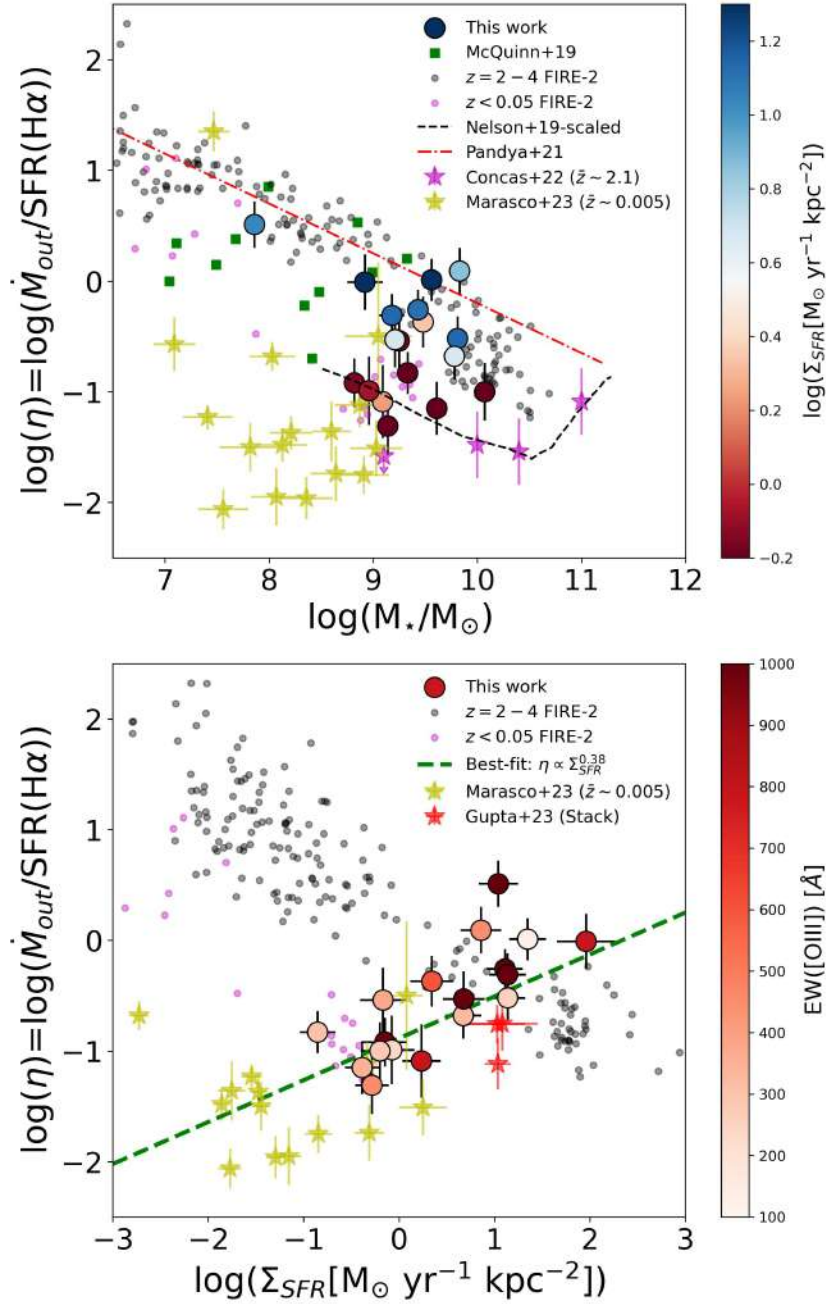


Figure 4.5.3: *Top panel:* Relation between mass loading factor and stellar mass. Our sample is color-coded by  $\Sigma_{SFR}$ . The black dashed line is the re-scaled relation found in simulations according to Nelson et al. (2019b). The dotted-dashed line is the relation found in Pandya et al. (2021). The small black (magenta) circles are single simulated haloes from Pandya et al. (2021) at redshift range 2-4 (< 0.05). We also include observational results from McQuinn et al. (2019); Concas et al. (2022); Marasco et al. (2023). *Bottom panel:* Relation between mass loading factor and  $\Sigma_{SFR}$ . Symbols are the same as in the top panel, but our sample is color-coded by  $EW([OIII])$ . The red stars are stacks at  $z = 3 - 4$  from Gupta et al. (2023). The green dashed line is the best fit for  $\log(\Sigma_{SFR}[M_\odot \text{ yr}^{-1} \text{ kpc}^{-2}]) > -3$  including our sample and the observed galaxies and stacks from literature.

$\text{cm}^{-3}$ , which is based on the stacking of 33 galaxies with SF-driven outflows (Förster Schreiber et al., 2019). This assumption makes our estimate consistent with other works using the same value (e.g.,

Davies et al., 2019; Concas et al., 2022; Gupta et al., 2023). If we use the mean (global) density of  $560 \text{ cm}^{-3}$  obtained for our sample, the resulting  $\eta$  values are 0.16 dex lower, which is smaller than the mean uncertainties (0.23 dex), it does not affect our results and conclusions.

For the mass outflow rate, we assume a constant outflow rate that starts at  $-t = -R_{\text{out}}/v_{\text{max}}$  that leads to  $C = 1$ , as in other works (Concas et al., 2022). We assume that the outflow radius  $R_{\text{out}}$  is the effective radius measured in the F160W band in WFC3/HST, as described in Section 4.3.3, which has values ranging from 0.2 to 3.6 kpc, with a mean  $R_{\text{out}} = 1.6$  kpc. We assume that the outflow velocity is the maximum velocity (see Table 4.3.3, Section 4.4.6). We find mass outflow rates ranging from 1.4 to  $57 M_{\odot} \text{ yr}^{-1}$ , with a mean  $\dot{M}_{\text{out}} = 13.3 M_{\odot} \text{ yr}^{-1}$ , nearly half the mean SFR derived for the sample. As a comparison, we find that our sample is in agreement with the relation  $M_{\text{out}}\text{-SFR}$  reported in Avery et al. (2021) at the more extreme SFR values, which indicates that SF is the driver of the outflow. They found a linear slope of  $\dot{M}_{\text{out}} \propto \text{SFR}^{0.97}$  for integrated outflows on local MaNGA galaxies using  $\text{H}\alpha$  to measure outflows. This relation is also consistent with the values reported in Marasco et al. (2023) for a sample of 19 nearby systems above the local MS and that shows lower values of SFRs and  $\dot{M}_{\text{out}}$  than our sample. We also note that some of our galaxies show higher values than those found in Xu et al. (2022b) for a sample of local dwarf galaxies using UV absorption lines with similar high SFRs.

In order to estimate  $\eta$ , we considered the instantaneous SFR using Balmer lines, as explained in Sec. 4.3.3. We report the obtained values in Table 4.3.3. We find a mean value of  $\eta = 0.54$  with values ranging from 0.05 to 3.26. Our mean value is higher than the estimation of  $\eta \sim 0.2$  using stacking from a sample of SFGs at  $z = 3 - 4$  with  $\text{EW}(\text{H}\beta + [\text{OIII}]\lambda 5007) > 600 \text{ \AA}$  (Gupta et al., 2023) and for a local GP galaxy (Hogarth et al., 2020). On the other hand, our mean value is lower than the typical  $\eta$  of 1.5 for neutral and low-ionization gas of SFGs at  $z \sim 3$  derived from absorption lines (e.g., Calabrò et al., 2022).

In Figure 4.5.3 (top panel), we display the relation between the mass loading factor and stellar mass for our sample galaxies and compare it with similar theoretical and observational results from the literature. Our galaxies show a very large range of  $\eta$  values in a limited range of  $M_{\star}$ . While this precludes a rigorous study of possible trends in  $\eta$  with  $M_{\star}$  at  $z \sim 3$ , we find that, for a given stellar mass, galaxies show more than one order of magnitude scatter in  $\eta$  values according to their star formation rate surface density. We find a clear trend in the scatter with galaxies with more compact star formation, i.e.,  $\Sigma_{\text{SFR}} \gtrsim 10 M_{\odot} \text{ yr}^{-1} \text{ kpc}^{-2}$ , showing larger  $\eta$  for a given  $M_{\star}$ . Instead, galaxies with  $\Sigma_{\text{SFR}} \lesssim 10 M_{\odot} \text{ yr}^{-1} \text{ kpc}^{-2}$  show on average  $\sim 1$  dex lower  $\eta$  values. While the former appears roughly consistent with the trend predicted by FIRE-2 simulations (dotted-dashed lines, Pandya et al., 2021), the latter appears more consistent with the scaled (by a factor  $\sim 1/141$  lower) trend predicted by the Illustris-TNG simulations (Nelson et al., 2019b).

Compared to recent observational studies using a similar two-Gaussian decomposition of strong emission lines, in Fig. 4.5.3 we typically find larger  $\eta$  values than main sequence galaxies at cosmic noon (e.g., Concas et al., 2022) and nearby dwarf galaxies (e.g., Marasco et al., 2023). The relative disagreement with simulation predictions found by these authors, i.e., a dropoff of  $\eta$  at  $M_{\star} \lesssim 10^{10} M_{\odot}$  compared to the predicted increasing trend, was interpreted as evidence of possible inefficient feedback efficiency in low-mass galaxies.

However, our results suggest that the compactness of the SF regions in low-mass galaxies, i.e., their  $\Sigma_{\text{SFR}}$ , is key to determining the impact of outflows and stellar feedback in low-mass systems.

Our results are in good agreement with recent findings by (McQuinn et al., 2019), who also show a clear increasing trend for the outflow mass-loading factors of local dwarf galaxies with centrally concentrated star formation (green squares in Fig. 4.5.3). Indeed, the few blue compact dwarfs included in (Marasco et al., 2023) also show comparably larger  $\eta$  values. This is also evident from Fig. 4.5.3 (bottom panel), in which we find a clear trend with galaxies of higher  $\Sigma_{\text{SFR}}$  showing higher  $\eta$  (best-fit in green line). The resulting trend consistently includes local dwarfs and results from stacking of EELGs at  $z \sim 3 - 4$  (Gupta et al., 2023) (red stars in Fig. 4.5.3).

The above results strongly suggest that galaxies of a given stellar mass may have different feedback effects according to their SF surface density, with low-mass galaxies of larger  $\Sigma_{\text{SFR}}$  experiencing more effective feedback. These results are in tension with simulations where an opposite trend is found (e.g., Nelson et al., 2019a; Pahl et al., 2022). As discussed in Nelson et al. (2019a), this trend depends on the velocity threshold of outflow particles and the tension with observations might be explained by small-scale relationships that are not considered in simulations (see also McQuinn et al., 2019, for a detailed discussion). Within this context, we note that our sample of galaxies is mainly strong [OIII] emitters with high EWs, which are somehow pushing the relation with  $\eta$  towards higher  $\Sigma_{\text{SFR}}$ , as shown in Fig. 4.5.3. Thus, it appears possible that low-mass galaxies with moderate SFR and lower emission-line EWs are more consistent with literature data and values observed in simulated haloes at low- $z$  ( $z < 0.05$ ).

Interestingly, recent works suggest a relation between the SFR surface density and the escape of ionizing photons (i.e.,  $\Sigma_{\text{SFR}} \propto f_{\text{esc}}$ ), which is intimately related to the ability of stellar feedback, i.e., outflows, to clear out young star-forming regions from dust and neutral hydrogen, thus creating optically thin channels from which ionizing photons may eventually escape (e.g., Naidu et al., 2020; Flury et al., 2022b). Within this context, our results suggest that young low-mass galaxies with strongly mass-loaded outflows, i.e., showing broad emission line components, could be clear candidates to have favorable conditions for LyC photon escape.

Recently, the spatially resolved study of the Sunburst arc, a lensed metal-poor galaxy at  $z = 2.37$  showing LyC escape, presented by Mainali et al. (2022), revealed a strong blue-shifted broad emission component in [OIII]. Remarkably, the broad-to-narrow ratio in the leaking clump is 120%, whereas for the non-leaker regions this ratio falls to 35%. If we compare these results with the  $f_B$  values obtained for our sample and other LyC indirect diagnostics (e.g., Flury et al., 2022b), we find that only a few galaxies with the higher  $f_B$  and  $\Sigma_{\text{SFR}}$ , as well as high [OIII]/[OII], could be considered as our best candidates for LyC leakage.

#### 4.5.4 Effects of stellar feedback on chemical abundances

We discuss the impact of stellar feedback, traced by outflows, in the chemical abundances of the host galaxies. We use Fig. 4.5.4, in which we plot oxygen and carbon nebular abundances versus  $\eta$  and  $\beta = \log(\text{SFR}_{\text{H}\alpha}/\text{SFR}_{\text{SED}})$ , the ratio between the instantaneous SFR, traced by H $\alpha$ , and the SED-based  $\text{SFR}_{\text{SED}}$ , tracing longer-timescales.  $\beta$  is often considered a burstiness parameter (Scalo, 1986; Guo et al., 2016).

For our sample, we find no significant correlation ( $\rho = -0.15$ ,  $0.6\sigma$  significance) between metallicity and  $\eta$  suggesting that metallicity is insensitive to the strength of the outflow at global spatial

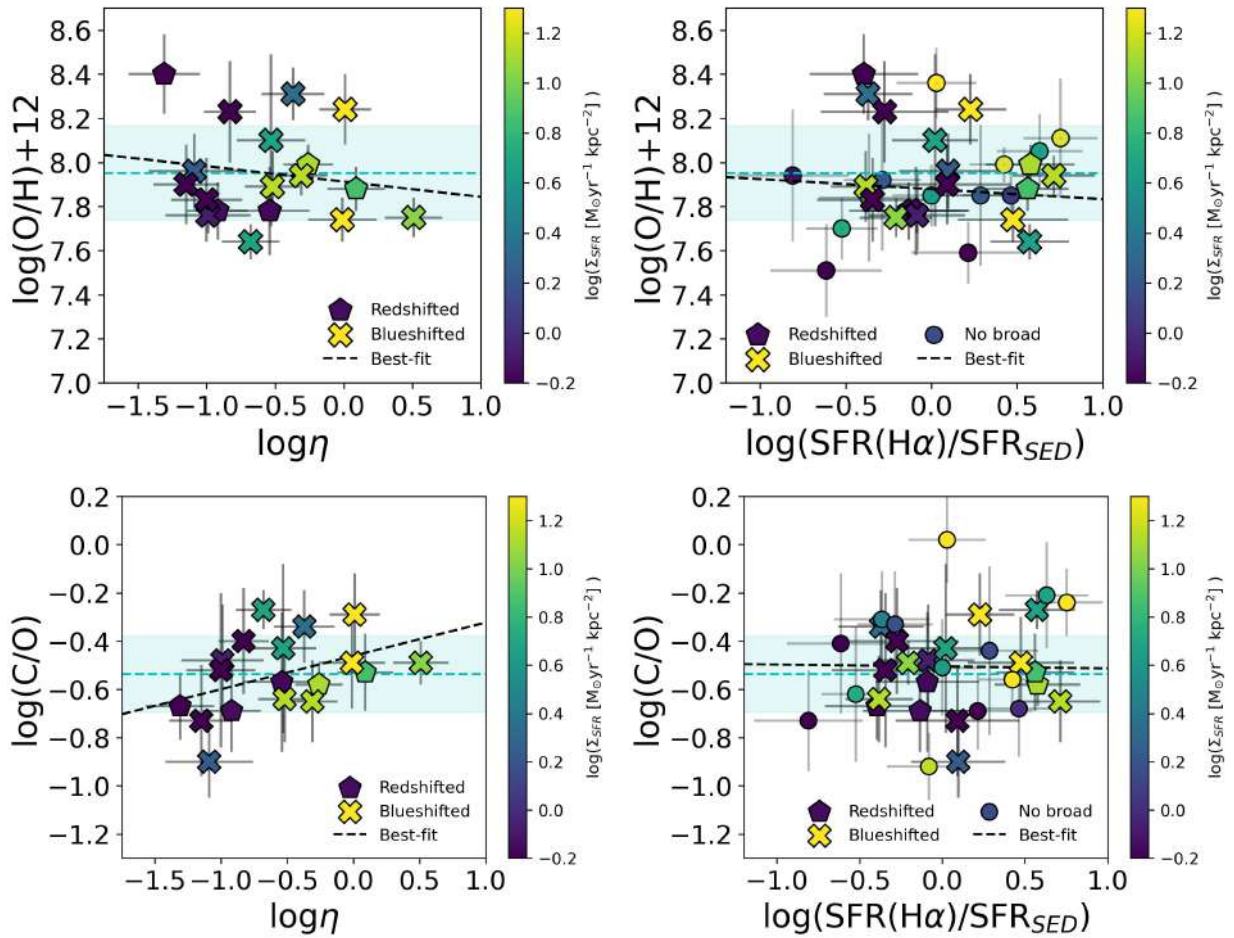


Figure 4.5.4: Relation of the chemical abundances (Oxygen abundance on top panels and C/O on bottom panels) with mass loading factor (left panels) and with burstiness (right panels). Our sample is divided into galaxies with broad component blueshifted (blue crosses) or redshifted (red pentagons) or without broad component detected (black squares). The dashed cyan lines are the mean value, and the shaded region is the mean observed scatter. Our sample is color-coded by  $\Sigma_{\text{SFR}}$ .

scales. We do not find compelling evidence that younger starbursts (high  $\beta$ ) show lower metallicities ( $\rho = -0.04$ ,  $0.17\sigma$  significance), suggesting also that metallicity is insensitive to SF timescale at global spatial scales. No correlation is found with C/O either ( $\rho \sim 0$ ,  $0.1\sigma$  significance). These results are somehow consistent with the position of our sample in the mass-metallicity-SFR relations and the large scatter they show in the relation between  $\eta$  and  $M_{\star}$ .

However, galaxies with higher  $\eta$  appear to have a weak increasing trend with the C/O abundance, which is slightly larger for galaxies with stronger outflows and denser star formation. This implies a certain level of selective enrichment due to outflows that could be in place in such galaxies. Our best fit is consistent with a weak correlation ( $\rho=0.42$ ,  $2\sigma$  significance), not far from the scatter we measure around the mean C/O value for the sample (cyan regions in Fig. 4.5.4). For this reason, a more complete analysis of the impact of stellar feedback on the chemical properties of the galaxies will be done in future works.

Finally, in Fig. 4.5.4 we identify galaxies with blue- and red-shifted broad components to explore potential differences for in(out)flows, but we do not find any clear distinction among them and com-

pared them to galaxies without broad emission. While this may suggest that we do not detect those components because of the geometry of the gas flow or the depth of our spectra, rather than because of different nebular physical conditions, it may also indicate that a global parameter such as  $\beta$  is not efficient to identify chemo-dynamical differences in these unresolved galaxies.

Therefore, we conclude that unresolved spectroscopy is likely insufficient to discern between these two possible scenarios in our sample. Spatially resolved spectroscopy is needed to consider the geometry of the ISM, compare with models and further explore the connection between gas flows, chemical abundances, and star formation of galaxies at  $z \sim 3$ , which is now possible using the NIRSpec IFU onboard the JWST.

## 4.6 Conclusions

In this work, we present a detailed analysis of the chemical abundances and kinematics of the ionized gas of low mass ( $10^{7.9}$ - $10^{10.3}M_{\odot}$ ) SFGs at  $z \sim 3$ . We use new follow-up NIR spectroscopy for a sample of 35 SFGs selected on the basis of their rest-UV emission line properties (from Ly $\alpha$  to CIII]) from two previous works using ultra-deep optical spectra of the VANDELS (Llerena et al., 2022) and VUDS (Amorín et al., 2017) surveys. For VANDELS targets, our sample was assembled from Keck/MOSFIRE spectra of the NIRVANDELS survey (Cullen et al., 2021). For VUDS targets, our sample was assembled from MOSDEF spectra (Kriek et al., 2015) and from new spectra obtained with VLT/X-shooter and Magellan/FIRE.

We focus our analysis of the NIR spectra on strong emission lines in the rest-optical, from [OII] $\lambda$ 3727 to H $\alpha$ . We characterize the main properties of the sample based on the UV and optical datasets. We discuss scaling relations involving galaxies' gas metallicity and C/O abundances, which are derived using  $T_e$ -consistent methods based on photoionization models and the observed UV and optical emission line ratios. In addition, using the available high-resolution spectra, we perform an analysis of the [OIII] $\lambda\lambda$ 4959,5007 emission line profiles with a multi-Gaussian fitting technique to investigate the ionized gas kinematics of the galaxies and discuss the connection between stellar feedback and chemical enrichment in these young low-mass SFGs. We summarize our main results and conclusions as follows:

- i) According to diagnostic diagrams based on both UV and optical emission line ratios, the dominant source of ionization in our sample of SFGs is massive stars. While 14% of the sample show UV emission line ratios that are closer to those expected from AGN models, we find that their optical line ratios are instead consistent with pure stellar photoionization. Overall, our sample is characterized by high [OIII]/H $\beta$   $> 4$  ratios, which suggests high ionization conditions in the ISM.
- ii) We find rest-frame EW(CIII]) ranging from 1Å to 15Å and EW([OIII]) ranging from 102Å to 1715Å. We derive positive correlations between the EWs of bright UV and optical emission lines. About 15% of our sample show EW([OIII] $\lambda\lambda$ 4959,5007)  $> 1000\text{Å}$  that closely resemble those measured in  $z > 6$  EoR galaxies with photometric data (e.g., Endsley et al., 2021) and, more recently, with JWST spectroscopy (e.g., Matthee et al., 2022).

- iii) For galaxies with reliable measurements of the  $\text{OIII}] \lambda 1666 / [\text{OIII}] \lambda 5007$  ratio, we find mean electron temperatures  $T_e = 1.8 \times 10^4 \text{K}$ . Consequently, we use the code HCM-UV based on UV photoionization models to consistently derive low gas-phase metallicities and C/O abundances. We find a wide range of metallicity ( $12 + \log(\text{O}/\text{H}) \sim 7.5\text{--}8.5$ ) with a mean value of  $12 + \log(\text{O}/\text{H}) = 7.91$  or 17% solar. Using alternative methods, we find differences of up to  $\sim 0.3$  dex toward higher (lower) metallicities when using pure optical (UV) strong-line calibrations, which are larger than typical uncertainties. We also derive a wide range of C/O abundance ratios ranging from  $\log(\text{C}/\text{O}) = -0.9$  to  $\log(\text{C}/\text{O}) = -0.15$  (23% and 128% solar, respectively) with a mean value of  $\log(\text{C}/\text{O}) = -0.52$  (54% solar) that is consistent with previous results for SFGs at  $z \sim 3$  based on stacking spectra (Shapley et al., 2003; Llerena et al., 2022). Both oxygen and carbon abundances for the highest EW galaxies in our sample are in excellent agreement with values obtained for galaxies at  $z > 6$  with JWST spectra (Arellano-Córdova et al., 2022; Jones et al., 2023)
- iv) Our sample follows a mass-metallicity relation with a slope consistent with previous work at similar redshifts but showing an offset of about 0.3 dex to lower metallicities, which appears consistent with the low-metallicity envelope of the MZR scatter (Curti et al., 2020; Sanders et al., 2021). While these differences could be explained by the different methods used to estimate the metallicities, we conclude that the high ionization properties of our sample are most likely driving these offsets. Furthermore, we find that for a given stellar mass, galaxies with lower metallicities tend to show larger deviations from the FMR. These results suggest that our SFGs are experiencing a rapid and active episode of massive star formation in which outflows from stellar feedback and accretion of fresh gas can be acting as significant regulators of their mass and metal content.
- v) From the analysis of the CO-O/H relation, we find no apparent increase of C/O with metallicity, as models predict (e.g., Mattsson, 2010; Nicholls et al., 2017), but a large scatter of C/O values around metallicity  $\sim 10 - 20\%$  solar. On the other hand, our galaxies appear consistent with an increase of C/O with stellar mass, suggesting that a fraction of their C/O may have a secondary origin. One possible interpretation for these trends is that a recent metal-poor inflow may dilute O/H while keeping the C/O as large as expected for their stellar mass. To explore further this and other possible interpretations larger representative samples over a wide range of mass and metallicity are needed.
- vi) From a detailed multi-Gaussian component fitting of  $[\text{OIII}] \lambda \lambda 4959, 5007$  line profiles, we find 65% of our galaxies showing two distinct kinematic components: a narrow component with intrinsic velocity dispersion of  $\sigma_N \sim 57 \text{ km s}^{-1}$  accounting for the core of the lines and a broader component with  $\sigma_B \sim 121 \text{ km s}^{-1}$  that best fit the extended line wings. We find the broad component is typically blue- or red-shifted by  $\sim 30 - 40 \text{ km s}^{-1}$  with respect to the narrow one in most galaxies. Following the close similarities with local analogs, such as the Green Peas (Amorín et al., 2012a; Hogarth et al., 2020), we interpret the narrow and broad kinematic components as gas tracing virial motions and turbulent outflowing ionized gas driven by strong star formation, respectively. From our kinematic analysis, we find typical outflow velocities of  $\sim 280 \text{ km s}^{-1}$ , which are found to correlate weakly with stellar mass but strongly with the instantaneous SFR traced by Balmer lines and  $\Sigma_{\text{SFR}}$ .
- vii) From our kinematic analysis, we find a mean mass-loading factor  $\eta = 0.54$  (with a large range of 0.05-3.26 and a typical uncertainty of 0.3) that is larger compared to the typical value observed in SFGs at similar redshift. We find galaxies with more compact star formation,

i.e.,  $\Sigma_{\text{SFR}} \gtrsim 10 M_{\odot} \text{yr}^{-1} \text{kpc}^{-2}$ , showing larger  $\eta$  for a given  $M_{\star}$  at the stellar mass range covered by our sample ( $\log(M_{\star}/M_{\odot}) < 10.2$ ). This suggests that for a given stellar mass, denser starbursts in low-mass, low-metallicity galaxies produce stronger outflows. This indicates that stellar mass alone, as concluded by some studies at lower redshift, does not necessarily determine how effectively gas is removed due to stellar feedback and that the star formation and ISM densities can regulate this process in low-mass galaxies, as some simulations predict.

Overall, our results suggest a complex interplay between star formation, gas kinematics, and chemical enrichment in relatively young galaxies at  $z \sim 3$ . When observed during a young burst of SF, ionization properties are extreme and their chemical abundances are strongly regulated by their significant gas accretion and stellar feedback, which make them outliers of key scaling relations. In this phase, SFGs may show broad emission line components imprinting the turbulent ionized gas that is outflowing from the starbursting regions. While outflows appear ubiquitous in the rapid star-forming episodes of low-mass galaxies at  $z \sim 3$ , their role as a regulator of the gas metallicity could be significantly stronger in galaxies developing denser starbursts. Outflows are in turn suggested as an important mechanism to shape the ISM properties and to facilitate the escape of ionizing photons. Due to the close resemblance of EELGs at  $z > 6$  with a subsample of galaxies in this work, we conclude that the above results suggest that similar findings could be common in galaxies at higher redshifts observed with deep JWST high-resolution spectra.

# Characterization of extreme emission-line galaxies at $z \gtrsim 4$ with JWST data

In this Chapter, we present preliminary results of an ongoing project where we aim to select a sample of EELGs at  $z > 4$  photometrically by exploiting the capabilities of the Near Infrared Camera (NIRCam; [Beichman et al., 2012](#)) in JWST from the Cosmic Evolution Early Release Science Survey (CEERS; [Finkelstein et al., 2023](#))\*. We use a set of broad (F277W-F356W-F444W) and medium (F410M) band filters to identify EELGs at high- $z$  by their [OIII] $\lambda$ 5007 emission line in 10 NIRCam pointings. We intend to provide a sample of EELG candidates using templates of rare local metal-poor starbursts. We selected candidates with color excess in broad and medium-band filters, depending on the photometric redshift of the source. The set of filters covers the [OIII] line at  $3.78 < z < 9.13$ . We removed possible contaminants using an S/N cut. We performed a SED fitting to estimate the physical properties of the galaxies: line fluxes, equivalent widths (EWs), stellar masses, stellar metallicities, and so on. We identify 521 EELGs at  $3.86 < z < 8.32$ . Most show compact morphologies with F200W sizes  $< 1$  kpc, low stellar masses ( $\log(M_*/M_\odot) \sim 8.5$ ), and low dust extinction ( $A_V \sim 0.34$  mag). Our selection method is tested with Near Infrared Spectrograph (NIRSpec; [Jakobsen et al., 2022](#)) observations for a subsample of our candidate list.

This Chapter is organized as follows: in Sec. 5.2, we present the photometry and the templates of EELGs we considered in this chapter. In Sec. 5.3, we present our NIRCam synthetic observations to estimate the color excess to identify EELG candidates. In Sec. 5.4.1, we present the color-color diagrams used and the final sample of EELG candidates. In Sec. 5.4.2 we present the physical properties of our sample based on SED fitting. In Sec. 5.4.3 we present the NIRSpec spectroscopy of a subsample of 34 galaxies in our candidate list. In Sec. 5.4.4, we present preliminary results on the ionization properties of the galaxies and scaling relations. Finally, in Sec. 5.5, we present a summary and plans for future work.

---

\*<https://ceers.github.io>

## 5.1 Context

Over the past decades, several studies have discovered a population of galaxies that undergo very strong star formation events. They are called extreme emission line galaxies (EELGs) and are characterized by typically high EWs of hundreds to thousands of angstroms which are driven by elevated specific star formation rates (sSFRs) up to  $10\text{-}100 \text{ Gyr}^{-1}$  in galaxies with stellar masses  $\lesssim 10^9 M_\odot$ , with subsolar metallicities and little dust (e.g., [van der Wel et al., 2011](#); [Maseda et al., 2014](#); [Amorín et al., 2015](#); [Forrest et al., 2017](#)). Such extreme systems are rare in the local universe. Examples of EELGs are the so-called Green Pea galaxies ([Cardamone et al., 2009](#)) or luminous compact galaxies ([Izotov et al., 2011](#)), but the number density of EELGs increases with increasing redshift (e.g., [Smit et al., 2014](#)) and are expected to be common in the EoR. Besides studying the properties of such extreme systems in the early universe, they are also essential to understand the process of reionization. Such starburst galaxies are currently presumed strongly to be the main drivers of Hydrogen reionization over  $5.5 < z < 15$  (e.g., [Robertson et al., 2015](#)), which serves to motivate many of the searches for high- $z$  EELGs as well. To understand the properties of EELGs, large and representative samples of EELGs must be assembled.

As we mentioned in previous chapters, the study of EELGs in the local Universe up to high redshifts has been a significant field in recent years because they resemble the properties of galaxies in the EoR with high EWs of UV and optical lines ([Smit et al., 2015](#); [Hutchison et al., 2019](#)). With the advent of the JWST era, the discoveries of young galaxies are rapidly moving deep into the EoR, where such systems can be studied now directly up to  $z \sim 9$  with NIRCcam and NIRSpec. The first step is to find and characterize such systems to conduct detailed spectroscopic studies, usually performed with local analogs.

Many of the searches for EELGs select samples using either narrow- (e.g., [Sobral et al., 2013](#); [Iglesias-Páramo et al., 2022](#); [Lumbreras-Calle et al., 2022](#)), broad- (e.g., [van der Wel et al., 2011](#); [Onodera et al., 2020](#); [Kojima et al., 2020](#)) or medium-band photometry (e.g., [Cohn et al., 2018](#); [Withers et al., 2023](#)), and slitless spectroscopy (e.g., [Maseda et al., 2018](#); [Kashino et al., 2022](#)). Using photometry, EELGs are selected based on the enhancing effect the emission line fluxes have in some specific filter, depending on its redshift. Unlike the commonly used Lyman break technique, broad-band color selections do not require high S/N in the rest-frame UV-optical continuum. Faint continuum EELGs are difficult to be detected through their continuum emission alone but can be selected via their color excess due to their emission lines. This population of very faint galaxies may play an essential role in reionization (e.g., [Endsley et al., 2022](#)), yet it will not be detected using many of the typical selection criteria.

Deep imaging with new JWST capabilities opens a new window to identify such young metal-poor starbursts. The CEERS survey ([Finkelstein et al., 2023](#)) is a JWST Early Release Science program that is obtaining imaging and spectroscopy of the Extended Groth Strip (EGS,  $14\text{h}19\text{m}00\text{s} +52^\circ 48' 00''$ ) field with three instruments and five coordinated parallel observing modes. The complete program involves imaging with the NIRCcam short and long-wavelength channels in ten pointings, observed as coordinated parallels to primary observations with the NIRSpec and the MidInfrared Instrument (MIRI; [Wright et al., 2015](#)). In this project, we used mainly data from the photometry using NIRCcam and NIRSpec. The CEERS observations were split into two epochs. The first epoch was executed in June 2022, and the second in December 2022. In total, 10 pointing were taken with NIRCcam imaging, including seven filters per pointing (F115W, F150W, F200W, F277W, F356W,

F410M, and F444W), reaching  $5\sigma$  depths of  $\sim 28.5 - 29.2$  mag for point sources for a total area of  $\sim 85$  arcmin<sup>2</sup>.

In this chapter, we will use this new photometry and synthetic NIRCcam observations of templates of local EELGs to find such systems at  $z > 4$ .

## 5.2 Data

### 5.2.1 Photometry catalogs

We used version v0.51.2 of the CEERS Photometric Catalogs (Finkelstein et al. in prep.). The catalog contains 101808 sources. The NIRCcam images used are publicly available, and we refer the reader to the original paper by Bagley et al. (2023) for a complete description of the data reduction. For the pointing 1, 2, 3, and 6, the images are available in the Data Release 0.5<sup>†</sup>, while for the pointings 4, 5, 7, 8, 9, and 10, the images are available in the Data Release 0.6<sup>‡</sup>.

The details of the photometric catalog will be presented in Finkelstein et al. (in prep.), but briefly, the photometry was performed with SExtractor (v2.25.0; Bertin & Arnouts, 1996) with F277W and F356W as the detection image. The fiducial fluxes are measured in small Kron apertures corrected by large-scale flux, following the methodology in Finkelstein et al. (2023).

Photometric redshifts were estimated with EAZY (Brammer et al., 2008), following the methodology in Finkelstein et al. (2023). The code fits nonnegative linear combinations of user-supplied templates to derive probability distribution functions for the redshift based on the fit quality to the observed photometry for each detected source. The redshift is allowed to vary between 0 – 20. For this catalog, new templates from Larson et al. (2022) were included to improve the goodness of the fit in high- $z$  sources. This new set of templates includes models with low metallicity, young stellar populations, and high ionization parameters. In this project, we use the best-fitting photometric redshift defined as  $z_a$  in EAZY.

### 5.2.2 Templates of EELGs

To create synthetic NIRCcam observations of EELGs, we use the templates of the Automated Spectroscopic K-means-based (ASK) classes presented in (Sánchez Almeida et al., 2010). According to this scheme, the  $\sim$  one-million SDSS-DR7 galaxies with an apparent magnitude brighter than 17.8 can be classified in only 28 ASK classes based exclusively on the features and shape of their rest-frame and normalized by  $u$  mag optical spectrum.

The classification details are described in Sánchez Almeida et al. (2010) but very briefly; to classify a galaxy, the spectrum is considered a multidimensional vector, and it is assumed that the vectors are clustered around several cluster centers, known as classes. Then, the algorithm works

---

<sup>†</sup><https://ceers.github.io/dr05.html>

<sup>‡</sup><https://ceers.github.io/dr06.html>

iteratively to assign each spectrum to the nearest class and then the class template as the average over all the class members. In the end, the algorithm finds the number of classes and their templates and assigns to each galaxy spectrum one of the classes according to a certain probability. All the galaxies in a class have very similar spectra; their average spectrum is the template spectrum of the class.

These ASK classes are labeled according to their  $u - g$  color, from the reddest, ASK 0, to the bluest, ASK 27. Most ( $\sim 99\%$ ) galaxies in the SDSS-DR7 were classified into only 17 ASK major classes, with 11 additional minor classes including the remaining  $\sim 1\%$ . [Sánchez Almeida et al. \(2012\)](#) show that these rare classes correspond to metal-poor starbursts, and strong emission lines dominate their spectra. These minor classes, in particular, the classes ASK 15, ASK 17, ASK 20, ASK 21, ASK 25, ASK 26 and ASK 27 show  $\text{EW}([\text{OIII}]\lambda 5007)$  and  $\text{EW}(\text{H}\alpha) > 150\text{\AA}$  in both lines (see Table 5.2.1 our measurements using LiMe <sup>§</sup>). The complete and detailed analysis of these templates will be presented in a following paper (Amorín et al. in prep.). This chapter uses the templates of these minor classes as EELG templates to estimate their colors in the new NIRCcam photometry at high- $z$ .

Table 5.2.1: EWs of bright optical emission lines for the ASK templates considered EELGs in this project. We considered the underlying absorptions in recombination lines due to older stellar populations. The obtained values are comparable with the measurements reported in [Sánchez Almeida et al. \(2010\)](#).

ASK class	EW(H $\beta$ ) Å	EW([OIII]) Å	EW(H $\alpha$ ) Å
15	169.6	1097.9	918.3
17	144.9	874.3	782.3
20	92.3	496.2	484.9
21	85.9	460.1	457.5
25	63.9	298.1	334.4
26	45.1	172.8	232.0
27	57.4	234.1	302.4

### 5.3 Synthetic NIRCcam observations

A simple and effective way of searching for EELGs using broad and medium band photometry is by using color selections. These color selections target the extreme colors produced by extreme emission lines, which can reach colors excess up to  $\sim 2$  mag in neighboring filters (e.g., [Withers et al., 2023](#)).

Each spectrum of the 28 ASK classes was taken to a common wavelength range from 3030 to 9000Å considering the continuum slope. The ASK 15 has a shorter spectral range from 3747 to 8800Å. Each spectrum was redshifted to  $z = 2 - 10$  (with  $\Delta z = 0.05$  step sizes). Synthetic NIRCcam observations for the seven filters observed in CEERS were created for each redshift to search for broad and medium band color excesses driven by strong [OIII] + H $\beta$  and H $\alpha$  emission. The mean

<sup>§</sup><https://lime-stable.readthedocs.io/en/latest/>

density flux of each template in each filter for each redshift was calculated by

$$f_{\nu} \propto \frac{\int \lambda T f_{\lambda} d\lambda}{\int \frac{T}{\lambda} d\lambda} \quad (5.3.1)$$

where  $T$  is the transmission curve of each filter, and  $f_{\lambda}$  is the normalized template spectrum. In this way, the color in AB mag is given by  $\text{color}_{\text{AB}} = -2.5[\log(f_{\nu_1}) - \log(f_{\nu_2})]$ . Given that the template has a limited spectral range, our synthetic NIRCcam observations are limited only to the filters where the templates fall completely in the filters. Due to this, we estimate the magnitudes only in the filters where the template is within 10% of the filter transmission. An illustration is shown in Fig. 5.3.1 for  $z = 6$ , where the magnitudes for ASK templates are estimated only in filters in magenta. A video for the complete  $z$  range is available in [https://youtu.be/ltU8i\\_bsK4U](https://youtu.be/ltU8i_bsK4U).

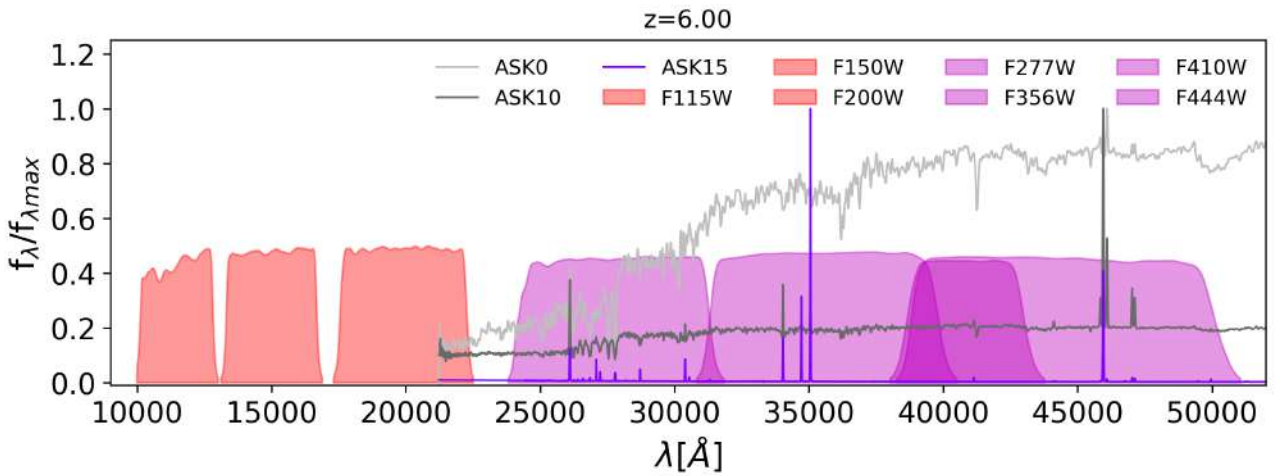


Figure 5.3.1: Illustration of the ASK templates at  $z \sim 6$  in the NIRCcam filters. In red are the NIRCcam filters where the templates are outside the filter. Three ASK templates are illustrated as examples (ASK0, ASK10, and ASK15).

In Fig. 5.3.2, we show the evolution with redshift of the colors used in this project based on the synthetic NIRCcam observations. With these results, we define color cuts based on the colors of the EELGs templates, which are separated from the other ASK classes in redshift windows.

## 5.4 Results

### 5.4.1 Color-color diagrams

We use the color cuts obtained in section 5.3 to select candidates based on their position in color-color diagrams. While it is possible to identify EELGs by targeting emission from a single emission line complex, our strategy requires strong emission in both  $[\text{OIII}] + \text{H}\beta$  and  $\text{H}\alpha$ . In this project, we focus on the most extreme EELG candidates, and because of that, we consider only the templates ASK 15, 17, 20, and 21, which show  $\text{EW}([\text{OIII}]) > 450 \text{ \AA}$ .

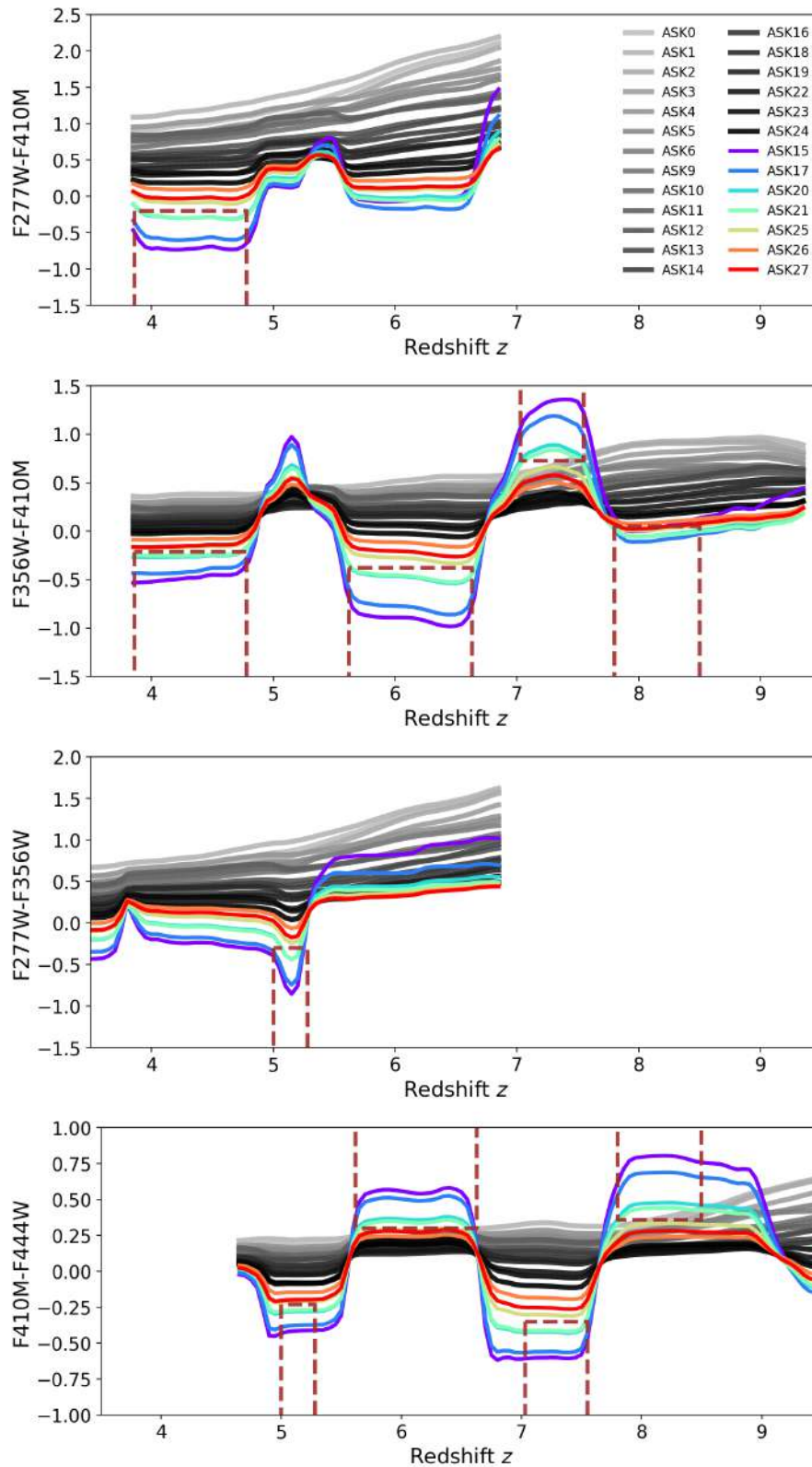


Figure 5.3.2: Redshift evolution of NIRCcam colors of ASK templates. The major ASK classes are in gray-scale colors, according to the legend. The minor ASK classes, i.e., EELGs, are in colors according to the legend. The dashed brown lines are the  $z$  ranges and color cuts used to select EELGs.

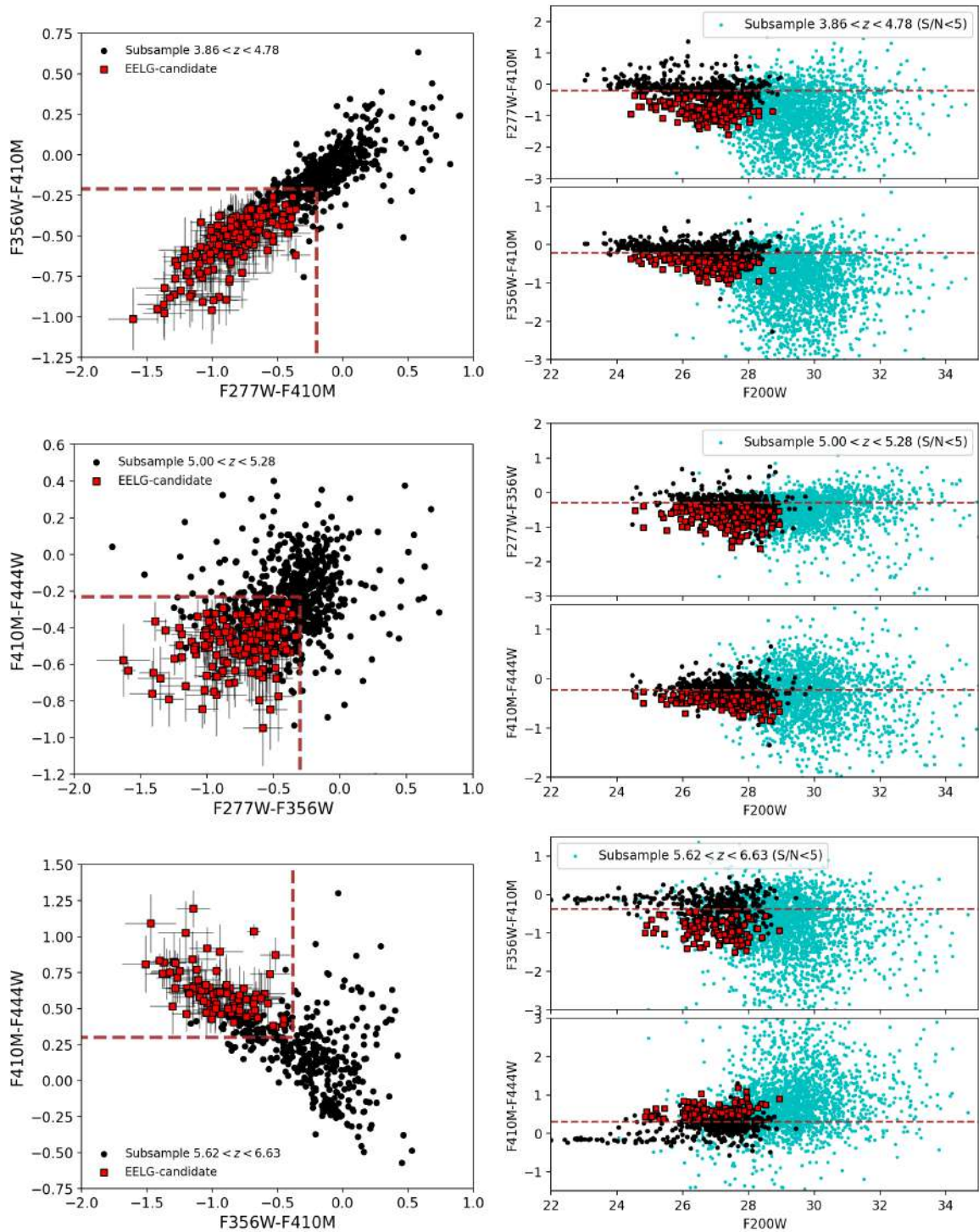


Figure 5.4.1: *Left panels:* Color diagrams to select EELGs at each redshift range. The color cuts are marked in brown dashed lines in each panel according to Eq. 5.4.1, 5.4.2, and 5.4.3, respectively. The selected EELG candidates are in red squares, while parent samples at similar redshifts are in black circles. *Right panels:* Color-magnitude diagrams for the colors in the selection criteria. Symbols are the same as in the left panels. The galaxies in the redshift window but with  $S/N < 5$  in any of the considered bands are shown in cyan circles. On the x-axis, the magnitude tracing the continuum bluewards  $[OII]\lambda 3727$  is shown.

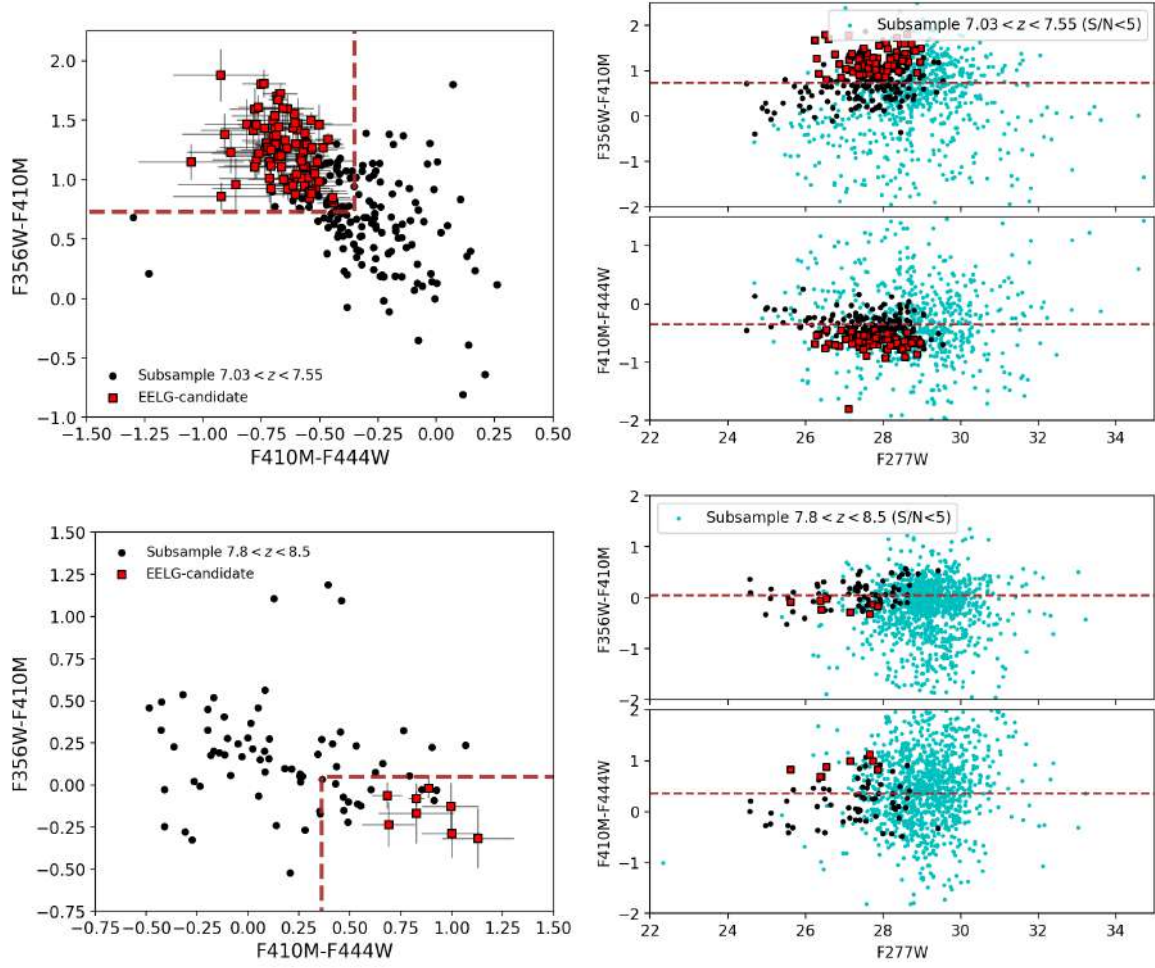


Figure 5.4.2: Same as in Fig. 5.4.1 but for Eq. 5.4.4, and 5.4.5, respectively.

We focus on five redshift ranges (see color-color diagrams in Fig. 5.4.1 and 5.4.2), and we consider only sources with  $S/N > 5$  in the photometry used in the color criteria. In the color criteria,  $\sigma$  refers to the color uncertainty.

First, we consider  $z = 3.86 - 4.78$  (top left panel in Fig. 5.4.1). In this redshift range, [OIII] falls in F277W, and  $H\alpha$  falls only in F356W. Based on our synthetic NIRCcam color, we define the following color criteria:

$$\begin{cases} F277W - F410M + \sigma(F277W - F410M) < -0.2 \\ F356W - F410M + \sigma(F356W - F410M) < -0.21 \end{cases} \quad (5.4.1)$$

There are 4218 sources in this redshift range. 162 sources ( $\sim 4\%$ ) satisfy the above conditions. An example of a candidate in this  $z$  range is shown in Fig. 5.4.3.

After that we consider the range  $z = 5.0 - 5.28$  (middle left panel in Fig. 5.4.1). In this range, [OIII] falls in F277W (or F356W) and  $H\alpha$  only in F410M. Based on our synthetic NIRCcam color, we define the following color criteria:

$$\begin{cases} F277W - F356W + \sigma(F277W - F356W) < -0.3 \\ F410M - F444W + \sigma(F410M - F444W) < -0.23 \end{cases} \quad (5.4.2)$$

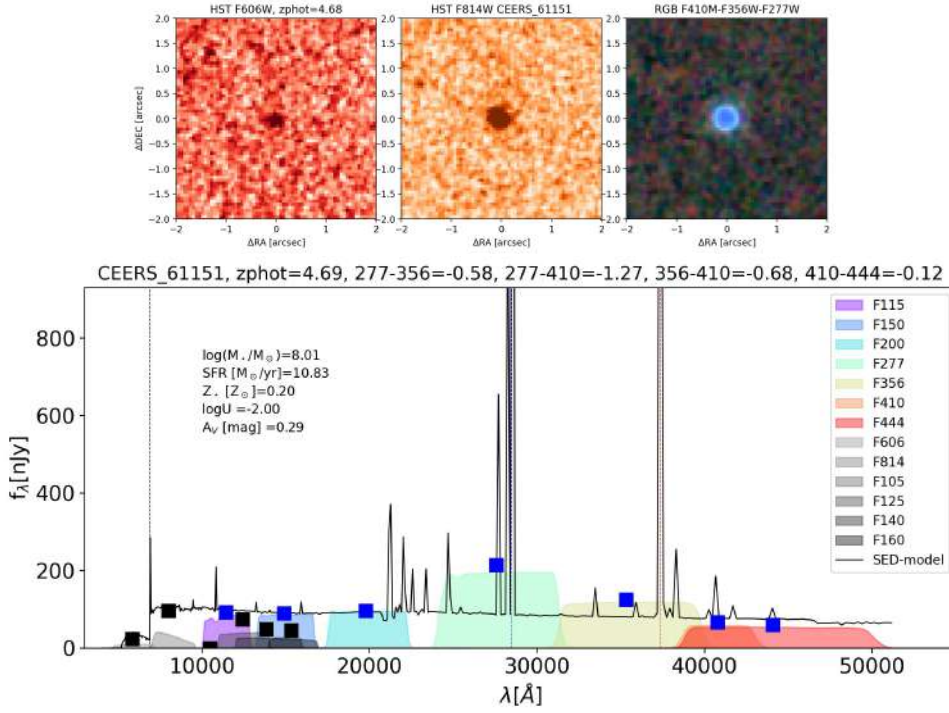


Figure 5.4.3: Example of an EELG candidate at  $z_{\text{phot}} = 4.68$ . In the top panels, images ( $2'' \times 2''$ ) of the galaxy in filters HST/F606W (left), HST/F814W (middle), and RGB image (right) with Red=F410M, Green=F356W, and Blue=F277W. On the bottom panel, SED of the galaxy. The blue (black) squares are the NIRCcam (HST) photometric points. NIRCcam (HST) filters are in rainbow-scale (gray-scale) colors, according to legend. The black solid line is the SED model (see in Sec. 5.4.2). The vertical dashed lines represent the position of Ly $\alpha$  (black), [OIII] (blue), and H $\alpha$  (red), according to their  $z_{\text{phot}}$ .

There are 3021 sources in this redshift range. 166 sources ( $\sim 5\%$ ) satisfy the above conditions. An example of a candidate in this  $z$  range is shown in Fig. 5.4.4.

We also consider the range  $z = 5.62 - 6.63$  (bottom left panel in Fig. 5.4.1). In this range, [OIII] falls in F356W and H $\alpha$  in F444W. Based on our synthetic NIRCcam color, we define the following color criteria:

$$\begin{cases} F356W - F410M + \sigma(F356W - F410M) < -0.38 \\ F410M - F444W - \sigma(F410M - F444W) > 0.3 \end{cases} \quad (5.4.3)$$

There are 3640 sources in this redshift range. 93 sources ( $\sim 2.5\%$ ) satisfy the above conditions. An example of a candidate in this  $z$  range is shown in Fig. 5.4.5.

We consider the redshift range from  $z = 7.03 - 7.55$  (top left panel in Fig. 5.4.2). In this range, [OIII] falls in F410M and F444W. Based on our synthetic NIRCcam color, we define the following color criteria:

$$\begin{cases} F356W - F410M - \sigma(F356W - F410M) > 0.73 \\ F410M - F444W + \sigma(F410M - F444W) < -0.35 \end{cases} \quad (5.4.4)$$

There are 998 sources in this redshift range. 92 sources ( $\sim 9\%$ ) satisfy the above conditions. An

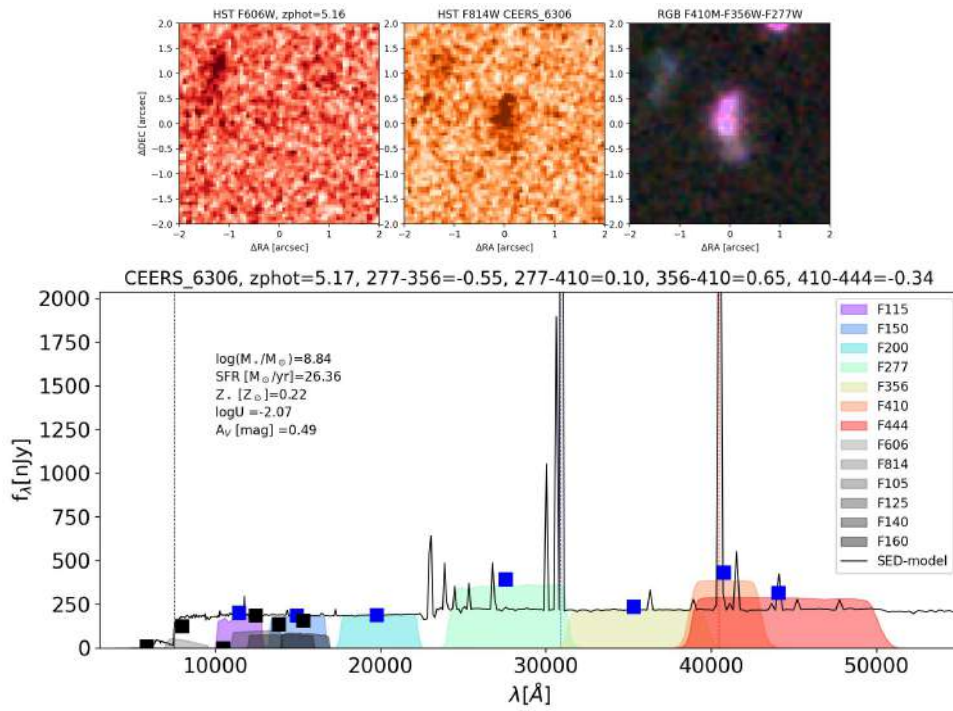


Figure 5.4.4: Example of an EELG candidate at  $z_{\text{phot}} = 5.17$ . Symbols as in 5.4.3.

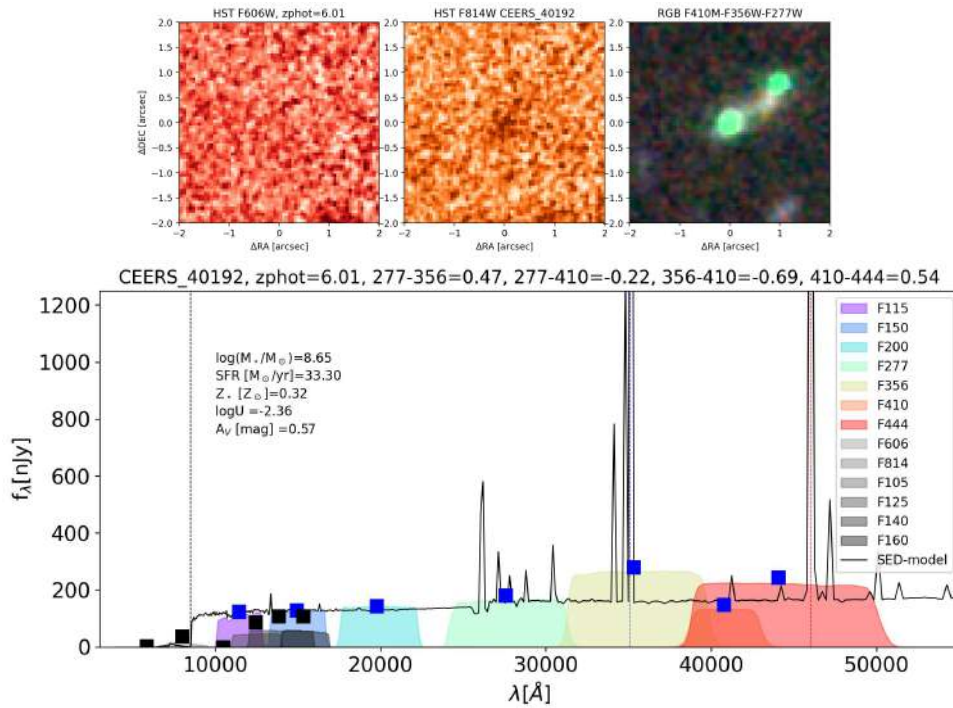


Figure 5.4.5: Example of an EELG candidate at  $z_{\text{phot}} = 6.01$ . Symbols as in 5.4.3.

example of a candidate in this  $z$  range is shown in Fig. 5.4.6.

The final redshift range we consider ranges from  $z = 7.8 - 8.5$  (bottom left panel in Fig. 5.4.2). In this range, [OIII] falls only in F444W. Based on our synthetic NIRCcam color, we define the following color criteria:

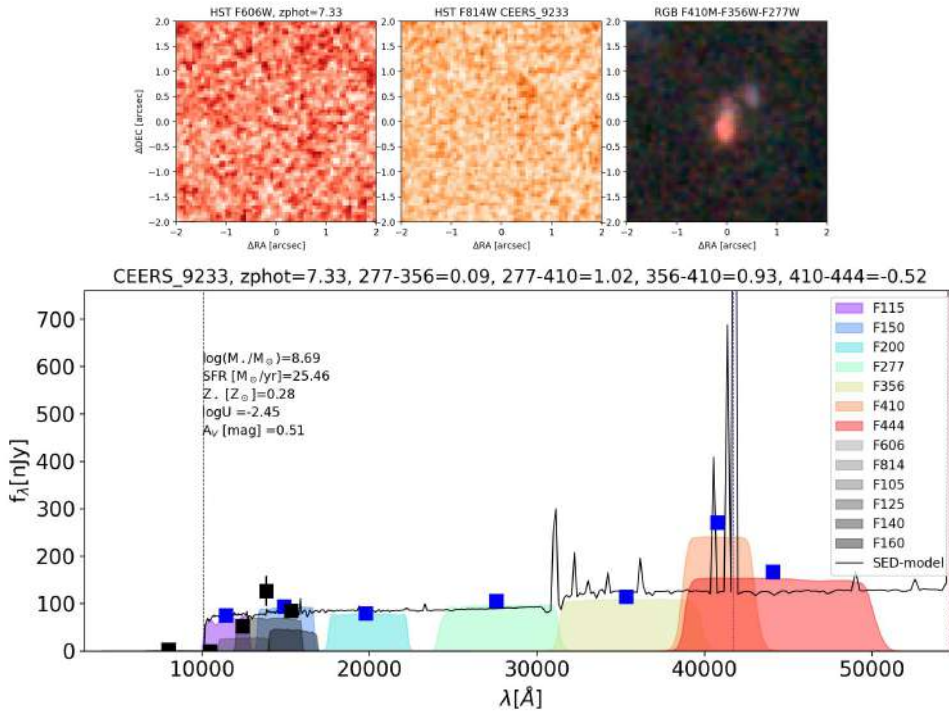


Figure 5.4.6: Example of an EELG candidate at  $z_{\text{phot}} = 7.33$ . Symbols as in 5.4.3.

$$\begin{cases} F356W - F410M - \sigma(F356W - F410M) < 0.05 \\ F410M - F444W + \sigma(F410M - F444W) > 0.36 \end{cases} \quad (5.4.5)$$

There are 1357 sources in this redshift range. 8 sources ( $\sim 0.6\%$ ) satisfy the above conditions. An example of a candidate in this  $z$  range is shown in Fig. 5.4.7.

Our final sample of EELG candidates consists of 521 galaxies<sup>¶</sup>. We highlight that by limiting our selection of galaxies with  $S/N > 5$  in their photometry, we are selecting the brighter ( $< 28-29$  mag) galaxies of the corresponding parent samples (see right panels in Fig. 5.4.1 and 5.4.2). This secures the more reliable candidates but softening that condition is a factor we will explore in the future. The final redshift distribution of the EELG candidates is shown in Fig. 5.4.8.

## 5.4.2 Physical parameters

To obtain the physical properties of the sample, we perform SED fitting with HST+JWST photometry. We consider the HST filters F606W, F814W, F105W, F125W, F140W, F160W. We consider the entire set of filters used in the CEERS surveys, which are F115W, F150W, F200W, F277W, F356W, F410M, and F444W. We used BAGPIPES (Carnall et al., 2018) to estimate the physical parameters with the Bruzual & Charlot (2003) stellar population models. We consider an exponential  $\tau$ -model for the SFH with age ranging from 10Myr to the age of the Universe at the observed redshift. We allow the  $\tau$  parameter to vary between 0.1 to 10 Gyr. We allow the metallicity to vary up to  $0.5Z_{\odot}$  freely. For

<sup>¶</sup>All the images of the EELG candidates are available in [https://github.com/mfillerena/EELGs/blob/71c958d5b67d4a40f1750243c141ec51e132bfd6/RGB\\_EELG\\_candidates.pdf](https://github.com/mfillerena/EELGs/blob/71c958d5b67d4a40f1750243c141ec51e132bfd6/RGB_EELG_candidates.pdf)

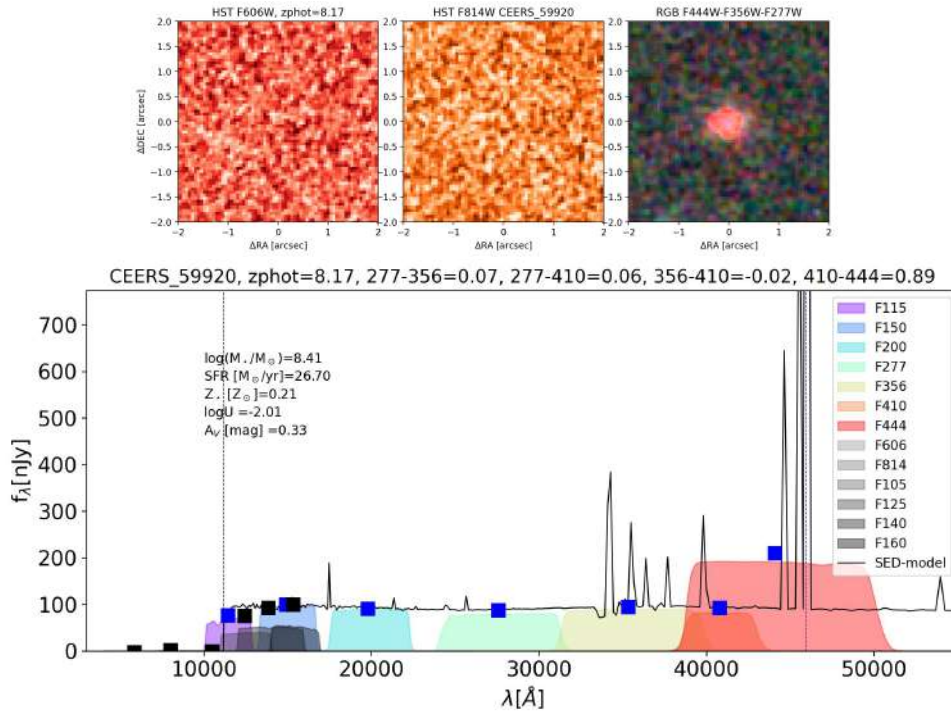


Figure 5.4.7: Example of an EELG candidate at  $z_{\text{phot}} = 8.17$ . Symbols as in 5.4.3.

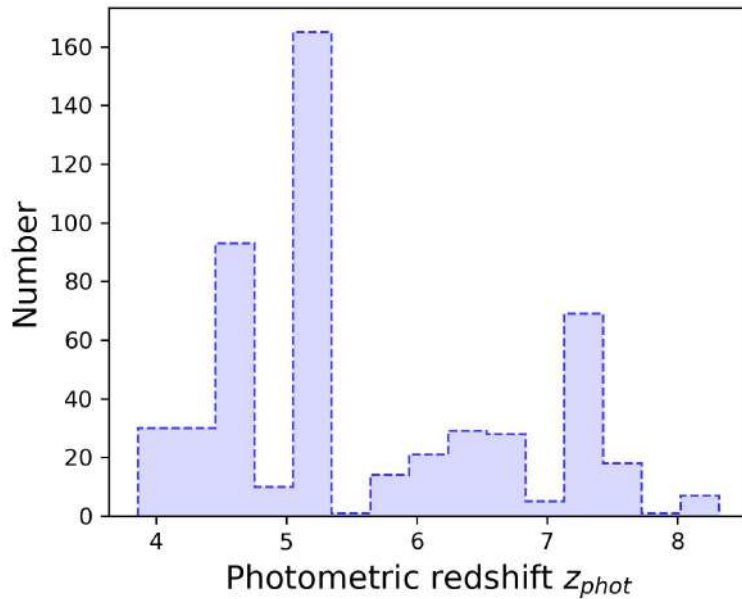


Figure 5.4.8: Distribution of photometric redshift of the final sample of EELG candidates.

the dust component, we consider the [Calzetti et al. \(2000\)](#) attenuation curve and let the  $A_V$  parameter vary between 0 – 2 mag. We also include a nebular component in the model, and we let the ionization parameter freely vary between  $-3$  and  $-2$ . Some examples of the SED model are shown in [Fig. 5.4.3](#), [5.4.4](#), [5.4.5](#), [5.4.6](#).

The distribution of the main obtained SED parameters is shown in [Fig. 5.4.9](#), which includes stellar mass, SFR, sSFR,  $\log U$ , stellar metallicity, and absolute attenuation  $A_V$ .

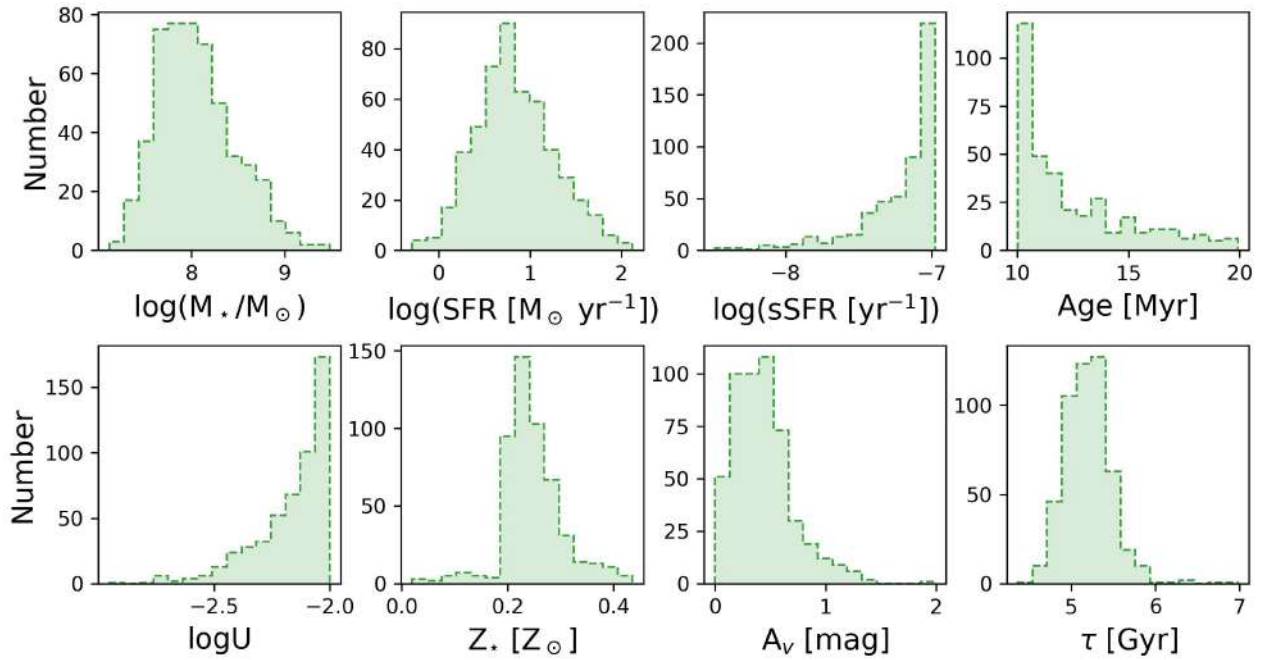


Figure 5.4.9: Distribution of the physical parameters based on the SED fitting for the sample of EELG candidates.

We find that our sample shows stellar masses between  $10^{7.1}M_{\odot}$  and  $10^{9.5}M_{\odot}$  with a mean value of  $10^{8.05}M_{\odot}$ . They are actively forming stars with SFRs between  $0.52$  to  $131 M_{\odot} \text{ yr}^{-1}$ , with a mean value of  $11.5 M_{\odot} \text{ yr}^{-1}$ . This implies they show very high sSFR above  $10^{-8.45} \text{ yr}^{-1}$  and up to  $10^{-7} \text{ yr}^{-1}$ , which makes them capable of doubling their stellar content in  $\sim 10$ - $280$  Myr. We also find that these galaxies are young, with times after the onset of star formation of roughly  $10$ - $20$  Myr, with a mean value of  $12.5$  Myr.

Regarding their ISM properties, we find they show high ionization parameters with a mean value of  $\log U = -2.16$ , with subsolar metallicities ranging from  $0.02$  to  $0.43 Z_{\odot}$  with a mean value of  $\sim 0.25 Z_{\odot}$ . They also show low dust extinction with  $A_V$  values ranging from  $\sim 0$  to  $2$  mag, but the mean value is  $0.43$  mag. We note that we are considering a  $\tau$ -model for the SFH, but the results of the SED fitting indicate  $\tau$  values, i.e., the timescale of the decrease of the SFH, of  $\sim 5.2$  Gyr on average which indicates that they are consistent with a constant SFH.

In order to constrain the sizes of the EELG candidates, we use the Galfit catalogs of the collaboration (McGrath in prep.). Galfit (Peng et al., 2002, 2010a) was run for sources with  $F356W < 28.5$  mag using background-subtracted mosaics. Most of the EELG candidates are in the catalog (90% of the sample). The photometry catalogs were used for making first guesses on source location, magnitude, size, position angle, and axis ratio. The Kron radius was used to determine an appropriate image thumbnail region for Galfit to fit. All galaxies within 3 magnitudes of the primary source, but no fainter than 27 mag, that fell within the thumbnail region were fit simultaneously. Galaxies that were not fit simultaneously were masked during the fitting process using the segmentation map. This procedure was performed for both F200W and F356W. Here we only considered the F200W results since they are tracing mostly the FUV or NUV (depending on the redshift) in order to put constraints on the stellar regions rather than on the diffused gas. We only consider 303 sources with good fit quality (so-called Flag=0). The distribution of the effective radius and Sersic index are displayed in

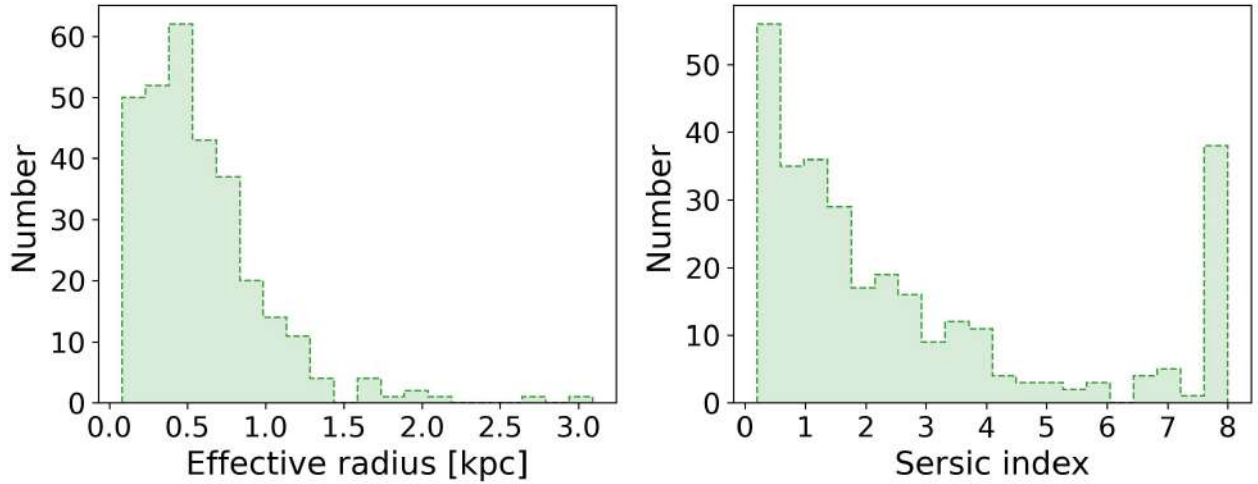


Figure 5.4.10: Distribution of the effective radius and Sersic index for the sample of EELG candidates.

Fig. 5.4.10. The subsample shows effective radii ranging from 80pc to 3kpc, with a mean value of 0.58kpc. Additionally, they show Sersic indexes from 0.2 to 8, with a mean value of 2.7.

### 5.4.3 NIRSpec spectroscopy

The CEERS survey also includes six NIRSpec pointings, numbered p4, p5, p7, p8, p9, and p10. Each of these pointings has observations with the three NIRSpec medium resolution (G140M, G235M, and G395M) gratings and with the low-resolution Prism. The grating set covers from  $0.97\text{--}5.10\mu\text{m}$  with a resolving power of  $\sim 1000$ , while the prism covers from  $0.60\text{--}5.30\mu\text{m}$  with a resolving power of  $\sim 100$ . More objects can be observed simultaneously with the prism thanks to the shorter length (in pixels) of the prism spectra.

A subsample of our EELG candidates was included as potential NIRSpec targets of this spectroscopy follow-up. We restrict our selection to the brightest candidates ( $F150W < 27$  mag) at  $z \sim 3.8\text{--}4.8$ . In the end, three galaxies were included in the follow-up program. Two of them were observed only with the prism, while one of them was observed with prism and medium-resolution grating. The three galaxies are shown in Fig. 5.4.11.

Additionally, CEERS team members, scientific collaborators, and some scientists external to the team contributed lists of potential NIRSpec targets. In total, 34 galaxies of our EELG candidates have NIRSpec spectra. Of them, 27 have reduced spectra already public. Here, we use the data products of the collaboration. In particular, the fluxes of emission lines and spectroscopic redshifts were measured using LiMe (Fernández et al., 2023). 19 of the galaxies in our sample already have measurements of their emission lines.

In Fig. 5.4.12 (top left panel), we compare the photometric and the spectroscopic redshift. We find that photometric redshifts can be up to 0.6 larger than spectroscopic redshifts. And, on average, they are 0.16 larger than  $z_{\text{spec}}$ . We also compared the line flux ratio  $[\text{OIII}]/\text{H}\beta$  from the spectra and the SED modeling (see the top right panel in Fig. 5.4.12). They generally show a mean difference of 0.08 dex towards higher values from fluxes determined from the spectra. But the differences can

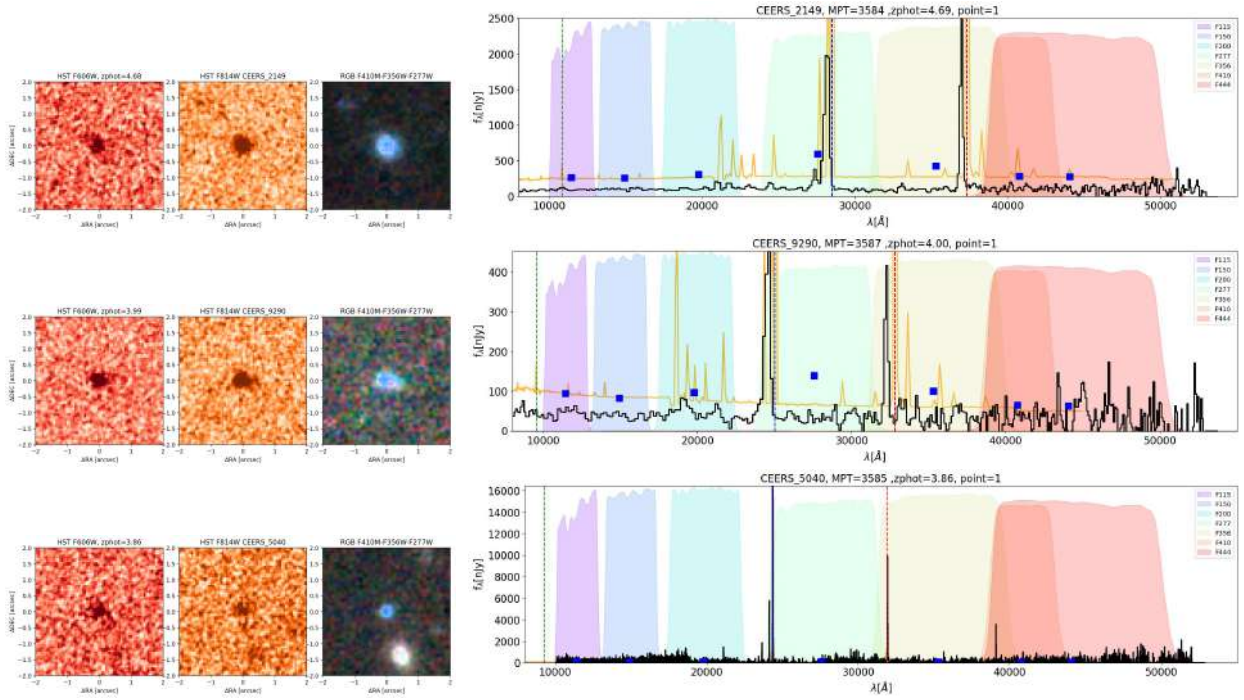


Figure 5.4.11: Sample selected based on this technique for spectroscopy follow-up. Symbols as in 5.4.3, but the black solid line is the NIRSpect observed spectrum. The orange line is the SED model.

reach up to 0.35 dex. The differences are larger at  $[\text{OIII}]/\text{H}\beta \gtrsim 0.7$ , which indicates that models tend to underpredict the flux ratios at high ionization.

We perform a similar comparison between the estimated EWs of  $[\text{OIII}]$  (see the bottom left panel in Fig. 5.4.12) and  $\text{H}\beta$  (see the bottom right panel in Fig. 5.4.12). For the SED EWs, we considered the predicted fluxes from the nebular component of the model and the continuum at  $\lambda_{\text{peak}} \pm 20\text{\AA}$  from the SED spectrum. We find that most of the  $\text{EW}([\text{OIII}])$  from SED model tend to be underpredicted by up to 0.5dex. In a few galaxies, the SED models tend to overpredict the  $\text{EW}([\text{OIII}])$  up to 0.3dex. In the case of  $\text{EW}(\text{H}\beta)$ , the differences are up to 0.5dex over- and underpredicting the EWs from the SED model.

We also validate our method by comparing the EWs of galaxies with NIRSpect spectra that are not classified as EELGs according to our selection criteria. There are 31 galaxies with measurements of their emission lines with spectroscopic redshifts in the redshift range we considered in our selection. From them, 24 show  $\text{EW}([\text{OIII}]) > 0$ . We highlight that the measurement of the EWs directly from the spectra may be affected by the faint continuum of these sources, which makes it difficult to determine the continuum level. In Fig. 5.4.13 we show the  $\text{EW}([\text{OIII}])$  directly from the NIRSpect spectrum of the EELGs and the galaxies that are excluded as candidates. We note that 10 out of the 31 galaxies have a spectroscopic redshift in the window ranges, but the photometric redshift is outside the range, which excludes these galaxies from our selection. Few of them show EWs higher than the selection threshold (red dashed line in Fig. 5.4.13). This indicates that we may be missing some candidates whose photometric redshift is not exact. Most of the galaxies excluded from our selection criteria show indeed lower EWs than our candidates.

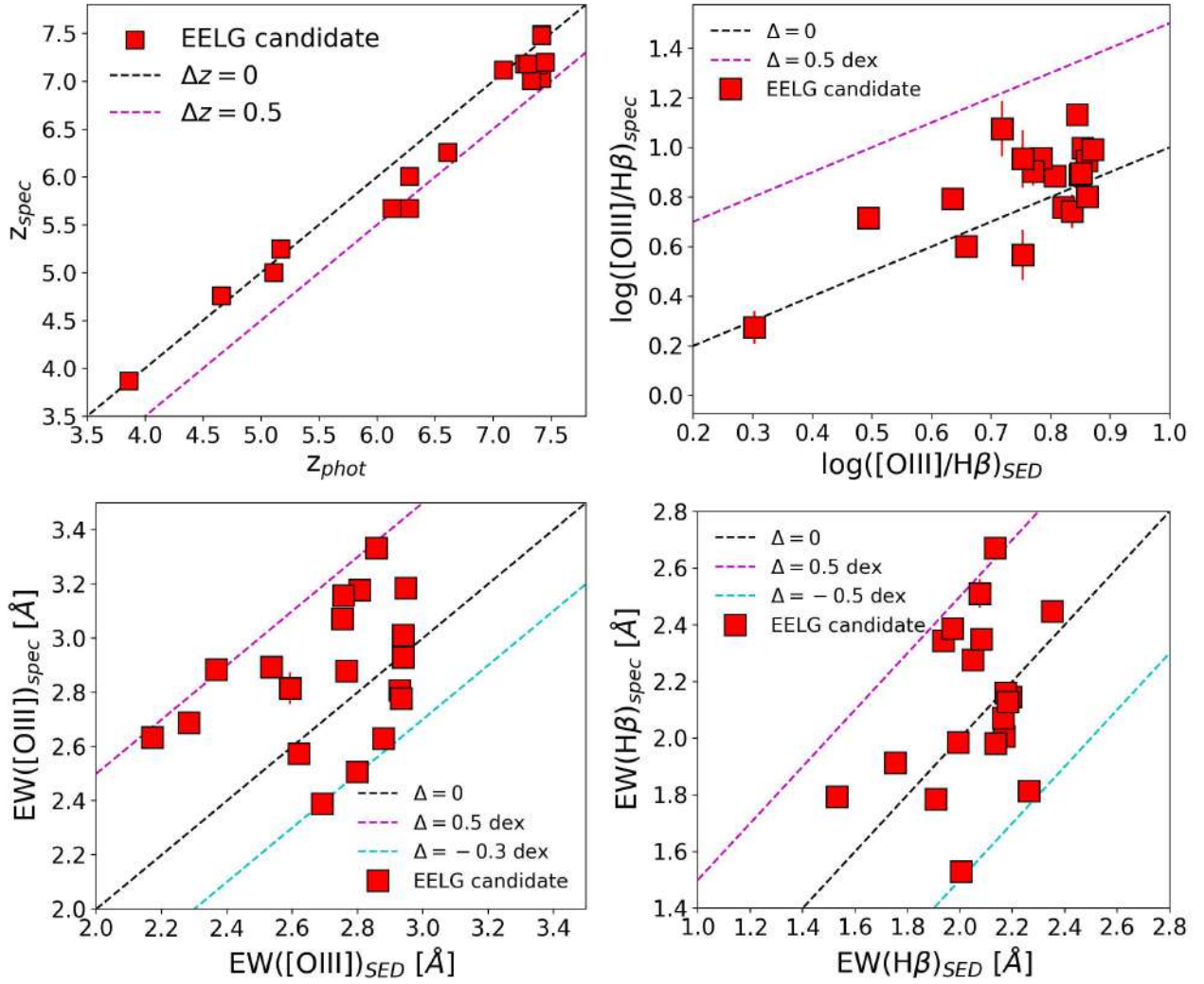


Figure 5.4.12: Comparison between parameters based on photometry and spectroscopy for the sub-sample of EELG candidates with NIRSpec spectroscopy. On the left top panel, a comparison between photometric and spectroscopic redshift. On the right top panel, a comparison between  $\log([\text{OIII}]/\text{H}\beta)$  based on the SED model and the spectrum. On the bottom panels, we show the comparison between EWs of [OIII] (left) and H $\beta$  (right) from spectra and the SED model. The dashed lines represent the differences  $\Delta$  between both parameters.

#### 5.4.4 Ionization source and scaling relations

We use the predicted fluxes of emission lines from the SED model to explore the nature of the ionizing source in the sample of EELG candidates. In Fig. 5.4.14, we show the position of our sample in the classical BPT diagram. We find that their position is consistent with the minor ASK templates of metal-poor starbursts with high  $\log([\text{OIII}]/\text{H}\beta) \gtrsim 0.7$  and low  $\log([\text{NII}]/\text{H}\alpha) \lesssim -1$  ratios. This region is populated by local analogs of these high- $z$  systems such as GP (e.g., Cardamone et al., 2009). Some galaxies show lower [OIII]/H $\beta$  ratios than these templates, which indicates that they are contaminants in the sense that they do not show similar properties as the other selected candidates and the color cuts should be revised in more detail. We left this analysis as future work. Therefore, all candidates are consistently powered by massive stars with no contribution from AGN.

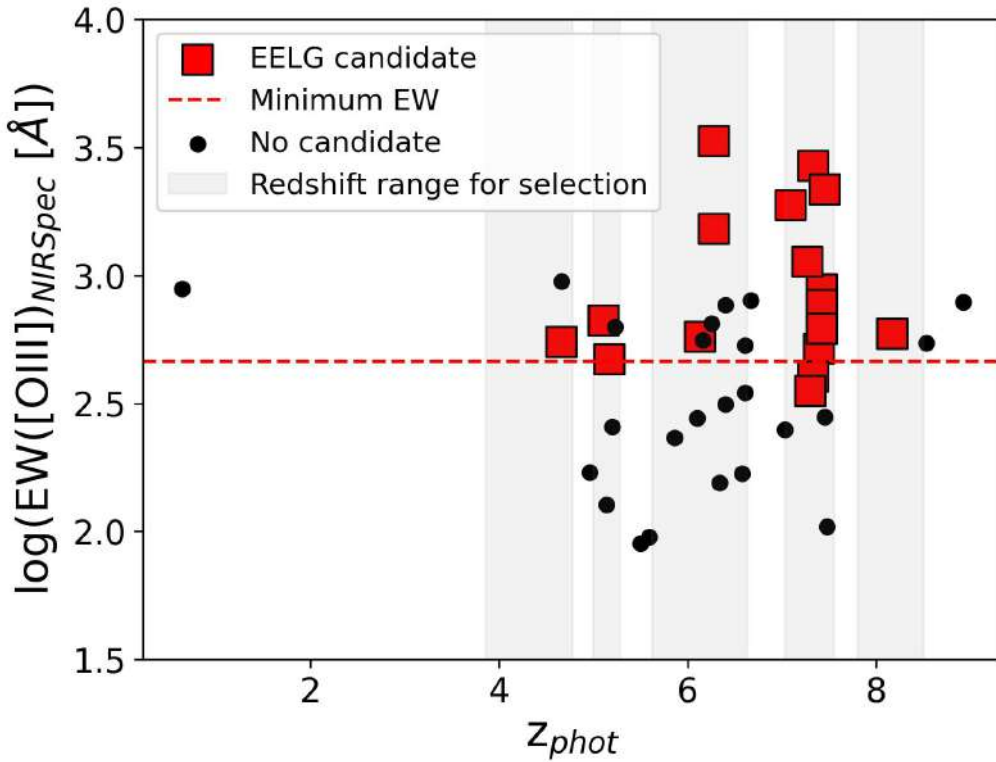


Figure 5.4.13: EW([OIII]) for the EELG candidates (in red squares) and excluded galaxies from our selection criteria (in black circles) as a function of their photometric redshift. The gray-shaded regions are the redshift ranges considered for the selection. The red line is the minimum EW from the selected ASK templates.

Due to the offsets shown in Fig. 5.4.12, their position in the y-axis might be underpredicted, and they can reach the  $z \sim 3$  demarcation line. Still, spectroscopic confirmation is needed to constrain their nature better. Still, hints suggest they are metal-poor young starbursts.

The final analysis we present in this ongoing project is the scaling relations between EWs and the physical properties of the galaxies. A clear negative correlation between emission line EW and stellar mass has been found in the literature at different redshifts (e.g., Tang et al., 2019; Lumberras-Calle et al., 2022; Matthee et al., 2022). This indicates that galaxies with lower masses tend to have stronger recent star formation events relative to their mass (higher sSFR). As shown in the top panel in Fig. 5.4.15, we find that the spectroscopically-confirmed EELGs in our sample follow the trend observed at lower redshift ( $z \sim 3$ , black dashed line in Fig.). This is consistent with other works based on stacking of  $z > 5.5$  galaxies (red squares, Matthee et al., 2022). Regarding the EELG candidates, the trend is less clear. Galaxies with the highest sSFR ( $\sim 10^{-7} \text{ yr}^{-1}$ ), tend to show saturated  $\text{EW}([\text{OIII}] + \text{H}\beta) \sim 1400 \text{ \AA}$ . This may be an effect due to the grid of models considered that can not reproduce higher EWs due to the age limit of 10 Myr or due to the ionization parameter limit of -2. We will explore this scenario in the future. We also note that galaxies with lower sSFR tend to show lower EWs than the ASK templates of our selection criteria. In any case, galaxies with low stellar masses and high sSFR tend to show EWs and then are more likely to show extreme ISM conditions reflected in their extreme EWs.

We also explore the relationship with the star formation surface density. We estimate it as  $\Sigma_{\text{SFR}} =$

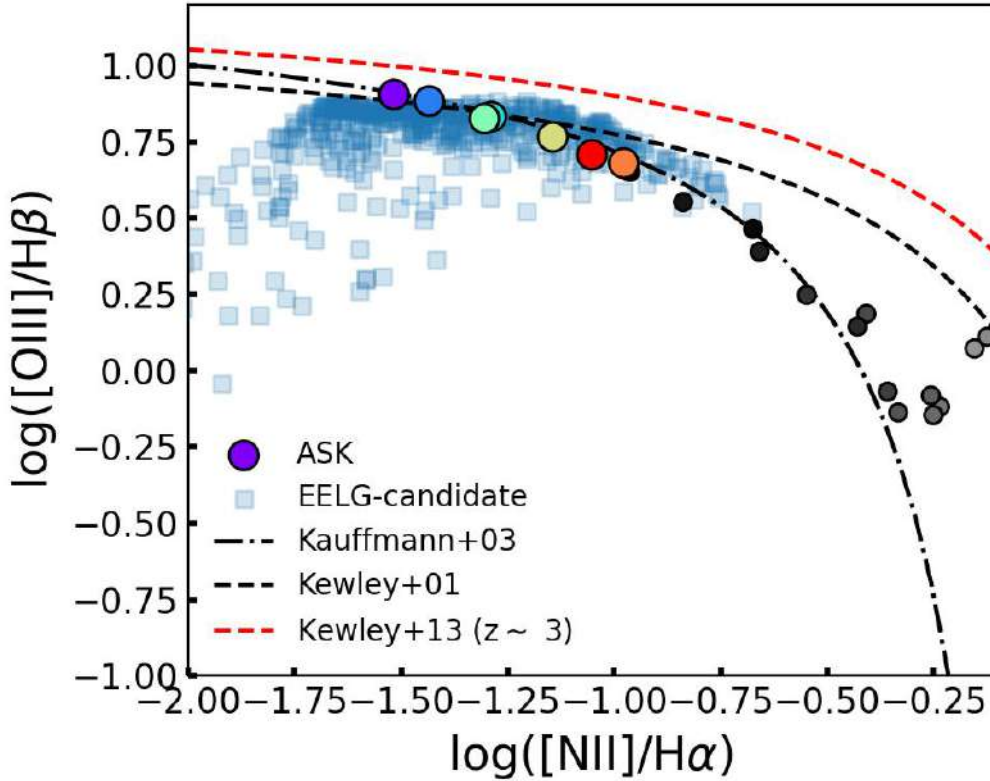


Figure 5.4.14: BPT diagram. The EELG candidates are in blue squares based on emission line ratios from the SED model. The circles are ASK templates with colors as in Fig. 5.3.2. The black lines are demarcation limits between star-forming galaxies and AGN, according to Kewley et al. (2001); Kauffmann et al. (2003). The red line is the demarcation at  $z \sim 3$  (Kewley et al., 2013).

$\frac{\text{SFR}_{\text{SED}}}{2\pi r_{\text{eff}}^2}$ , where  $r_{\text{eff}}$  is the effective radius as discussed in Sec. 5.4.2. We find that the galaxies in our sample show  $\Sigma_{\text{SFR}}$  values ranging from 0.2 to  $41 \text{ M}_{\odot} \text{ yr}^{-1} \text{ kpc}^{-2}$ , with a mean value of  $5 \text{ M}_{\odot} \text{ yr}^{-1} \text{ kpc}^{-2}$ . As displayed in the bottom panel in Fig. 5.4.15, we find that our sample of EELG candidates tends to show higher EWs while increasing the  $\Sigma_{\text{SFR}}$ . We also note the saturation in EWs as in the top panel. Regarding the spectroscopically-confirmed EELGs, we find that they show high  $\Sigma_{\text{SFR}}$  and similarly to the relation with the stellar mass, we find that few of them show EWs lower to the selection threshold, but they are the ones with lower sSFRs.

## 5.5 Summary

We demonstrate that NIRCcam can identify a large sample of previously unknown EELGs in a wide range of redshifts showing unique properties similar to the rare metal-poor local starburst. Our color selections can effectively identify galaxies with  $\text{EW}([\text{OIII}] + \text{H}\beta) > 680 \text{ \AA}$  at all redshifts targeted in this work. This is an ongoing but promising project, and we have some improvements that we will address in the near future. First, we note that we are using templates that are representative of the galaxies within the class. However, within each class, there is an intrinsic scatter in their properties (Amorín et al. in prep.), e.g., they show different  $[\text{OIII}]/\text{H}\beta$  ratios that we are not considering while

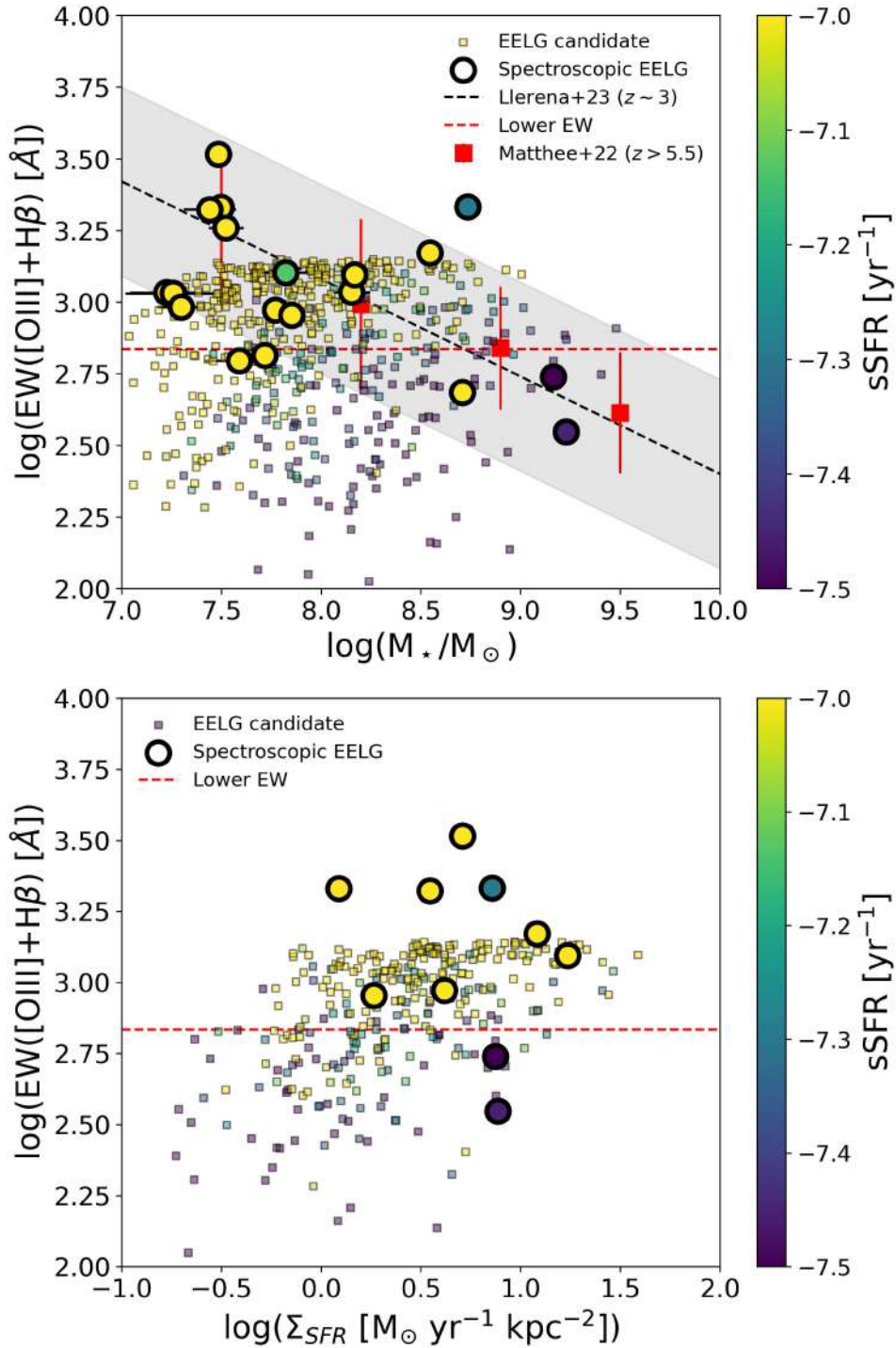


Figure 5.4.15: *Top panel:* Relation between stellar mass and  $\text{EW}([\text{OIII}]+\text{H}\beta)$ . In squares, the sample of EELG based on their SED model. In circles, the subsample of candidates with NIRSspec spectroscopy. Both are color-coded by their  $\text{sSFR}$ . The black dashed line is the relation at  $z \sim 3$  and the observed scatter (Llerena et al., 2023). The red line is the minimum EW in the ASK templates for EELGs used in the color cuts. The red squares are stacks of  $z > 5.5$  galaxies (Matthee et al., 2022). *Bottom panel:* Relation between  $\Sigma_{\text{SFR}}$  and  $\text{EW}([\text{OIII}]+\text{H}\beta)$ . Symbols are the same as in the left panel.

performing the synthetic observations. This may be an explanation for the properties we estimate for some candidates, for example, their position in the BPT diagram, which does not depend exclusively

on EWs which is our selection criteria.

We also remark that we observed that some parameters in the SED model are saturated. For example, the considered models do not show ages lower than 10Myr or ionization parameters higher than  $-2$ . This may have an effect on the ionization properties that may be underestimated as can be seen in Fig. 5.4.15 where no  $\text{EW}([\text{OIII}]+\text{H}\beta) \gtrsim 1600 \text{ \AA}$  are obtained. We plan to test alternative SFHs or different stellar population models such as BPASS (Eldridge et al., 2017) to improve the physical parameters of these more extreme cases.

We also are imposing a very restrictive high S/N cut in all the bands we used in the color-color diagrams for each redshift. This allows us to secure the more robust bright candidates, but we may be losing fainter candidates which are also interesting to study. Shortly, we aim to address this point by comparing the results by reducing the S/N cut and determining how many good candidates we are losing due to this criteria and how many contaminants we might be including.

Additionally, we are trusting the photometric redshifts in our selection method. But, as we mentioned in Sec. 5.4.3, we may be losing candidates whose photometric redshift is slightly (or totally) different than the spectroscopic redshift and is left out of the redshift windows in our selection criteria. One improvement is to make redshift-independent cuts based only on extreme color, if possible.

Finally, these candidates are extreme laboratories that now can be studied in such detail that was very hard years ago. This project aims to select this list of candidates for further analysis to unveil the extreme ISM conditions with exquisite details as is done in local metal-poor starbursts. In the context of this Thesis, it is interesting to study the rest-UV spectra of these galaxies to test the results obtained in previous Chapters 3 and 4, but directly in galaxies approaching, and deep into, the EoR.

# Conclusions and perspectives for future

## 6.1 Concluding remarks

We conclude this Thesis with our general conclusions and our perspective for the future to come. We have performed a detailed analysis of the properties of low-mass star-forming galaxies from the point of view of their UV+optical properties.

First, we study a large representative sample of 217 galaxies with CIII] detection at  $2 < z < 4$  covering a range of  $\sim 2$  dex in stellar mass and our results provide new insight into the nature of UV line emitters at  $z \sim 3$ , paving the way for future studies at higher- $z$  using the JWST. Our strategy is based on stacking by different bins. This is what we have learned from this analysis:

- i) **What is the nature of CIII] emitters?** Although we only find reliable CIII] emitters in  $\sim 30\%$  of the VANDELS parent sample, it seems that CIII] is common in normal SFGs, and it is a useful tool to study the ISM of galaxies. On the other hand, extreme emitters ( $\text{EW}(\text{CIII])} \gtrsim 8\text{\AA}$ ) are exceedingly rare ( $\sim 3\%$ ) in VANDELS, which is expected as the C3 sample is drawn from a parent sample of main-sequence galaxies. Their extreme emission lines are powered by stellar photoionization, suggesting no other ionization source than massive stars.
- ii) **What are the physical conditions that favor CIII]1909 emission?** We show that CIII] emission is complex since it depends on several factors, such as global properties, such as stellar mass content, SFRs, luminosity, and stellar metallicity. Galaxies with higher  $\text{EW}(\text{CIII])}$  show lower stellar metallicities. This result suggests that extremely low metallicities ( $< 10\%$  solar) should be expected for the most extreme galaxies in terms of their  $\text{EW}(\text{CIII])}$ . The stellar metallicities of CIII] emitters are not significantly different from that of the parent sample, increasing from  $\sim 10\%$  to  $\sim 40\%$  solar for stellar masses  $\log(M_*/M_\odot) \sim 9-10.5$ .
- iii) **Is CIII] useful for redshift determinations at  $z > 6$ ?** Stacks with larger  $\text{EW}(\text{CIII])}$  show larger  $\text{EW}(\text{Ly}\alpha)$ , but not all CIII] emitters are  $\text{Ly}\alpha$  emitters. CIII] emitters are good markers of LAEs, especially for galaxies with low stellar mass, low luminosity, and high star formation rates. This confirms the potential use of CIII] to identify and study galaxies at the EoR, for which

Ly $\alpha$  emission is strongly attenuated due to IGM opacity. However, this could be challenging due to the lower EWs of CIII] than that of Ly $\alpha$  in SFGs. A similar stacking approach will be useful with large enough samples at  $z > 6$  for studying their global properties, but CIII] may be the only robust and high S/N emission that may be observed to have individual detections from the ground.

- iv) **Are these galaxies chemically young?** We find the C/O abundances of CIII] emitters ranging 35%-150% solar, with a noticeable increase with FUV luminosity and a smooth decrease with CIII] EWs. Fainter FUV galaxies have lower C/O, higher EW(CIII]), and lower  $Z_*$ , which suggest a UV spectrum dominated by massive stars and a bright nebular component that is still chemically unevolved. We discuss for the first time the C/O-Fe/H and the C/O-O/H relations for star-forming galaxies at  $z \sim 3$ . They show stellar and nebular abundances consistent with the trends observed in Milky Way halo and thick disc stars and local HII galaxies, respectively. We find a good agreement with modern chemical evolution models, which suggest that CIII] emitters at  $z \sim 3$  are experiencing an active phase of chemical enrichment.

After, we present a detailed analysis of the chemical abundances and kinematics of the ionized gas of low mass ( $10^{7.9}$ - $10^{10.3}M_{\odot}$ ) SFGs at  $z \sim 3$ . We use new follow-up NIR spectroscopy for a sample of 35 SFGs selected based on their rest-UV emission line properties (from Ly $\alpha$  to CIII]) from two previous works using ultra-deep optical spectra of the VANDELS (Llerena et al., 2022) and VUDS (Amorín et al., 2017) surveys. We focus our analysis of the NIR spectra on strong emission lines in the rest-optical, from [OII] $\lambda$ 3727 to H $\alpha$ . Overall, our results suggest a complex interplay between star formation, gas kinematics, and chemical enrichment in relatively young galaxies at  $z \sim 3$ . This is what we have learned from this analysis:

- i) **What are the ISM properties of CIII] emitters?** Our sample is characterized by high [OIII]/H $\beta$  > 4 ratios, suggesting high ISM ionization conditions. About 15% of our sample show EW([OIII]) > 1000Å that closely resemble those measured in  $z > 6$  EoR galaxies with photometric data (e.g., Endsley et al., 2021) and, more recently, with JWST spectroscopy (e.g., Matthee et al., 2022). They show mean electron temperatures  $T_e = 1.8 \times 10^4$  K with a mean  $12 + \log(\text{O}/\text{H}) = 7.91$  or 17% solar. We also derive a wide range of C/O abundance ratios ranging from  $\log(\text{C}/\text{O}) = -0.9$  to  $\log(\text{C}/\text{O}) = -0.15$  (23% and 128% solar, respectively) with a mean value of  $\log(\text{C}/\text{O}) = -0.52$  (54% solar). From the analysis of the CO-O/H relation, we find no apparent increase of C/O with metallicity, as models predict (e.g., Mattsson, 2010; Nicholls et al., 2017), but a large scatter of C/O values around metallicity  $\sim 10 - 20\%$  solar. On the other hand, our galaxies appear consistent with an increase of C/O with stellar mass, suggesting that a fraction of their C/O may have a secondary origin. One possible interpretation for these trends is that a recent metal-poor inflow may dilute O/H while keeping the C/O as large as expected for their stellar mass. To explore further this and other possible interpretations, larger representative samples over a wide range of mass and metallicity are needed.
- ii) **Are outflows shaping the properties of EELGs?** These results suggest that our SFGs are experiencing a rapid and active episode of massive star formation in which outflows from stellar feedback and fresh gas accretion can be significant regulators of their mass and metal content. From a detailed multi-Gaussian component fitting of [OIII] $\lambda\lambda$ 4959,5007 line profiles, we find 65% of our galaxies showing two distinct kinematic components: a narrow component with intrinsic velocity dispersion of  $\sigma_N \sim 57 \text{ km s}^{-1}$  accounting for the core of the lines and a

broader component with  $\sigma_B \sim 121 \text{ km s}^{-1}$  that best fit the extended line wings. We find the broad component is typically blue- or red-shifted by  $\sim 30 - 40 \text{ km s}^{-1}$  with respect to the narrow one in most galaxies. Following the close similarities with local analogs, such as the Green Peas (Amorín et al., 2012a; Hogarth et al., 2020), we interpret the narrow and broad kinematic components as gas tracing virial motions and turbulent outflowing ionized gas driven by strong star formation, respectively. From our kinematic analysis, we find typical outflow velocities of  $\sim 280 \text{ km s}^{-1}$ , which are found to correlate weakly with stellar mass but strongly with the instantaneous SFR traced by Balmer lines and  $\Sigma_{\text{SFR}}$ .

- iii) **How important is stellar feedback in low-mass galaxies at Cosmic Noon?** From our kinematic analysis, we find a mean mass-loading factor  $\eta = 0.54$  (with a large range of 0.05-3.26 and a typical uncertainty of 0.3) that is larger compared to the typical value observed in SFGs at similar redshift. We find galaxies with more compact star formation, i.e.  $\Sigma_{\text{SFR}} \gtrsim 10 M_{\odot} \text{ yr}^{-1} \text{ kpc}^{-2}$ , showing larger  $\eta$  for a given  $M_{\star}$  at the stellar mass range covered by our sample ( $\log(M_{\star}/M_{\odot}) < 10.2$ ). This suggests that denser starbursts in low-mass, low-metallicity galaxies produce stronger outflows for a given stellar mass. This indicates that stellar mass alone, as concluded by some studies at lower redshift, does not necessarily determine how effectively gas is removed due to stellar feedback and that the star formation and ISM densities can regulate this process in low-mass galaxies, as some simulations predict.

Finally, EELGs can be studied directly deep into the EoR in the JWST era. We propose a new method to select EELGs at  $z \gtrsim 4$  based on their photometry with medium and broad NIRCcam bands. We also characterize their SED global properties based on HST and JWST photometry. This is what we have learned from this analysis.

- i) **Is the new broad-band photometry from JWST/NIRCcam useful to select EELGs?** We demonstrate the potential use of synthetic NIRCcam observations to select galaxies with color excess in given bands that are associated with strong emission lines at different redshifts. We use empirical templates of metal-poor starburst with high EWs which are not easily reproduced by templates based on theoretical models. We select EELG candidates in a wide range of redshifts ( $3.8 < z < 8.5$ ) using this method. We validate our selection with the spectroscopy from NIRSspec for a subsample of these candidates, and we find they indeed show extreme emission lines. We conclude our method is successful in finding EELGs at very high- $z$  and we will improve our selection as we discuss in Chapter 5.
- ii) **What are the observed physical properties of EELGs in the EoR?** We characterize the properties of the EELG candidates using the new photometry from NIRCcam and SED modeling. We conclude they show global properties as expected from the analysis of their analogs at lower- $z$ . They have low stellar masses with high sSFR, which indicates they can double their stellar content in short periods of a few tens of Myrs. They show extreme ISM conditions such as high ionization, low dust content, and low metallicity.

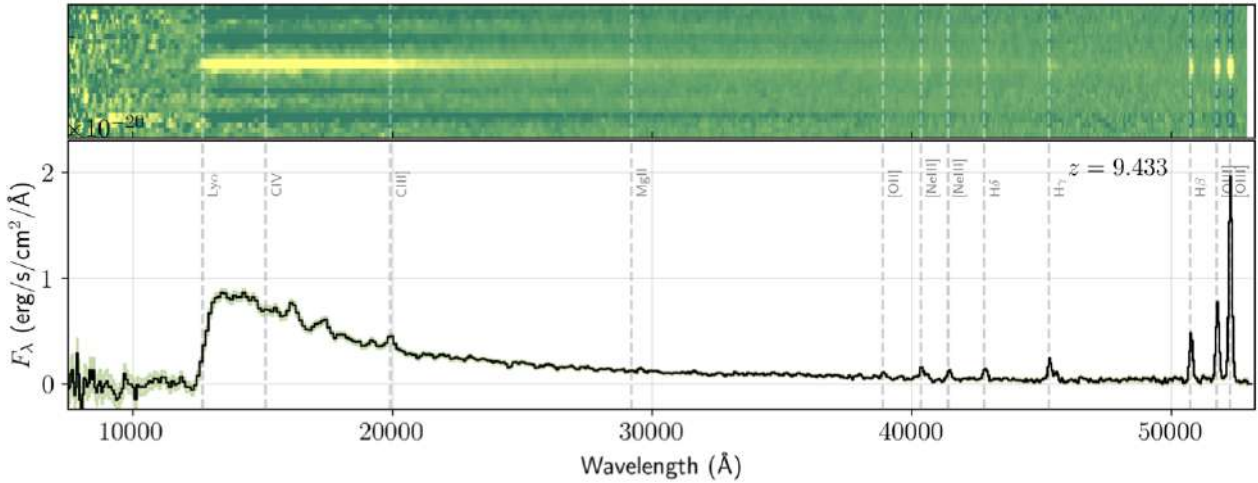


Figure 6.2.1: Low-dispersion prism spectra (1D and 2D) of a galaxy at  $z = 9.4327$ . Green shaded regions on the 1D spectra denote the  $1\sigma$  errors. Vertical lines denote the wavelengths of common emission lines. Figure taken from (Bunker et al., 2023a).

## 6.2 My perspectives for future work

The results presented in this Thesis set the path for further development on several topics. Shortly, we plan to address some of the questions that remain open. In what follows, we describe some of these open questions:

- i) JWST is rapidly opening a new window to study EELGs deeply into the EoR. An example of the JWST spectrum of a galaxy at  $z = 9.4$  is shown in Fig. 6.2.1. As can be seen, using the Prism mode, the main UV and optical lines (from Ly $\alpha$  up to [OIII] $\lambda$ 5007) used in this Thesis to estimate the ISM properties and the gas kinematics are obtained in a single observation for galaxies in the EoR. The scientific cases regarding the ISM properties presented in Chapters 3 and 4 can now be explored at very high- $z$ . All the experience we have gained with their analogs now can be faced with galaxies in situ (e.g., Saxena et al., 2023; Bunker et al., 2023a).
- ii) On the other hand, the rare local analogs resembling early-formed galaxies are also essential to study. Notably, we still need to understand how well they mimic the properties of their high- $z$  counterpart. How the evolved underlying SFH may affect our comparisons with high- $z$  galaxies? CLASSY is a key survey given the unique UV spectroscopy provided by HST. No other UV instrument will be available in the near future. Currently, we have built a sample of CIII and OIII emitters in CLASSY (local universe) and in VUDS and VANDELS ( $z = 2 - 4$ ) to constrain their chemical abundances and gain knowledge about their stellar population. As this project is in its early stages, we preferred to keep it out of this Thesis. However, we plan to continue the analysis and be able to provide further insight into the UV nebular properties of local analogs in the future (see, e.g., Mingozzi et al., 2022).
- iii) We have focused this Thesis on the UV and optical properties of galaxies. However, their FIR emission provides crucial information on their unobscured ISM properties. In particular, combining CIII] and the FIR line [CII]158 $\mu$ m with state-of-the-art models (e.g., Ferrara et al., 2019; Vallini et al., 2020) is probed to be a tool to determine two crucial (spatially averaged)

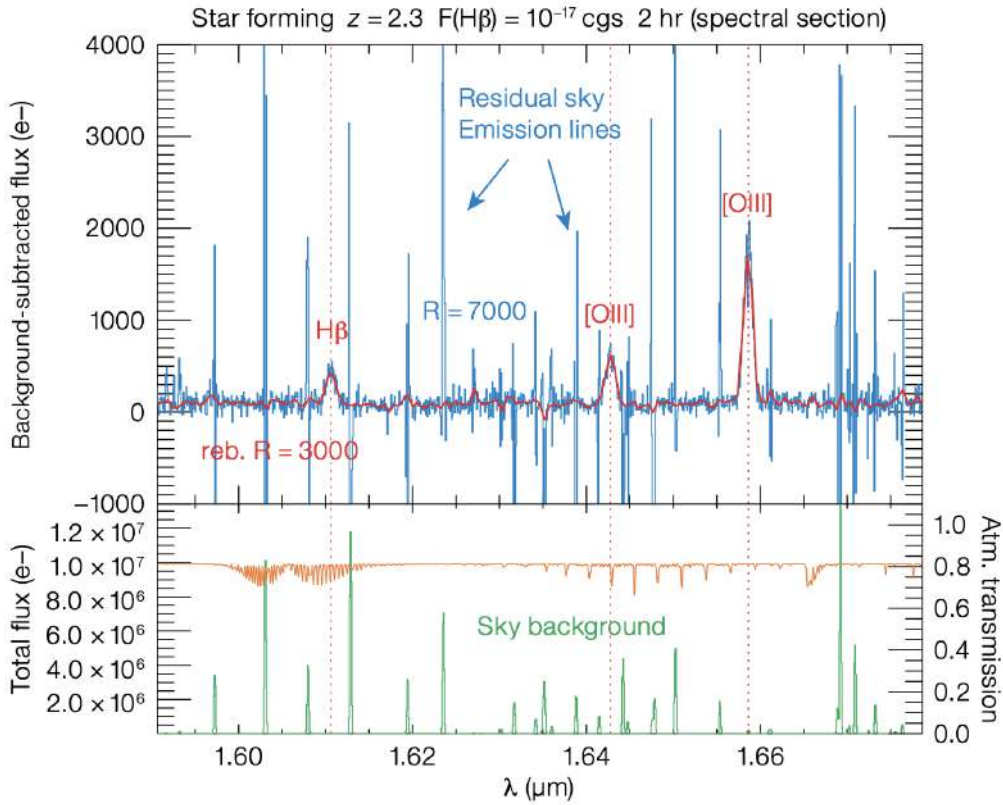


Figure 6.2.2: *Top panel*: MOONS simulated spectra of a SFGs ( $H_{AB} = 23.5$ ) at  $z = 2.3$  observed for two hours on-source. The background-subtracted spectrum (in blue) and the same spectrum rebinned to lower resolution after masking the OH sky lines (in red) are displayed *Bottom panel*: The total observed spectrum (in green), including sky emission and the atmospheric transmission (in brown) for the same simulation are shown. Figure is taken from (Maiolino et al., 2020).

properties of the ISM: the gas density and the deviation from the Kennicutt-Schmidt relation (Kennicutt, 1998). With this approach, we will gain a deeper understanding of the efficiency of star formation at early epochs. I submitted an ALMA proposal for cycle 10 to take this approach, which is a potential tool to constrain ISM properties in the EoR as the JWST era dawns. The samples built in this Thesis contain excellent candidates to probe this synergy with ALMA to understand better the ISM of EELGs (e.g., Markov et al., 2022).

iv) Despite the extensive observational and analysis effort invested in this Thesis, several questions remain open regarding how stellar feedback affects the evolution of young low-mass galaxies. One piece of information we are missing is the spatial distribution and the location of such outflowing gas. Spatially-resolved – i.e., Integral Field Units (IFU) – observations are then crucial to better understand the source and extent of outflowing gas, its energetics, and the overall impact in the evolution of young low-mass galaxies. Detailed studies, similar to those being carried out in local analogs (e.g., del Valle-Espinosa et al., 2023), will be possible at higher redshift shortly with the new generation instruments working in the NIR, such as JWST/NIRSpec (Jakobsen et al., 2022), ELT/HARMONI (Thatte et al., 2010), and GMT/GMTIFS (Sharp et al., 2016).

v) New generation of instruments such as VLT/MOONS\* with high multiplexity (up to  $\sim 1000$

\*<https://vl moons.org/>

fibers simultaneously), high sensitivity, and high spectral resolution will be key to studying the feedback of galaxies at Cosmic Noon, following the methodology we used in Chapter 4. Surveys, such as MOONRISE (Maiolino et al., 2020), will observe large samples of SFGs at  $1 < z < 2.5$ . Depending on the final strategy, more than 50000 SFGs at  $2 < z < 2.5$  will be observed. With an  $R \sim 7000$  in the H band (see Fig. 6.2.2 for a simulated spectrum with MOONS), a similar approach as in Chapter 4 but with larger statistics will be possible with this survey which unveils more robust conclusions on the complex ionized kinematics observed in SFGs while forming most of their stellar mass.

In conclusion, I expect a bright future for this research field. We are already witnessing groundbreaking discoveries, and over the next few years, unprecedented details on the physical properties of the youngest galaxies of the universe will be unveiled.

# Bibliography

- Abel T., Bryan G. L., Norman M. L., 2002, *Science*, 295, 93
- Amarsi A. M., Nissen P. E., Skúladóttir Á., 2019, *A&A*, 630, A104
- Amorín R. O., Pérez-Montero E., Vílchez J. M., 2010, *ApJ*, 715, L128
- Amorín R., Pérez-Montero E., Vílchez J. M., Papaderos P., 2012a, *ApJ*, 749, 185
- Amorín R., Vílchez J. M., Hägele G. F., Firpo V., Pérez-Montero E., Papaderos P., 2012b, *ApJ*, 754, L22
- Amorín R., et al., 2014, *A&A*, 568, L8
- Amorín R., et al., 2015, *A&A*, 578, A105
- Amorín R., et al., 2017, *Nature Astronomy*, 1, 0052
- Andrews B. H., Martini P., 2013, *ApJ*, 765, 140
- Arellano-Córdova K. Z., et al., 2022, *ApJ*, 940, L23
- Arribas S., Colina L., Bellocchi E., Maiolino R., Villar-Martín M., 2014, *A&A*, 568, A14
- Asplund M., Grevesse N., Sauval A. J., Scott P., 2009, *ARA&A*, 47, 481
- Avery C. R., et al., 2021, *MNRAS*, 503, 5134
- Bacon R., et al., 2017, *A&A*, 608, A1
- Bagley M. B., et al., 2023, *ApJ*, 946, L12
- Baldry I. K., Glazebrook K., Brinkmann J., Ivezić Ž., Lupton R. H., Nichol R. C., Szalay A. S., 2004, *ApJ*, 600, 681
- Baldwin J. A., Phillips M. M., Terlevich R., 1981, *PASP*, 93, 5
- Bayliss M. B., Rigby J. R., Sharon K., Wuyts E., Florian M., Gladders M. D., Johnson T., Oguri M., 2014, *ApJ*, 790, 144
- Begley R., et al., 2022, *MNRAS*, 513, 3510
- Beichman C. A., Rieke M., Eisenstein D., Greene T. P., Krist J., McCarthy D., Meyer M., Stansberry J., 2012, in Clampin M. C., Fazio G. G., MacEwen H. A., Oschmann Jacobus M. J., eds, Society of Photo-Optical Instrumentation Engineers (SPIE) Conference Series Vol. 8442, Space Telescopes and Instrumentation 2012: Optical, Infrared, and Millimeter Wave. p. 84422N, doi:10.1117/12.925447
- Bell E. F., 2004, *arXiv e-prints*, pp astro-ph/0408023
- Bell E. F., et al., 2004, *ApJ*, 608, 752

- Berg D. A., Skillman E. D., Henry R. B. C., Erb D. K., Carigi L., 2016, *ApJ*, **827**, 126
- Berg D. A., Erb D. K., Auger M. W., Pettini M., Brammer G. B., 2018, *ApJ*, **859**, 164
- Berg D. A., Erb D. K., Henry R. B. C., Skillman E. D., McQuinn K. B. W., 2019, *ApJ*, **874**, 93
- Berg D. A., et al., 2022, *ApJS*, **261**, 31
- Bertin E., Arnouts S., 1996, *A&AS*, **117**, 393
- Bian F., Kewley L. J., Dopita M. A., 2018, *ApJ*, **859**, 175
- Blumenthal G. R., Faber S. M., Primack J. R., Rees M. J., 1984, *Nature*, **311**, 517
- Bosch G., et al., 2019, *MNRAS*, **489**, 1787
- Bouché N., et al., 2010, *ApJ*, **718**, 1001
- Bouwens R., 2016, in Mesinger A., ed., *Astrophysics and Space Science Library* Vol. 423, *Understanding the Epoch of Cosmic Reionization: Challenges and Progress*. p. 111 ([arXiv:1511.01133](https://arxiv.org/abs/1511.01133)), [doi:10.1007/978-3-319-21957-8\\_4](https://doi.org/10.1007/978-3-319-21957-8_4)
- Bouwens R. J., et al., 2015, *ApJ*, **803**, 34
- Bouwens R. J., Smit R., Labbé I., Franx M., Caruana J., Oesch P., Stefanon M., Rasappu N., 2016, *ApJ*, **831**, 176
- Brammer G. B., van Dokkum P. G., Coppi P., 2008, *ApJ*, **686**, 1503
- Bressan A., Marigo P., Girardi L., Salasnich B., Dal Cero C., Rubele S., Nanni A., 2012, *MNRAS*, **427**, 127
- Bromm V., Coppi P. S., Larson R. B., 1999, *ApJ*, **527**, L5
- Bruzual G., Charlot S., 2003, *MNRAS*, **344**, 1000
- Bunker A. J., et al., 2023a, *arXiv e-prints*, p. [arXiv:2302.07256](https://arxiv.org/abs/2302.07256)
- Bunker A. J., et al., 2023b, *arXiv e-prints*, p. [arXiv:2306.02467](https://arxiv.org/abs/2306.02467)
- Byler N., Dalcanton J. J., Conroy C., Johnson B. D., Levesque E. M., Berg D. A., 2018, *ApJ*, **863**, 14
- Byler N., Kewley L. J., Rigby J. R., Acharyya A., Berg D. A., Bayliss M., Sharon K., 2020, *ApJ*, **893**, 1
- Calabrò A., et al., 2017, *A&A*, **601**, A95
- Calabrò A., et al., 2021, *A&A*, **646**, A39
- Calabrò A., et al., 2022, *A&A*, **667**, A117
- Calzetti D., Armus L., Bohlin R. C., Kinney A. L., Koornneef J., Storchi-Bergmann T., 2000, *ApJ*, **533**, 682
- Cardamone C., et al., 2009, *MNRAS*, **399**, 1191
- Cardamone C. N., et al., 2010, *ApJS*, **189**, 270
- Cardelli J. A., Clayton G. C., Mathis J. S., 1989, *ApJ*, **345**, 245
- Carigi L., 1994, *ApJ*, **424**, 181
- Carigi L., Peimbert M., 2011, *Rev. Mexicana Astron. Astrofis.*, **47**, 139
- Carnall A. C., 2017, *arXiv e-prints*, p. [arXiv:1705.05165](https://arxiv.org/abs/1705.05165)
- Carnall A. C., McLure R. J., Dunlop J. S., Davé R., 2018, *MNRAS*, **480**, 4379

- Carroll S. M., 2001, *Living Reviews in Relativity*, 4, 1
- Cassata P., et al., 2015, *A&A*, 573, A24
- Castaneda H. O., Vilchez J. M., Copetti M. V. F., 1990, *ApJ*, 365, 164
- Castellano M., et al., 2014, *A&A*, 566, A19
- Castellano M., et al., 2016, *ApJ*, 818, L3
- Castellano M., et al., 2022, *A&A*, 662, A115
- Ceverino D., Sánchez Almeida J., Muñoz Tuñón C., Dekel A., Elmegreen B. G., Elmegreen D. M., Primack J., 2016, *MNRAS*, 457, 2605
- Chabrier G., 2003, *PASP*, 115, 763
- Charlot S., Bruzual A. G., 1991, *ApJ*, 367, 126
- Chiappini C., Romano D., Matteucci F., 2003, *MNRAS*, 339, 63
- Chisholm J., Tremonti C. A., Leitherer C., Chen Y., Wofford A., 2016, *MNRAS*, 457, 3133
- Chisholm J., Tremonti C. A., Leitherer C., Chen Y., 2017, *MNRAS*, 469, 4831
- Chisholm J., Tremonti C., Leitherer C., 2018, *MNRAS*, 481, 1690
- Christensen L., et al., 2012, *MNRAS*, 427, 1973
- Cohn J. H., et al., 2018, *ApJ*, 869, 141
- Coil A. L., et al., 2015, *ApJ*, 801, 35
- Cole S., Lacey C., 1996, *MNRAS*, 281, 716
- Concas A., et al., 2022, *MNRAS*, 513, 2535
- Conroy C., 2013, *ARA&A*, 51, 393
- Cullen F., et al., 2019, *MNRAS*, 487, 2038
- Cullen F., et al., 2020, *MNRAS*, 495, 1501
- Cullen F., et al., 2021, *MNRAS*, 505, 903
- Curti M., Mannucci F., Cresci G., Maiolino R., 2020, *MNRAS*, 491, 944
- Curti M., et al., 2023, *MNRAS*, 518, 425
- Daddi E., Cimatti A., Renzini A., Fontana A., Mignoli M., Pozzetti L., Tozzi P., Zamorani G., 2004, *ApJ*, 617, 746
- Davé R., Rafieferantsoa M. H., Thompson R. J., Hopkins P. F., 2017, *MNRAS*, 467, 115
- Davies R. L., et al., 2019, *ApJ*, 873, 122
- Dayal P., Ferrara A., 2018, *Phys. Rep.*, 780, 1
- Dayal P., Ferrara A., Dunlop J. S., 2013, *MNRAS*, 430, 2891
- Dayal P., et al., 2020, *MNRAS*, 495, 3065
- De Barros S., et al., 2017, *A&A*, 608, A123

- De Barros S., Oesch P. A., Labbé I., Stefanon M., González V., Smit R., Bouwens R. J., Illingworth G. D., 2019, *MNRAS*, **489**, 2355
- Dijkstra M., 2014, *PASA*, **31**, e040
- Du X., Shapley A. E., Tang M., Stark D. P., Martin C. L., Mobasher B., Topping M. W., Chevallard J., 2020, *ApJ*, **890**, 65
- Duarte Puertas S., Vilchez J. M., Iglesias-Páramo J., Mollá M., Pérez-Montero E., Kehrig C., Pilyugin L. S., Zinchenko I. A., 2022, *A&A*, **666**, A186
- Edmunds M. G., 1990, *MNRAS*, **246**, 678
- Edmunds M. G., Pagel B. E. J., 1978, *MNRAS*, **185**, 77P
- Eldridge J. J., Stanway E. R., Xiao L., McClelland L. A. S., Taylor G., Ng M., Greis S. M. L., Bray J. C., 2017, *PASA*, **34**, e058
- Endsley R., Stark D. P., 2022, *MNRAS*, **511**, 6042
- Endsley R., Stark D. P., Chevallard J., Charlot S., 2021, *MNRAS*, **500**, 5229
- Endsley R., Stark D. P., Whitley L., Topping M. W., Chen Z., Plat A., Chisholm J., Charlot S., 2022, *arXiv e-prints*, p. [arXiv:2208.14999](https://arxiv.org/abs/2208.14999)
- Erb D. K., Shapley A. E., Pettini M., Steidel C. C., Reddy N. A., Adelberger K. L., 2006, *ApJ*, **644**, 813
- Erb D. K., Pettini M., Shapley A. E., Steidel C. C., Law D. R., Reddy N. A., 2010, *ApJ*, **719**, 1168
- Esteban C., García-Rojas J., Carigi L., Peimbert M., Bresolin F., López-Sánchez A. R., Mesa-Delgado A., 2014, *MNRAS*, **443**, 624
- Fabozzi F. J., Focardi S. M., T. R. S., G. A. B., 2014, *The Basics of Financial Econometrics: Tools, Concepts, and Asset Management Applications*. Wiley
- Falcón-Barroso J., Sánchez-Blázquez P., Vazdekis A., Ricciardelli E., Cardiel N., Cenarro A. J., Gorgas J., Peletier R. F., 2011, *A&A*, **532**, A95
- Fall S. M., Efstathiou G., 1980, *MNRAS*, **193**, 189
- Fan X., et al., 2006, *AJ*, **132**, 117
- Feltre A., Charlot S., Gutkin J., 2016, *MNRAS*, **456**, 3354
- Feltre A., et al., 2020, *A&A*, **641**, A118
- Ferland G. J., et al., 2013, *Rev. Mexicana Astron. Astrofis.*, **49**, 137
- Fernández V., Amorín R., Sanchez-Janssen R., del Valle-Espinosa M. G., Papaderos P., 2023, *MNRAS*, **520**, 3576
- Ferrara A., Vallini L., Pallottini A., Gallerani S., Carniani S., Kohandel M., Decataldo D., Behrens C., 2019, *MNRAS*, **489**, 1
- Finkelstein S. L., et al., 2012, *ApJ*, **756**, 164
- Finkelstein S. L., et al., 2019, *ApJ*, **879**, 36
- Finkelstein S. L., et al., 2023, *ApJ*, **946**, L13
- Firpo V., Bosch G., Hägele G. F., Morrell N., 2010, *MNRAS*, **406**, 1094
- Flury S. R., et al., 2022a, *ApJS*, **260**, 1

- Flury S. R., et al., 2022b, *ApJ*, **930**, 126
- Forrest B., et al., 2017, *ApJ*, **838**, L12
- Förster Schreiber N. M., Wuyts S., 2020, *ARA&A*, **58**, 661
- Förster Schreiber N. M., et al., 2019, *ApJ*, **875**, 21
- Freeman W. R., et al., 2019, *ApJ*, **873**, 102
- Freudling W., Romaniello M., Bramich D. M., Ballester P., Forchi V., García-Dabó C. E., Moehler S., Neeser M. J., 2013, *A&A*, **559**, A96
- Fuller S., et al., 2020, *ApJ*, **896**, 156
- Furlanetto S. R., Oh S. P., 2008, *ApJ*, **681**, 1
- Galametz A., et al., 2013, *The Astrophysical Journal Supplement Series*, 206, 10
- Gallazzi A., Charlot S., Brinchmann J., White S. D. M., Tremonti C. A., 2005, *MNRAS*, **362**, 41
- Garilli B., et al., 2021, *A&A*, **647**, A150
- Garnett D. R., Skillman E. D., Dufour R. J., Peimbert M., Torres-Peimbert S., Terlevich R., Terlevich E., Shields G. A., 1995, *ApJ*, **443**, 64
- Garnett D. R., Skillman E. D., Dufour R. J., Shields G. A., 1997, *ApJ*, **481**, 174
- Garnett D. R., Shields G. A., Peimbert M., Torres-Peimbert S., Skillman E. D., Dufour R. J., Terlevich E., Terlevich R. J., 1999, *ApJ*, **513**, 168
- Genel S., et al., 2014, *MNRAS*, **445**, 175
- Giallongo E., et al., 2015, *A&A*, **578**, A83
- Gnedin N. Y., 2000, *ApJ*, **542**, 535
- Gnedin N. Y., Kravtsov A. V., Chen H.-W., 2008, *ApJ*, **672**, 765
- Grand R. J. J., et al., 2017, *MNRAS*, **467**, 179
- Grazian A., et al., 2018, *A&A*, **613**, A44
- Grogin N. A., et al., 2011, *ApJS*, **197**, 35
- Guo Y., et al., 2013, *The Astrophysical Journal Supplement Series*, 207, 24
- Guo Y., et al., 2016, *ApJ*, **833**, 37
- Gupta A., et al., 2023, *MNRAS*, **519**, 980
- Guseva N. G., et al., 2020, *MNRAS*, **497**, 4293
- Gutkin J., Charlot S., Bruzual G., 2016, *MNRAS*, **462**, 1757
- Hayes M., 2015, *PASA*, **32**, e027
- Heckman T. M., Alexandroff R. M., Borthakur S., Overzier R., Leitherer C., 2015, *ApJ*, **809**, 147
- Heger A., Woosley S. E., 2002, *ApJ*, **567**, 532
- Heintz K. E., et al., 2022, arXiv e-prints, p. [arXiv:2212.02890](https://arxiv.org/abs/2212.02890)

- Henry R. B. C., Edmunds M. G., Köppen J., 2000, *ApJ*, **541**, 660
- Hirschmann M., Charlot S., Feltre A., Naab T., Somerville R. S., Choi E., 2019, *MNRAS*, **487**, 333
- Hogarth L., et al., 2020, *MNRAS*, **494**, 3541
- Hopkins P. F., et al., 2018, *MNRAS*, **480**, 800
- Hutchison T. A., et al., 2019, *ApJ*, **879**, 70
- Iglesias-Páramo J., et al., 2022, *A&A*, **665**, A95
- Inoue A. K., Shimizu I., Iwata I., Tanaka M., 2014, *MNRAS*, **442**, 1805
- Izotov Y. I., Chaffee F. H., Foltz C. B., Green R. F., Guseva N. G., Thuan T. X., 1999, *ApJ*, **527**, 757
- Izotov Y. I., Guseva N. G., Thuan T. X., 2011, *ApJ*, **728**, 161
- Izotov Y. I., Schaerer D., Thuan T. X., Worseck G., Guseva N. G., Orlitová I., Verhamme A., 2016, *MNRAS*, **461**, 3683
- Izotov Y. I., Worseck G., Schaerer D., Guseva N. G., Thuan T. X., Fricke Verhamme A., Orlitová I., 2018, *MNRAS*, **478**, 4851
- Izotov Y. I., Schaerer D., Worseck G., Verhamme A., Guseva N. G., Thuan T. X., Orlitová I., Fricke K. J., 2020, *MNRAS*, **491**, 468
- Jakobsen P., et al., 2022, *A&A*, **661**, A80
- James B. L., et al., 2014, *MNRAS*, **440**, 1794
- Jaskot A. E., Ravindranath S., 2016, *ApJ*, **833**, 136
- Jones T., Stark D. P., Ellis R. S., 2018, *ApJ*, **863**, 191
- Jones T., et al., 2023, *arXiv e-prints*, p. [arXiv:2301.07126](https://arxiv.org/abs/2301.07126)
- Juneau S., et al., 2014, *ApJ*, **788**, 88
- Kakiichi K., Gronke M., 2021, *ApJ*, **908**, 30
- Kashino D., Lilly S. J., Matthee J., Eilers A.-C., Mackenzie R., Bordoloi R., Simcoe R. A., 2022, *arXiv e-prints*, p. [arXiv:2211.08254](https://arxiv.org/abs/2211.08254)
- Kassin S. A., et al., 2012, *ApJ*, **758**, 106
- Kauffmann G., White S. D. M., Guiderdoni B., 1993, *MNRAS*, **264**, 201
- Kauffmann G., et al., 2003, *MNRAS*, **346**, 1055
- Kehrig C., et al., 2016, *MNRAS*, **459**, 2992
- Kennicutt Robert C. J., 1998, *ApJ*, **498**, 541
- Kennicutt R. C., Evans N. J., 2012, *ARA&A*, **50**, 531
- Kewley L. J., Dopita M. A., Sutherland R. S., Heisler C. A., Trevena J., 2001, *ApJ*, **556**, 121
- Kewley L. J., Dopita M. A., Leitherer C., Davé R., Yuan T., Allen M., Groves B., Sutherland R., 2013, *ApJ*, **774**, 100
- Kewley L. J., Nicholls D. C., Sutherland R. S., 2019, *ARA&A*, **57**, 511
- Khusanova Y., et al., 2020, *A&A*, **634**, A97

- Kim C.-G., et al., 2020, *ApJ*, **900**, 61
- Kobayashi C., Karakas A. I., Lugaro M., 2020, *ApJ*, **900**, 179
- Kobulnicky H. A., Skillman E. D., 1998, *ApJ*, **497**, 601
- Kobulnicky H. A., Skillman E. D., Roy J.-R., Walsh J. R., Rosa M. R., 1997, *ApJ*, **477**, 679
- Kocevski D. D., et al., 2018, *ApJS*, **236**, 48
- Koekemoer A. M., et al., 2011, *ApJS*, **197**, 36
- Kojima T., et al., 2020, *ApJ*, **898**, 142
- Kriek M., et al., 2015, *ApJS*, **218**, 15
- Kroupa P., 2001, *MNRAS*, **322**, 231
- Kurt C. M., Dufour R. J., Garnett D. R., Skillman E. D., Mathis J. S., Peimbert M., Torres-Peimbert S., Walter D. K., 1995, in Pena M., Kurtz S., eds, *Revista Mexicana de Astronomía y Astrofísica Conference Series Vol. 3, Revista Mexicana de Astronomía y Astrofísica Conference Series*. p. 223
- Laigle C., et al., 2016, *ApJS*, **224**, 24
- Laporte N., Nakajima K., Ellis R. S., Zitrin A., Stark D. P., Mainali R., Roberts-Borsani G. W., 2017, *ApJ*, **851**, 40
- Larson R. L., et al., 2022, *arXiv e-prints*, p. [arXiv:2211.10035](https://arxiv.org/abs/2211.10035)
- Laursen P., 2010, PhD thesis, Niels Bohr Institute for Astronomy, Physics and Geophysics
- Le Fèvre O., et al., 2003, in Iye M., Moorwood A. F. M., eds, *Society of Photo-Optical Instrumentation Engineers (SPIE) Conference Series Vol. 4841, Instrument Design and Performance for Optical/Infrared Ground-based Telescopes*. pp 1670–1681, doi:[10.1117/12.460959](https://doi.org/10.1117/12.460959)
- Le Fèvre O., et al., 2015, *A&A*, **576**, A79
- Le Fèvre O., et al., 2019, *A&A*, **625**, A51
- Leitherer C., Robert C., Heckman T. M., 1995, *ApJS*, **99**, 173
- Leitherer C., Tremonti C. A., Heckman T. M., Calzetti D., 2011, *AJ*, **141**, 37
- Leitherer C., Ekström S., Meynet G., Schaerer D., Agienko K. B., Levesque E. M., 2014, *ApJS*, **212**, 14
- Lemaux B. C., et al., 2022, *A&A*, **662**, A33
- Lequeux J., Peimbert M., Rayo J. F., Serrano A., Torres-Peimbert S., 1979, *A&A*, **80**, 155
- Lian J. H., Li J. R., Yan W., Kong X., 2015, *MNRAS*, **446**, 1449
- Lilly S. J., Carollo C. M., Pipino A., Renzini A., Peng Y., 2013, *ApJ*, **772**, 119
- Llerena M., et al., 2022, *A&A*, **659**, A16
- Llerena M., Amorín R., Pentericci L., Calabrò A., Shapley A. E., Boutsia K., Pérez-Montero E., Vílchez J. M., 2023, *arXiv e-prints*, p. [arXiv:2303.01536](https://arxiv.org/abs/2303.01536)
- Lumbreras-Calle A., et al., 2022, *A&A*, **668**, A60
- Luo B., et al., 2017, *ApJS*, **228**, 2
- Luridiana V., Morisset C., Shaw R. A., 2012, *IAU Symposium*, **283**, 422

- Luridiana V., Morisset C., Shaw R. A., 2015, *A&A*, **573**, A42
- Lutz D., et al., 2020, *A&A*, **633**, A134
- Ma X., Kasen D., Hopkins P. F., Faucher-Giguère C.-A., Quataert E., Kereš D., Murray N., 2015, *MNRAS*, **453**, 960
- Ma X., Hopkins P. F., Faucher-Giguère C.-A., Zolman N., Muratov A. L., Kereš D., Quataert E., 2016, *MNRAS*, **456**, 2140
- Ma X., Quataert E., Wetzel A., Hopkins P. F., Faucher-Giguère C.-A., Kereš D., 2020, *MNRAS*, **498**, 2001
- Madau P., Dickinson M., 2014, *ARA&A*, **52**, 415
- Madau P., Haardt F., 2015, *ApJ*, **813**, L8
- Mainali R., Kollmeier J. A., Stark D. P., Simcoe R. A., Walth G., Newman A. B., Miller D. R., 2017, *ApJ*, **836**, L14
- Mainali R., et al., 2018, *MNRAS*, **479**, 1180
- Mainali R., et al., 2022, *ApJ*, **940**, 160
- Maiolino R., Mannucci F., 2019, *A&A Rev.*, **27**, 3
- Maiolino R., et al., 2008, *A&A*, **488**, 463
- Maiolino R., et al., 2020, *The Messenger*, **180**, 24
- Mannucci F., Cresci G., Maiolino R., Marconi A., Gnerucci A., 2010, *MNRAS*, **408**, 2115
- Marasco A., et al., 2023, *A&A*, **670**, A92
- Marchi F., et al., 2017, *A&A*, **601**, A73
- Marchi F., et al., 2019, *A&A*, **631**, A19
- Marigo P., Bressan A., Nanni A., Girardi L., Pumo M. L., 2013, *MNRAS*, **434**, 488
- Markov V., Carniani S., Vallini L., Ferrara A., Pallottini A., Maiolino R., Gallerani S., Pentericci L., 2022, *A&A*, **663**, A172
- Martins L. P., González Delgado R. M., Leitherer C., Cerviño M., Hauschildt P., 2005, *MNRAS*, **358**, 49
- Maseda M. V., et al., 2014, *ApJ*, **791**, 17
- Maseda M. V., et al., 2017, *A&A*, **608**, A4
- Maseda M. V., et al., 2018, *ApJ*, **854**, 29
- Mason C. A., et al., 2019, *MNRAS*, **485**, 3947
- Matthee J., et al., 2021, *MNRAS*, **505**, 1382
- Matthee J., Mackenzie R., Simcoe R. A., Kashino D., Lilly S. J., Bordoloi R., Eilers A.-C., 2022, arXiv e-prints, p. [arXiv:2211.08255](https://arxiv.org/abs/2211.08255)
- Mattsson L., 2010, *A&A*, **515**, A68
- McLean I. S., et al., 2012, in McLean I. S., Ramsay S. K., Takami H., eds, Society of Photo-Optical Instrumentation Engineers (SPIE) Conference Series Vol. 8446, Ground-based and Airborne Instrumentation for Astronomy IV. p. 84460J, [doi:10.1117/12.924794](https://doi.org/10.1117/12.924794)
- McLure R. J., et al., 2018, *MNRAS*, **479**, 25

- McQuinn K. B. W., van Zee L., Skillman E. D., 2019, *ApJ*, **886**, 74
- Meiksin A., 2005, *MNRAS*, **356**, 596
- Mingozzi M., et al., 2022, *ApJ*, **939**, 110
- Miralda-Escudé J., 2003, *Science*, **300**, 1904
- Modigliani A., et al., 2010, in Silva D. R., Peck A. B., Soifer B. T., eds, Society of Photo-Optical Instrumentation Engineers (SPIE) Conference Series Vol. 7737, Observatory Operations: Strategies, Processes, and Systems III. p. 773728, doi:10.1117/12.857211
- Mollá M., García-Vargas M. L., Bressan A., 2009, *MNRAS*, **398**, 451
- Mollá M., Cavichia O., Gavilán M., Gibson B. K., 2015, *MNRAS*, **451**, 3693
- Morisset C., et al., 2016, *A&A*, **594**, A37
- Muratov A. L., Kereš D., Faucher-Giguère C.-A., Hopkins P. F., Quataert E., Murray N., 2015, *MNRAS*, **454**, 2691
- Naidu R. P., Tacchella S., Mason C. A., Bose S., Oesch P. A., Conroy C., 2020, *ApJ*, **892**, 109
- Naidu R. P., et al., 2022, *MNRAS*, **510**, 4582
- Nakajima K., Fletcher T., Ellis R. S., Robertson B. E., Iwata I., 2018a, *MNRAS*, **477**, 2098
- Nakajima K., et al., 2018b, *A&A*, **612**, A94
- Nakajima K., et al., 2022, *ApJS*, **262**, 3
- Nelson D., et al., 2018, *MNRAS*, **475**, 624
- Nelson D., et al., 2019a, *Computational Astrophysics and Cosmology*, **6**, 2
- Nelson D., et al., 2019b, *MNRAS*, **490**, 3234
- Newville M., Stensitzki T., Allen D. B., Rawlik M., Ingargiola A., Nelson A., 2016, Lmfit: Non-Linear Least-Square Minimization and Curve-Fitting for Python, Astrophysics Source Code Library, record ascl:1606.014 (ascl:1606.014)
- Nicholls D. C., Sutherland R. S., Dopita M. A., Kewley L. J., Groves B. A., 2017, *MNRAS*, **466**, 4403
- Onodera M., et al., 2016, *ApJ*, **822**, 42
- Onodera M., et al., 2020, *ApJ*, **904**, 180
- Ouchi M., Ono Y., Shibuya T., 2020, *ARA&A*, **58**, 617
- Pahl A. J., Shapley A., Steidel C. C., Reddy N. A., Chen Y., Rudie G. C., Strom A. L., 2022, *arXiv e-prints*, p. arXiv:2210.16697
- Palla M., Calura F., Matteucci F., Fan X. L., Vincenzo F., Lacchin E., 2020, *MNRAS*, **494**, 2355
- Pandya V., et al., 2021, *MNRAS*, **508**, 2979
- Paoletti D., Hazra D. K., Finelli F., Smoot G. F., 2020, *J. Cosmology Astropart. Phys.*, **2020**, 005
- Peña-Guerrero M. A., Leitherer C., de Mink S., Wofford A., Kewley L., 2017, *ApJ*, **847**, 107
- Peebles P. J. E., 1980, The large-scale structure of the universe
- Peebles P. J. E., 1984, *ApJ*, **284**, 439
- Peebles M. S., et al., 2019, *ApJ*, **873**, 129

- Peng C. Y., Ho L. C., Impey C. D., Rix H.-W., 2002, *AJ*, 124, 266
- Peng C. Y., Ho L. C., Impey C. D., Rix H.-W., 2010a, *AJ*, 139, 2097
- Peng Y.-j., et al., 2010b, *ApJ*, 721, 193
- Pentericci L., et al., 2014, *ApJ*, 793, 113
- Pentericci L., et al., 2018a, *A&A*, 616, A174
- Pentericci L., et al., 2018b, *A&A*, 619, A147
- Pérez-González P. G., et al., 2008, *ApJ*, 675, 234
- Pérez-Montero E., 2017, *PASP*, 129, 043001
- Pérez-Montero E., Amorín R., 2017, *MNRAS*, 467, 1287
- Pérez-Montero E., Contini T., 2009, *MNRAS*, 398, 949
- Pérez-Montero E., et al., 2013, *A&A*, 549, A25
- Pérez-Montero E., Amorín R., Sánchez Almeida J., Vílchez J. M., García-Benito R., Kehrig C., 2021, *MNRAS*, 504, 1237
- Pérez-Montero E., Amorín R., Pérez-Díaz B., Vílchez J. M., García-Benito R., 2023, *MNRAS*, 521, 1556
- Pettini M., Steidel C. C., Adelberger K. L., Dickinson M., Giavalisco M., 2000, *ApJ*, 528, 96
- Planck Collaboration et al., 2016, *A&A*, 594, A13
- Planck Collaboration et al., 2020, *A&A*, 641, A1
- Ravindranath S., Monroe T., Jaskot A., Ferguson H. C., Tumlinson J., 2020, *ApJ*, 896, 170
- Reddy N. A., et al., 2015, *ApJ*, 806, 259
- Reddy N. A., et al., 2023a, *arXiv e-prints*, p. arXiv:2302.10213
- Reddy N. A., Topping M. W., Sanders R. L., Shapley A. E., Brammer G., 2023b, *arXiv e-prints*, p. arXiv:2303.11397
- Ribeiro B., et al., 2016, *A&A*, 593, A22
- Ribeiro B., et al., 2017, *A&A*, 608, A16
- Rigby J. R., Bayliss M. B., Gladders M. D., Sharon K., Wuyts E., Dahle H., Johnson T., Peña-Guerrero M., 2015, *ApJ*, 814, L6
- Roberts-Borsani G. W., et al., 2016, *ApJ*, 823, 143
- Robertson B. E., Ellis R. S., Furlanetto S. R., Dunlop J. S., 2015, *ApJ*, 802, L19
- Rodríguez del Pino B., Arribas S., Piqueras López J., Villar-Martín M., Colina L., 2019, *MNRAS*, 486, 344
- Romano D., Franchini M., Grisoni V., Spitoni E., Matteucci F., Morossi C., 2020, *A&A*, 639, A37
- Runco J. N., et al., 2021, *MNRAS*, 502, 2600
- Salim S., Boquien M., Lee J. C., 2018, *ApJ*, 859, 11
- Salpeter E. E., 1955, *ApJ*, 121, 161
- Sánchez Almeida J., Aguerri J. A. L., Muñoz-Tuñón C., de Vicente A., 2010, *ApJ*, 714, 487

- Sánchez Almeida J., Terlevich R., Terlevich E., Cid Fernandes R., Morales-Luis A. B., 2012, *ApJ*, **756**, 163
- Sánchez-Blázquez P., et al., 2006, *MNRAS*, **371**, 703
- Sanders R. L., et al., 2016, *ApJ*, **816**, 23
- Sanders R. L., et al., 2020, *MNRAS*, **491**, 1427
- Sanders R. L., et al., 2021, *ApJ*, **914**, 19
- Santini P., et al., 2017, *ApJ*, **847**, 76
- Saxena A., et al., 2020, *A&A*, **636**, A47
- Saxena A., et al., 2022a, *MNRAS*, **511**, 120
- Saxena A., et al., 2022b, *MNRAS*, **517**, 1098
- Saxena A., et al., 2023, *arXiv e-prints*, p. [arXiv:2306.04536](https://arxiv.org/abs/2306.04536)
- Scalo J. M., 1986, *Fund. Cosmic Phys.*, **11**, 1
- Schaerer D., 2003, *A&A*, **397**, 527
- Schaerer D., de Barros S., 2010, *A&A*, **515**, A73
- Schaerer D., Izotov Y. I., Verhamme A., Orlitová I., Thuan T. X., Worseck G., Guseva N. G., 2016, *A&A*, **591**, L8
- Schaerer D., Izotov Y. I., Nakajima K., Worseck G., Chisholm J., Verhamme A., Thuan T. X., de Barros S., 2018, *A&A*, **616**, L14
- Schaerer D., et al., 2022a, *A&A*, **658**, L11
- Schaerer D., Marques-Chaves R., Barrufet L., Oesch P., Izotov Y. I., Naidu R., Guseva N. G., Brammer G., 2022b, *A&A*, **665**, L4
- Schmidt K. B., et al., 2016, *ApJ*, **818**, 38
- Schneider P., 2006, *Extragalactic Astronomy and Cosmology*
- Senchyna P., et al., 2017, *MNRAS*, **472**, 2608
- Senchyna P., Stark D. P., Charlot S., Chevallard J., Bruzual G., Vidal-García A., 2021, *MNRAS*, **503**, 6112
- Shapley A. E., 2011, *ARA&A*, **49**, 525
- Shapley A. E., Steidel C. C., Pettini M., Adelberger K. L., 2003, *ApJ*, **588**, 65
- Sharp R., et al., 2016, in Evans C. J., Simard L., Takami H., eds, *Society of Photo-Optical Instrumentation Engineers (SPIE) Conference Series Vol. 9908, Ground-based and Airborne Instrumentation for Astronomy VI*. p. 99081Y, [doi:10.1117/12.2231561](https://doi.org/10.1117/12.2231561)
- Shen S., Mo H. J., White S. D. M., Blanton M. R., Kauffmann G., Voges W., Brinkmann J., Csabai I., 2003, *MNRAS*, **343**, 978
- Silk J., Mamon G. A., 2012, *Research in Astronomy and Astrophysics*, **12**, 917
- Simcoe R. A., et al., 2010, in McLean I. S., Ramsay S. K., Takami H., eds, *Society of Photo-Optical Instrumentation Engineers (SPIE) Conference Series Vol. 7735, Ground-based and Airborne Instrumentation for Astronomy III*. p. 773514, [doi:10.1117/12.856088](https://doi.org/10.1117/12.856088)
- Smit R., et al., 2014, *ApJ*, **784**, 58

- Smit R., et al., 2015, *ApJ*, **801**, 122
- Sobral D., Smail I., Best P. N., Geach J. E., Matsuda Y., Stott J. P., Cirasuolo M., Kurk J., 2013, *MNRAS*, **428**, 1128
- Sobral D., Matthee J., Darvish B., Schaerer D., Mobasher B., Röttgering H. J. A., Santos S., Hemmati S., 2015, *ApJ*, **808**, 139
- Somerville R. S., Davé R., 2015, *ARA&A*, **53**, 51
- Sommariva V., Mannucci F., Cresci G., Maiolino R., Marconi A., Nagao T., Baroni A., Grazian A., 2012, *A&A*, **539**, A136
- Speagle J. S., Steinhardt C. L., Capak P. L., Silverman J. D., 2014, *ApJS*, **214**, 15
- Springel V., et al., 2005, *Nature*, **435**, 629
- Springel V., et al., 2018, *MNRAS*, **475**, 676
- Stark D. P., 2016, *ARA&A*, **54**, 761
- Stark D. P., et al., 2014, *MNRAS*, **445**, 3200
- Stark D. P., et al., 2015, *MNRAS*, **450**, 1846
- Stark D. P., et al., 2017, *MNRAS*, **464**, 469
- Starkenbug T. K., Helmi A., Sales L. V., 2016, *A&A*, **595**, A56
- Stasińska G., Szczerba R., 2001, *A&A*, **379**, 1024
- Steidel C. C., Giavalisco M., Pettini M., Dickinson M., Adelberger K. L., 1996, *ApJ*, **462**, L17
- Steidel C. C., Pettini M., Adelberger K. L., 2001, *ApJ*, **546**, 665
- Steidel C. C., Adelberger K. L., Shapley A. E., Pettini M., Dickinson M., Giavalisco M., 2003, *ApJ*, **592**, 728
- Steidel C. C., Erb D. K., Shapley A. E., Pettini M., Reddy N., Bogosavljević M., Rudie G. C., Rakic O., 2010, *ApJ*, **717**, 289
- Steidel C. C., et al., 2014, *ApJ*, **795**, 165
- Steidel C. C., Strom A. L., Pettini M., Rudie G. C., Reddy N. A., Trainor R. F., 2016, *ApJ*, **826**, 159
- Steidel C. C., Bogosavljević M., Shapley A. E., Reddy N. A., Rudie G. C., Pettini M., Trainor R. F., Strom A. L., 2018, *ApJ*, **869**, 123
- Storey P. J., Zeppen C. J., 2000, *MNRAS*, **312**, 813
- Strateva I., et al., 2001, *AJ*, **122**, 1861
- Sun F., et al., 2022a, arXiv e-prints, p. [arXiv:2209.03374](https://arxiv.org/abs/2209.03374)
- Sun F., et al., 2022b, *ApJ*, **936**, L8
- Sutherland R. S., Dopita M. A., 1993, *ApJS*, **88**, 253
- Tang M., Stark D. P., Chevallard J., Charlot S., 2019, *MNRAS*, **489**, 2572
- Tang M., Stark D. P., Chevallard J., Charlot S., Endsley R., Congiu E., 2021, *MNRAS*, **501**, 3238
- Tang M., et al., 2023, arXiv e-prints, p. [arXiv:2301.07072](https://arxiv.org/abs/2301.07072)
- Tasca L. A. M., et al., 2015, *A&A*, **581**, A54

- Tasca L. A. M., et al., 2017, *A&A*, **600**, [A110](#)
- Thatte N., et al., 2010, in McLean I. S., Ramsay S. K., Takami H., eds, Society of Photo-Optical Instrumentation Engineers (SPIE) Conference Series Vol. 7735, Ground-based and Airborne Instrumentation for Astronomy III. p. 77352I, [doi:10.1117/12.857445](#)
- Thuan T. X., Izotov Y. I., Foltz C. B., 1999, *ApJ*, **525**, [105](#)
- Tody D., 1986, in Crawford D. L., ed., Society of Photo-Optical Instrumentation Engineers (SPIE) Conference Series Vol. 627, Instrumentation in astronomy VI. p. 733, [doi:10.1117/12.968154](#)
- Topping M. W., Shapley A. E., Reddy N. A., Sanders R. L., Coil A. L., Kriek M., Mobasher B., Siana B., 2020, *MNRAS*, **495**, [4430](#)
- Torrey P., et al., 2018, *MNRAS*, **477**, [L16](#)
- Torrey P., et al., 2019, *MNRAS*, **484**, [5587](#)
- Trayford J. W., et al., 2015, *MNRAS*, **452**, [2879](#)
- Tremonti C. A., et al., 2004, *ApJ*, **613**, [898](#)
- Troncoso P., et al., 2014, *A&A*, **563**, [A58](#)
- Trump J. R., et al., 2022, arXiv e-prints, p. [arXiv:2207.12388](#)
- Tumlinson J., Peebles M. S., Werk J. K., 2017, *ARA&A*, **55**, [389](#)
- Übler H., et al., 2019, *ApJ*, **880**, [48](#)
- Übler H., et al., 2022, arXiv e-prints, p. [arXiv:2210.03106](#)
- Vallini L., Ferrara A., Pallottini A., Carniani S., Gallerani S., 2020, *MNRAS*, **495**, [L22](#)
- Vanzella E., et al., 2016, *ApJ*, **821**, [L27](#)
- Vanzella E., et al., 2021, *A&A*, **646**, [A57](#)
- Vernet J., et al., 2011, *A&A*, **536**, [A105](#)
- Villar-Martín M., Cerviño M., González Delgado R. M., 2004, *MNRAS*, **355**, [1132](#)
- Vincenzo F., Kobayashi C., 2018, *A&A*, **610**, [L16](#)
- Vogelsberger M., Marinacci F., Torrey P., Puchwein E., 2020, *Nature Reviews Physics*, **2**, [42](#)
- Walcher J., Groves B., Budavári T., Dale D., 2011, *Ap&SS*, **331**, [1](#)
- Wang B., et al., 2021, *ApJ*, **916**, [3](#)
- Weiner B. J., et al., 2009, *ApJ*, **692**, [187](#)
- Whitaker K. E., van Dokkum P. G., Brammer G., Franx M., 2012, *ApJ*, **754**, [L29](#)
- Wise J. H., 2019, arXiv e-prints, p. [arXiv:1907.06653](#)
- Wise J. H., Demchenko V. G., Halicek M. T., Norman M. L., Turk M. J., Abel T., Smith B. D., 2014, *MNRAS*, **442**, [2560](#)
- Wisnioski E., et al., 2019, *ApJ*, **886**, [124](#)
- Withers S., et al., 2023, arXiv e-prints, p. [arXiv:2304.11181](#)
- Witten C., et al., 2023, arXiv e-prints, p. [arXiv:2303.16225](#)

- Worseck G., Prochaska J. X., Hennawi J. F., McQuinn M., 2016, *ApJ*, **825**, 144
- Wright G. S., et al., 2015, *PASP*, **127**, 595
- Xu X., et al., 2022a, *ApJ*, **933**, 202
- Xu X., et al., 2022b, *ApJ*, **933**, 222
- Yang Y., Zabludoff A., Jahnke K., Davé R., 2014, *ApJ*, **793**, 114
- Yang J., et al., 2020, *ApJ*, **904**, 26
- Yoshida N., Abel T., Hernquist L., Sugiyama N., 2003, *ApJ*, **592**, 645
- Yue B., et al., 2018, *ApJ*, **868**, 115
- Zahid H. J., Dima G. I., Kudritzki R.-P., Kewley L. J., Geller M. J., Hwang H. S., Silverman J. D., Kashino D., 2014, *ApJ*, **791**, 130
- Zahid H. J., Kudritzki R.-P., Conroy C., Andrews B., Ho I. T., 2017, *ApJ*, **847**, 18
- de Barros S., et al., 2016, *A&A*, **585**, A51
- del Valle-Espinosa M. G., Sánchez-Janssen R., Amorín R., Fernández V., Sánchez Almeida J., García Lorenzo B., Papaderos P., 2023, *MNRAS*, **522**, 2089
- van der Wel A., et al., 2011, *ApJ*, **742**, 111
- van der Wel A., et al., 2012, *ApJS*, **203**, 24
- van der Wel A., et al., 2014, *ApJ*, **788**, 28

## Publications

### First-author publications

1. *The VANDELS survey: Global properties of CIII]λ1908Å emitting star-forming galaxies at  $z \sim 3$*   
**Llerena M.**, Amorín R., Cullen F., Pentericci L., et al.  
A&A, Volume 659, A16, <https://doi.org/10.1051/0004-6361/202141651>.
2. *Ionized gas kinematics and chemical abundances of low-mass star-forming galaxies at  $z \sim 3$*   
**Llerena M.**, Amorín R., Pentericci L., Calabrò A., et al.  
Accepted for publication in A&A, <https://doi.org/10.1051/0004-6361/202346232>.

### Co-authored publications

1. Naidu R. P., et al. (included **Llerena M.**), The synchrony of production and escape: half the bright Ly $\alpha$  emitters at  $z \sim 2$  have Lyman continuum escape fractions  $\sim 50$  per cent, MNRAS, 510, 4582, <https://doi.org/10.1093/mnras/stab3601>.
2. Matthee, J., et al. (included **Llerena M.**), *(Re)Solving Reionization with Ly $\alpha$ : How Bright Ly $\alpha$  Emitters account for the  $z \sim 2 - 8$  Cosmic Ionizing Background*, MNRAS, Volume 512, Issue 4, pp.5960-5977, <https://doi.org/10.1093/mnras/stac801>.
3. Saxena A., et al. (included **Llerena M.**), *No strong dependence of Lyman continuum leakage on physical properties of star-forming galaxies at  $3.1 < z < 3.5$* , MNRAS, 511, 120, <https://doi.org/10.1093/mnras/stab3728>.
4. Begley, R., et al. (included **Llerena M.**), *The VANDELS survey: a measurement of the average Lyman-continuum escape fraction of star-forming galaxies at  $z = 3.5$* , MNRAS, Volume 513, Issue 3, pp.3510-3525, <https://doi.org/10.1093/mnras/stac1067>.
5. Berg, D. A. et al. (included **Llerena M.**), *The COS Legacy Archive Spectroscopy Survey (CLASSY) Treasury Atlas*, ApJ Supplement Series, Volume 261, Issue 2, id.31, 41 pp., <https://iopscience.iop.org/article/10.3847/1538-4365/ac6c03>.
6. James, Bethan L. et al. (included **Llerena M.**), *CLASSY II: A technical Overview of the COS Legacy Archive Spectroscopic Survey*, ApJS, 262, 37, <https://iopscience.iop.org/article/10.3847/1538-4365/ac8008>.
7. Calabrò, A. et al. (included **Llerena M.**), *The properties of the Interstellar Medium in star-forming galaxies at redshifts  $2 < z < 5$  from the VANDELS survey*, A&A, volume 667, A117, <https://doi.org/10.1051/0004-6361/202244364>.
8. Saxena A., et al. (included **Llerena M.**), *Strong C IV emission from star-forming galaxies: a case for high Lyman continuum photon escape*, MNRAS, Volume 517, Issue 1, November 2022, Pages 1098-1111, <https://doi.org/10.1093/mnras/stac2742>.

9. Mingozi, M. et al. (included **Llerena M.**), *CLASSY IV: Exploring UV diagnostics of the interstellar medium in local high- $z$  analogs at the dawn of the JWST era*, ApJ, 939, 110, <https://iopscience.iop.org/article/10.3847/1538-4357/ac952c>.
10. Mascia, S. et al. (included **Llerena M.**), *Insights into the reionization epoch from cosmic-noon-CIV emitters in the VANDELS survey*, A&A, Volume 674, A221, <https://doi.org/10.1051/0004-6361/202245152>.
11. Calabrò, A. et al. (included **Llerena M.**), *The environmental dependence of the stellar and gas-phase mass-metallicity relation at  $2 < z < 4$* , A&A, Volume 664, id.A75, <https://doi.org/10.1051/0004-6361/202142615>.

---

## Acknowledgments

What a ride! After lots of written words, hundreds of plots, and unmeasurable effort during this Thesis, I want to thank you, the *reader*. If you are reading this, everything was worth it. I use this last page to extend my sincere gratitude to people and teams for their invaluable contributions to the completion of this Thesis.

First and foremost, I express my deepest appreciation to Ricardo for their guidance, wisdom, and tenacious support throughout this research work. His expertise, encouragement, and insightful feedback have been instrumental in shaping my research and academic growth. Working these four years in a framework including an *estallido social* and a pandemic was not easy, but his support and constant ideas helped me to go forward.

I am immensely grateful to all the faculty members of the Astronomy Department at ULS for fostering an enriching research environment. In particular, I want to thank the members of my Doctoral Advisory Committee for their constructive and positive feedback at the end of each semester.

I extend my heartfelt appreciation to the reviewers and examiners who took the time to evaluate my Thesis and provide constructive feedback. Their valuable comments and suggestions have helped me refine and strengthen the final version of this work.

I had the fantastic opportunity to work with great teams and to meet researchers whom I extend my genuine thanks for their support and for creating a collaborative atmosphere. I would like to thank people from the VANDELS, VUDS, NIRVANDELS, CLASSY, and CEERS teams.

I would like to acknowledge the financial support provided by the National Agency for Research and Development (ANID) through the Scholarship Program/Doctorado Nacional/2019-21191036 and the corresponding 2-year *Gastos Operacionales* benefit. Their generosity and investment in scientific research have enabled me to pursue this PhD and have had a profound impact on the success of my project. I also want to thank the financial support from ANID/FONDECYT Regular/Grant 1202007 (PI Amorín, Ricardo), SOCHIAS/Scholarship/Adelina Gutiérrez, and PhD Program in Astronomy/ULS that has allowed me to participate in different conferences while doing this Thesis.

I want to thank the faculty members of the Instituto de Astrofísica de Andalucía and the INAF – Osservatorio Astronomico di Roma for making me feel incredibly welcome during my research visits. In particular, I am grateful to Enrique, Pepe, Laura, and Antonello who, besides being extremely supportive of my research, they were exceptionally thoughtful.

I am grateful to my colleagues, office mates, and fellow researchers in the Astronomy Department for their stimulating discussions and collaboration. Especially, I want to thank people from the *Gaussianas* group for sharing their experiences (good and bad news) that continuously expanded my knowledge in the field. From a personal point of view, I want to thank Camila, Dania, Ciria, Catalina, and Piera, who since day zero, were always kind in this roller coaster of emotions.

Finally, I express my deepest gratitude to my family, who always believe in me and make me believe in myself. This journey would have been impossible without the support and patience of Sebas, to whom I dedicate this Thesis. His encouragement, love, and belief in my abilities have been the driving force behind my achievements.



**UNIVERSIDAD  
DE LA SERENA**  
CHILE



**DEPARTAMENTO  
ASTRONOMÍA**